Neutral Pion Electroproduction and development of a Neutral Particle Spectrometer

Ho San Ko

▶ To cite this version:

Ho San Ko. Neutral Pion Electroproduction and development of a Neutral Particle Spectrometer. High Energy Physics - Experiment [hep-ex]. Université Paris-Saclay; Seoul National University, 2020. English. NNT : 2020UPASS129 . tel-02927155

HAL Id: tel-02927155
https://theses.hal.science/tel-02927155v1

Submitted on 1 Sep 2020

Thèse de doctorat

NNT : 2020UPASS129

Neutral Pion Electroproduction and development of a Neutral Particle Spectrometer

Thèse de doctorat de l'université Paris-Saclay

École doctorale n°576 Particules hadrons énergie et noyau : instrumentation, image, cosmos et simulation (PHENIICS)
Spécialité de doctorat: Physique hadronique
Unité de recherche : Université Paris-Saclay, CNRS, IJCLab, 91405, Orsay, France
Référent : Faculté des sciences d'Orsay

Thèse présentée et soutenue à Séoul, le 07/07/2020, par

Ho San KO

Composition du Jury

Nicole D'HOSE Docteure, CEA/Irfu/DPhN-Saclay	Présidente
Hélène FONVIEILLE Docteure, Laboratoire de Physique de Clermont-Ferrand	Rapportrice & Examinatrice
Barbara PASQUINI Professeure, Università di Pavia	Rapportrice & Examinatrice
Sunghoon JUNG Professeur, Seoul National University	Examinateur
Sun Kee KIM Professeur, Seoul National University	Examinateur
Un-ki YANG Professeur, Seoul National University	Examinateur
Carlos MUÑOZ CAMACHO Docteur, Laboratoire de Physique des 2 Infinis Irène Joliot-Curie	Directeur de thèse
Seonho CHOI Professeur, Seoul National University	Co-Directeur de thèse

Acknowledgments

I would like to start by thanking all the jury members for spending their time examining this work. Even though the time given to them was relatively short, they kindly accepted their roles. I especially thank one of the rapportrices, Hélène Fonvieille for the comments she gave me to improve the quality of my thesis.

My five-year PhD was a joint program between Seoul National University in Korea and Université Paris-Saclay in France. I did my first two years in Korea taking lectures and participating in several projects under the supervision of Seonho Choi. Thanks to Seonho, I took my hands on different fields of physics from elementary particle physics to nuclear physics. Also, it was he who made it possible for me to come to France and start a Joint-PhD program.

For the last three years, I carried out my thesis in the Physique des Hautes Énergies (PHE) group at Laboratoire de Physique des 2 Infinis Irène Joliot-Curie (IJCLab) and Carlos Muñoz Camacho was my supervisor. His endless day and night guidance helped me doing my work very much. I enjoyed every moment with him from discussing my work to just casual talking. I was always at ease due to his open minds and was able to ask whatever question I had in my mind: physics-related of course but other topics also. He always made the best environment for me to focus on work by providing as much support as he could and by taking care of the administrative works. No one would have been better than him as my supervisor. I feel sad that I am no longer under his supervision.

I would also like to show my thanks to people in the Détecteurs et Instrumentation group. Giulia Hull always gave me insights on how efficiently and effectively tackle the hardware problems. She also provided me the best environment for me to work in the laboratory by providing the tools whenever I needed. Thi Nguyen Trung helped me with using the power supplies and the electronic read-out systems. I was fascinated by him taking thousands of power supplies and read-out channels in an elegant way. Whenever Emmanuel Rindel showed the collaboration with the newest design or the prototype of the detector frame, I was impressed. His request on the simulation results or the hardware measurements pushed me harder to work more. Working on hardware always tends to (at least for me) break something and Emmanuel and Thi were always there to help me taking care of the problems.

From time to time, with Carlos, Emmanuel, or Giulia, I met people in the Mécanique group. Meeting and having feedbacks from them was always fruitful. I still remember the moment that we found out that it is better to use the optical grease than the silicon cookie: you guys saved me a great amount of time.

Valera Dormenev gave me a lot of insights into the radiation damage and curing of the crystals. Irradiation tests and light yield measurements with Rong Wang were always fun. I admire his learning and working speeds: even though it was his first time doing hardware works, I learned a lot working with him. I hope we get to see the fully constructed NPS in action together someday.

Comments and requests from NPS collaboration were always interesting and helped my work to become richer. I have learned a lot from Rolf Ent, Bogdan Wojtsekhowski, Tanja Horn, and many others. I am grateful to be part of a great collaboration.

The discussions I had with the Hall A DVCS collaboration boosted the speed of my analysis. Charles Hyde-Wright's and Julie Roche's consultations advanced my understanding of the work. Po-Ju Lin also gave me enough guidance in the analysis, directly and indirectly. Thank you for dedicating your time to discuss and explain the works.

Thank you Jean-Yves Zana in the Division Achats et Logistique for always welcoming me and making everything easier to go on missions.

The PHE group, with the staff members: Silvia Niccolai; Raphaël Dupré; Mostafa Hoballah; Dominique Marchand; Eric Voutier; and Carlos, gave me only good advice not only on works but the ways of living in general. To my friends from the lab: IPN kindergarden (it is not a typo, it is a name); Rotative Flageolet Frames; WhoWillWinTheBets; Gabriel Charles and Olga Kochebina Charles; and Chun-Lu Huang and Sizar Aziz on the other side of the corridor, I thank you for making my life in Orsay and Paris crazy.

To my parents, I am sorry that I do not call you often. Thank you for trying to understand that and I love you. I thank my wife Suji for being with a crazy weird guy: I appreciate all your mental and physical supports. To my

sister, Soo Weon. I do not know how to start thanking you. I cannot imagine my life without you. Whomever in this paragraph, I love you all.

Contents

Introduction

Protons and neutrons, i.e. nucleons, are the basic building blocks of the matter in the visible universe. The strong force binds the nucleons to form nuclei. The electromagnetic force forms the atoms by binding the electrons with the nuclei. The electromagnetic interaction is well understood by Quantum Electrodynamics (QED), which shows the most precise predictability amongst all the theories in physics. In QED, charges interact with each other by exchanging photons.

The Quantum Chromodynamics (QCD) describes the strong interaction. Its degrees of freedom are quarks and gluons, the fundamental constituents of the nucleons. The quarks interact with each other by exchanging gluons. However, unlike QED, the gluons interact amongst themselves. This feature of self bindings of the gluons confines the quarks and gluons in the nucleons/hadrons, never to be seen as free. In order to study some of the features of QCD, such as confinement or the structure of the nucleon, one usually needs to rely on experiments. Electromagnetic probes, governed by the well-understood QED, are excellent tools to probe the nucleon.

In general, different scales, e.g. electron beam energies, probe different regions of the nucleon. At low energy, of the order of a few GeV, the electron probes the nucleon in the valence quark region. As its energy increases, the electron probes the sea quark and gluon regions. The study of the nucleon structure in all these regions is needed to fully understand QCD.

Form factors and parton distribution functions measured from elastic scattering and deep inelastic scattering of leptons off nucleons have provided a partial view of the internal structure of the nucleon. In the mid-1990s, Generalized Parton Distributions (GPDs) were developed. These new objects are a generalization of the form factors and parton distribution functions, but contain richer information on the nucleon internal structure. GPDs are accessible experimentally by deep exclusive reactions. Deeply virtual Compton scattering (DVCS) and deeply virtual meson production (DVMP) are some examples.

The first dedicated DVCS/DVMP experiment took place in 2004 in Hall A at The Thomas Jefferson National Accelerator Facility, i.e. Jefferson Lab, in Virginia, U.S.A. A new DVCS/DVMP experiment, after the beam energy upgrade of Jefferson Lab, was carried out in Hall A in a wider kinematic range. Its data were taken from 2014 to 2016. In Hall C at Jefferson Lab, the next DVCS/DVMP experiment will take place. The Hall C experiment will further exploit the kinematic range with higher precision. A Neutral Particle Spectrometer (NPS) is in development to measure DVCS/DVMP events under high background conditions. Jefferson Lab will provide the highest precision data in the valence quark region for various exclusive reactions.

The Electron-Ion Collider (EIC) is a future experimental facility currently planned to start operations around 2030 in the U.S.A. Its high energy and high luminosity will probe the sea quark and gluon regions providing answers to the outstanding questions of QCD, in particular in the region where matter is dominated by gluons.

First of all, this document describes the data analysis and results of the Hall A neutral pion electroproduction off the proton, from the data taken in 2014-2016. Later, some of the developments towards the construction of the electromagnetic calorimeter of the NPS for the upcoming DVCS/DVMP experiment in Hall C are presented. Finally, one of the candidate materials for the EIC calorimeter, a glass scintillator, will be briefly introduced. I have participated to all these projects, in collaboration with many colleagues.

I present in this thesis my contributions to each of these projects. My contributions to the neutral pion data analysis were focused on background subtractions on the calorimeter, acceptance calculations, and the estimation of the systematic uncertainty associated to the event selection cuts. Some necessary information on calibrations of the detectors and data analysis methods are also described. In the NPS project, I performed background dose calculations and energy and position resolution studies of the calorimeter, all using Monte Carlo simulations, with realistic geometries of the experimental apparatus. Characterization of the crystals of the calorimeter was also done. Additionally, I measured the radiation hardness of some glass scintillator in its early stage of development. In order to have a future reference when the glass calorimeter prototype will be tested, I simulated the energy resolution of the prototype.

The text is organized as follows:

- Chapter 1 briefly reviews the theoretical framework to describe the structure of the nucleon. A short overview of the experimental status in the field is also included.
- Chapter 2 presents preliminary results of the $ep \to e'p'\pi^0$ (DVMP) cross section in one of the kinematics of the Hall A experiment. The experimental apparatus, the calibration of the detectors, and the data analysis methods are shown. A Monte Carlo simulation to calculate the acceptance of the calorimeter is described. Finally, the systematic uncertainties associated to the event selection cuts are discussed.
- Chapter 3 presents the development of the NPS. The background dose estimates and the energy and position resolution calculations using Monte Carlo simulations are described. The characterization of lead tungsten crystals for the electromagnetic calorimeter is shown, together with a method to maintain the energy resolution of the calorimeter in a high radiation environment.
- Chapter 4 is relatively short, and discusses a new glass scintillator which could be a good cost-efficient candidate for forward calorimeters at EIC. The glass radiation hardness measurements are shown. Also, simulations of the energy resolution of a future prototype are described.

Chapter I

Accessing the nucleon structure

The electron is one of the best probes of the nucleon internal structure. Firstly, it is point-like, with no internal structure itself. Secondly, it only interacts through the electromagnetic force, which is well-known and governed by the laws of Quantum Electrodynamics (QED).

The cross section of elastic scattering of electrons (leptons in general) off the nucleon is parameterized by the form factors. Their Fourier transform from the momentum space to position space provides the spatial distribution of the constituents inside the nucleon. Deep inelastic scattering of electrons off the nucleon gives access to parton distribution functions. The parton distribution functions give us information about the momentum distribution of the nucleon internal constituents.

However, the description of the nucleon structure provided by form factors and parton distribution functions is incomplete. Generalized Parton Distributions (GPDs), which are a generalization of the form factors and the parton distribution functions, have an additional dimension and thus have richer information about the nucleon.

Experiments play an important role in the parameterization of GPDs and the GPDs are accessible via deep exclusive reactions. One of the cleanest and easiest exclusive reaction is deeply virtual Compton scattering (DVCS). Deeply virtual meson production (DVMP) also gives access to GPDs and by detecting different types of meson, the flavor separations of the GPDs are possible.

This chapter provides a brief overview of elastic scattering and deep inelastic scattering with their form factors and parton distribution functions. In the following, GPDs with DVCS and DVMP are presented. A few experimental results are discussed to give the current status of the experiments. Finally, upcoming and future experiments of interest are mentioned.

1 Form factors and elastic scattering

The charge distribution of a system can be determined by measuring the angular distribution of the scattered electrons and comparing it to the known cross section of electron scattering off a point charge:

$$\frac{d\sigma}{d\Omega} = \left(\frac{d\sigma}{d\Omega}\right)_{\text{point}} |F(q)|^2 , \tag{I.1}$$

where the momentum transfer between the incident electron and the target is represented as q (see Fig. I.1). The structure of the system is then deduced from the form factor $F(q)$. For the case of a static target, the form factor is the Fourier transform of the charge distribution:

$$F(\mathbf{q}) = \int \rho(\mathbf{x}) e^{i\mathbf{q}\cdot\mathbf{x}} d^3x, \tag{I.2}$$

where $\rho(\mathbf{x})$ denotes the charge distribution of the target. If $|\mathbf{q}|$ is not too large, the exponential in Eq. (I.2) can be expanded to

$$\begin{aligned} F(\mathbf{q}) &= \int \left(1 + i\mathbf{q}\cdot\mathbf{x} - \frac{(\mathbf{q}\cdot\mathbf{x})^2}{2} + \cdots\right) \rho(\mathbf{x}) d^3x \\ &= 1 - \frac{1}{6} |\mathbf{q}|^2 \left\langle r^2 \right\rangle + \mathcal{O}(|\mathbf{q}|^4), \end{aligned} \tag{I.3}$$

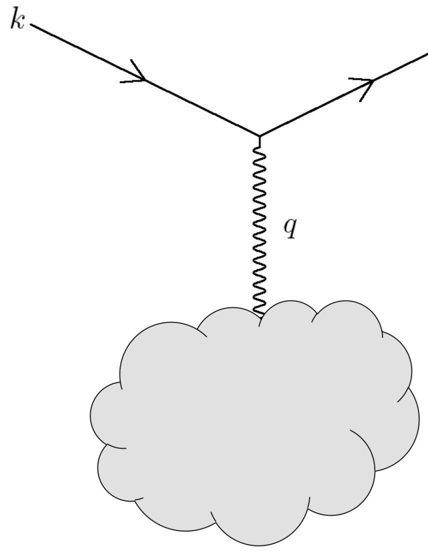

Figure I.1: The electron scatters from a charged object in the one-photon exchange approximation. The electron with initial momentum $k = (E, \mathbf{k})$ scatters off the charged object, and change its momentum to $k' = (E', \mathbf{k}')$ by transferring the momentum $q = k - k' = (\nu, \mathbf{q})$ to the object.

with an assumption of spherically symmetric charge distribution. From Eq. (I.3), one can therefore measure the mean square of the radius $\langle r^2 \rangle = -6 \left. \frac{dF(\mathbf{q})}{d|\mathbf{q}|^2} \right|_{|\mathbf{q}|^2=0}$ by electron scattering with a small momentum transfer.

The cross section of an electron elastically scattering off a spin-less and point-like target with charge e leads to the Mott differential cross section:

$$\left(\frac{d\sigma}{d\Omega}\right)_{\text{point}} \equiv \left(\frac{d\sigma}{d\Omega}\right)_{\text{Mott}} = \frac{\alpha^2}{4E^2 \sin^4\frac{\theta}{2}} \frac{E'}{E} \cos^2\frac{\theta}{2}, \tag{I.4}$$

with θ indicating the angle between the directions of the initial and final electrons in the target rest frame (rest mass of M), α representing fine-structure constant, and where

$$\frac{E'}{E} = \frac{1}{1 + \frac{2E}{M} \sin^2\frac{\theta}{2}} \tag{I.5}$$

arises from the conservation of the energy and momentum of the scattering process. The Mott differential cross section of an electron elastically scattering off a point-like spin 1/2 target with Dirac magnetic moment is given by

$$\left(\frac{d\sigma}{d\Omega}\right)_{\text{Mott, spin 1/2}} = \frac{\alpha^2}{4E^2 \sin^4\frac{\theta}{2}} \frac{E'}{E} \cos^2\frac{\theta}{2} \left\{1 - \frac{q^2}{2M^2} \tan^2\frac{\theta}{2}\right\}. \tag{I.6}$$

It is worth noting that the first term in the brackets of Eq. (I.6) appears due to the spin of the projectile (electron), which also appears in Eq. (I.4), and the second term is due to the spin of the target and does not appear in Eq. (I.4).

When the target with spin 1/2 has an extended structure and an anomalous magnetic moment (e.g. a nucleon), one obtains the Rosenbluth cross section [1]:

$$\frac{d\sigma}{d\Omega} = \left(\frac{d\sigma}{d\Omega}\right)_{\text{Mott}} \left\{F_1^2(Q^2) + \frac{Q^2}{4M^2}\left[F_2^2(Q^2) + 2\left(F_1(Q^2) + F_2(Q^2)\right)^2 \tan^2\frac{\theta}{2}\right]\right\}, \tag{I.7}$$

with Dirac and Pauli form factors $F_1(Q^2)$ and $F_2(Q^2)$ respectively and the momentum transfer between the target and the electron $Q^2 \equiv -q^2$. The Q^2-dependence of the form factors arises from the finite size of the target. These two form factors parameterize the structure of the target in Fig. I.2 and can be determined experimentally by measuring the differential cross section as a function of the angle θ and Q^2. By measuring the cross section at different beam

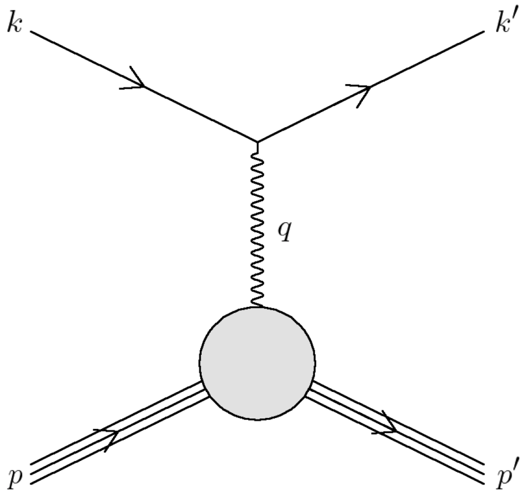

Figure I.2: The electron-nucleon elastic scattering in the one-photon exchange approximation. The electron with an initial momentum k scatters off the nucleon with an initial momentum p. After the scattering with the momentum transfer $q = k - k'$, the momenta of the final states are indicated as k' and p' for the electron and the nucleon, respectively.

energies but constant Q^2, it is possible to separate the form factors $F_1(Q^2)$ and $F_2(Q^2)$: this method is called a *Rosenbluth separation.* As in Eq. (I.6), the $\tan^2\frac{\theta}{2}$ term is due to the spin of the target.

The Sachs form factors are obtained by re-arranging the Dirac and Pauli form factors:

$$G_E(Q^2) = F_1(Q^2) - \frac{Q^2}{4M^2}F_2(Q^2), \tag{I.8a}$$

$$G_M(Q^2) = F_1(Q^2) + F_2(Q^2). \tag{I.8b}$$

Then the Rosenbluth cross section (Eq. (I.7)) can be written in terms of the Eq. (I.8) as

$$\frac{d\sigma}{d\Omega} = \left(\frac{d\sigma}{d\Omega}\right)_{\text{Mott}} \left\{ \frac{G_E^2 Q^2 + \frac{Q^2}{4M^2}G_M^2(Q^2)}{1 + \frac{Q^2}{4M^2}} + \frac{Q^2}{2M^2}G_M^2(Q^2)\tan^2\frac{\theta}{2} \right\}. \tag{I.9}$$

G_E is referred as electric and G_M as magnetic form factor. Following the Eq. (I.3), the mean square of the charge (r_E) and magnetic (r_M) radius of the nucleon can be obtained as:

$$\langle r_E^2 \rangle = -6\, \frac{dG_E(Q^2)}{dQ^2}\bigg|_{Q^2=0}, \tag{I.10a}$$

$$\langle r_M^2 \rangle = \frac{-6}{G_M(0)}\, \frac{dG_M(Q^2)}{dQ^2}\bigg|_{Q^2=0}. \tag{I.10b}$$

The proton charge radius measurements via elastic electron-proton (*ep*) scattering and hydrogen spectroscopy yielded consistent results of about 0.88 fm [2, 3, 4]. However, in 2010, from muonic hydrogen spectroscopy, the proton charge radius was measured to be 0.84184(67) fm [5], giving 7σ discrepancy from the previous measurements and started the *Proton radius puzzle.* The most recent elastic *ep* scattering at Jefferson Lab (PRad) measured a proton charge radius of 0.831(7)(12) fm [6]. Unlike other elastic *ep* scattering, PRad measured the form factor G_E at the lowest value of Q^2 ever, which is an order of magnitude lower than that of the previous elastic *ep* scattering [4]: indeed, low Q^2 values are crucial since the data need to be extrapolated to $Q^2 = 0$ as shown in Eq. (I.10).

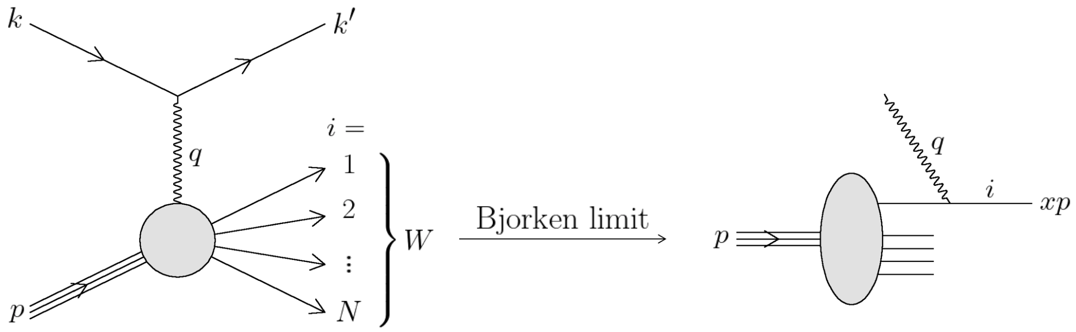

Figure I.3: Left: the $ep \to e'X$ scattering process in the one-photon exchange approximation. The photon with high virtuality breaks the nucleon and the escaped partons hadronize into numerous hadrons leaving the final states undetermined. Right: the $ep \to e'X$ scattering process in the Bjorken limit. The virtual photon strikes a quasi-free parton inside the nucleon. During the interaction between the parton and the photon, the spectator partons in the nucleon seem frozen.

2 Parton distribution functions and inclusive deep inelastic scattering

To further study the detailed structure of the nucleon, one might want to use higher Q^2 of the virtual photon for better spatial resolution. However, as the photon energy increases, the invariant mass (W, $W^2 = (q+p)^2$) of the system also increases. When the invariant mass of the system gets close to the mass of the resonance particles, the probability of the initial electron exciting the nucleon into a resonance particle becomes large. If one keeps increasing the Q^2 to a higher value, the invariant mass becomes large enough (approximately $W > 2$ GeV) to break the nucleon into pieces.

When not all the particles of the final state are detected, it is called inclusive scattering. The differential cross section for the inclusive inelastic $ep \to e'X$ (the undetected final states are denoted as X) scattering can be written as:

$$\frac{d^2\sigma}{dE'd\Omega} = \frac{\alpha^2}{4E^2 \sin^4\frac{\theta}{2}} \cos^2\frac{\theta}{2} \left\{ W_2(\nu, Q^2) + 2W_1(\nu, Q^2) \tan^2\frac{\theta}{2} \right\}, \tag{I.11}$$

where $W_1(\nu, Q^2)$ and $W_2(\nu, Q^2)$ are the structure functions. The left side of the Fig. I.3 illustrates the $ep \to e'X$ process.

When Q^2 and ν approach infinity, the so-called Bjorken limit, the structure functions become [7]:

$$MW_1(\nu, Q^2) = F_1(\omega), \tag{I.12a}$$

$$\nu W_2(\nu, Q^2) = F_2(\omega), \tag{I.12b}$$

where

$$\omega = \frac{2q \cdot p}{Q^2} = \frac{2M\nu}{Q^2}. \tag{I.13}$$

The $ep \to e'X$ process in the Bjorken limit is called deep inelastic scattering. The structure functions in Eq. (I.12) no longer depend on Q^2 and thus the differential cross section in Eq. (I.11) resembles the one in Eq. (I.6) with the identity $\frac{E'}{E} = \int dE' \delta(\nu - \frac{Q^2}{2M})$. This *scaling* behavior infers that the electron is scattering off a point-like particle with spin of 1/2 and it is called Bjorken scaling. To understand the Bjorken scaling, it is best to adopt the so-called infinite-momentum frame, where the momentum of the nucleon is infinite. In this frame, the motion of the constituents in the nucleon slows down by the time dilation and the charge distribution of the nucleon also Lorentz-contracts, from the view point of the electron. Then the electron interacts with an individual constituent of the nucleon instantaneously and incoherently. The right side of the Fig. I.3 illustrates this process. This is the famous *parton model*, developed by R. P. Feynman [8].

In the parton model, the point-like partons make up the nucleon. If the probability of the struck parton i to carry a fraction x of the momentum of the nucleon p is $q_i(x)$, then

$$\sum_i \int dx\ x\ q_i(x) = 1^*, \tag{I.14}$$

and the structure functions of the electron hitting the parton with a momentum fraction x and unit charge become

$$F_1(\omega) = \frac{1}{2x^2\omega}\delta\left(1 - \frac{1}{x\omega}\right), \tag{I.15a}$$

$$F_2(\omega) = \delta\left(1 - \frac{1}{x\omega}\right). \tag{I.15b}$$

By summing over the partons of the nucleon, one obtains:

$$F_1(\omega) = \sum_i \int dx e_i^2 q_i(x) x \delta\left(x - \frac{1}{\omega}\right), \tag{I.16a}$$

$$F_2(\omega) = \frac{\omega}{2} F_2(\omega). \tag{I.16b}$$

From the delta function $\delta\left(x - \frac{1}{\omega}\right)$ in Eq. (I.16), one finds that the momentum fraction x is identical to the dimensionless variable $x_B \equiv \frac{Q^2}{2M\nu}$ which is purely dependent on the virtual photon. Therefore, it is possible to interpret that the function $q_i(x)$ describes the probability of the virtual photon to strike the parton i with momentum fraction x_B. The probability $q_i(x)$ is called parton distribution function.

In the infinite-momentum frame, the nucleon approaches the speed of light in a certain direction. Therefore, the momentum fraction x carried by the parton is, to be precise, a "longitudinal" momentum fraction with respect to the virtual photon. The parton distribution function, thus, represents the longitudinal momentum distribution of the partons inside the nucleon.

Experimentally, the ratio of the photo-absorption cross sections between longitudinally polarized (L) and transversely polarized (T) virtual photons (at high Q^2 and ν with fixed ω), σ_L/σ_T, was found small and not increasing with Q^2 [9] which is an indication that the partons have spin 1/2. This is one of the many experimental results favoring that the partons from the Feynman's model are indeed the quarks from the Gell-Mann's model [10].

The Bjorken scaling which had led to the birth of the parton model gets violated at large or small x_B: see Fig. I.4. This violation of Bjorken scaling is a signature of gluon emission. This section have shown that at high Q^2, the virtual photon starts to interact with point-like particles. However, beyond the value of Q^2 resulting the Bjorken scaling, the Quantum Chromodynamics (QCD) predicts that the virtual photon starts to see that the quark itself is surrounded by a cloud of additional partons. Therefore, with increasing Q^2, the probability to find quarks with large x decreases and it increases with small x because quarks with high x radiate gluons.

3 Factorization and light-cone coordinate

3.1 Factorization

The parton model successfully describes the deep inelastic scattering (DIS) cross section. The DIS cross section can be separated into the cross section of the electron-quark scattering ($eq \to eq$) and the parton distribution functions:

$$\sigma_{DIS}(x, Q^2) = \sum_i \sigma_{eq\to eq}(x, Q^2) q_i(x). \tag{I.17}$$

As it can be seen in Eq. (I.17), the DIS cross section is expressed by the combination of two probabilities: $\sigma_{eq\to eq}(x, Q^2)$ and $q_i(x)$. This is the concept of the QCD factorization [12] and the Eq. (I.17) has later been proven in QCD in the Bjorken limit. The factorization scheme separates the short-distanced hard subprocess and long-distanced soft subprocess† (see Fig. I.5):

$$\text{Scattering amplitude} = \int d^4k H(k) \otimes A(k), \tag{I.18}$$

---

[*] At sufficiently high Q^2, this does not yield the value 1. It is because the photon does not couple to gluons which carry about half of the momentum of the nucleon. It is better to consider the value 1 as the total momentum sum of the quarks.

[†] However, factorization is not always applicable. For example, the factorization for the meson electroproduction off the nucleon with transversely polarized photons has not been proven: see section 4.3.2.

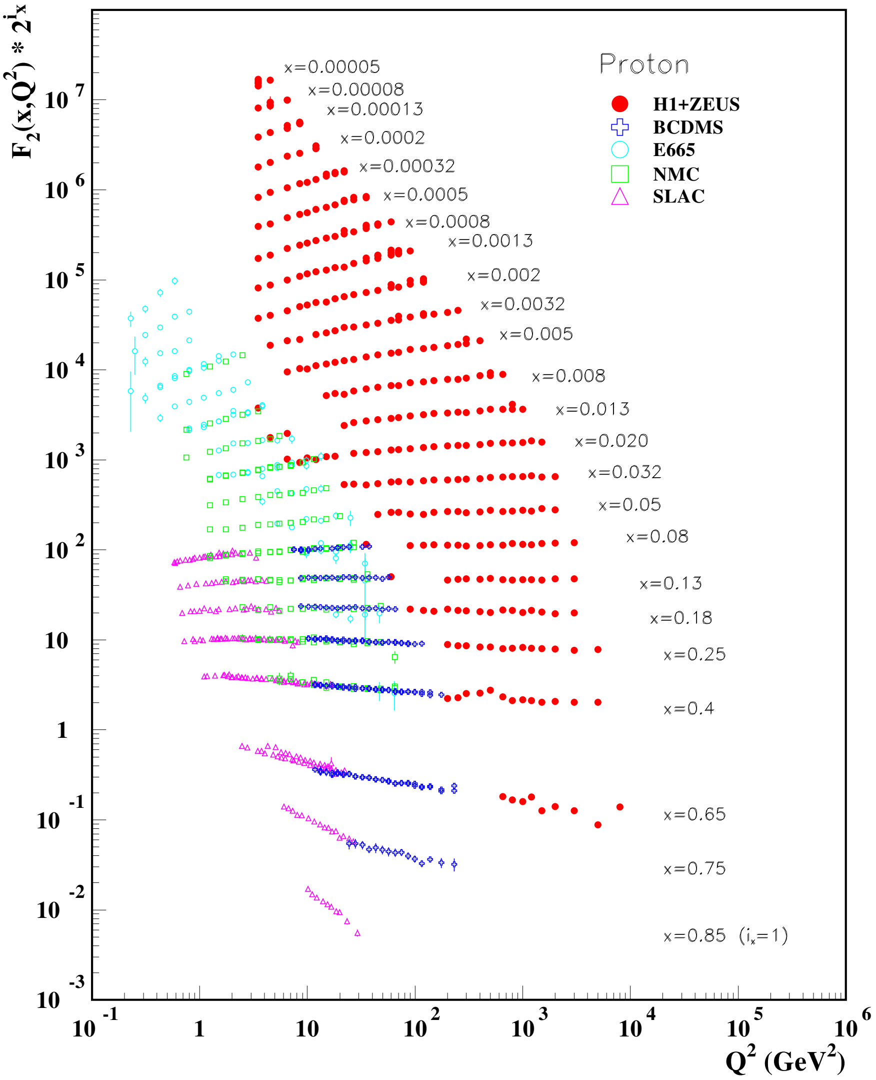

Figure I.4: The structure function $F_2(x_B)$ with variables x_B and Q^2 measured from the experiments [11]. Near the value $x_B \sim 0.2$, the structure function has a clear scaling behavior. As the Q^2 increases, the scaling is violated. For $x_B \lesssim 0.2$, $F_2(x_B)$ increases with Q^2 while for $x_B \gtrsim 0.25$, it decreases.

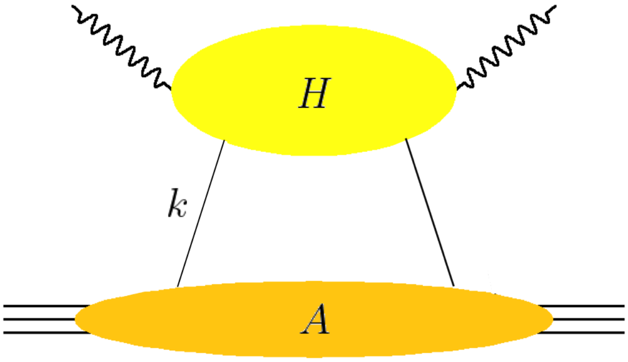

Figure I.5: Visual representation of the factorization scheme. H represents the hard subprocess and A represents the soft subprocess.

where the hard subprocess amplitude is represented as $H(k)$ and the soft subprocess as $A(k)$. The hard subprocess is perturbatively calculable due to the *asymptotic freedom* of QCD: the strong coupling constant $\alpha_s(Q^2)$ approaches zero as Q^2 increases. The soft subprocess on the other hand is non-perturbative and all the ignored dynamics of the partons in the nucleon during the scattering are absorbed in $A(k)$. In the case of the DIS, the hard part is the $\sigma_{eq\to eq}(x, Q^2)$ and the soft part is the $q_i(x)$. Factorization allows to access the universal nucleon structure parameterized by $A(k)$ by using different hard subprocesses $H(k)$.

3.2 Light-cone coordinate

It is possible to further simplify the scattering amplitude (Eq. (I.18)) by adopting a frame reference where the initial and final nucleons are collinear along the z-axis and the light-cone components are defined as

$$w^{\pm} = (w^0 \pm w^3)/\sqrt{2}, \tag{I.19a}$$

$$\mathbf{w} = (w^1,\ w^2). \tag{I.19b}$$

Some of their properties are:

$$w \cdot v = (w^- v^+ + w^+ v^-)/2 - \mathbf{w} \cdot \mathbf{v}, \tag{I.20a}$$

$$w^+ \xrightarrow[\alpha \text{ in } z\text{-axis}]{\text{Lorentz boost}} e^a w^+, \tag{I.20b}$$

$$w^- \xrightarrow[\alpha \text{ in } z\text{-axis}]{\text{Lorentz boost}} e^{-a} w^-, \tag{I.20c}$$

$$\mathbf{w} \xrightarrow[\alpha \text{ in } z\text{-axis}]{\text{Lorentz boost}} \mathbf{w}, \tag{I.20d}$$

where a is $\frac{1}{2}\ln\frac{1+\alpha}{1-\alpha}$. In the frame of reference where the initial and final momenta of the proton are in the positive z-direction and the initial and final momenta of the photon are in the negative z-direction, one can perform a Taylor expansion of the hard subprocess scattering amplitude: $H(k^+, k^-, \mathbf{k}) \simeq H(k^+, 0, 0,)$. This approximation treats the incoming and outgoing partons in the hard scattering subprocess as exactly collinear ($\mathbf{k} = 0$) and on-shell ($k^- = 0$). Therefore, the scattering amplitude gets further simplified as

$$\int d^4k H(k) A(k) \approx \int dk^+ H(k^+, 0, 0) \int dk^- d^2\mathbf{k} A(k^+, k^-, \mathbf{k}). \tag{I.21}$$

Throughout this thesis, the hard subprocess $H(k)$ will include only a single virtual photon exchange with a single quark, i.e. leading-order and leading-twist[‡]. This remains a good approximation at sufficiently high Q^2.

[‡] The formal definition of *twist* is the mass dimension of the operator minus its spin. In a more simplistic description, one can consider that the number of quark and gluon lines connected to the soft part indicates the level of twist. The leading-twist is then 2. The amplitude of higher twist contributions is suppressed by increasing powers of $\frac{1}{Q}$.

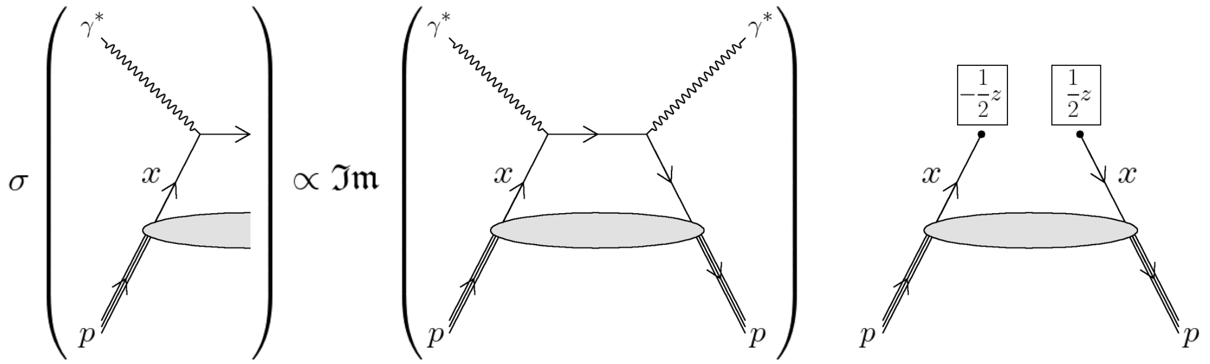

Figure I.6: Illustration of the optical theorem for inclusive deep inelastic scattering (left) and the associated matrix element of forward Compton scattering (right).

3.2.1 Matrix elements of parton distribution functions and form factors

The optical theorem [13] allows to identify the total deep inelastic scattering cross-section to the imaginary part of the amplitude of the forward Compton scattering. The corresponding matrix element of this soft process is

$$\langle p|\,\overline{\psi}_q(-\frac{1}{2}z)\Gamma\psi_q(\frac{1}{2}z)\,|p\rangle\,, \tag{I.22}$$

where $\psi_q(z)$ denotes the quark field operator of flavor q at space-time point z and the superscript Γ represents the Dirac matrices, 1, γ^5, γ^μ, $\gamma^\mu\gamma^5$, and $\sigma^{\mu\nu} = \frac{i}{2}[\gamma^\mu, \gamma^\nu]$. This is a "non-local" (two space-time points, $-\frac{1}{2}z$ and $\frac{1}{2}z$, are involved) "forward" (the initial and final nucleon momenta are the same) matrix element. The Fig. I.6 illustrates the optical theorem for the deep inelastic scattering and the matrix element of the forward Compton scattering.

The Fourier transformation of this matrix element gives rise to the parton distribution functions from the deep inelastic scattering:

$$q(x) = \frac{p^+}{2}\int\frac{dz^-}{2\pi}e^{ixp^+z^-}\,\langle p|\,\overline{\psi}_q(-\frac{1}{2}z)\gamma^+\psi_q(\frac{1}{2}z)\,|p\rangle\Big|_{z^+=0,\mathbf{z}=0}\,, \tag{I.23a}$$

$$\Delta q(x) = \frac{p^+}{2}\int\frac{dz^-}{2\pi}e^{ixp^+z^-}\,< p|\overline{\psi}_q(-\frac{1}{2}z)\gamma^+\gamma^5\psi_q(\frac{1}{2}z)|p>\Big|_{z^+=0,\mathbf{z}=0}\,. \tag{I.23b}$$

Therefore, the collinear parton density only depends on k^+ $(= xp^+)$. There are only two quark helicity conserving parton distribution functions at leading-twist: unpolarized $(q(x))$ and polarized $(\Delta q(x))$. There is a transversity distribution at leading-twist. However, the quark helicity is not conserved: $(\Gamma = \sigma^{\mu\nu})$.

Similar to deep inelastic scattering, the matrix element for the elastic scattering can be written as:

$$\langle p'|\,\overline{\psi}_q(0)\Gamma\psi_q(0)\,|p\rangle\,, \tag{I.24}$$

where in this case, it is "local" (only one interaction space-time point 0 is involved) and "off-forward" (the initial and final momenta of the nucleon are different). Fig. I.7 illustrates the matrix element of elastic scattering. The matrix element of Eq. (I.24) gives rise to the form factors:

$$\langle p'|\,\overline{\psi}_q(0)\gamma^+\psi_q(0)\,|p\rangle = F_1^q(t)\overline{N}(p')\gamma^+N(p) + F_2^q(t)\overline{N}(p')\frac{i\sigma^{+\nu}\Delta_\nu}{2M}N(p), \tag{I.25a}$$

$$\langle p'|\,\overline{\psi}_q(0)\gamma^+\gamma^5\psi_q(0)\,|p\rangle = G_A^q(t)\overline{N}(p')\gamma^+\gamma^5N(p) + G_P^q(t)\overline{N}(p')\frac{\gamma^5\Delta^+}{2M}N(p), \tag{I.25b}$$

where G_A^q and G_P^q represents the axial and pseudoscalar form factors and $\Delta = p' - p$ denotes the momentum transfer of the nucleon.

As it have been shown, form factors depend only on the momentum transfer t $(= Q^2$ for the elastic scattering) and its Fourier transformation to the position space yields the spatial distribution of partons inside the nucleon (see also the footnote § in page 22). Parton distribution functions which depend only on the longitudinal momentum fractions x can be interpreted as the probability to strike a parton with momentum fraction x inside the nucleon. Form factors and parton distributions have been measured for half a century and they are still being studied with great interests. However, the correlation between the spatial and momentum distributions of partons is not present in either form factors or parton distribution.

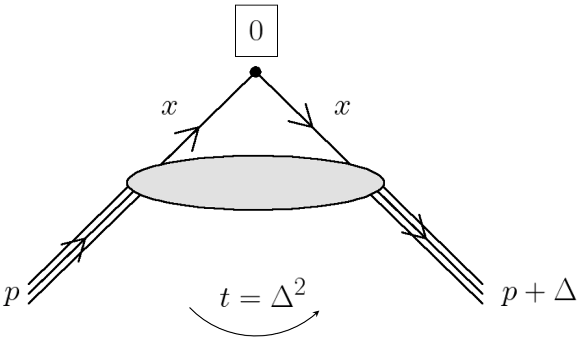

Figure I.7: Illustration of the matrix element of the elastic scattering.

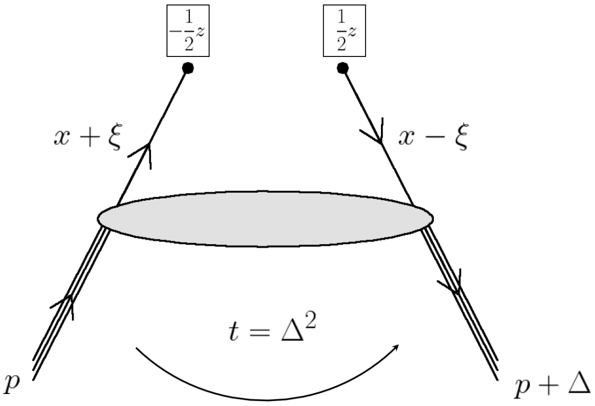

Figure I.8: Illustration of a non-local off-forward matrix element.

4 Generalized Parton Distributions

In the 1990s, the matrix element presented in the previous section were generalized to “non-local” “off-forward” matrix elements [14, 15, 16]:

$$\langle p'|\, \overline{\psi}_q(-\frac{1}{2}z)\Gamma\psi_q(\frac{1}{2}z)\, |p\rangle\,. \tag{I.26}$$

Following the convention of [17], the Fourier transformation of the matrix element yields:

$$\begin{aligned}
&P^+\int\frac{dz^-}{2\pi}e^{ixP^+z^-}\,\langle p'|\,\overline{\psi}_q(-\frac{1}{2}z)\gamma^+\psi_q(\frac{1}{2}z)\,|p\rangle\Big|_{z^+=0,\mathbf{z}=0}\\
&= H^q(x,\xi,t)\overline{N}(p')\gamma^+N(p) + E^q(x,\xi,t)\overline{N}(p')\frac{i\sigma^{+\nu}\Delta_\nu}{2M}N(p),
\end{aligned}\tag{I.27a}$$

$$\begin{aligned}
&P^+\int\frac{dz^-}{2\pi}e^{ixP^+z^-}\,\langle p'|\,\overline{\psi}_q(-\frac{1}{2}z)\gamma^+\gamma^5\psi_q(\frac{1}{2}z)\,|p\rangle\Big|_{z^+=0,\mathbf{z}=0}\\
&= \widetilde{H}^q(x,\xi,t)\overline{N}(p')\gamma^+\gamma^5N(p) + \widetilde{E}^q(x,\xi,t)\overline{N}(p')\frac{\gamma^5\Delta^+}{2M}N(p),
\end{aligned}\tag{I.27b}$$

where $P = \frac{p+p'}{2}$ stands for the average momentum of the initial and final nucleons and $\xi = -\frac{\Delta^+}{2P^+}$ represents the variable describing the so-called *skewness* of the initial and final momenta of the quark participating in the hard process. One can see that the variable ξ consists of purely longitudinal components of the momentum transfer whereas the variable $t = \Delta^2$ contains transverse momentum transfer. The functions $H^q(x,\xi,t)$, $E^q(x,\xi,t)$, $\widetilde{H}^q(x,\xi,t)$, and $\widetilde{E}^q(x,\xi,t)$ in Eq. (I.27) are the leading-twist generalized parton distributions (GPDs) of the quark of flavor q in the nucleon. This non-local off-forward matrix element is illustrated in Fig. I.8.

4.1 Properties of GPDs

The GPDs H^q and E^q in Eq. (I.27a) correspond to the averages over quark helicities and are called "unpolarized" GPDs. The GPDs $\widetilde{H}^q$ and $\widetilde{E}^q$ in Eq. (I.27b), on the other hand, are related to differences over the quark helicity and are called "polarized" GPDs. At the nucleon level, H^q and $\widetilde{H}^q$ leave the helicity of the nucleon unchanged whereas E^q and $\widetilde{E}^q$ flip it.

As previously hinted, when there is neither momentum transfer between the initial and the final states of the nucleon ($t = 0$) nor longitudinal momentum transfer between the initial and final states of the quark ($\xi = 0$), the GPDs H^q and $\widetilde{H}^q$ become the parton distribution functions q and Δq, respectively:

$$H^q(x, \xi = 0, t = 0) = q(x), \tag{I.28a}$$

$$\widetilde{H}^q(x, \xi = 0, t = 0) = \Delta q(x). \tag{I.28b}$$

Also, the first moments of the GPDs give rise to Dirac and Pauli form factors:

$$\int dx\ H^q(x, \xi, t) = F_1^q(t)\ ,\quad \int dx\ E^q(x, \xi, t) = F_2^q(t), \tag{I.29a}$$

$$\int dx\ \widetilde{H}^q(x, \xi, t) = G_A^q(t)\ ,\quad \int dx\ \widetilde{E}^q(x, \xi, t) = G_P^q(t). \tag{I.29b}$$

The impact-parameter ($\mathbf{b}$) interpretation of the GPDs [18, 19, 20] at $\xi = 0$ is acquired by Fourier transforming the transverse momenta of the light-cone components to the transverse space, while keeping the "+"-momentum unchanged:

$$\rho^q(x, \mathbf{b}) = \int \frac{d^2\boldsymbol{\Delta}}{(2\pi)^2} e^{i\mathbf{b}\cdot\boldsymbol{\Delta}} H_-^q(x, \xi = 0, t = -|\boldsymbol{\Delta}|^2), \tag{I.30}$$

where $\mathbf{b} = \frac{\sum_i p_i^+ \mathbf{b}_i}{\sum_i p_i^+}$ describes the center of momentum of the partons in the nucleon and $H_-^q(x, 0, t) \equiv H^q(x, 0, t) + H^q(-x, 0, t)$ (with $0 \leq x \leq 1$) defines a so-called non-singlet or valence GPD combination. The Eq. (I.30) can be interpreted as a density of the quarks of flavor q with longitudinal momentum fraction x at a given transverse distance $\mathbf{b}$ from the center of the nucleon. Furthermore, the x-dependent mean square of the radius of the quark density in the transverse plane is defined as:

$$\begin{aligned} \left\langle \mathbf{b}^2 \right\rangle^q (x) &= \frac{\int d^2\mathbf{b}\ \mathbf{b}^2 \rho^q(x, \mathbf{b})}{\int d^2\mathbf{b} \rho^q(x, \mathbf{b})}, \\ &= -4 \frac{\partial}{\partial \boldsymbol{\Delta}^2} \ln H_-^q(x, \xi = 0, t = -|\boldsymbol{\Delta}|^2)\big|_{\boldsymbol{\Delta}=0}. \end{aligned} \tag{I.31}$$

One retrieves the usual x-independent mean square of the radius of the transverse charge distribution of the quark q in the nucleon[§] from Eq. (I.31) by integrating over x:

$$\left\langle \mathbf{b}^2 \right\rangle^q = \frac{1}{N_q} \int_0^1 dx q(x) \left\langle \mathbf{b}^2 \right\rangle^q (x), \tag{I.32}$$

where $q(x)$ represents the parton distribution function of quark q and N_q denotes the integrated number of valence quarks. For the case of the proton, as an example, $N_u = 2$ and $N_d = 1$ which yields $\left\langle \mathbf{b}^2 \right\rangle = 2e_u \left\langle \mathbf{b}^2 \right\rangle^u + e_d \left\langle \mathbf{b}^2 \right\rangle^d$ with the electric charge of the quarks $e_u = (2/3)e$ and $e_d = -(1/3)e$.

In [21], using the DVCS data with an electron beam and a proton target at Jefferson Lab, the authors managed to obtain a model-dependent $\left\langle \mathbf{b}^2 \right\rangle (x)$ for quarks in the proton. The result in Fig. I.9 shows that the mean square of the radius of the transverse quark distributions increases as the longitudinal momentum fraction decreases. One should note that the utilized range for x is limited to around [0.05, 0.2].

The kinematic variable x of the GPDs, unlike the other two variables ξ and t, is experimentally inaccessible. The GPDs are convoluted with x in the DVCS amplitude through quark propagators, for example, $1/(x - \xi + i\epsilon)$ in a form of

$$\int_{-1}^{1} \frac{F^q(x, \xi, t)}{x - \xi + i\epsilon} dx = \mathcal{P} \int_{-1}^{1} \frac{F^q(x, \xi, t)}{x - \xi} dx - i\pi F^q(\xi, \xi, t), \tag{I.33}$$

[§] The transverse charge distribution is obtained by Fourier transforming the form factor F_1 in the infinite-momentum frame ($Q^2 = t = -\boldsymbol{\Delta}^2$): $\rho(\mathbf{b}) = \int \frac{d^2\boldsymbol{\Delta}}{(2\pi)^2} e^{i\mathbf{b}\cdot\boldsymbol{\Delta}} F_1(t = -|\boldsymbol{\Delta}|^2)$. Then, $\left\langle \mathbf{b}^2 \right\rangle = \int d^2\mathbf{b}\ \mathbf{b}^2 \rho(\mathbf{b})$. The Taylor expansion (as in Eq. (I.3)) of the F_1 yields $1 - \frac{1}{6} |\boldsymbol{\Delta}|^2 \left\langle r^2 \right\rangle + \mathcal{O}(|\boldsymbol{\Delta}|^4)$. Finally, one finds the relation $\left\langle \mathbf{b}^2 \right\rangle = (2/3) \left\langle r^2 \right\rangle$.

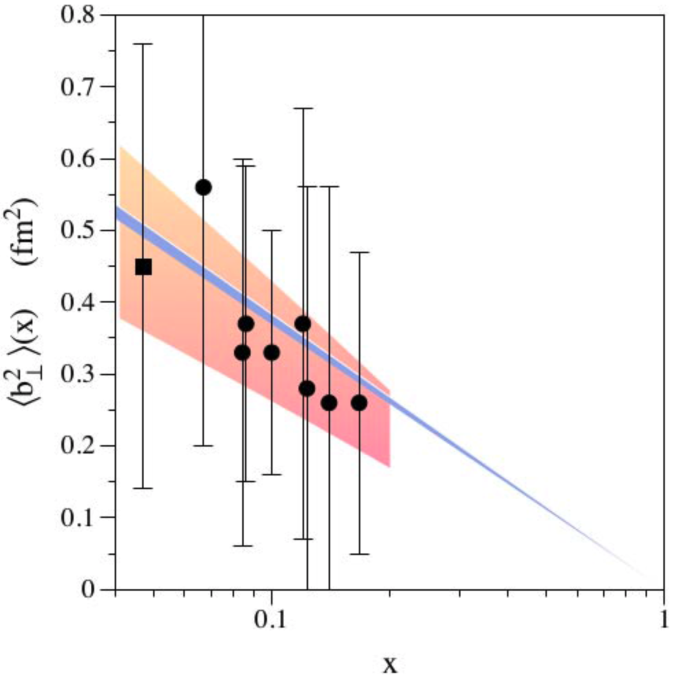

Figure I.9: Longitudinal momentum fraction x dependent mean square of the radius of the quark density in the transverse plane of the proton. The black points and blue band correspond to the results obtained using two similar GPD models. The red band represents the total model uncertainty. See [21] for more details.

where F^q represents the GPDs H^q, E^q, $\widetilde{H}^q$, and $\widetilde{E}^q$ and $\mathcal{P}$ indicates the principal value integral. Therefore, the observables of the GPDs are parameterized by the Compton form factors (CFFs):

$$\mathfrak{Re}\mathcal{H}^q(\xi,t) \equiv \mathcal{P}\int_0^1 dx\,[H^q(x,\xi,t) - H^q(-x,\xi,t)]\,C^+(x,\xi), \tag{I.34a}$$

$$\mathfrak{Re}\mathcal{E}^q(\xi,t) \equiv \mathcal{P}\int_0^1 dx\,[E^q(x,\xi,t) - E^q(-x,\xi,t)]\,C^+(x,\xi), \tag{I.34b}$$

$$\mathfrak{Re}\widetilde{\mathcal{H}}^q(\xi,t) \equiv \mathcal{P}\int_0^1 dx\,[H^q(x,\xi,t) + H^q(-x,\xi,t)]\,C^-(x,\xi), \tag{I.34c}$$

$$\mathfrak{Re}\widetilde{\mathcal{E}}^q(\xi,t) \equiv \mathcal{P}\int_0^1 dx\,[E^q(x,\xi,t) + E^q(-x,\xi,t)]\,C^-(x,\xi), \tag{I.34d}$$

$$\mathfrak{Im}\mathcal{H}^q(\xi,t) \equiv -\pi H(\xi,\xi,t) - H(-\xi,\xi,t), \tag{I.34e}$$

$$\mathfrak{Im}\mathcal{E}^q(\xi,t) \equiv -\pi E(\xi,\xi,t) - E(-\xi,\xi,t), \tag{I.34f}$$

$$\mathfrak{Im}\widetilde{\mathcal{H}}^q(\xi,t) \equiv -\pi H(\xi,\xi,t) + H(-\xi,\xi,t), \tag{I.34g}$$

$$\mathfrak{Im}\widetilde{\mathcal{E}}^q(\xi,t) \equiv -\pi E(\xi,\xi,t) + E(-\xi,\xi,t), \tag{I.34h}$$

(I.34i)

with the coefficient functions $C^\pm$ defined as

$$C^\pm(x,\xi) = \frac{1}{x-\xi} \pm \frac{1}{x+\xi}. \tag{I.35}$$

One might notice that the range of x integration has reduced from $[-1,\ 1]$ to $[0,\ 1]$ in the convolution and the variable x is either integrated over or evaluated at $x = \xi$.

The dispersion relation relates the real part and the imaginary part of the leading-twist CFFs [22, 23]:

$$\mathfrak{Re}\mathcal{H}(\xi,t) = D(t) - \mathcal{P}\int_{-1}^1 dx\ \mathfrak{Im}\mathcal{H}(x,t)C^+(x,\xi), \tag{I.36}$$

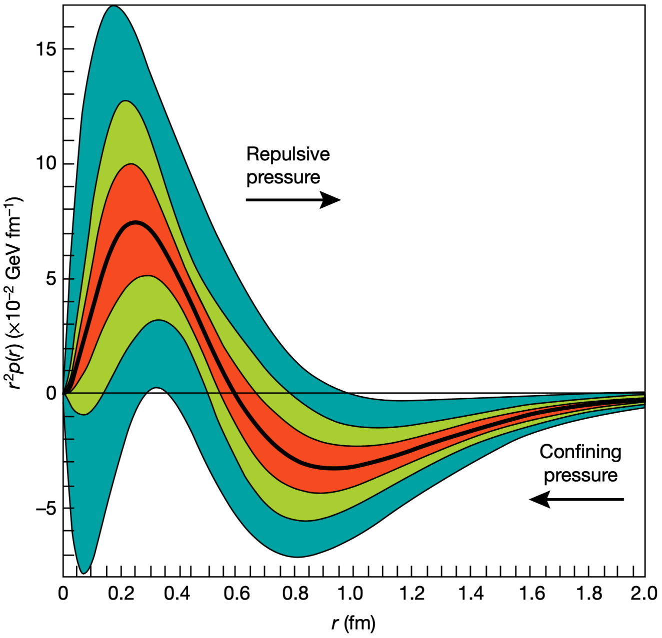

Figure I.10: Radial pressure distribution in the proton. The thick black line corresponds to the pressure extracted from the D-term parameters fitted to the experimental data, with the green band indicating the associated estimated uncertainties. The blue area represents the uncertainties from the experiments at Jefferson Lab using an electron beam of energy up to 6 GeV. The red band shows the projected experimental uncertainties when the beam energy goes up to 12 GeV. See [26] for more details.

where the subtraction constant $D(t)$ on the right hand side is usually referred to as the D-term [24].

In the Breit frame, the D-term can be related to the spatial distributions of the shear forces and the pressures inside the nucleon [25]. In [26], the authors obtained a model-dependent D-term by fitting the CFFs $\mathfrak{Re}\mathcal{H}$ and $\mathfrak{Im}\mathcal{H}$ on the experimental data from Jefferson Lab. Their extracted radial quark pressure distribution in the proton is presented in Fig. I.10.

4.2 Generalized transverse-momentum dependent parton distributions and sum rules

One can define even more generalized objects than GPDs: the generalized transverse-momentum dependent parton distributions (GTMDs) [27]. The GTMDs depend on the longitudinal momentum fraction x, the transverse momentum $\mathbf{k}$ of the parton and the momentum transfer to the nucleon, $\mathbf{\Delta}$ and ξ, in the light-cone frame. GTMDs reduce to form factors or parton distributions when taken to the forward limit and/or their variables are integrated. For example, if one integrates the GTMDs over $\mathbf{k}$, it reduces to the GPDs: see Fig. I.11 for the illustration.

The total angular momentum contribution J_z^q carried by the quark q to the nucleon spin along the virtual photon direction is related to the second moment of the GPDs [28, 15, 17, 29]:

$$J_z^q = \frac{1}{2}\int dx\, x[H^q(x,\xi=0,t=0) + E^q(x,\xi=0,t=0)], \tag{I.37}$$

where J_z^q can be decomposed into the spin contribution (s_z^q) and the orbital angular momentum contribution (L_z^q) of the quark: $J_z^q = \frac{1}{2}s_z^q + L_z^q$. The spin contribution of the quark is measured through the polarized deep inelastic scattering and is related to the GPD $\widetilde{H}^q$: $s_z^q = \int dx\, \widetilde{H}^q(x,\xi=0,t=0)$. By subtracting the spin contribution of the quarks from J_z^q, one can access the quark orbital angular momentum contribution to the nucleon spin along the virtual photon direction [29]:

$$L_z^q = \frac{1}{2}\int dx\, \left\{x[H^q(x,\xi=0,t=0) + E^q(x,\xi=0,t=0)] - \widetilde{H}^q(x,\xi=0,t=0)\right\}. \tag{I.38}$$

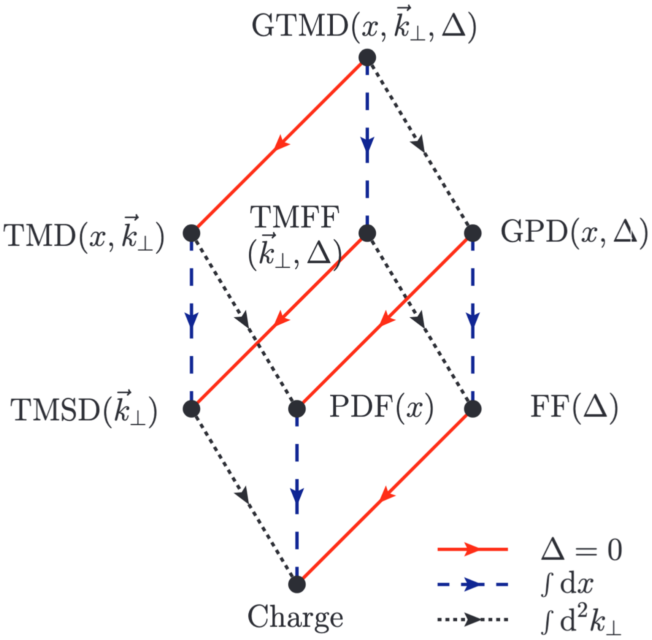

Figure I.11: Illustration of the GTMDs (generalized transverse-momentum dependent parton distributions) reducing to other form factors and parton distributions. PDF and FF represents the parton distribution functions and form factors, respectively, introduced in the previous sections. Transverse-momentum dependent parton distributions (TMDs) are accessible via semi-inclusive deep inelastic scattering. TMFF denotes transverse-momentum dependent form factors and TMSD stands for transverse-momentum dependent spin densities. In this figure, the transverse momentum **k** of the quark is denoted as $\vec{k}_\perp$. Figure extracted from [27].

4.3 Accessing GPDs through hard exclusive processes

The GPDs are accessible via suitable exclusive processes, in which the momentum transfer t is much smaller than the hard scale Q^2, and the main processes are deeply virtual Compton scattering (DVCS) and deeply virtual meson production (DVMP).

4.3.1 Deeply virtual Compton scattering

Deeply virtual Compton scattering (DVCS) is the simplest and cleanest exclusive reaction to access GPDs. In the initial state, the virtual photon emitted from the electron with high Q^2 interacts with one of the quarks in the nucleon and the struck quark emits an on-shell photon in the final state and get re-absorbed into the nucleon. Fig. I.12 shows the DVCS diagram at leading-order and leading-twist.

The differential cross section of the photon electroproduction off the nucleon ($ep \to e'p'\gamma$) can be written as [30]

$$\frac{d^5\sigma}{dt d\phi_e d\phi dQ^2 dx_B} = \frac{\alpha^3 x_B y}{16\pi^2 Q^2 \sqrt{1+\epsilon^2}} \left| \frac{\mathcal{T}}{e^3} \right|^2, \tag{I.39}$$

with e the electron charge, $y = (p \cdot q)/(p \cdot k)$, the variable $\epsilon \equiv 2x_B \frac{M}{Q}$, ϕ_e the azimuthal angle between the leptonic plane and a plane of reference (e.g. plane in the laboratory), and ϕ the azimuthal angle between the leptonic plane and the hadronic plane. Fig. I.13 illustrates the definition of the angle ϕ, the leptonic plane, and the hadronic plane: the leptonic plane is defined by the directions of the electron and the virtual photon and the hadronic plane by the real photon in the final process and the recoiled nucleon.

There is another $ep \to e'p'\gamma$ process than the DVCS: the Bethe-Heitler (BH) process. However, unlike the DVCS where the final photon is emitted from the nucleon, the BH process emits the photon from the electron. Therefore, the BH amplitude $\mathcal{T}_{\rm BH}$ is parameterized in terms of the electromagnetic form factors whereas the DVCS amplitude $\mathcal{T}_{\rm DVCS}$ is parameterized in terms of the GPDs. The amplitude $\mathcal{T}$ of the $ep \to e'p'\gamma$ process is the sum of the amplitudes of the DVCS and the BH processes: $\mathcal{T} = \mathcal{T}_{\rm BH} + \mathcal{T}_{\rm DVCS}$. Fig. I.14 illustrates the entanglement of the two processes at

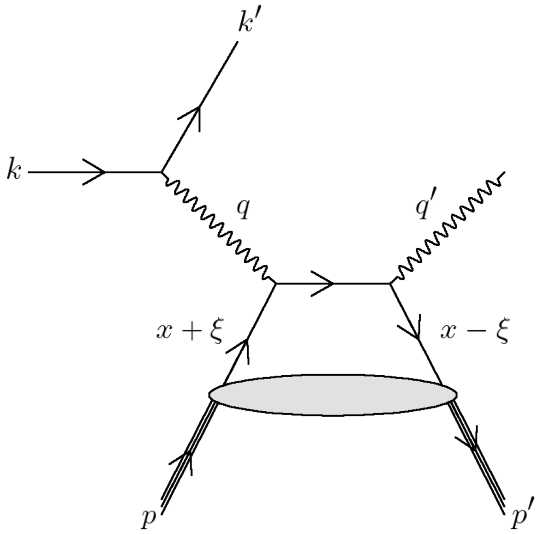

Figure I.12: The leading-order and leading-twist DVCS. The photon with high virtuality strikes one of the quarks inside the nucleon and the quark gets re-absorbed into the nucleon by emitting an on-shell photon.

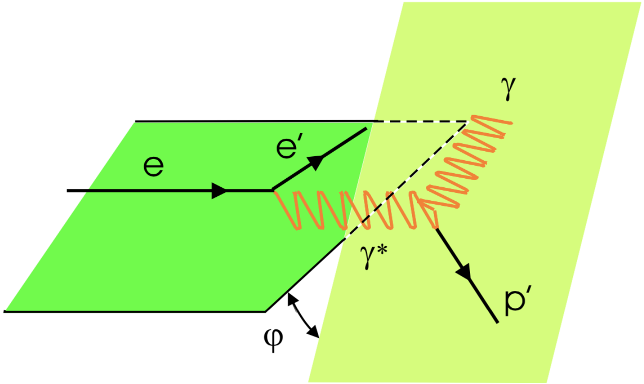

Figure I.13: The illustration of the leptonic plane, the hadronic plane, and the angle ϕ ($= \varphi$).

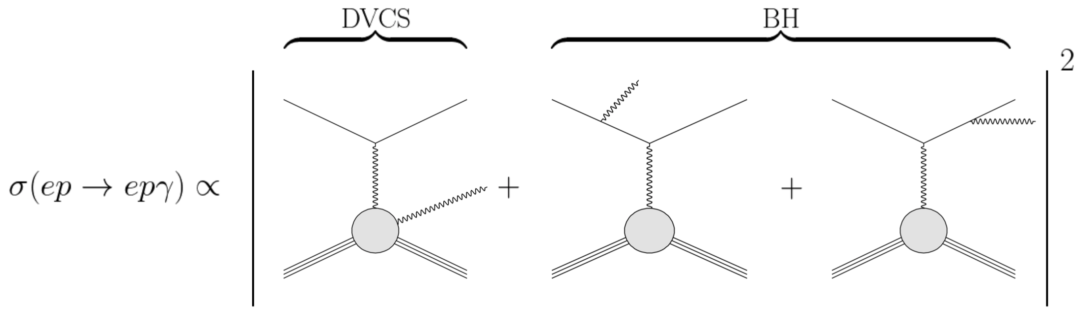

Figure I.14: The cross section of the photon electroproduction off the nucleon ($ep \rightarrow e'p'\gamma$) is proportional to the squared amplitude $|\mathcal{T} = \mathcal{T}_{\text{BH}} + \mathcal{T}_{\text{DVCS}}|^2$: the DVCS and the BH interfere.

the amplitude level. The amplitude squared in Eq. (I.39) is then:

$$|\mathcal{T}|^2 = |\mathcal{T}_{\text{BH}}|^2 + |\mathcal{T}_{\text{DVCS}}|^2 + \mathcal{I}, \tag{I.40}$$

with the interference term

$$\mathcal{I} = \mathcal{T}^*_{\text{BH}}\mathcal{T}_{\text{DVCS}} + \mathcal{T}_{\text{BH}}\mathcal{T}^*_{\text{DVCS}}. \tag{I.41}$$

In [30], Belitsky et al. performed azimuthal expansions in ϕ of each term in Eq. (I.40) up to twist-3:

$$\begin{aligned}|\mathcal{T}_{\text{BH}}|^2 =& \frac{e^6}{x_B^2 y^2 (1+\epsilon^2)^2 t \mathcal{P}_1(\phi)\mathcal{P}_2(\phi)} \\ & \times \left\{ c_0^{\text{BH}} + \sum_{n=1}^{2} c_n^{\text{BH}} \cos(n\phi) + s_1^{\text{BH}} \sin(n\phi) \right\}, \end{aligned} \tag{I.42a}$$

$$|\mathcal{T}_{\text{DVCS}}|^2 = \frac{e^6}{y^2 Q^2} \left\{ c_0^{\text{DVCS}} + \sum_{n=1}^{2} \left[c_n^{\text{DVCS}} \cos(n\phi) + s_n^{\text{DVCS}} \sin(n\phi) \right] \right\}, \tag{I.42b}$$

$$\mathcal{I} = \frac{\pm e^6}{x_B y^3 \mathcal{P}_1(\phi)\mathcal{P}_2(\phi) t} \left\{ c_0^{\mathcal{I}} + \sum_{n=1}^{3} \left[c_n^{\mathcal{I}} \cos(n\phi) + s_n^{\mathcal{I}} \sin(n\phi) \right] \right\}, \tag{I.42c}$$

where the sign + and − in the interference term is for the negatively charged and positively charged lepton beams, respectively. The variables $\mathcal{P}_1(\phi)$ and $\mathcal{P}_2(\phi)$ in Eq. (I.42) are the BH propagators:

$$Q^2\mathcal{P}_1 \equiv (k - q')^2, \tag{I.43a}$$

$$Q^2\mathcal{P}_2 \equiv (k - \Delta)^2. \tag{I.43b}$$

The GPDs are thus embedded in the coefficients in Eq. (I.42): as bilinear combinations in $|\mathcal{T}_{\text{DVCS}}|^2$ (Eq. (I.42b)) and linear combinations in $\mathcal{I}$ (Eq. (I.42c)).

Since the BH is an elastic scattering with an internal Bremsstrahlung, $|\mathcal{T}_{\text{BH}}|^2$ is calculable with the known electromagnetic form factors and QED with a precision of ∼ 1%. The other two terms in Eq. (I.40) can also be separated up to some level by using the ϕ-dependence of the harmonics. Moreover, the separation between the $|\mathcal{T}_{\text{DVCS}}|^2$ and the $\mathcal{I}$ can be enhanced by using their different beam-energy (E_b) dependence:

$$|\mathcal{T}_{\text{DVCS}}|^2 \propto y^3 = (E_b/\nu)^3, \tag{I.44a}$$

$$\mathcal{I} \propto y^2 = (E_b/\nu)^2. \tag{I.44b}$$

4.3.2 Deeply virtual meson production

The deeply virtual meson production (DVMP) is another exclusive reaction where instead of the real photon in the DVCS, a meson is produced in the final state. Fig. I.15 illustrates the DVMP at leading-order and leading-twist.

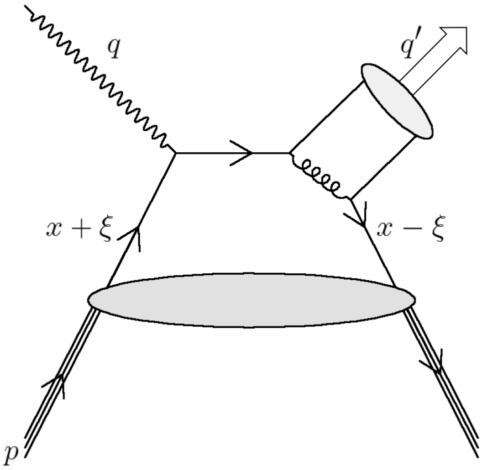

Figure I.15: The illustration of the DVMP at leading-order and leading-twist. Unlike the DVCS, an additional soft process is involved in DVMP due to the meson in the final state.

The differential cross section for the electroproduction of meson can be expressed as [31]:

$$\begin{aligned}\frac{d^5\sigma}{dtd\phi_e d\phi_{\pi^0} dQ^2 dx_B} &= \frac{1}{(2\pi)^2}\Gamma_{\gamma^*}(Q^2,x_B,E)\left[\frac{d\sigma_T}{dt}+\epsilon^*\frac{d\sigma_L}{dt}+\sqrt{2\epsilon^*(1+\epsilon^*)}\frac{d\sigma_{TL}}{dt}\cos(\phi_{\pi^0})\right.\\ &\left.+\epsilon^*\frac{d\sigma_{TT}}{dt}\cos(2\phi_{\pi^0})+h\sqrt{2\epsilon^*(1-\epsilon^*)}\frac{d\sigma_{TL'}}{dt}\sin(\phi_{\pi^0})\right] \text{ with}\\ \Gamma_{\gamma^*}(Q^2,x_B,E) &= \frac{\nu}{2EE'x_B}\frac{\alpha}{2\pi^2}\frac{E'}{E}\frac{W^2-M^2}{2M}\frac{1}{Q^2}\frac{1}{1-\epsilon^*} \text{ and}\\ \epsilon^* &= (1+2(\frac{|\mathbf{q}|^2}{Q^2}\tan^2(\theta/2)))^{-1},\end{aligned} \tag{I.45}$$

where each term on the right-hand-side of the equation (σ_T, σ_L, σ_{TT}, σ_{TL}, and $\sigma_{TL'}$) corresponds to the cross section associated with different states of the virtual photon polarization. The angle ϕ_{π^0} is defined in the same way as the ϕ of the DVCS in Fig. I.13: the only difference is that the final photon in the DVCS is replaced by the meson. The variable $\Gamma_{\gamma^*}(Q^2, x_B, E)$ represents the flux of the virtual photon field, ϵ^* describes its degree of transverse polarization, and h $(= \pm 1)$ stands for the helicity of the initial electron. The first two terms in Eq. (I.45), σ_T and σ_L refer to the transverse (T) and longitudinal (L) cross sections, respectively. The third and the fifth term describe the transverse-longitudinal interferences (TL and TL'). Finally, the fourth term denotes the transverse-transverse interference (TT). Since this document does not consider the helicity of the electron beam, the fifth term of Eq. (I.45) will be ignored from now on.

Unlike DVCS, an additional soft non-perturbative subprocess is involved in DVMP: the distribution amplitude (DA) of the meson which is produced. The DA parameterizes the momentum fraction distributions of quarks in the meson. The leading-twist DA for the pseudoscalar meson (pion) in the light-cone frame is [32]

$$\Phi_\pi(x) = \int \frac{dz^-}{2\pi} e^{i(2x-1)P^+z^-/2} \langle\pi(P)|\,\overline{\psi}(-\frac{z}{2})\gamma^+\gamma^5\psi(\frac{z}{2})\,|0\rangle\Big|_{z^+=0,\mathbf{z}=0}. \tag{I.46}$$

Due to the additional complexity from the DA, the model-independent factorization of the DVMP has been proven only for the longitudinally polarized virtual photons (γ_L^*) [33]. For the case of π^0, at leading-twist, the DVMP amplitude ($M^L_{\pi^0}$) for longitudinally polarized virtual photon involves the GPDs $\widetilde{H}$ and $\widetilde{E}$ [34]:

$$\begin{aligned}M^L_{\pi^0} &= (-ie4\pi\alpha_s)\frac{4}{9}\frac{1}{\sqrt{Q^2}}\left[\int_0^1 dz\frac{d\Phi_{\pi^0}(z)}{z}\right]\times\frac{1}{2}\left[\frac{1}{x-\xi+i\epsilon}+\frac{1}{x+\xi+i\epsilon}\right]\\ &\times\left\{\widetilde{H}\overline{N}(p')\,\not{n}\gamma^5N(p)+\frac{\xi}{2M}\widetilde{E}\overline{N}(p')\gamma^5N(p)\right\},\end{aligned} \tag{I.47}$$

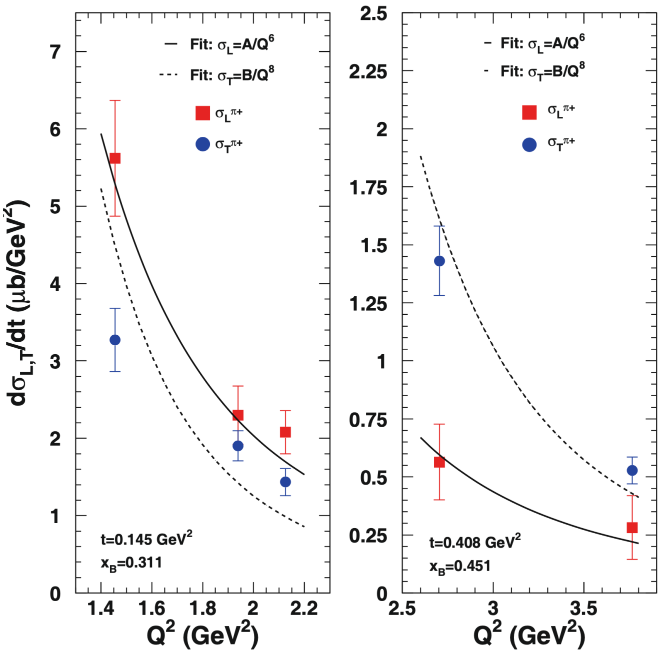

Figure I.16: The L/T separated π^+ hard exclusive electroproduction cross section $(H(e, e'\pi^+)n)$. The solid line shows a fit to the σ_L term with the form A/Q^6 and the dashed line the σ_T term with the form A/Q^8. Figure extracted from [36].

where α_s represents a strong coupling constant. In Eq. (I.47), the function $\Phi_{\pi^0}(z)$ represents the meson DA of the π^0 and $\widetilde{H}$ and $\widetilde{E}$ are defined as the linear combinations of u and d quark GPDs respectively:

$$\widetilde{H} = \frac{1}{\sqrt{2}} \left\{ \frac{2}{3}\widetilde{H}^u + \frac{1}{3}\widetilde{H}^d \right\}, \tag{I.48a}$$

$$\widetilde{E} = \frac{1}{\sqrt{2}} \left\{ \frac{2}{3}\widetilde{E}^u + \frac{1}{3}\widetilde{E}^d \right\}. \tag{I.48b}$$

To be noted, with different types of mesons[¶], it is possible to perform flavor separations of the GPDs of the nucleon.

At sufficiently high Q^2, σ_T is suppressed by a power of $1/Q^2$ with respect to σ_L in Eq. (I.45) [33]: σ_T scales as Q^{-8} while σ_L as Q^{-6}. However, the experimental results of the L/T separated cross sections of the π^+ off the proton $(H(e, e'\pi^+)n)$ [36] imply that we have not yet reached the regime where σ_L dominates: in Fig. I.16, the σ_L term scales as predicted but the σ_T term does not follow the prediction. Although it shows a dominance of the σ_L term over the σ_T term at small t (< 0.3 GeV^2) (see the left plot of Fig. I.16), the result is consistent with a dominant meson pole description in that region: the pion pole, at leading-twist accuracy, includes a factor $t/(t - m_\pi^2)^2$ for the longitudinally polarized virtual photon [36]. Furthermore, the right plot of Fig. I.16 shows a σ_T dominance over σ_L at higher t and Q^2 which implies that the leading-twist does not apply in the kinematic region shown. Also, it indicates a strong participation of the transversely polarized virtual photon in the hard exclusive electroproduction of pseudoscalar meson at leading-order[‖].

For the case of π^0, since the π^0 has no spin nor charge, the direct coupling to the virtual photon is suppressed. Therefore, the pion pole contribution is removed in the longitudinal cross section for the π^0 electroproduction and it is possible to determine the amount of contribution from the transverse polarization more directly.

4.3.2.1 Transversity GPDs and twist-3 DA

There have been theoretical approaches ([42, 43, 44] and [45, 46]) to utilize the transversity GPDs in the calculation of the hard exclusive electroproduction of pseudoscalar mesons for the case of the transversely polarized virtual

---

[¶] For example, the CLAS collaboration measured cross sections for exclusive η electroproduction off the proton [35].

[‖] It is worth noting that the beam-target spin asymmetry measurements also suggest a dominance of transversely-polarized virtual photon amplitudes in the exclusive pseudoscalar meson electroproduction. The examples are in [37, 38, 39, 40, 41].

photons. With $\Gamma = \sigma^{\mu\nu}$, the Fourier transformation of the Eq. (I.26) yields [47]:

$$\begin{aligned} P^+ \int \frac{dz^-}{2\pi} e^{ixP^+z^-} \left. \langle p'| \overline{\psi}_q(-\frac{1}{2}z) i\sigma^{+i} \psi_q(\frac{1}{2}z) |p\rangle \right|_{z^+=0, \mathbf{z}=0} \\ = \overline{N}(p') \Big[H_T^q(x,\xi,t) i\sigma^{+i} + \widetilde{H}_T^q(x,\xi,t) \frac{P^+\Delta^i - \Delta^+ P^i}{M^2} \\ E_T^q(x,\xi,t) \frac{\gamma^+\Delta^i - \Delta^+\gamma^i}{2M} + \widetilde{E}_T^q(x,\xi,t) \frac{\gamma^+ P^i - P^+\gamma^i}{M} \Big] N(p), \end{aligned} \tag{I.49}$$

where $i = 1$, 2 stands for the index of the transverse directions in the light-cone frame. These H_T^q, E_T^q, $\widetilde{H}_T^q$, and $\widetilde{E}_T^q$ are the chiral-odd (transversity) GPDs of the quark of flavor q. Although they do not conserve the quark helicity (they flip the helicity by ±1), they contribute at leading-twist. The previous 4 GPDs (H^q, E^q, $\widetilde{H}^q$, and $\widetilde{E}^q$) are chiral-even (non-helicity flip) GPDs and therefore, there are a total of 8 GPDs at leading-twist.

The chiral-odd GPDs are little known compared to the chiral-even GPDs from both the theoretical and the experimental point of view. The only known constraint on the chiral-odd GPDs is the forward limit of H_T^q:

$$H_T^q(x, \xi = 0, t = 0) = h_1^q(x), \tag{I.50}$$

where the function $h_1^q(x)$ denotes the transversity distribution of the quarks q. The $h_1^q(x)$ describes the difference between the densities of the quarks of flavor q with their spins parallel and anti-parallel to the proton spin which is transverse to its momentum.

The transversity GPDs are chiral-odd, thus they need to couple to a chiral-odd DA. The chiral-odd DA appears at twist-3 as the transverse momentum of the quark enters the meson [46]. The higher-twist contribution is kinematically suppressed compared to the leading-twist contribution by $\frac{1}{Q^2}$. In the so-called GK model, developed by Goloskokov and Kroll [45, 46], the DA contains a factor $\mu_\pi = \frac{m_\pi^2}{m_u + m_d}$, with m_π the pion mass and m_u and m_d the current quark masses of the u and d quarks respectively, which does not appear in the leading-twist DA. Consequently, it increases the pion electroproduction cross section by boosting the transverse response.

The contributing GPDs, according to the GK model, to the response to the transversely polarized virtual photon of the pseudoscalar meson electroproduction are H_T and $\overline{E}_T$ ($= 2\widetilde{H}_T + E_T$) [45, 46]: the H_T characterizes the quark distribution involved in the nucleon helicity flip and the $\overline{E}_T$ characterizes that in helicity non-flip. The σ_T and σ_{TT} in Eq. (I.45) have the GPDs dependence [46, 48]:

$$\frac{d\sigma_T}{dt} = \frac{4\pi\alpha}{2k'} \frac{\mu_\pi^2}{Q^8} \left[(1 - \xi^2) \left| \langle H_T \rangle \right|^2 - \frac{t'}{8M^2} \left| \langle \overline{E}_T \rangle \right|^2 \right], \tag{I.51a}$$

$$\begin{aligned} \frac{d\sigma_{TT}}{dt} &= \frac{4\pi\alpha}{k'} \frac{\mu_\pi^2}{Q^8} \frac{t'}{16M^2} \left| \langle \overline{E}_T \rangle \right|^2 \text{ with} \\ k' &= \frac{16\pi}{Q^2} \left(\frac{1}{x_B} - 1 \right) \times \sqrt{(W^2 - M^2)^2 + Q^4 + 2W^2Q^2 + 2Q^2M^2}, \end{aligned} \tag{I.51b}$$

where the quantity k' refers to the phase space factor and $\langle F \rangle$ ($\equiv \sum_\lambda \int_{-1}^{1} dx \mathcal{H}_{\mu'\lambda'\mu\lambda} F$) describes a convolution of the GPD here (of generic name F) with a hard scattering kernel, $\mathcal{H}_{\mu'\lambda'\mu\lambda}$ which is perturbatively calculated from an appropriate set of Feynman graphs. The symbols μ and μ' indicate the helicities of the virtual photon and the meson and λ and λ' the helicities of the initial and final quarks respectively.

There is another theoretical approach developed by Goldstein, Gonzalez-Hernandez, and Liuti utilizing the chiral-odd GPDs in the calculation of pseudoscalar meson electroproduction [49, 50, 43]: let us call it a GGL model, for convenience. This model is not used in the analysis of the thesis. However, it is worth noting that the GGL model has described the previous experimental results of pseudoscalar meson electroproduction successfully in some degree. Examples of the GGL model descriptions are presented in the next section along with the GK model descriptions.

5 Experimental status

In this section, we briefly review the experimental status of DVCS and DVMP. The DVMP experimental results shown here are mainly from the recent publications of the pion electroproduction.

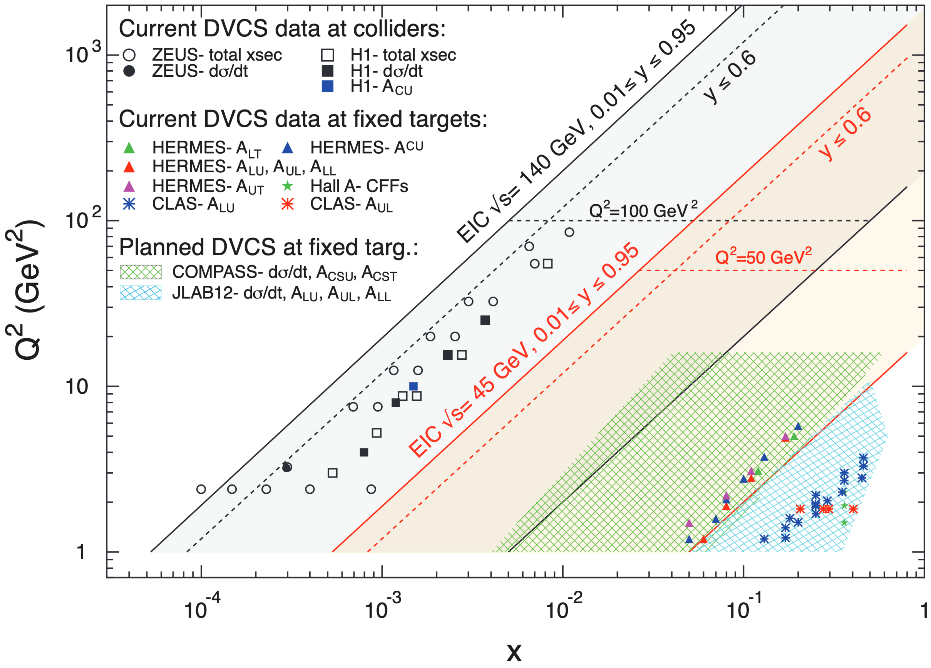

Figure I.17: An overview of existing and planned measurements of DVCS in the $x_B - Q^2$ representation. The figure is extracted from [51].

5.1 DVCS

During the era of HERA, H1 and ZEUS measured the DVCS with electron and positron beams of energy up to 28 GeV colliding with an unpolarized proton beam of energy up to 920 GeV. The kinematic region was in $x_B = [10^{-4},\ 10^{-2}]$ which is dominated by sea quarks and gluons. However, the integrated luminosity of the collider was 500 pb^{-1} and resulted in low statistics leaving many questions on sea quarks and gluons unanswered.

HERMES at HERA used a fixed proton target with the electron and the positron beam of energy up to 28 GeV surveying the kinematic range of $x_B = [0.04,\ 0.2]$. Similarly, Jefferson Lab used a 6 GeV electron beam surveying mostly the valence quark region. The measurements from these two facilities proved that it is possible to measure the angular and polarization asymmetries of DVCS and that they can be interpreted in terms of the GPDs. However, since the measurements were done only at relatively low Q^2 (or low statistics at high Q^2), it is hard to see the evolution of the GPDs with Q^2. Nonetheless, the scaling of the DVCS observables from the experimental data shows evidence that the leading-twist dominant regime is reached at $Q^2 > 1$ GeV^2 [52, 53]: the leading-twist dominance is the foundation of the GPDs formalism.

COMPASS at CERN took DVCS and DVMP data from 2016 to 2017 using a muon beam energy of 160 GeV with a fixed proton target. Their measurements will provide the first imaging of the partons at $x_B = [0.005,\ 0.3]$ where the transition between sea quarks and valence quarks happens, with $Q^2 = [1.0,\ 16.]$ GeV^2 [54]. Therefore, the COMPASS collaboration will cover the uncharted kinematic region between where the collider experiments (H1 and ZEUS) have explored and where the fixed target experiments (HERMES and Jefferson Lab) have and will.

The 12 GeV upgrade of Jefferson Lab accompanying high statistics opens the first era of precise parton imaging. Although it is mostly probing the valence region, the highest precision data available over a wide kinematic range will minimize the model dependence in the parameterization of GPDs. The kinematic domain it can cover is approximately $x_B = [0.1,\ 0.7]$ with $Q^2 = [1.0,\ 10.]$ GeV^2.

5.2 DVMP

As a reminder of the experimental results in Fig. I.16 shown in section 4.3.2, the cross section σ_L following the Q^{-6} scaling in the kinematic region $Q^2 = [2.15,\ 3.91]$ GeV^2 and $x_B = [0.31,\ 0.45]$ alone does not prove that the QCD factorization is applicable. The term σ_T fails to follow the scaling prediction and the value m gives $m = 4.2 \pm 0.78$ for $x_B = 0.31$ and $m = 6.01 \pm 0.90$ for $x_B = 0.45$ when it is used as a free parameter of Q^{-m} [55]. The scaling

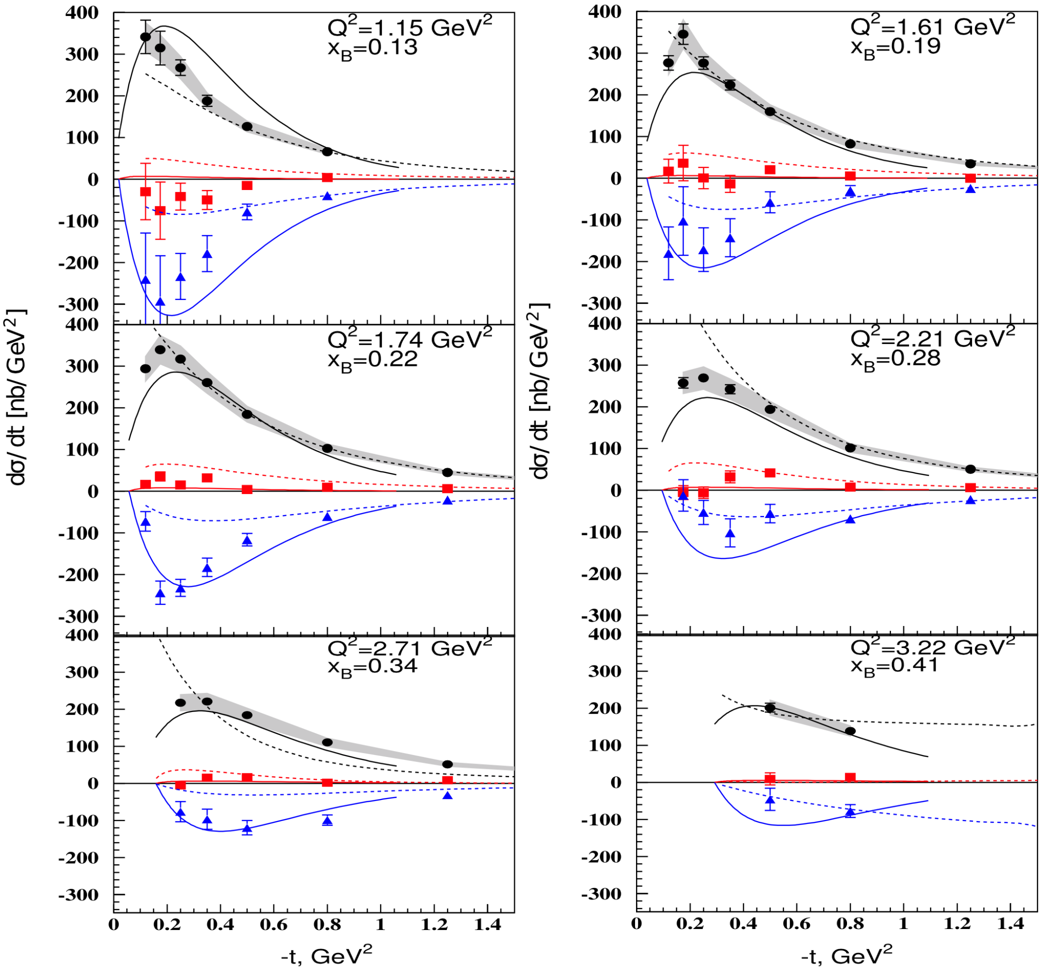

Figure I.18: The extracted $ep \to e'p'\pi^0$ cross sections with theoretical calculations over different values of Q^2, x_B, and t [57]. The experimental data are represented as dots with their statistical uncertainties: black circles for the $\sigma_T + \epsilon^*\sigma_L$ term, blue triangles for the σ_{TT}, and red squares for the σ_{TL}. The solid curves shows the theoretical prediction using the GK model [46] and the dashed curves using the GGL model [49, 50, 43]. The shaded bands reflect the experimental systematic uncertainties.

behavior of σ_L might be from higher order contributions which mimic the scaling behavior. Therefore, experiments at higher Q^2 are necessary.

Several L/T unseparated π^0 leptoproduction cross sections off proton were measured in Hall A [56] and Hall B (CLAS) [57] at Jefferson Lab and at COMPASS [58]. In Hall A [56], at $Q^2 = [1.9,\ 2.3]$ GeV^2, $x_B = 0.36$, and $W \geq 2$ GeV, assuming that the σ_T term is negligible, it was found that the σ_L does not scale as Q^{-6} and instead it scales as Q^{-3}. However, the assumption of the σ_T term being negligible is highly unlikely [56]. Furthermore, the cross section $\sigma_T + \epsilon^*\sigma_L$ was found to scale as $Q^{-4.5}$ which is similar to what was found for σ_T for π^+ electroproduction in [55] (Fig. I.16). The CLAS collaboration [57] found that in the kinematic domain $Q^2 = [1.0,\ 4.6]$ GeV^2, $x_B = [0.1,\ 0.58]$, and $W \geq 2$ GeV, the σ_{TT} has a magnitude comparable to that of the L/T unseparated cross section $\sigma_T + \epsilon^*\sigma_L$. On the other hand, the σ_{TL} was found very small compared to the other two. Fig. I.18 shows the extracted cross sections $\sigma_T + \epsilon^*\sigma_L$, σ_{TT}, and σ_{TL} measured by the CLAS collaboration. Likewise, the COMPASS collaboration [58] found a large σ_{TT} contribution and small σ_{TL} contribution at $Q^2 = [1.0,\ 5.]$ GeV^2 and $x_B = [0.01,\ 0.15]$ above the resonance region with muon beam. These experimental results indicate that there is a strong contribution of transversely polarized virtual photons in the π^0 leptoproduction off the proton.

The L/T Rosenbluth separated cross sections of the π^0 electroproduction off the proton were measured in Hall A at Jefferson Lab [59] in the kinematic domain $Q^2 = [1.5,\ 2.0]$ GeV^2 and $x_B = 0.36$ above the resonance region. As can be seen from Fig. I.19, the σ_L is compatible with zero but also with the leading-twist chiral-even GPD Vanderhaeghen-Guichon-Guidal (VGG) model [60]. Despite that the transversity GPDs models (GGL [49] and GK

[46]) and the data do not agree in the sign of the σ_{TL}, they all show the σ_T dominance over σ_L. Moreover, the GK model and the data are in good agreement especially at high Q^2 ($= 2.0$ GeV^2).

As described in the previous section, σ_T can be enhanced over σ_L by the factor μ_π boosting the transversely polarized virtual photon contribution (Eq. (I.51)) and by the suppression of the pion pole in the longitudinally polarized virtual photon contribution. Although one cannot ignore the fact that it is a model-dependent interpretation, these results show that at $Q^2 > 1.5$ GeV^2, the neutral pion electroproduction facilitates the access to transversity GPDs.

Leptoproduction of vector mesons is one of the most studied exclusive processes due to its relatively high cross section. The experimental data, existing in a wide range of energy scales, tend to follow the leading-twist factorization scheme at small x_B and $Q^2 > 50$ GeV^2 [36]. This, combined with the pseudoscalar meson production results, indicates that most of the existing data are not in the regime where the leading-twist approximation is applicable. Yet, the DVMP is still important in understanding the structure of the nucleon through its cross section measurements. One of the examples is stressed in the previous section: by taking into account the dominant contribution of the transverse photons, the transversity GPDs might be accessible via hard exclusive electroproduction of the pseudoscalar mesons.

6 Upcoming results and future experiments

The upcoming results in the next 10 years will provide DVCS and DVMP data with high precision in a wide kinematic domain, $x_B = [0.005,\ 0.7]$ and $Q^2 = [1.0,\ 16.]$ GeV^2. Briefly in the final subsection, a future experimental facility and another deep exclusive reaction to access the GPDs are mentioned.

6.1 DVCS

The experiment E12-06-114 [61] which took place from 2014 to 2016 in Hall A at Jefferson Lab measured all the DVCS observables accessible by a polarized electron beam with an unpolarized proton target. The kinematic domain it covered is $x_B = [0.36,\ 0.60]$ and $Q^2 = [3.2,\ 9.0]$ GeV^2. With high luminosity and high precision, this experiment will provide the most precise data currently available in its kinematic regime. The Q^2 scaling tests of the observables are being performed and preliminary results indicate that there are higher twist contributions. However, a subtlety exists in the interpretation since the azimuthal angle ϕ is not sufficient to separate the $|\mathcal{T}_{DVCS}|^2$ term and the $\mathcal{I}$ term in Eq. (I.40) [62].

The upcoming experiment E12-13-010 [63] in Hall C at Jefferson Lab will perform similar measurements as those of Hall A but also use different beam energies at fixed Q^2 and x_B. This Rosenbluth-like separation (Eq. (I.44)) will further separate the $|\mathcal{T}_{DVCS}|^2$ and the $\mathcal{I}$ terms giving more constraints on parameterizing GPDs.

In the COMPASS experiment, the x_B dependence of the t slope of the DVCS cross sections will be measured [54]. Therefore, the transverse proton radius as a function of x_B will be extracted [54, 64, 65]: see Fig. I.20. The measured transverse proton radius will be further extended from $x_B = 0.01$ of HERA to $x_B = 0.1$[**].

A major detector to study DVCS is CLAS12 in Hall B at Jefferson Lab. It is an upgraded version of CLAS from the 6 GeV era to the 12 GeV era of Jefferson Lab. By exploiting the large acceptance of the detector, CLAS12 covers the wide range of kinematics accessible by the Jefferson Lab 12 GeV electron beam: $x_B = [0.1,\ 0.7]$ and $Q^2 = [1.0,\ 9.0]$ GeV^2. The kinematic coverage is larger than that in Hall A and C and they are complementary to one another: Hall A provides high precision data in selected kinematic regions, CLAS12 covers a wide kinematic domain, and Hall C offers higher momentum reach with relatively high precision.

6.2 DVMP

Neutral pion electroproduction data were also taken alongside with DVCS in the E12-06-114 experiment [61]. The experiment further tests the production mechanism of meson electroproduction by covering a wider kinematic range in Q^2 and x_B. Although this experiment does not perform a Rosenbluth separation, by exploiting its wide range of Q^2, it will test the Q^2 dependence of the L/T unseparated cross section. The interference terms will be also obtained. Finally, comparisons with the GK model will give a hint of applicability of transversity GPDs. One of the kinematic settings of the π^0 electroproduction data of the E12-06-114 experiment is analyzed and presented in Ch. II.

[**] In 2019, a transverse extension of partons in the proton has been extracted [66]: $\sqrt{\langle r_\perp^2 \rangle} = (0.58 \pm 0.04_{\text{stat}} \left. {}^{+0.01}_{-0.02} \right|_{\text{sys}} \pm 0.04_{\text{model}})$ fm at $\langle Q^2 \rangle = 1.8$ GeV^2 and $\langle x_B \rangle = 0.056$.

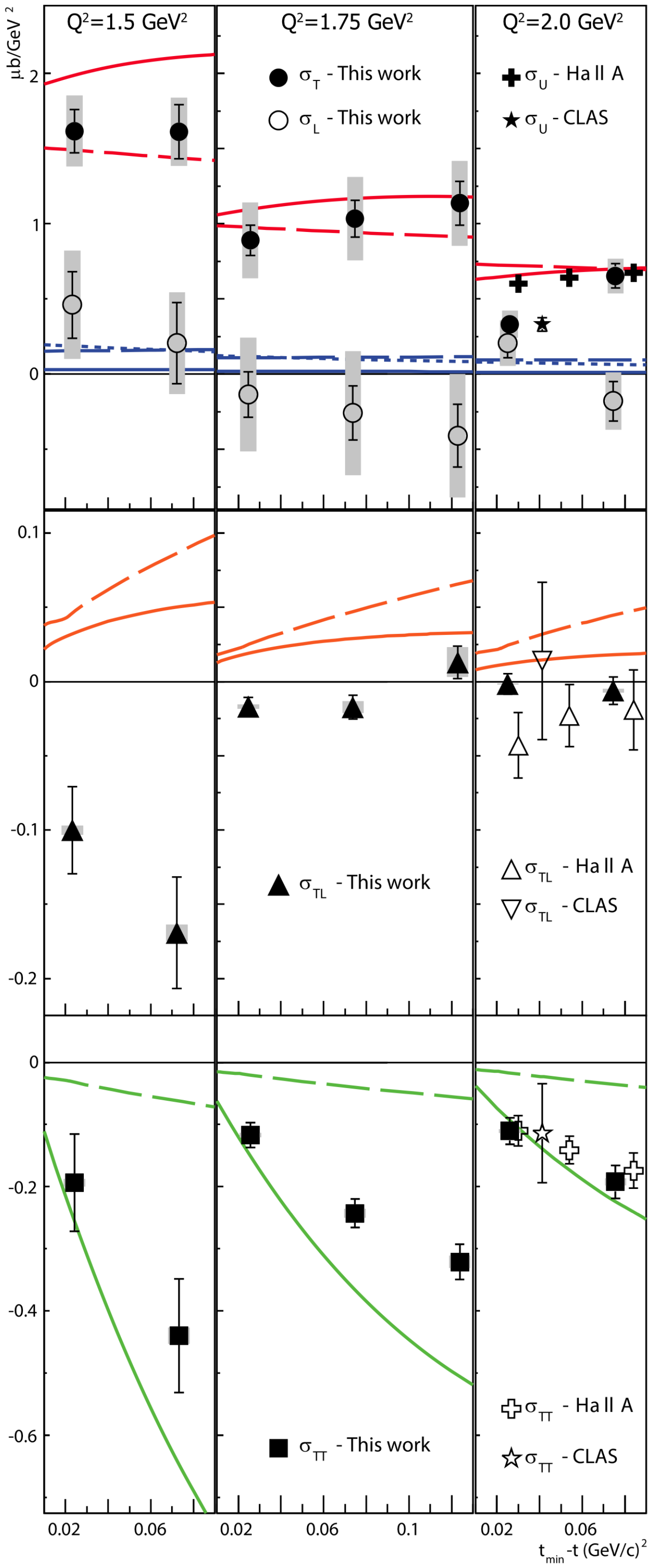

Figure I.19: The extracted $ep \to e'p'\pi^0$ cross sections with the theoretical calculations over different values of Q^2, and t at $x_B = 0.36$ [59]. The left column is for $Q^2 = 1.5$ GeV^2, the middle $Q^2 = 1.75$ GeV^2, and the right $Q^2 = 2.0$ GeV^2. t_{min} denotes the value t with minimal $|t|$. The cross section σ_T is represented in full circles, σ_L in open circles, σ_{TL} in triangles, and σ_{TT} in squares with their statistical uncertainties. The systematic uncertainties are shown in grey boxes. The solid curves represent the theoretical prediction of the GK model [46], the long-dashed curves of the GGL model [49], and the short-dashed curves of the VGG model [60].

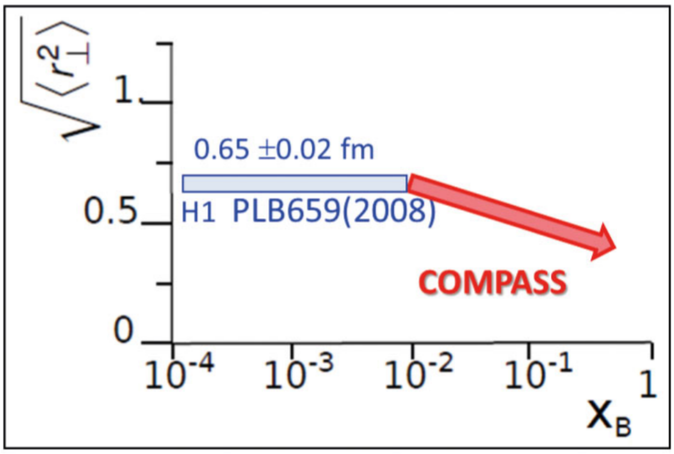

Figure I.20: Projected COMPASS transverse proton radius as a function of x_B. The figure is extracted from [65].

The L/T separated cross sections for the pseudoscalar meson productions provide a direct information of the participation of transverse virtual photons. Similar to DVCS, the E12-13-010 experiment [63] will perform the Rosenbluth separation of the π^0 electroproduction giving the L/T separated cross sections in a wider range of kinematics than the previous experiment did [59].

The COMPASS collaboration also took data on hard exclusive muoproduction of vector and pseudoscalar mesons. The various types of mesons will help separating the different flavors of GPDs of quarks and gluons[††].

6.3 EIC

The Electron-Ion Collider (EIC) is a future experimental facility to explore the sea quarks and gluons in the nucleon and nucleus. Its center-of-mass energy of about 140 GeV with a luminosity of at least 10^{34} cm^{-2}s^{-1} will cover a wide range of x_B and Q^2 as was already shown in Fig. I.17. It will address questions related to the fundamental understanding of QCD such as [51]:

- the spatial and momentum distributions of the sea quarks, the gluons, and their spins inside the nucleon;
- the boundary of the gluon saturation;
- the effects of nuclear environment in the distributions of the quarks and gluons and their interactions in nuclei (EMC effect).

The polarization of the nucleon will play a huge role in studying the GPDs. For example, only HERMES has provided data with a transversely polarized nucleon so far.[‡‡] A transversely polarized nucleon gives better access to the GPD E [30, 65] which is elusive in other settings: the GPD E is a key to understand the total angular momentum contribution of the quarks to the nucleon spin (see Eq. (I.38)). The high statistics and precision in the wide kinematic region of the EIC will also facilitate measuring the Q^2 evolution of GPDs.

6.4 DDVCS

DVCS and DVMP give a limited access to GPDs due to their convolution with the quark momentum x (see Eq. (I.33) and (I.47)). The real part of the CFFs (Eq. (I.34)) gives access to the GPDs convoluted with x and the imaginary part only for $x = \pm\xi$. This restriction is lifted when the final photon of the DVCS is also off-shell and it is called double deeply virtual Compton scattering (DDVCS) [68, 69, 70, 71]. The virtuality of the final photon allows one to measure GPDs for each x, ξ, and t independently. However, due to an additional QED coupling and kinematic factors appearing in the process of the final photon decaying into dileptons ($\gamma^* \to l^+l^-$), the DDVCS cross section is suppressed by more than 2 orders of magnitude. The experimental feasibility of this measurement is currently being studied by several groups.

[††] Gluon GPDs contribute at the same order in α_s as the quark GPDs in the case of the vector meson production.

[‡‡] CLAS12 [67] and COMPASS [54] collaborations are proposing DVCS/DVMP experiments with transversely polarized targets.

Chapter II

Neutral pion electroproduction data analysis

This DVCS/DVMP experiment in Hall A (E12-06-114) [61] is the very first experiment performed in Jefferson Lab after its upgrade from 6 GeV to 12 GeV electron beam. It is an extension of the previous DVCS/DVMP experiments (E00-110 [72] and E07-007 [73]) to higher beam energy. A longitudinally polarized electron beam with an unpolarized liquid hydrogen target are used for the experiment. The data were taken during Fall 2014, Spring 2016, and Fall 2016. The kinematics and the beam energies are shown in Fig. II.1.

This chapter describes the data analysis of one of the kinematics of the experiment: the beam energy is 7.383 GeV, Q^2 is 3.2 GeV^2, and x_B is 0.36. The chapter starts with introductions of the experimental equipment. Calibration of the detectors, especially the electromagnetic calorimeter, are shown in the following section. The π^0 data analysis of the experiment is described in section 3. In the last section of the chapter, a Monte Carlo simulation for the cross section extraction is introduced, Systematic uncertainties of the data analysis are presented together with the preliminary results of the extracted cross sections.

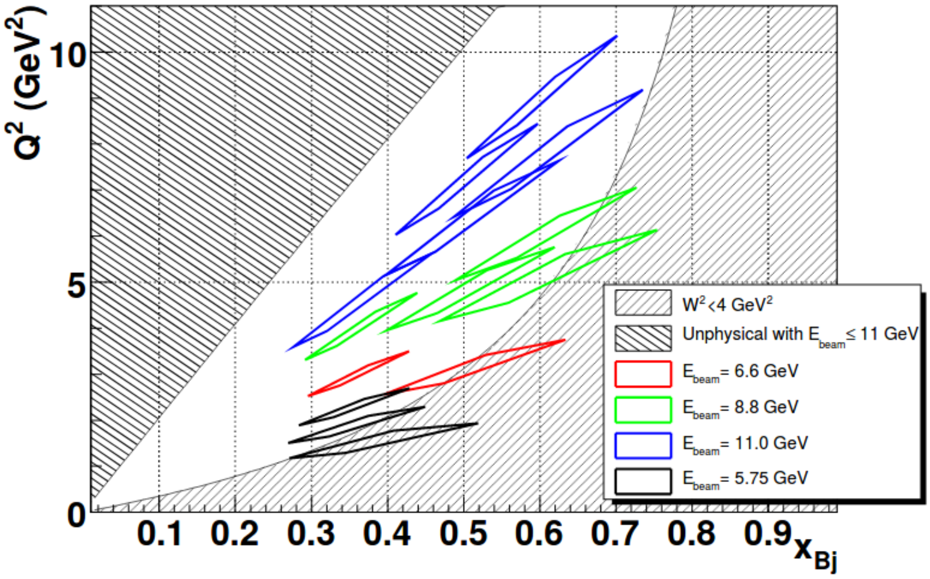

Figure II.1: Kinematic region that the Hall A DVCS/DVMP experiment covers [61]. The regions in black were covered in the previous experiments. The unphysical region is the domain that the beam energy of 11 GeV cannot access. The experiment is not accessing the W < 2 GeV region to suppress the contributions from resonances.

1 Experimental setup

The Thomas Jefferson National Accelerator Facility, i.e. Jefferson Lab, is a research facility that explores the atomic nucleus and its fundamental constituents by probing its structure using the electromagnetic interaction. It is located in Newport News, Virginia, U.S.A. A Continuous Electron Beam Accelerator Facility (CEBAF) delivers polarized electron beam to 4 experimental halls with a maximum energy of 12 GeV. Each experimental hall has its own unique capabilities: Hall A has a high momentum resolution, Hall B has a large acceptance, Hall C has a high momentum reach, and Hall D uses a photon beam instead of the electron beam.

This experiment, as mentioned earlier, was done in Hall A. The beam line and the basic instrumentation of the Hall are introduced in the first two parts of this section. In the remaining part of the section, an electromagnetic calorimeter, designed for the DVCS/DVMP experiment, and its data acquisition system are described.

1.1 Continuous Electron Beam Accelerator Facility

The CEBAF generates electrons with a photocathode gun. A Ti-Sapphire laser illuminates a gallium-arsenide cathode with a frequency of 250 MHz at a wavelength of 850 nm. The polarized, by the laser, electrons escaping the photocathode are then extracted and accelerated by Radio-Frequency (RF) cavities to 45 MeV. These polarized electrons enter a linear accelerator (linac). The laser in the photocathode gun is circularly polarized and changes its polarization with a frequency of 30 Hz. This generates periodically-flipping longitudinal helicity of the electron beam. There are 4 lasers with phase offsets. These lasers independently send the electrons to each experimental hall, sequentially. Therefore, the electrons are generated with a frequency of 4 × 250 MHz.

There are two linacs and re-circulation arcs in CEBAF. Each linacs, paralleled to each other, accelerate the electron beam. The re-circulation arcs bend the accelerated beam to the linac on the other side: see Fig II.2 for a schematic view of the CEBAF. The linac is made of 25 cryomodules and each of those cryomodule is made of 8 RF cavities. The cavities, made of pure Niobium, are synchronized to a frequency of 1 GHz so that each electron bunch is individually accelerated. Each time the electron beam goes through the linac, its energy increases by 1.1 GeV. The electron beam needs a 5-time circulation to reach the energy of 11 GeV: the beam passes two linacs in one circulation. Therefore, there are 5 re-circulation arcs at each end of the linacs to bend the electron beams with different energies. At the end of the acceleration, each hall (A, B, and C) can receive the electron beam, simultaneously at the maximum beam energy. The beam currents in the halls can also be controlled independently from the other halls and the maximum current the machine can reach at its maximum energy is 90 μA. Hall D is located on the opposite side of the linacs.

1.2 Hall A

In this section, the basic instrumentation of the beam line, targets, and detectors of the Hall A are briefly described.

1.2.1 Beam line

The instruments of the beam line of Hall A allow to measure the position, current, energy, and polarization of the electron beam. Two beam position monitors (BPMs), at different locations, determine the position and direction of the beam at the target location. Each BPM consists of a set of four antennas displayed around the beam. The induced current in each antenna by the beam is used to determine its position of the beam. The position information from two BPMs provides the direction of the beam. The BPMs have a position resolution of 100 μm for currents above 1 μA.

The beam current monitor (BCM) measures the current of the beam with using RF cavities. The cavities are designed to have a resonance at the frequency of the beam. The resulting voltage from the resonance is proportional to the beam current. In order to obtain the absolute value of the beam current, the BCM is calibrated periodically against a parametric current transformer: the Unser monitor. The accuracy of the BCM is better than 0.5% down to a current of 1 μA.

The electron beam enters Hall A from the accelerator through the 40-meter arc. The arc contains eight dipole magnets and nine quadrupole magnets which bend and direct the beam 34.4° (nominally). The momentum (p) of the beam is measured using the relation with the known magnetic field $\vec{B}$:

$$p = k\frac{\int \vec{B} \cdot d\vec{l}}{\theta}, \tag{II.1}$$

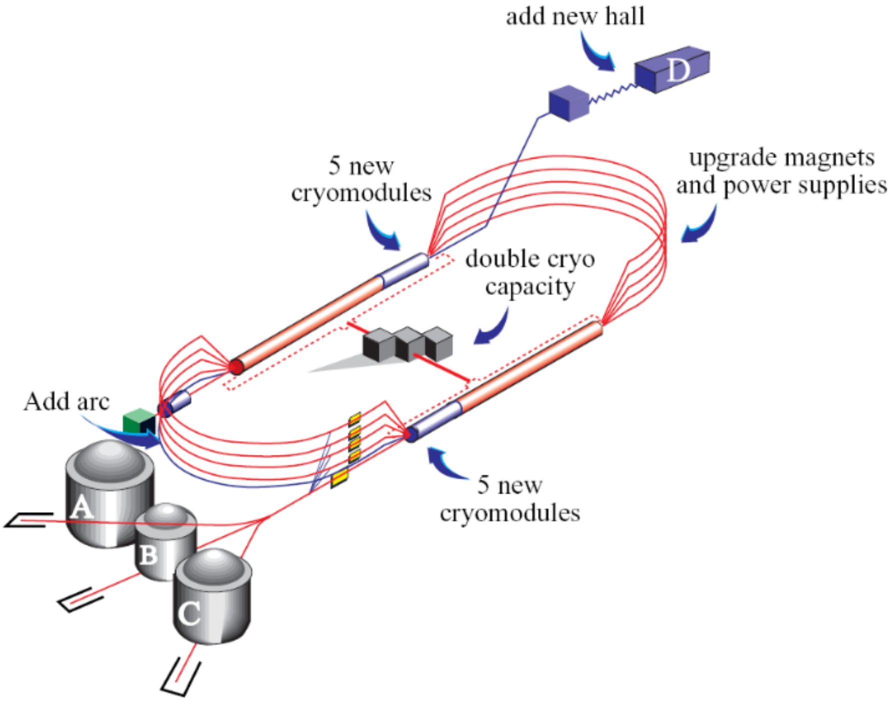

Figure II.2: Schematic view of the CEBAF and its 4 experimental halls. It consists of two linacs and 5 re-circulation arcs at each end. It was upgraded in 2014 from 6 GeV to 12 GeV: 5 cryomodules were added in each linac to accelerate the electron beam up to 12 GeV. Figure extracted from [74].

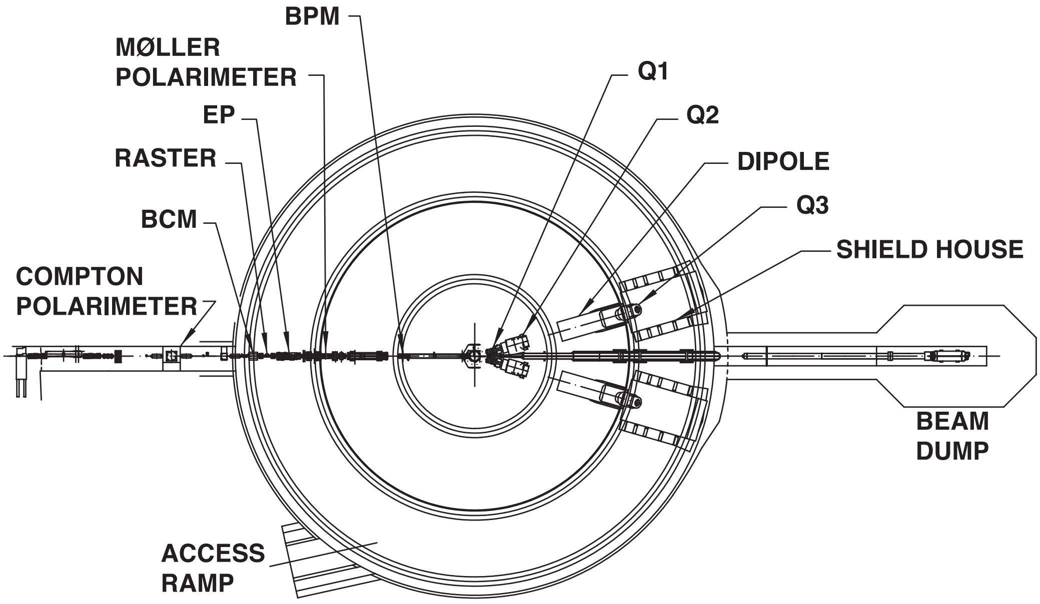

Figure II.3: Schematic aerial view of Hall A with its basic instrumentation. The center of the Hall is the target chamber.

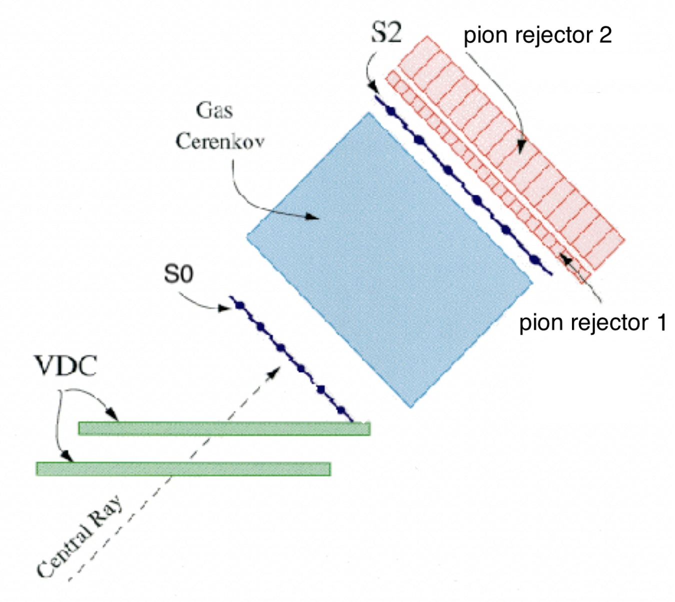

Figure II.4: Schematic view of the detectors in the left HRS.

where k = 0.299792 GeV rad $T^{-1}m^{-1}/c$ and θ is the net bending angle through the arc section. The accuracy of the measurement is better than 0.03%.

The analysis of the data in this document does not contain the beam helicity dependent parts. Therefore, the details of the measurements of the beam polarization are omitted. More information on the beam polarization measurements and all other Hall A instrumentation are described in [75].

1.2.2 Target

The target system is made of a cylindrical scattering vacuum chamber with several targets mounted in a ladder inside. By moving the ladder up and down, the target is switched to the desired one for the experiment. For the DVCS/DVMP experiment, a liquid hydrogen target inside a cylindrical aluminum cell, 63.5 mm in diameter and 15-cm-long is used. The temperature and the pressure for the cell are 19 K and 0.17 MPa, with a density of around 0.0723 g·cm^{-3}. The liquid hydrogen is cooled by circulating liquid helium supplied at 15 K. The maximum electron beam current the target can take is 130 μA. There are also other targets mounted in the ladder. For example, cryogenic cells without the liquid hydrogen inside are used to study the effects of the target walls. Five 1-mm thick carbon foils each spaced by 3.75 cm are used to calibrate the optics of the spectrometer. A single carbon foil target with a 2-mm-diameter hole at its center is used to position the beam at the center of the target.

1.2.3 HRS

Hall A has identical twin magnetic spectrometers: a left High Resolution Spectrometer and a right High Resolution Spectrometer (HRS)*. The HRS has a vertically bending (45° upward) design with a pair of superconducting quadrupole magnets, followed by a dipole magnet, and a third quadrupole magnet. It has a momentum range of [0.3, 4.0] GeV/c, a momentum resolution of 0.01%, and an momentum acceptance of ±4.5%. The angular acceptance is ±30 mrad horizontally and ±60 mrad vertically. The left HRS, which is used for the DVCS/DVMP experiment, can rotate horizontally in a range [12.5, 150.]° from the beam line.

Detectors of the HRS consists, in the order of the direction of the particle being detected, of two sets of vertical drift chambers (VDCs), a scintillator (S0), a gas Čerenkov detector, another set of scintillators (S2), and finally, two layers of electromagnetic calorimeters called pion rejectors. See Fig. II.4 for a schematic view of the detector layout. The VDC planes lie in the laboratory horizontal plane and all other detector planes are angled 45° to that: it is parallel to the nominal particle track.

---

*They were identical when they were constructed. However, the detector packages inside those spectrometers are now different from each other.

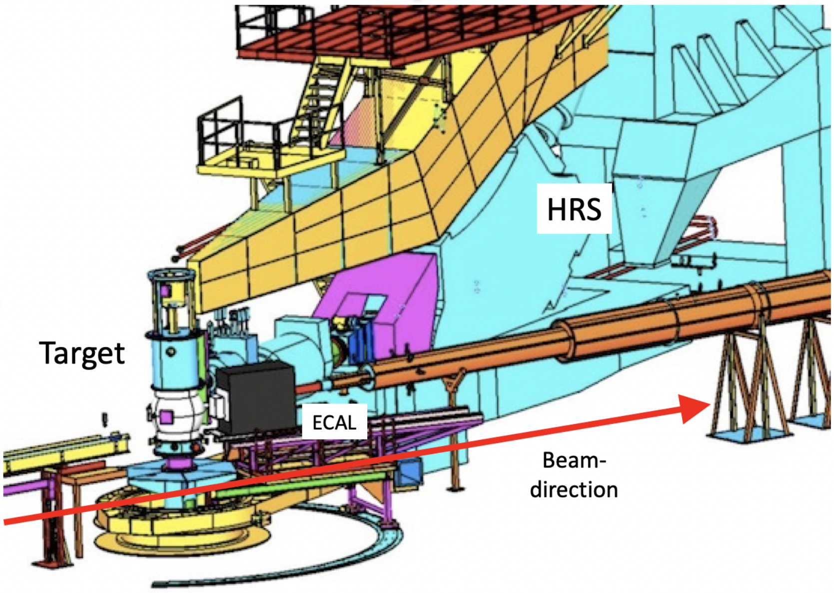

Figure II.5: Schematic view of the Hall A DVCS/DVMP experimental apparatus. The electromagnetic calorimeter is colored in black and put on the right side of the target chamber. The left HRS is on the other side of the downstream beam pipe colored in cyan. The right HRS, which is not on the figure is not used for the experiment.

The charged particle first goes through the VDCs. Each VDC is composed of two wire planes and each plane is oriented at 90° to one another and filled with a standard gas mixture of argon (62%) and ethane (38%). The VDCs provide tracking information of the charged particle: they allow to reconstruct the vertex and the momentum of the particle. The particle then goes through the S0, gas Čerenkov detector, and S2, successively. The S0 is made of a single 10-mm-thick plastic paddle and the S2 is a set of sixteen 5-mm-thick plastic paddles. Each of the paddle has two PMTs attached at the ends. The time resolution of the S2 is approximately 0.30 ns. The gas Čerenkov detector is filled with CO_2 at atmospheric pressure and has ten spherical mirrors focused to their corresponding PMTs to view the Čerenkov light. It allows an electron identification with 99% efficiency. After the S2, the particle goes to the pion rejectors. Both pion rejectors are composed of 34 lead glass blocks, each coupled to a PMT. The particles create showers in the blocks and deposit their energy. Since the pion deposit its energy less than the electron does, the identification of the pion is possible. The pion events above 2 GeV/c are suppressed by a factor of 2×10^5 with a combination of the gas Čerenkov and the pion rejectors.

The HRSs can change their polarity from negative to positive to detect from negatively to positively charged particles, or vice versa.

1.3 DVCS/DVMP experiment apparatus

For the DVCS/DVMP experiment, the left HRS is used with negative polarity to detect the scattered electron. The final photon/π^0 is detected with an electromagnetic calorimeter built for this experiment. The calorimeter is put between the downstream beam pipe and the right HRS: see Fig. II.5. The right HRS is not used for the experiment. Finally, the recoiled proton is not directly detected but identified using a missing mass technique: $M_X^2 = (e + p - e' - \pi^0)^2 = (e + p - e' - \gamma_1 - \gamma_2)^2$. The details of this technique are described in section 3.4.2.

1.3.1 Electromagnetic calorimeter

The electromagnetic calorimeter (ECAL) for the DVCS/DVMP is made of 208 PbF_2 crystals in an array of 13×16: see Fig. II.6. Each crystal has a dimension of $3 \times 3 \times 18.6$ cm^3 and is wrapped with Tyvek© and Tedlar© for inner and outer wrapping, respectively. The Tyvek© wrapper reflects the Čerenkov light in the crystal and the Tedlar© prevents the light leaks from and to other crystals. Each crystal is optically coupled to a PMT (Hamamatsu R7700). The calorimeter is in a light-tight box in order to protect the PMTs from the direct exposure to the Hall light.

The considerations that went into the design choice of the calorimeter were [61]:

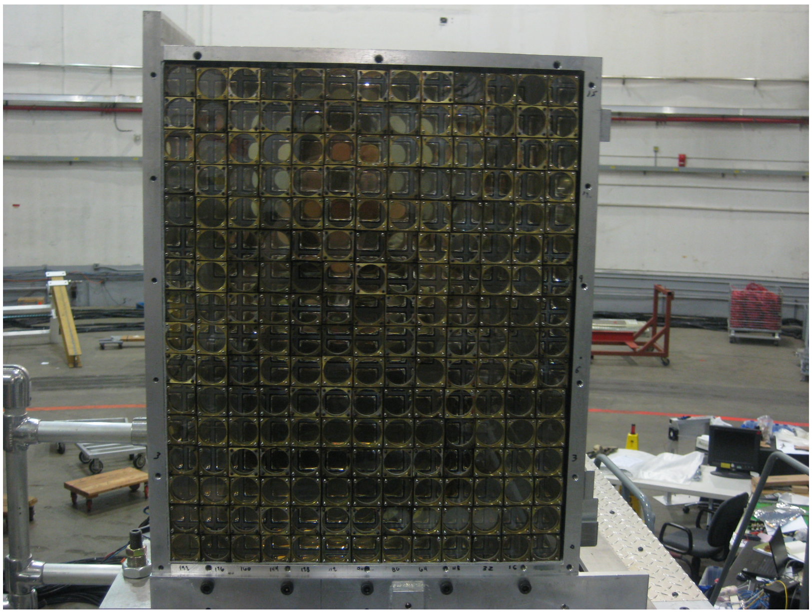

Figure II.6: Electromagnetic calorimeter for the DVCS/DVMP experiment. During the data taking, the front face of the calorimeter is closed so that no light from the outside is leaked into the calorimeter.

- PbF_2 is radiation hard and produces light purely by Čerenkov effect. The rise and fall time of the signal from the Čerenkov light is fast, which minimizes pile-up. Since it does not produce light by scintillation, the calorimeter signal is insensitive to low energy particles.
- the short radiation length minimizes the fluctuations in light collection.
- the small Molière radius of 2.2 cm allows the identification of the π^0, whose decay photons typically hit the calorimeter very close to each other. It also minimizes the energy leaks at the edges of the calorimeter;

To protect the calorimeter from the background radiation created from the target chamber and the beam pipes, tungsten plates are placed on the downstream beam pipe near the scattering chamber. Two plastic plates are also placed in front of the calorimeter in order to reduce the low energy backgrounds on the calorimeter.

1.3.2 Data acquisition

The data acquisition (DAQ) is managed by a Jefferson Lab developed system, CODA (CEBAF online data acquisition). The detectors in the Hall are connected to analog to digital converters (ADCs) or time to digital converters (TDCs) and/or scalers. They are gathered in VME crates and each VME crate is controlled by a read-out controller (ROC). The ROCs are connected to a trigger supervisor (TS) which oversees the triggers of the experiment and requests recording of the data. When the recording is requested from the TS, the ROCs send the gathered data from the VME crates to an event builder (EB). The EB sends the built event to an event recorder (ER) and the ER writes the data on local disks. The data on the local disks get transferred to a mass storage tape silo (MSS) and get erased from the local disks. The ROCs buffer the memory when gathering and sending the data from the VME crate to the EB. The TS only takes a new trigger when all ROCs are free. The buffering of the ROCs causes acquisition dead time.

Due to the high luminosity ($\sim 10^{38}$ cm^{-2}s^{-1}) of the experiment and the calorimeter being placed close to the target and the beam pipe (the crystal closest to the beam pipe is about 7° from the beam pipe and 1.5 m from the target), a high signal rate from the calorimeter is expected. An analog ring sampler (ARS) was designed [76] to manage the pile-up events. The ARS is a circular array of 128 capacitor cells with a data sampling rate of 1 GHz. This sampling rate allows the separation of the pile-up events. The ARS is connected to each channel of the calorimeter and it continuously samples the signal. When the TS demands the recording of the data, the ARS stops the sampling and the charges in the capacitors are digitized and recorded. The dead time of this procedure is 128 μs.

The trigger of the HRS for this experiment is a coincidence between the gas Čerenkov detector and the S2: see Fig. II.4. When the trigger from the HRS is fired, the TS stops the ARS sampling and starts the read-out of flash-ADCs: the signal of each PMT is split and one copy is sent to the flash-ADC and another to the ARS. The flash-ADC integrates the signal over the 128 ns. By summing the flash-ADC values over 2 × 2 neighboring channels, the trigger module checks whether the sum of the ADC values is higher than a set threshold value. If the sum is higher than the threshold, the TS requests the recording of the ARS signal. If not, the ARS resumes its sampling. The total dead time when the signal does not get recorded is 500 ns, which is much faster than the dead time of the ARS signal recording.

2 Calibration of detectors

After the alignment of the beam line and the detectors, time offsets and gain calibrations of the detectors are needed in order to get a correct momentum of the particles.

2.1 HRS

The vertical drift chambers (VDCs) track particles using time-to-digital converter (TDC) information with a relationship between the drift time and the drift distance. Therefore, each TDC time offset of the wire is calibrated to as close to zero as possible to make zero drift time corresponds to zero drift distance [77]. The Čerenkov detector and the pion rejectors discriminate the π^- from the electrons. They use the energy deposition difference between the π^- and the electron: the π^- deposits less energy than the electron does. Thus, the PMTs of each detector are calibrated so that their gains are the same from one another. For the timing information of the detected particle, the scintillator S2 is used. Therefore, the time offset of each of the sixteen plastic paddles of the S2 is calibrated to zero [78].

2.2 ECAL

The electromagnetic calorimeter for the DVCS/DVMP is calibrated using three methods: cosmic ray calibration, elastic calibration, and π^0 calibration.

2.2.1 Cosmic ray calibration

The cosmic ray calibration uses one plastic scintillator at the top and another at the bottom of the calorimeter. When the cosmic ray passes through the calorimeter vertically, a coincidence between the top and the bottom plastic scintillator occurs and the PMTs of the calorimeter record the signals. In the case of a minimum ionizing particle (MIP), it leaves the same amount of energy in each crystal when it travels the same amount of distance in it. The energy deposition by the MIP in each crystal is expected to be around 35 MeV. Therefore, the high voltage of each PMT is adjusted to get the same signal amplitude of the cosmic ray from one another. One can also estimate the required high voltage to detect photons with GeV energy.

The status of each channel of the calorimeter is checked during this calibration. If one of the channels in the calorimeter is not working due to electrical problems, it shows during this calibration: all other 15 channels in the same column give signals whilst the dead channel does not.

2.2.2 Elastic calibration

This method uses the elastic scattering process of electron and proton: $ep \to e'p'$. During the elastic calibration, the HRS changes its polarity from negative to positive to detect the recoiled proton and the calorimeter detects the scattered electron. Since it is an exclusive process, one can calculate the expected momentum of the detected scattered electron by measuring the momentum of the recoiled proton. Then the calibration coefficient C_i for each channel $i \in [1,...,208]$ is obtained by comparing the signal from the calorimeter to the expected energy of the scattered electron.

The total energy E^j of the jth electron, out of N number of events, deposited in the calorimeter is:

$$E^j = \sum_i C_i A_i^j. \tag{II.2}$$

Using the Eq. (II.2) and the elastic scattering kinematics, one can perform a χ^2 minimization with C_i as the variable:

$$\chi^2 = \sum_j^N \left(E^j - \sum_i C_i A_i^j \right)^2 , \tag{II.3a}$$

$$-\frac{1}{2}\frac{\partial \chi^2}{\partial C_k}\bigg|_{\overline{C}_k} = \sum_j^N \left(E^j - \sum_i C_i A_i^j \right) A_k^j = 0 \quad \text{with } \; k \in [1,...,208], \tag{II.3b}$$

$$\sum_i C_i \left[\sum_j^N A_i^j A_k^j \right] = \sum_j^N E^j A_k^j, \tag{II.3c}$$

where the value $\overline{C}_k$ is the coefficient obtained by minimizing the χ^2. The Eq. (II.3c) is a linear equation in a matrix form $\mathcal{AC} = \mathcal{B}$, with $\mathcal{A}_{i,k} = \sum_j^N A_i^j A_k^j$ and $\mathcal{B}_k = \sum_j^N E^j A_k^j$. The fitted calibration coefficients are then $\mathcal{C} = \mathcal{A}^{-1}\mathcal{B}$.

The measured energy resolution of the calorimeter from the elastic scattering calibration is 3% at 7.0 GeV [78]. Although it has the advantage of acquiring a precise coefficient for each channel of the calorimeter, the elastic calibration cannot be performed every other day. It not only takes about a day of dedicated beam time, but also has a different configuration from the DVCS/DVMP kinematic settings: 1) the calorimeter has to be moved back to a distance of 5.5-6 m away from the target, 2) the angle between the calorimeter and the beam line has to change into 3 different configurations, and 3) the HRS polarity has to be changed from negative to positive. The reasons 1) and 2) are due to the small acceptance of the HRS.

2.2.3 π^0 calibration

The calorimeter suffers radiation damage and each channel changes its response to the events continuously throughout the experiment. Thus, the calibration of the calorimeter needs to be performed often. Unlike the elastic calibration, the π^0 is detected without changing the configuration of the kinematic settings. Therefore, the calibration using π^0 can be done periodically throughout the experiment and it is done by finding an extremum of a single global function of the data [79]:

$$F = \sum_{i=1}^N (m_i^2 - m_{\pi^0}^2)^2 + 2\lambda \sum_{i=1}^N (m_i^2 - m_{\pi^0}^2), \tag{II.4}$$

where m_{π^0} is the invariant mass of the π^0 (0.135 GeV/c^2) and m_i is the reconstructed mass of π^0 from the calorimeter of the ith event out of N number of detected π^0 events. The first term in F measures the width of the reconstructed mass peak and the second term with the Lagrange multiplier λ is to embody the constraint $\langle m_i^2 \rangle = m_{\pi^0}^2$.

The reconstructed invariant mass of the π^0 from the ith event is obtained from the sum of the deposited energies of the two photons $j \in [1,\ 2]$ from the pion decay: $\sum_k E_{ji}^{(k)}$, with $k \in$ [crystals out of 208 contributed to the reconstruction of the photon j]. The calibration proceeds in an iterative manner, where each step introduces a small channel-dependent gain correction factor ε_k:

$$E_{ji}^{(k)} \to E'^{(k)}_{ji} = (1 + \varepsilon_k) E_{ji}^{(k)}. \tag{II.5}$$

The variable ε_k needs to be taken small at each iteration step in order to simplify the minimization of the function F in Eq. (II.4), since the dependence of m_i^2 is non-linear to the deposited energy in the crystals.

The derivation of the solution is in [79] and the solution is given by:

$$\varepsilon_k = \sum_{k'} \left[C^{-1} \right]_{kk'} (D - \lambda L)_{k'}, \tag{II.6}$$

where:

$$C_{kk'} = \sum_{i=1}^{N} \left(\frac{\partial m_i^2}{\partial \varepsilon_k} \frac{\partial m_i^2}{\partial \varepsilon_{k'}} \right), \tag{II.7a}$$

$$D_k = -\sum_{i=1}^{N} \left((m_i^2 - m_{\pi^0}^2) \frac{\partial m_i^2}{\partial \varepsilon_k} \right), \tag{II.7b}$$

$$L_k = \sum_{i=1}^{N} \frac{\partial m_i^2}{\partial \varepsilon_k}, \tag{II.7c}$$

$$\lambda = \frac{B + L^T C^{-1} D}{L^T C^{-1} L}, \tag{II.7d}$$

$$B = \sum_{i=1}^{N} (m_i^2 - m_{\pi^0}^2). \tag{II.7e}$$

The iteration is performed 8 times where the correction factors $\varepsilon_{k,8\mathrm{th}}$ for the 8th iteration are almost 0 with one-day worth of data. The data after the corrections reconstruct the π^0 mass successfully. More details on the calibration of the calorimeter can be found in [62, 80].

3 Data analysis

This section describes analysis methods for the calorimeter: the ARS waveform analysis and the photon reconstruction. The event selection cuts on the vertex and the detectors are also introduced. Next, a method to subtract accidental events on the calorimeter is presented. The final section deals with corrections on the analysis.

3.1 Calorimeter waveform analysis

This section describes the waveform analysis of the ARS signal: the conversion of a raw signal to arrival time and amplitude of the pulse(s).

3.1.1 Base line fit

The wave form analyzer first looks for a base line b by minimizing;

$$\chi^2 = \sum_{i=i_{min}}^{i_{max}} (x_i - b)^2, \tag{II.8}$$

where the interval $i \in [i_{min},\ i_{max}]$ is an analysis window smaller than the full 128-ns ARS sampling window, and it is different for every channel due to their cablings and different signal arrival times with respect to the HRS trigger. The value x_i is the ARS signal of the ith capacitor, which has a 1-ns sampling width. After finding the base line b, the χ_t^2 is defined as:

$$\chi_t^2 = \sum_{i=\chi_{min}^2}^{\chi_{max}^2} (x_i - b)^2, \tag{II.9}$$

where the range $[\chi^2_{min},\ \chi^2_{max}]$ is different from the range $[i_{min},\ i_{max}]$, that may be larger. If the χ_t^2 is smaller than a set value of χ_0, the base line is deemed good enough.

3.1.2 One pulse fit

If $\chi_t^2 > \chi_0$, there is a possibility that there is a signal and the analysis algorithm does a one-pulse fit by minimizing;

$$\chi^2 = \sum_{i=i_{min}}^{i_{max}} (x_i - a_1 h_i - b)^2, \tag{II.10}$$

where h_i is the reference shape of the signal from the elastic scattering data and a_1 is the amplitude parameter to match the data. One will notice that this algorithm is assuming that the signal shape is independent of its amplitude.

The Eq. (II.10) does not take into account the arrival time of the pulse. By shifting the reference shape in time by t_1, one can consider the arrival time of the pulse. The amplitude parameter a_1 and the base line b are found by minimizing:

$$\chi^2(t_1) = \sum_{i=i_{min}}^{i_{max}} (x_i - a_1(t_1)h_{i-t_1} - b(t_1))^2. \tag{II.11}$$

The pulse arrival time t_1 is obtained by trying different values of t_1 which gives a minimum value in:

$$\chi_t^2(t_1) = \sum_{i=\chi^2_{min}}^{\chi^2_{max}} (x_i - a_1(t_1)h_{i-t_1} - b(t_1))^2. \tag{II.12}$$

If the minimum value of the $\chi_t^2(t_1)$ $(min\left\{\chi_t^2(t_1)\right\})$ is smaller than a set value of χ_1, one-pulse fit is deemed good enough.

3.1.3 Two pulse fit

If $min\left\{\chi_t^2(t_1)\right\} > \chi_1$, it is considered that there is a pile-up of signals and a two-pulse fit is done. As one might guess, it has the same procedure as the one-pulse fit but with an extra reference signal in a different pulse arrival time:

$$\chi^2(t_1,t_2) = \sum_{i=i_{min}}^{i_{max}} (x_i - a_1(t_1,t_2)h_{i-t_1} - a_2(t_1,t_2)h_{i-t_2} - b(t_1,t_2))^2, \tag{II.13}$$

where the amplitude parameter a_2 is for the additional pulse at the arrival time t_2. The variables $a_1(t_1,t_2)$, $a_2(t_1,t_2)$, and $b(t_1,t_2)$ are found by minimizing the Eq. (II.13). In the same manner as for the one-pulse fit, several t_1 and t_2 are tested to minimize:

$$\chi_t^2(t_1,t_2) = \sum_{i=\chi^2_{min}}^{\chi^2_{max}} (x_i - a_1(t_1,t_2)h_{i-t_1} - a_2(t_1,t_2)h_{i-t_2} - b(t_1,t_2))^2, \tag{II.14}$$

where the interval for t_1 is the same as for the one-pulse fit and for t_2 is slightly larger to find the pile-up events.

It is, however, possible to find more than a single solution for $a_1(t_1,t_2)$ and $a_2(t_1,t_2)$ if the arrival times of the pulses, t_1 and t_2, are too close. Therefore, for this experiment, if $|t_1 - t_2| < 4$ ns, the ARS signal is fitted with one-pulse fit method. This makes the energy reconstruction less reliable, however, it was found that the pile-up rate is low.

The thresholds χ_0 and χ_1 are obtained by measuring the energy resolution of the elastic scattering data, the mean value and the resolution of the missing mass squared and the π^0 invariant mass, etc., with the thresholds as the variables. The two-pulse fitting can yield negative pulse signals [81] and the threshold χ_1 is chosen so that the negative pulses are reduced whilst providing a good energy resolution of the calorimeter.

The analysis window $[i_{min},\ i_{max}]$ is 80-ns-wide to keep the window large enough to catch two pulses (one pulse of the ARS is approximately 30 ns) and not taking too much computation time. The starting time of the window is set around the expected arrival time of the events: it is set differently for each channel (time offset calibration). The window for χ^2 calculation $\left[\chi^2_{min},\ \chi^2_{max}\right]$ is set 40-ns-wide (smaller than the analysis window of 80 ns) centered around the reference shape, in order to avoid unimportant effects from signals far from the expected pulse. The time windows for t_1 and t_2 are also set around the reference shape: 25 ns below and 20 ns above for t_1, and ± 40 ns for t_2.

3.1.4 Time resolution optimization

The time resolution of the ARS sampling is 1 ns: each capacitor of the ARS samples the signal at 1 GHz. This can be improved by interpolating the χ_t^2 around the time $t \pm 1$ ns. The accuracy of the interpolation, of course, depends on the parameterization of the χ_t^2. For this experiment, a second order polynomial of the time t for the χ_t^2 is used. By minimizing the $\chi_t^2(t)$ with respect to the time t, the optimized time t^{opt} is obtained;

$$t^{opt} = t + \frac{\chi_t^2(t-1\text{ ns}) - \chi_t^2(t+1\text{ ns})}{2\left(\chi_t^2(t+1\text{ ns}) + \chi_t^2(t-1\text{ ns}) - 2\chi_t^2(t)\right)}. \tag{II.15}$$

This optimization increases the time resolution of the signal which becomes better than 1 ns. Further details of the analysis methods and the results of this experiment can be found in [62, 80].

3.2 Calorimeter photon reconstruction

The total energy of the photon deposited in the crystals is

$$E = \sum_i E_i \qquad \text{with } E_i = C_i A_i, \tag{II.16}$$

where A_i is the amplitude of the ARS pulse extracted from the waveform analysis (section 3.1) and C_i is the calibration coefficient of the crystal $i \in [1,...,208]$ (section 2.2.2).

In order to reconstruct the impact point of the photon on the calorimeter, the position of each crystal is weighted by the relative energy deposited in it. High energy photons deposit their energy in the calorimeter by creating an electromagnetic shower in the crystals dominated by Bremsstrahlung and electron-positron pair production. Therefore, the lateral photon energy profile, with a good approximation, follows:

$$\frac{1}{E}\frac{dE}{dR} \sim exp(-R), \tag{II.17}$$

where R is the distance from the trajectory of the photon. Thus, the weight is given logarithmically and the reconstructed impact point x and y are given as;

$$x = \frac{\sum_i w_i x_i}{\sum_i w_i} \qquad \text{with } w_i = \max\left\{0, \left[W_0 + \ln\frac{E_i}{E}\right]\right\}, \tag{II.18a}$$

$$y = \frac{\sum_i w_i y_i}{\sum_i w_i} \qquad \text{with } w_i = \max\left\{0, \left[W_0 + \ln\frac{E_i}{E}\right]\right\}, \tag{II.18b}$$

where x_i and y_i are the positions of the crystals. The parameter W_0 is used to tune the relative weight between the crystals. When $W_0 \to \infty$, the weight becomes constant and each crystal is treated equally. On the other hand, when W_0 is small, crystals with bigger deposited energy get larger weight. It also acts as an energy deposition threshold in the crystal for the position reconstruction: if the deposited energy in the crystal is smaller than Ee^{-W_0}, the crystal is ignored for the reconstruction.

The Eq. (II.18a) and (II.18b) are derived assuming that the shower centroid is at the surface of the calorimeter. However, that is not the case. The photon travels through the crystal before it develops a cascade at a certain depth. Furthermore, a correction due to the vertex position in the target is needed, since the calorimeter is few meters away from the target whereas the target is 15 cm long. The corrected impact point (e.g. x) on the calorimeter is then:

$$x_{corr} = x\left(1 - \frac{a}{\sqrt{L_{vc}^2 + x^2}}\right), \tag{II.19}$$

where a is the distance of the electromagnetic shower centroid from the calorimeter front face along the direction of the propagation, i.e. the shower depth. The value L_{vc} is the distance between the vertex and the calorimeter: see Fig. II.7.

Data from a Monte Carlo simulation and elastic scatterings are used in the optimization of the parameters a and W_0 for the correction of the position x_{corr}. The obtained values from the studies are $a = 7$ cm and $W_0 = 4.3$. With the elastic scattering data, the achieved position resolution of the calorimeter, 1.1 m away from the target with 4.2 GeV electron beam, is 2 mm. The parameter optimizations and the resolution calculation, just described before, were done in [77]. To be more precise, the parameters a and W_0 depend on the photon energy. The study done in [82] builds parameterizations of a and W_0 with respect to the photon energy. The parameterization of a is given by;

$$a = 0.30E^{0.28} + 4.862, \tag{II.20}$$

where the photon energy E is in MeV and the value a is in cm. The value W_0, on the other hand is found to depend weakly on the photon energy and the previously obtained value 4.3 is kept.

In an ideal case where the crystals of the calorimeter only detect the photons from the DVMP events , the photon reconstruction algorithm described above is all that is needed. However, due to noise from the electronics and the background, overestimation of the photon energy occurs. To prevent the overestimation, one can set an energy threshold to every crystal. Since most of the energy of the photon gets deposited in one crystal, there is a possibility that the rest of the energy deposited in the neighboring crystals is below the threshold and an underestimation of the photon energy can occur.

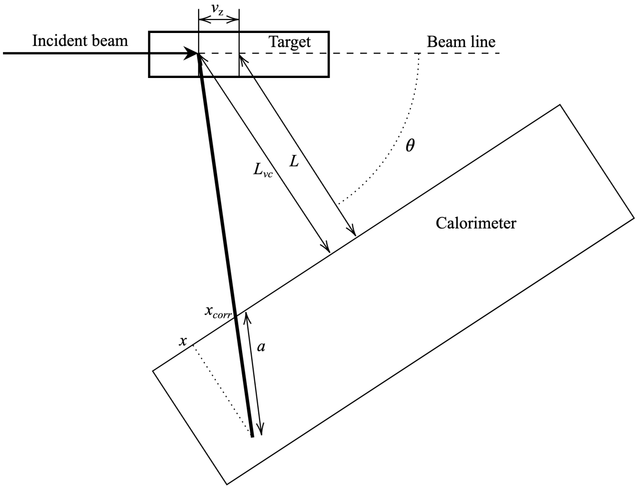

Figure II.7: Description for the shower depth a and the distance L_{vc}. The value v_z is the vertex position defined as the distance from the center of the target. The value L is the calorimeter distance from the target center. The value θ is the angle between the beam line and the calorimeter. The drawing is not to scale.

3.2.1 Clustering algorithm

A clustering algorithm is used to avoid both of the issues described above. A threshold is used not for one crystal but for a group of 2 × 2 crystals. If the total energy of the 4 crystals, adjacent to one another, is above a certain set energy, called clustering threshold, those crystals are kept for the photon reconstruction. If, on the other hand, it is below the clustering threshold, they are not kept for the photon reconstruction. The illustration of this algorithm is described in Fig. II.8. Another advantage of the clustering algorithm is that it can distinguish multiple photons when they are close to each other. After selecting crystals above the clustering threshold, the clustering algorithm uses a method called cellular automata [83] to associate crystals to each photon. The illustration of this method is in Fig. II.9. The algorithm looks for local maxima of the energy depositions. The local maxima are then registered as *viruses*. Then the algorithm assigns (*infects*) the values of the energy (viruses) of the local maxima to the neighboring crystals (*cells*), one by one. If the cell is already infected with the virus, it cannot be infected again with another virus. At the end, every cell is infected, and all cells with the same virus belong to the same cluster. Each cluster acquired from this procedure is then used for the photon reconstruction algorithm described before. The position resolution of two partially overlapping clusters yields 4 mm in the simulation [77].

The π^0 decays into two photons with a branching ratio of 99%. In the center-of-mass frame of the π^0, the decay photons have the opposite directions with equal amount of energy. However, in the reference frame of the calorimeter (laboratory frame), the π^0 is not at rest and a Lorentz boost must be applied from the center-of-mass frame to the laboratory frame. If the directions of the photons, in the π^0 center-of-mass frame, are perpendicular to the Lorentz boost direction, the energies of the photons are equal in the laboratory frame: see the top half of Fig. II.10. When it is not perpendicular, one of the photons has higher energy than the other has: see the bottom half of Fig. II.10. In extreme cases, one photon can have most of the energy of the π^0. Thus, if the clustering threshold is too high, one of the photons from the asymmetrically decaying π^0 can be undetected. To detect as much π^0 as possible, i.e. detecting both of the photons, the clustering threshold is set to the lowest: as close to the DAQ threshold as possible. The clustering threshold for the data analysis is 1.35 GeV and the associated systematic uncertainty is presented in section 4.2.2.1

3.3 Event selection

This section introduces DVMP events cuts on the vertex and the detectors.

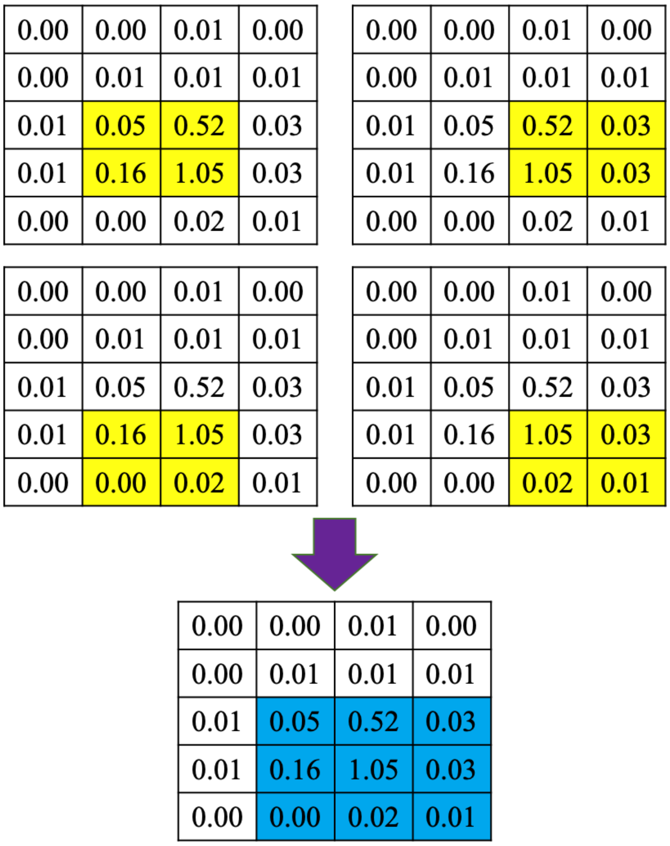

0.00	0.00	0.01	0.00
0.00	0.01	0.01	0.01
0.01	0.05	0.52	0.03
0.01	0.16	1.05	0.03
0.00	0.00	0.02	0.01

0.00	0.00	0.01	0.00
0.00	0.01	0.01	0.01
0.01	0.05	0.52	0.03
0.01	0.16	1.05	0.03
0.00	0.00	0.02	0.01

0.00	0.00	0.01	0.00
0.00	0.01	0.01	0.01
0.01	0.05	0.52	0.03
0.01	0.16	1.05	0.03
0.00	0.00	0.02	0.01

0.00	0.00	0.01	0.00
0.00	0.01	0.01	0.01
0.01	0.05	0.52	0.03
0.01	0.16	1.05	0.03
0.00	0.00	0.02	0.01

0.00	0.00	0.01	0.00
0.00	0.01	0.01	0.01
0.01	0.05	0.52	0.03
0.01	0.16	1.05	0.03
0.00	0.00	0.02	0.01

Figure II.8: Clustering algorithm. The crystals are grouped by 2 × 2 adjacent to one another with every possible combination. If the total energy of the group is above the clustering threshold set by the user, the crystals are kept for the photon reconstruction. The clustering threshold in the figure is 1.10 GeV.

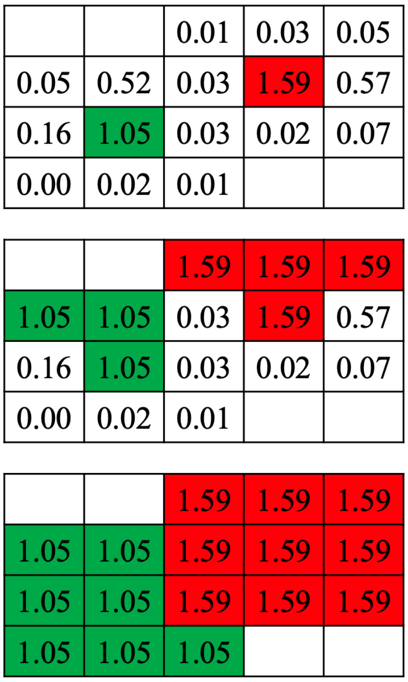

		0.01	0.03	0.05
0.05	0.52	0.03	1.59	0.57
0.16	1.05	0.03	0.02	0.07
0.00	0.02	0.01		

		1.59	1.59	1.59
1.05	1.05	0.03	1.59	0.57
0.16	1.05	0.03	0.02	0.07
0.00	0.02	0.01		

		1.59	1.59	1.59
1.05	1.05	1.59	1.59	1.59
1.05	1.05	1.59	1.59	1.59
1.05	1.05	1.05		

Figure II.9: Cellular automata. The viruses (in red and green in the top plot) infect the neighboring cells. The cells with the same virus belong to the same cluster. The infection stops when all cells are infected.

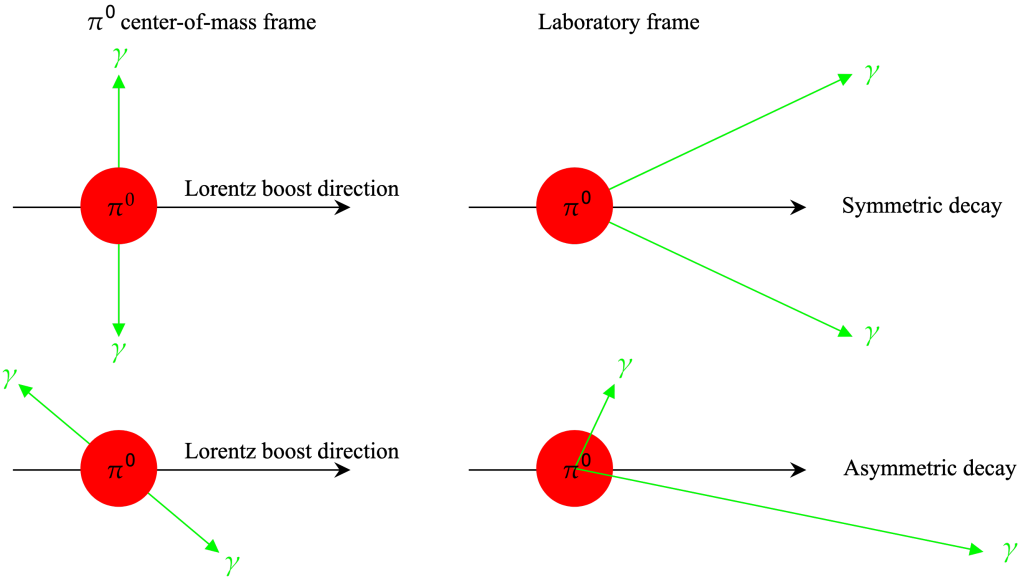

Figure II.10: π^0 decay examples in the π^0 center-of-mass frame and the laboratory frame. The less the directions of the photons are perpendicular to the Lorentz boost direction in the π^0 center-of-mass frame, the more asymmetrical the photons energies are in the laboratory frame.

3.3.1 Vertex cuts

The vertex position at the target is reconstructed from the spectrometer. When the reconstructed vertex is outside of the target, the event is discarded. By considering the thickness of the aluminum cell ($\sim$ 0.15 mm) of the liquid hydrogen and the vertex resolution of the spectrometer ($\sim$ 2 mm and $\sim$ 5.5 mm depending on the kinematics), 1 cm of the vertex at each end of the target is also removed. Presumably due to an uncertainty on the target alignment or a lack of calibration of one of the BPMs, the 1 cm cuts are not satisfactory and the cut on the positive side of the vertex (downstream side) is increased to 1.3 cm [62]: see Fig. II.11.

3.3.2 Spectrometer cuts

Pions (π^-) are the major background in the spectrometer and can be removed by using the gas Čerenkov detector and the pion rejectors of the spectrometer: see Fig. II.4. The electron emits light proportionally to the length of its trajectory in the gas Čerenkov detector whereas the pion produces no light. Furthermore, the pion deposits almost no energy compared to what the electron does in the pion rejectors. The tracks of the particles are reconstructed by the two VDCs (vertical drift chambers) of the spectrometer. In order to reconstruct the track, each wire plane in the VDCs should form at least one cluster. If multiple clusters are formed on more than one wire plane, the reconstruction software builds multiple tracks. In that case, it is difficult to identify which track belongs to which particle or it might falsely reconstruct multiple tracks out of one particle [84]. Therefore, those events are discarded.

The acceptance of the spectrometer can be described as a region in the 5-dimensional space of variables: x_{tg}, y_{tg}, ϕ_{tg}, θ_{tg}, δ_{tg}. The variable x_{tg} is related to the vertical (to the laboratory plane) vertex position and y_{tg} to the horizontal vertex position as seen by the HRS. The values ϕ_{tg} and θ_{tg} indicate the horizontal and vertical, respectively, angle of the scattering with respect to the angle and axis of the HRS. The relative momentum of the detected particle to the central momentum of the spectrometer is represented by δ_{tg}. The acceptance of the HRS depends on these variables in a correlated way. Thus, defining 1-dimensional cuts sequentially in each variable would be inefficient.

A “R-function” [85], which allows to place a 4-dimensional (y_{tg}, ϕ_{tg}, θ_{tg}, δ_{tg}) cut, is used instead of sequential 1-dimensional cuts. The value x_{tg} is ignored in this function since the beam position is constrained to $[-2,\ 2]$ mm, which is smaller than the spectrometer acceptance. This procedure shows to be almost twice more efficient than the sequential 1-dimensional cuts. The “R-value” indicates whether the electron is within the acceptance of the

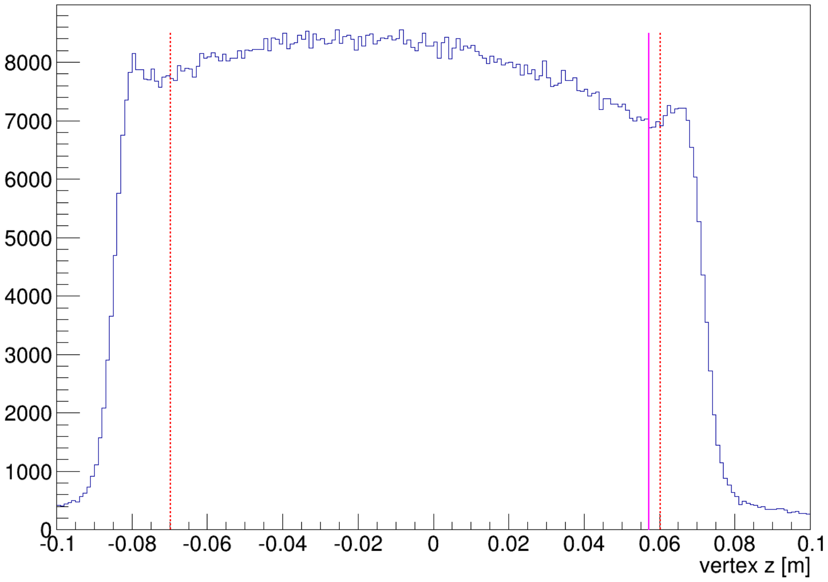

Figure II.11: Vertex distribution. The dotted red lines represent the 1-cm vertex cuts taking into account the reconstructed vertex offset. The magenta line shows the 1.3-cm vertex cut on the downstream side of the target.

spectrometer. An R-value larger than 0.003 rad indicates that the particle is well inside the acceptance.

3.3.3 Calorimeter cuts

Since the clustering threshold is set to the lowest, there is a high possibility to reconstruct photons from the background and the invariant mass of the two photons can yield that of the π^0. In order to reduce the backgrounds, an additional threshold on the reconstructed photon energy is used. In the left plot of Fig. II.12, the distributions of the reconstructed invariant mass $M_{inv} = \sqrt{(\gamma_1 + \gamma_2)^2}$ (where γ_1 and γ_2 are the 4-momenta of the reconstructed photons) are shown in two cases: with the additional photon energy threshold of 1.60 GeV in black and without it (i.e. only the clustering threshold of 1.35 GeV) in red. The distribution has a tail in the lower part of the reconstructed mass in the case of the red plot. If one extrapolates the tail to the higher mass part, near π^0 mass peak, one could see that the backgrounds would be included when selecting the π^0 events. The black plot, on the other hand, has no (or significantly smaller) tail outside the π^0 mass peak. Therefore, it is necessary to have the additional photon energy threshold for the event selection. The photon energy threshold is chosen 1.60 GeV, which is higher than the clustering threshold but not too high to lose too many events: see the right plot of Fig. II.12. The associated systematic uncertainty to the photon energy threshold is presented in section 4.2.2.1.

When the photon hits the edge of the calorimeter, part of its energy can be leaked outside of the calorimeter. Due to this reason, photons reconstructed within 3 cm from the edges of the calorimeter are discarded. In addition, the detector is unable to efficiently detect π^0 near the edges/corners of the calorimeter: one of the photons from the π^0 decay can be out of the calorimeter acceptance. To reduce these cases, an octogonal cut for the acceptance of the calorimeter is used [62]:

$$\begin{cases} x \leq 11\text{cm} \\ x \geq -20\text{cm} \\ y \leq 20\text{cm} \\ y \geq -20\text{cm} \\ y \leq x + 33\text{cm} \\ y \leq -x + 24\text{cm} \\ y \geq -x - 33\text{cm} \\ y \geq x - 24\text{cm} \end{cases} . \tag{II.21}$$

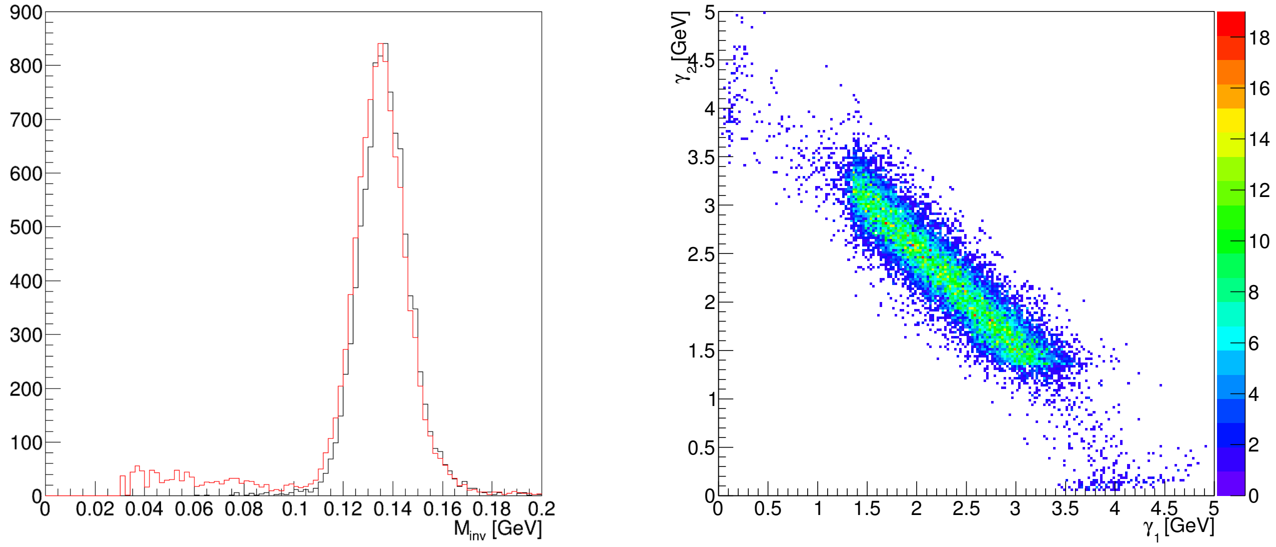

Figure II.12: Left: The distributions of the reconstructed invariant mass M_{inv} of the π^0 from the two photons. The red plot shows when only the clustering threshold of 1.35 GeV is applied and the black plot shows when additional photon energy threshold of 1.60 GeV is applied. To be noted, the red plot is normalized so that its height of the peak matches that of the black plot. Right: 2-dimensional photons energies distribution. No photon energy threshold is applied.

3.4 Background subtraction

After the event selection cuts described in the previous section, background subtractions are needed. The main sources of the background are;

- accidental coincidences: these are detected events where either the scattered electron or the reconstructed photons, do not belong to the same physical event.
- SIDIS (Semi-Inclusive DIS) events: these are events where there are other final products in addition to the recoiled proton and the π^0, $ep \to e'p'\pi^0 X$. These are non-exclusive events and become a source of background due to the fact that this experiment does not detect the final proton.
- DVMP from the resonance particle: the recoiled proton excites to a resonance particle, such as $ep \to e'\Delta\pi^0$. These events are expected to be suppressed but also become a source of background because the recoiled proton is not detected in the experiment.

3.4.1 Accidental events subtraction

The calorimeter reconstructs photons in a time window [-3, 3] ns with respect to the HRS trigger. When two reconstructed photons are acquired in that time window, i.e. in coincidence with the HRS trigger, the event is considered as a DVMP candidate. However, accidental coincidences can happen: 1) one of the reconstructed photons can be from a different event, 2) both of the reconstructed photons can be from the same π^0 decay but the scattered electron detected on the HRS can be from a different event, or 3) both the reconstructed photons and the scattered electron can all be from different events. To remove these accidental contaminations, photon reconstructions are done in several time windows. The number of potential DVMP events and the following contaminations from the accidental coincidences are listed as (see also Fig. II.13):

- N_{ccc}: Number of events where 2 photons are reconstructed in the time window [-3, 3] ns. These are the potential DVMP events since both of the photons are in coincidence with the scattered electron.
- N_{cca}: Number of events where 1 photon is reconstructed in the time window [-3, 3] ns and the other in the time window [-11, -5] ns. These are the events when only one of the photons is in coincidence with the scattered electron.

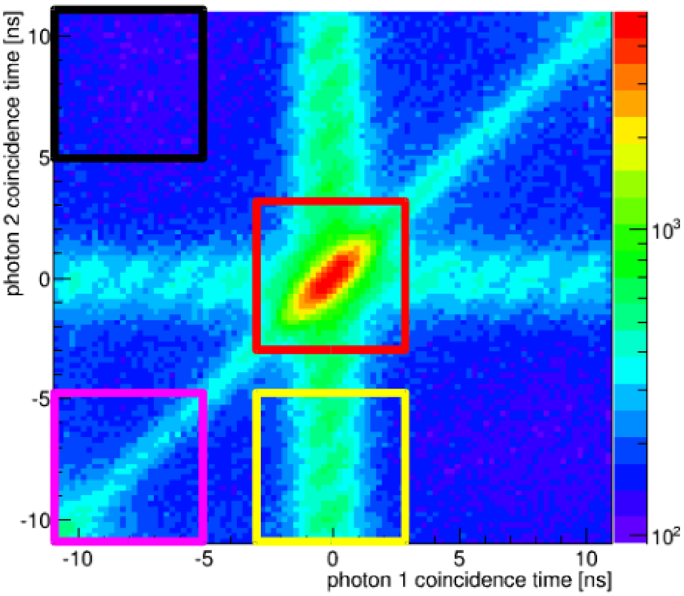

Figure II.13: Coincidence time spectrum. The red rectangle represents the time window of N_{ccc}, the yellow the N_{cca}, the magenta the N_{acc}, and the black the N_{aaa}.

- N_{acc}: Number of events where 2 photons are reconstructed in the time window [-11, -5] ns. These are the events when both of the photons are in coincidence but the scattered electron is not.
- N_{aaa}: Number of events where 1 photon is reconstructed in the time window [-11, -5] ns and the other in the time window [5, 11] ns. These are the events when neither of the three particles are in coincidence with one another.

This method relies on the fact that the accidental coincidence rates are independent of the detection time as long as the width of the window is constant. The time windows for the accidental subtraction are selected by considering the electron beam frequency (250 MHz, 4 ns, see section 1.1). They are shifted 2 × 4 ns to keep the size of the windows and not overlap with where the only true coincidence events are detected. To be noted, the same event selection cuts described in section 3.3 are applied to the accidental events.

The number of true coincident events is then obtained by N_{true} $=N_{ccc}$ - N_{cca} - N_{acc} + N_{aaa}. The N_{aaa} events happen in all cases. Thus, when subtracting N_{cca} and N_{acc} events from the N_{ccc} events, the N_{aaa} events get subtracted twice, therefore it needs to be added to compensate the double subtraction.

3.4.2 Missing Mass technique for the recoiled proton identification

As already described before, the recoiled proton from the DVCS/DVMP process is not detected. To identify the recoiled proton from the process to ensure the exclusivity of the reaction, a missing mass technique is used. The missing mass square is defined as $M_X^2 = (e + p - e' - \gamma_1 - \gamma_2)^2$, where the symbols e, p, e', and p' represent the 4-momenta of the initial electron, proton, final electron, and proton, respectively. The γ_1 and γ_2 are the 4-momenta of the reconstructed photons. Ideally, the M_X^2 distribution will have a peak at the mass squared of the proton with backgrounds from the SIDIS (such as additional π) and the resonances (such as Δ). However, due to the low energy resolution of the calorimeter (0.1 $\sim$ 0.2 photoelectrons/MeV), the proton mass squared peak broadens and the identification of the proton becomes challenging: see the left plot of Fig. II.14. On the other hand, the invariant mass of the π^0 from the reconstructed photons, M_{inv}, has a distinct peak around 0.135 GeV/c^2: see the right plot of Fig. II.14.

3.5 Corrections

Due to the techniques used in the event selection and the efficiencies of the machines used in the experiment, some of the events are lost. In this section, the corrections to those issues are presented.

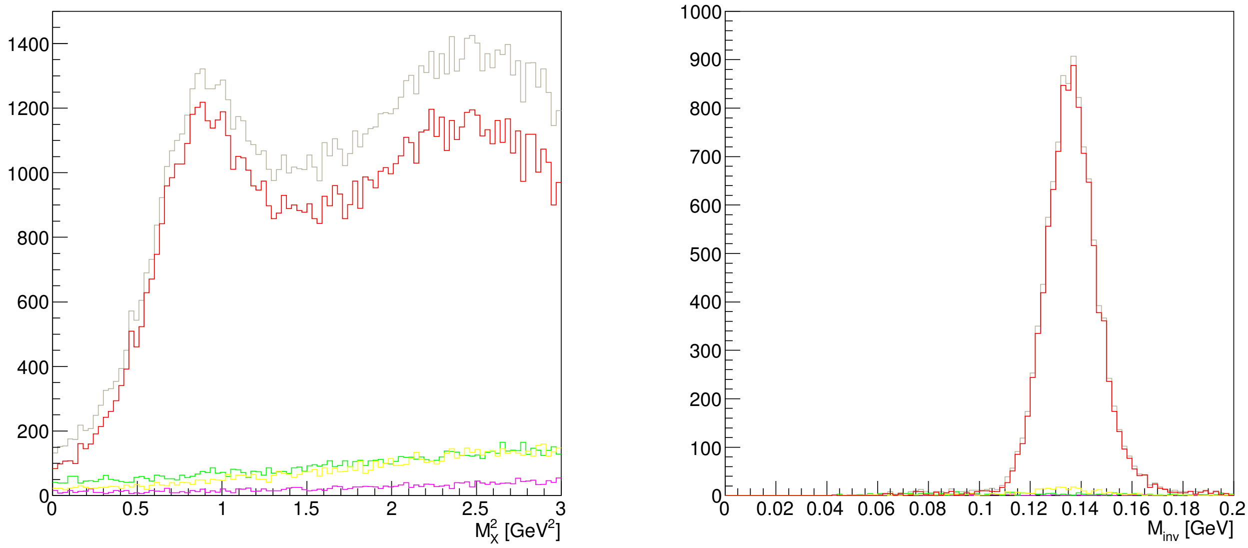

Figure II.14: M_X^2 (left) and M_{inv} (right) distribution. The grey line represents the distribution before the accidental subtraction and the red line corresponds to the one after the subtraction. Green: $\mathrm{N_{cca}}$ events, yellow: $\mathrm{N_{acc}}$ events, and magenta: $\mathrm{N_{aaa}}$ events. The proton peak is near 0.88 GeV^2 however due to the low energy resolution of the calorimeter, the distribution overlaps with those from other channels.

3.5.1 ECAL multi cluster corrections

The DVMP events are selected by requesting two reconstructed photons in the calorimeter as described in section 3.4.1. However, there can be events where both of the photons from the π^0 decay get detected and an additional particle from the other process is detected: 3 particles are reconstructed in the end. These events are ignored during the analysis process and need to be corrected for. The correction procedure is done by requesting three reconstructed photons in the time window of [-3, 3] ns. Then, if any combination of the two photons from those three satisfies all the event selection cuts, it is considered as a DVMP event lost during the analysis. These events are 7.1% of the number $\mathrm{N_{true}}$ obtained from section 3.4.1.

The accidental coincidences in 3-cluster events are not subtracted when calculating this correction since they are expected to be negligible. One might also consider the same correction with 4-cluster events. However, these events are additionally suppressed by nearly two orders of magnitude.

3.5.2 Spectrometer corrections

The coincidence between the Čerenkov detector and the scintillator S2 of the spectrometer is used as the HRS trigger of the DVCS/DVMP experiment. However, they do not have 100% efficiency and an underestimation of the DVCS/DVMP events occurs. Using another scintillator S0 (see Fig. II.4), their efficiencies are measured in dedicated runs. The trigger efficiency of, for example, the Čerenkov detector can be measured by selecting events that fire both S0 and S2 and counting how many of those also fire the Čerenkov detector. The number of DVCS/DVMP events (N) are then corrected with the trigger efficiencies η_{S2} and $\eta_{\check{C}er}$, each for the scintillator S2 and the Čerenkov detector, respectively:

$$N_{corrected} = N \times \frac{1}{\eta_{S2}\eta_{\check{C}er}}, \tag{II.22}$$

where the trigger efficiencies are $\eta_{S2} = 0.9974$ and $\eta_{\check{C}er} = 0.9984$ [86].

In section 3.3.2, multi-cluster events in more than one VDC wire plane are discarded. By doing so, events where single particle leaving multi clusters in more than one wire plane are lost. The correction factor η_{track} to compensate those lost events is:

$$\eta_{track} = \frac{N_1 + N_{mc}}{N_1}, \tag{II.23}$$

where N_1 is the number of events with multi clusters in only one of the wire planes and N_{mc} is the number of events with multi clusters in more than one wire plane. The value of the correction factor is 1.06 [86]. By taking the tracking correction factor into account, the number of DVCS/DVMP events from Eq. (II.22) becomes:

$$N_{corrected} = N \times \eta_{track} \times \frac{1}{\eta_{S2}\eta_{\check{C}er}}. \tag{II.24}$$

3.5.3 Dead time correction

As mentioned in section 1.3.2, dead time occurs during the DAQ and events are lost during the dead time. The dead time (T_{dead}) is obtained by:

$$T_{dead} = 1 - \frac{live}{raw}. \tag{II.25}$$

The term "*live*" in Eq. (II.25) indicates the number of HRS trigger from a scaler that only counts when the DAQ is available. Another independent scaler counts the number of HRS trigger without considering the DAQ availability and that number of counts is indicated as "*raw*" in Eq. (II.25). With the dead time correction, one can calculate the integrated luminosity $\mathcal{L}$:

$$\mathcal{L} = \frac{Q_{corrected}\rho l N_A}{eM_H}, \tag{II.26}$$

with $Q_{corrected}$ $(= Q \times (1 - T_{dead}))$ the corrected accumulated beam charge, ρ the target density, l the target length, N_A the Avogadro number, e the elementary charge, and M_H the hydrogen molar mass. The dead time is $1 - 0.981$.

4 Geant4 simulation and cross section extraction

In order to extract cross sections from the number of events detected, one needs to know the acceptance of the experiment. However, due to its complex configuration, a computation of the acceptance by hand is nearly impossible. Therefore, for the calculation of the acceptance, a Monte Carlo simulation with a realistic setup is used. Radiative corrections are also implemented.

A half of this section is dedicated to the basic description of the simulation. Later, the radiative effects and their correction are presented. Then the overall process of the simulation is described. The calibration of the calorimeter is shown next. The second half of this section describes the cross section extraction. The systematic uncertainties of the data analysis are shown afterwards. Finally, the preliminary results of the extracted cross sections are presented in the last part.

4.1 Geant4 simulation

The Monte Carlo simulation uses Geant4 libraries, version 9.6.4. The Geant4 libraries are widely used in high energy physics with reliability in the energy range up to 100 TeV.

4.1.1 Geometry

In order to extract the cross sections, a precise geometry of the set up is crucial. The experimental setup includes: the liquid hydrogen target and its chamber, the beam pipes, and their background shieldings [87]. The HRS itself is not fully simulated, as its acceptance is well-known and described by an R-function. Instead, only the geometry of its entrance window is included in the simulation.

The geometry of the calorimeter with its shieldings is fully simulated. The real position of each crystal, accurately surveyed during the experiment, is implemented. However, the generation of Čerenkov light in the PbF_2 crystals is not simulated. This is because the optical photons simulation is time consuming and the radiation damage during the data taking changes the optical properties of the crystals. It is thus faster and more efficient to smear the energy resolution of the calorimeter after the simulation is done in order to match the observed resolution in the data. The geometry of the simulation is depicted in Fig. II.15.

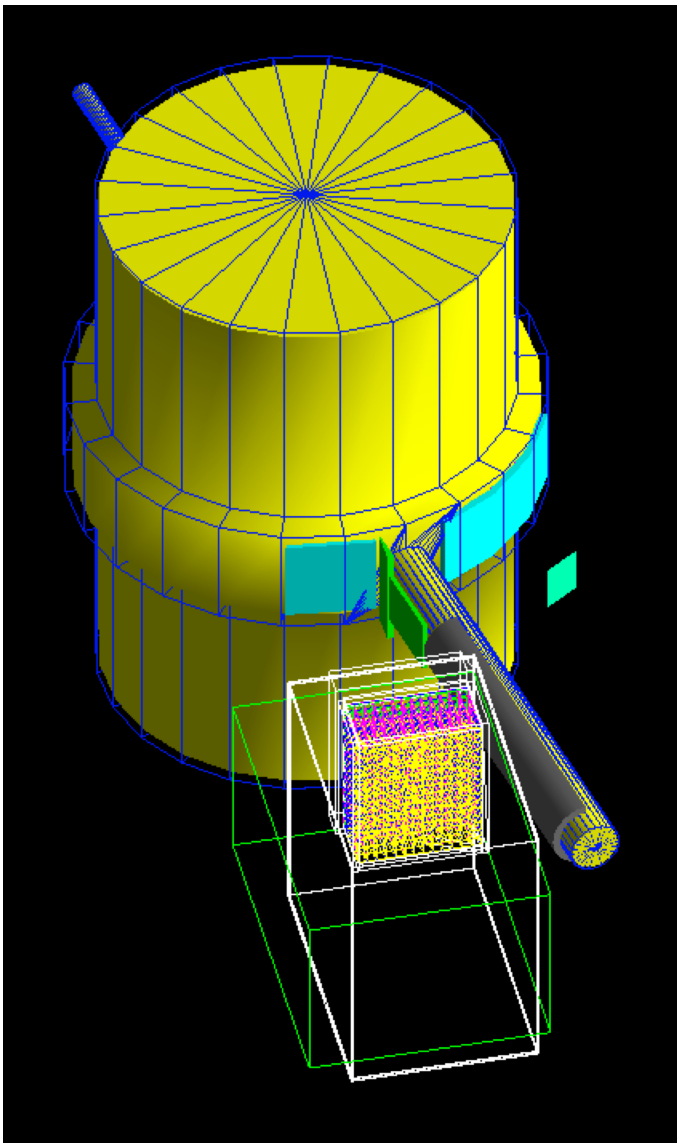

Figure II.15: Experimental geometry in the Geant4 simulation. The yellow cylindrical shape shows the target chamber. The liquid hydrogen target is inside. The light blue represents the kapton and aluminum windows of the target chamber. These windows are thinner areas of the chamber in order to let the scattered electron and the DVCS/π^0 photons go through by traversing a less amount of material. The grey cylinders upstream and downstream of the target chamber depicts the beam pipes and the green rectangles surrounding the beam pipe near the target chamber indicate the beam-line shieldings. The light green rectangle represents the HRS entrance window. The geometry of the calorimeter is fully simulated and can be seen on the left side of the beam pipe.

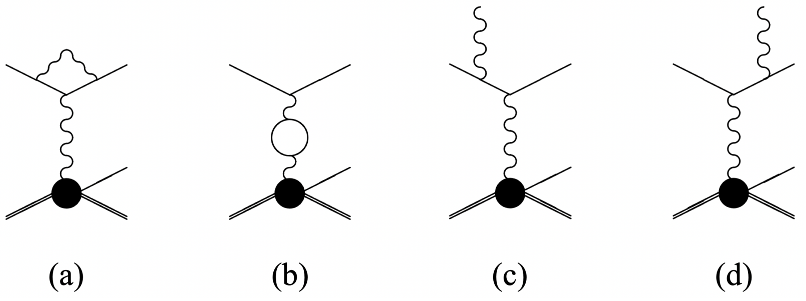

Figure II.16: First order internal radiative effects illustrated in the case of DVMP. Figure extracted from [91].

4.1.2 QED radiative correction

Due to radiative effects on the electron, the kinematic variables (Q^2, x_B) slightly change during the interaction. When the radiative effects occur before or after the interaction with the target, they are called *external.* When the radiative effects occur at the interaction vertex, they are called *internal.* The external and internal radiative effects where a real photon is emitted are incorporated into the event generator of the simulation in order to convolute their effects with the detector resolutions.

The radiative corrections are performed to the first order in Q^2/m^2, where m denotes the mass of the particle that the radiative correction is being applied to. Since the proton and the pion masses are much larger than that of the electron, the corrections are applied only to the leptonic part.

4.1.2.1 External radiative correction

The event generator generates the scattered electrons, the π^0, and the recoiled proton. Therefore, the radiation of the electron beam while traversing the target before scattering is not taken into account by the event generator. The electron loses its energy inside the target by the Bremsstrahlung and radiates real photons before and after the event vertex. With a good approximation, the loss of energy ΔE follows the distribution [88]:

$$I(E_0, \Delta E, t_{mat}) = \frac{bt_{mat}}{\Delta E}\left[\frac{\Delta E}{E_0}\right]^{bt_{mat}}, \tag{II.27}$$

where E_0 is the initial energy of the beam before the Bremsstrahlung, the t_{mat} is the thickness of the material in units of radiation length, and b $\sim 4/3$. The energy loss, when generated event by event in the Monte Carlo simulation, that follows the distribution $I(E_0, \Delta E, t_{mat})$ is:

$$\Delta E = E_0 r^{1/bt_{mat}}, \tag{II.28}$$

where r is a uniform random distribution function within the range of [0., 1.]. The above equation for the energy loss is within the peaking approximation [89], where the radiated photons are emitted along the direction of the electron. The external radiative corrections shown here are applied to the initial electron but not on the scattered electron: the energy loss of the scattered electron is taken care by the Geant4 libraries.

4.1.2.2 Internal radiative correction

In [90], the internal radiative corrections have been studied for the *ep* elastic scattering. The study can be applied for the DVMP since the leptonic part of the DVMP is identical to the elastic scattering.

At first order in QED, there are three radiative processes:

- the vertex correction (see Fig. II.16 (a)): the electron emits a photon before scattering and reabsorbs the photon after the scattering. The momentum of the electron changes during the scattering process;
- the vacuum polarization (see Fig. II.16 (b)): the virtual photon turns into a electron-positron pair.
- the internal Bremsstrahlung (see Fig. II.16 (c) and (d)): a real photon is emitted by the electron either before or after the scattering.

Taking these corrections above, the experimental cross section $\frac{d\sigma}{d\Omega}\big|_{Exp}$ is related to the Born cross section[†] $\frac{d\sigma}{d\Omega}\big|_{Born}$ by the expression [92]:

$$\left.\frac{d\sigma}{d\Omega}\right|_{Exp} = \left.\frac{d\sigma}{d\Omega}\right|_{Born} \left[1 + \delta_{ver} + \delta_{vac} + \delta_{Brem}(\Delta E)\right], \tag{II.29}$$

where δ_{vert} is the vertex correction, δ_{vac} the vacuum polarization, and δ_{Brem} the internal Bremsstrahlung. The correction terms are written as (in a limit of $Q^2 \gg m_e^2$):

$$\delta_{vert} = \frac{\alpha}{\pi}\left[\frac{3}{2}\ln\left(\frac{Q^2}{m_e^2}\right) - 2 - \frac{1}{2}\ln^2\left(\frac{Q^2}{m_e^2}\right) + \frac{\pi^2}{6}\right] \tag{II.30a}$$

$$\delta_{vac} = \frac{2\alpha}{3\pi}\left[\ln\left(\frac{Q^2}{m_e^2}\right) - \frac{5}{3}\right] \tag{II.30b}$$

$$\delta_{Brem} = \frac{\alpha}{\pi}\left\{2\ln\left(\frac{\Delta E}{\sqrt{EE'}}\right)\left[\ln\left(\frac{Q^2}{m_e^2}\right) - 1\right]\right. \tag{II.30c}$$

$$\left. - \frac{1}{2}\ln^2\left(\frac{E}{E'}\right) + \frac{1}{2}\ln^2\left(\frac{Q^2}{m_e^2}\right) - \frac{\pi^2}{3} + Sp\left(\cos^2\frac{\theta_e}{2}\right)\right\}, \tag{II.30d}$$

with α the fine structure constant, m_e the electron mass, E and E' the electron energy before and after the scattering, θ_e the electron scattering angle, and $Sp(x) \equiv -\int_0^x dt \frac{\ln(1-t)}{t}$ the Spence function. Note that only the correction term δ_{Brem} depends on the energy loss of the electron: ΔE (soft-photon energy). By splitting the correction term δ_{Brem} into ΔE-dependent and independent parts (neglecting the ΔE dependence of E' and Q^2), one can re-write the Eq. (II.29) as:

$$\left.\frac{d\sigma}{d\Omega}\right|_{Exp} = \left.\frac{d\sigma}{d\Omega}\right|_{Born} \left[\frac{e^{\delta_{vert}+\delta_{Brem,0}}}{(1-\delta_{vac}/2)^2}\right]\left(\frac{\Delta E}{\sqrt{EE'}}\right)^{\delta_s} \tag{II.31a}$$

$$\text{with} \quad \delta_s = \frac{2\alpha}{\pi}\left[\ln\left(\frac{Q^2}{m_e^2}\right) - 1\right], \tag{II.31b}$$

where $\delta_{Brem,0}$ is the Bremsstrahlung correction term independent of ΔE. The approximate resummation deriving Eq. (II.31a) from Eq. (II.29) is described in [90].

By differentiating Eq. (II.31a) with respect to ΔE, one obtains the radiative tail due to the internal Bremsstrahlung:

$$\left.\frac{d\sigma}{d\Omega d\Delta E}\right|_{Exp} = \left.\frac{d\sigma}{d\Omega}\right|_{Born} \left[\frac{e^{\delta_{vert}+\delta_{Brem,0}}}{(1-\delta_{vac}/2)^2}\right]\frac{\delta_s}{\Delta E}\left(\frac{\Delta E}{E}\right)^{\delta_s}\left(\frac{E}{E'}\right)^{\delta_s/2}. \tag{II.32}$$

Note that the term $\frac{\delta_s}{\Delta E}\left(\frac{\Delta E}{E}\right)^{\delta_s}$ has the same form as in Eq. (II.27), with an equivalent radiator [88, 93] thickness of δ_s. This term is from the soft-photons with energy not very small compared to the electron (ΔE-dependent part of δ_{Brem}: $\delta_{Brem,1}$). Thus, the internal Bremsstrahlung $\delta_{Brem,1}$ in the simulation is treated the same way as the external Bremsstrahlung. However, the correction is applied twice: one for the incoming electron and another for the outgoing electron at the vertex, each with the thickness of $\delta_s/2$.

There is an additional term $\left[\frac{e^{\delta_{vert}+\delta_{Brem,0}}}{(1-\delta_{vac}/2)^2}\right]\left(\frac{E}{E'}\right)^{\delta_s/2}$ in Eq. (II.32). These internal virtual radiative effects: vertex correction, vacuum polarization, and soft-photon emission (with energy much lower than the electron) can be applied after the cross section extraction since they do not depend on the detector acceptance. The value δ_s for the experiment is approximately 0.07 and by using the kinematic variables of the experiment, one can calculate the value $\left[\frac{e^{\delta_{vert}+\delta_{Brem,0}}}{(1-\delta_{vac}/2)^2}\right]\left(\frac{E}{E'}\right)^{\delta_s/2}$ and it is around 1.12.

4.1.3 Event generator and simulation process

The event generator for the DVMP simulation consists of largely two parts: a leptonic part and a hadronic part. The leptonic part generates $e \to e'\gamma^*$, with the external and internal Bremsstrahlung radiative corrections, and the hadronic part generates $\gamma^* p \to p'\pi^0 \to p'\gamma_1\gamma_2$. The final products from the event generator are the scattered electron, the recoiled proton, and the two photons from the π^0 decay.

[†] The Born cross section is the pure cross section without any radiative effects.

The vertex is created randomly along the beam axis within the target boundary. The length the initial electron travels through the target before the interaction is used for the external radiative correction, described in the previous section.

To speed up the event generation process, the leptonic part of the events is generated in a horizontal plane. The ranges $\left[\theta_e^{min}, \theta_e^{max}\right]$ and $\left[p_e^{min}, p_e^{max}\right]$ of the horizontal angle θ_e and the momentum p_e of the scattered electron are slightly larger than the spectrometer acceptance to fully cover it. The Q^2 and x_B are then generated uniformly in given ranges:

$$Q^2_{min} = 2p_e^{min}E_v^{ext}(1 - \cos\theta_e^{min}) < Q^2 < 2p_e^{max}E_v^{ext}(1 - \cos\theta_e^{max}) = Q^2_{max}, \tag{II.33a}$$

$$x_B^{min} = \max\left(\frac{p_e^{min}E_v^{ext}(1 - cos\theta_e^{min})}{M(E_v^{ext} - p_e^{min})}, 0.05\right) < x_B < \min\left(\frac{p_e^{max}E_v^{ext}(1 - cos\theta_e^{max})}{M(E_v^{ext} - p_e^{max})}, 0.95\right) = x_B^{max}, \tag{II.33b}$$

where E_v^{ext} is the energy of the initial electron after the external Bremsstrahlung correction and M is the proton mass. If $E_v^{ext} < p_e^{min}$, the event is considered lost. However, it is taken into account in the total number of the generated events for the simulation normalization. The phase space factor associated to the generated electron is then $\Delta Q^2 \Delta x_B = [Q^2_{max} - Q^2_{min}][x_B^{max} - x_B^{min}]$.

After the generation of Q^2 and x_B, the scattered electron at the vertex is calculated and its momentum and scattering angle θ_e are computed as:

$$p_e = E_v - \frac{Q^2}{2Mx_B}, \tag{II.34a}$$

$$\cos\theta_e = 1 - \frac{Q^2}{2p_eE_v}, \tag{II.34b}$$

where E_v is the energy of the initial electron at the vertex after the first internal Bremsstrahlung correction. If $p_e < 0$, the event is considered lost. As in the previous case, it is taken into account in the total number of the generated events. The second internal Bremsstrahlung correction is applied to the scattered electron.

The hadronic part of the generator calculates the two-body interaction $\gamma^* p \to p'\pi^0$ in the center-of-mass frame. The squared momentum transfer t is generated uniformly in a range $[t_{min}(Q^2, E_v) - 3,\ t_{min}(Q^2, E_v)]$ GeV^2. The $t_{min}(Q^2, E_v)$ is the value t when the direction of the π^0 is parallel to the direction of the virtual photon. This interval covers the entire calorimeter acceptance and its assigned phase space factor is $\Delta t = 3$ GeV^2. After the two-body interaction, the recoiled proton is boosted to the laboratory frame. Finally, the π^0 decays into two back-to-back photons in its center-of-mass frame and they are boosted to the laboratory frame.

The angle ϕ_{π^0} between the leptonic and the hadronic planes is generated in the interval $[0, 2\pi]$ uniformly and a phase space factor $\Delta\phi_{\pi^0} = 2\pi$ is associated to the event. To cover the vertical acceptance of the spectrometer, all the particles are rotated around the initial beam axis in the interval large enough to encompass the spectrometer vertical acceptance and its phase space factor is $\Delta\phi_e$.

The particles (scattered electron, recoiled proton, and two photons) at the vertex are now generated, and from there Geant4 handles their transportation. When the scattered electron passes through the entrance window of the HRS, the R-function is used to determine whether the particle is detected or not. The two photons deposit their energies into the calorimeter creating electromagnetic showers in the crystals.

One should also take the vertex resolution of the spectrometer σ_{vertex} into account. The vertex position (v_z) in the target is smeared ($v_z|_{smeared}$) with a Gaussian distribution:

$$v_z|_{smeared} = v_z + Gauss\left(0, \sigma_{vertex}\right) = v_z + Gauss\left(0, \frac{\sigma_{90^\circ}}{\sin\theta_{HRS}}\right), \tag{II.35}$$

where θ_{HRS} is the spectrometer angle with respect to the beam direction and σ_{90° is the spectrometer vertex resolution at $\theta_{HRS} = 90^\circ$. The vertex resolution of the spectrometer at $\theta_{HRS} = 90^\circ$ is: $\sigma_{90^\circ} = 1.5$ mm.

The general procedure of the event generation is represented in Fig. II.17. The associated phase space factor to the generated event is $\Delta\Omega = \Delta Q^2(E_v^{ext})\Delta x_B(E_v^{ext})\Delta t\Delta\phi_e\Delta\phi_{\pi^0}$ which is different for each event due to E_v^{ext}.

4.1.4 Simulation calibration and smearing

As mentioned before, the Čerenkov light in the crystals of the calorimeter is not generated and only the deposited energy in the crystals is recorded. To precisely calculate the acceptance, the calorimeter in the simulation needs to have the same energy resolution as that in the experiment. Therefore, proper energy (gain) calibration and smearing

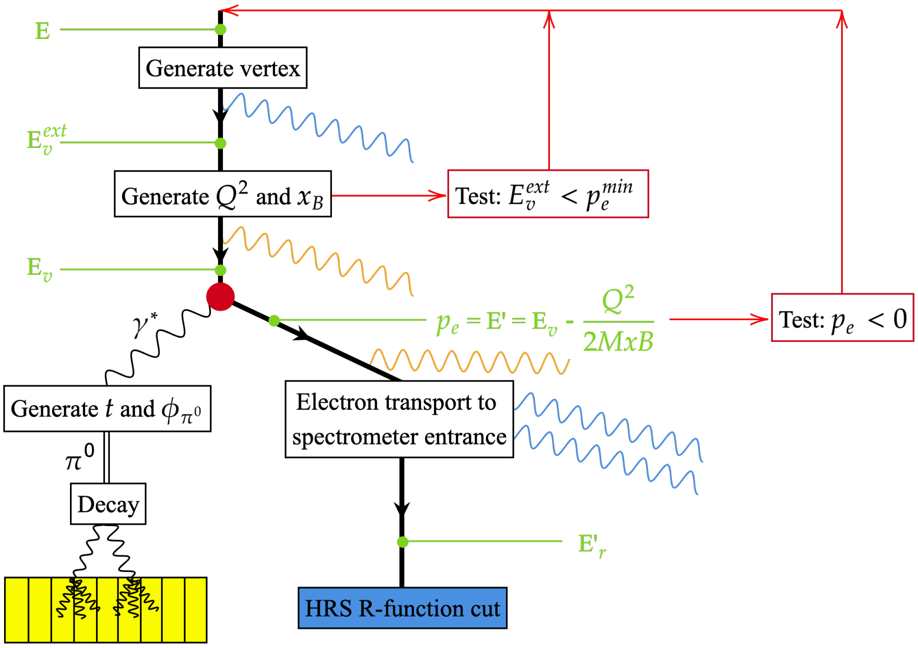

Figure II.17: Schematic representation of the main steps of the event generator in the Monte Carlo simulation. The blue and orange photons indicate the external and internal Bremsstrahlung, respectively. The energy E'_r denotes the final energy of the scattered electron transported to the entrance of the spectrometer after the Bremsstrahlung corrections and the energy loss managed by Geant4.

of the calorimeter in the simulation are needed. The M_X^2 and M_{inv} distributions of the simulation before the calibration and the smearing are presented in Fig. II.18. The distributions of the simulation have higher resolution than those of the experiment. It is because the simulation does not produce Čerenkov light: the fluctuation in the number of Čerenkov photons in the experiment produces relatively low resolution. Furthermore, the peaks of the M_X^2 and M_{inv} do not match between experiment and simulation. The calorimeter loses about 4% of the photon energy between the crystals and at the backside of the crystals. This loss is compensated during the calibration for the experiment. However, this is not the case in the simulation and it causes the underestimation of the photon energy.

The gain calibration and the smearing of the energy are performed event by event simultaneously. It multiplies the 4-momentum of the photon by a random variable following a Gaussian distribution $Gauss(\mu, \sigma)$ where the μ and the σ are the calibration and smearing coefficients, respectively:

$$\left.\begin{pmatrix} q_x \\ q_y \\ q_z \\ E \end{pmatrix}\right|_{new} = Gauss(\mu, \sigma) \times \begin{pmatrix} q_x \\ q_y \\ q_z \\ E \end{pmatrix}. \tag{II.36}$$

The coefficients depend on the energy of the photons: $\mu \propto E$, $\sigma \propto \sqrt{E}$. They are obtained for each kinematic setting to take into account the change/evolution of the radiation damage. Also, since the degradation of the crystal optical transmission varies for each crystal, the coefficients need to be evaluated for each crystal. That is for an ideal case, where there are enough number of events in the experiment. However, it is not the case and therefore, the calorimeter surface is divided into 7 × 7 partially overlapping rectangular areas. Each event is associated to the area where the projection of the π^0 direction lies, and both decay photons are smeared using the same coefficients. The coefficients μ_j and σ_j for the area $j \in [1, ..., 49]$ are obtained by minimizing the χ^2:

$$\chi_j^2(\mu_j, \sigma_j) = \frac{1}{N_{bin} - 2} \sum_{i=i_{min}}^{i=i_{max}} \left(\frac{N_{i,j}^{exp} - N_{i,j}^{MC}}{\sigma_{i,j}^{exp}} \right)^2, \tag{II.37}$$

where the variable i runs over $N_{bin}(= i_{max} - i_{min} + 1)$ missing mass bins. The number of events in the experiment

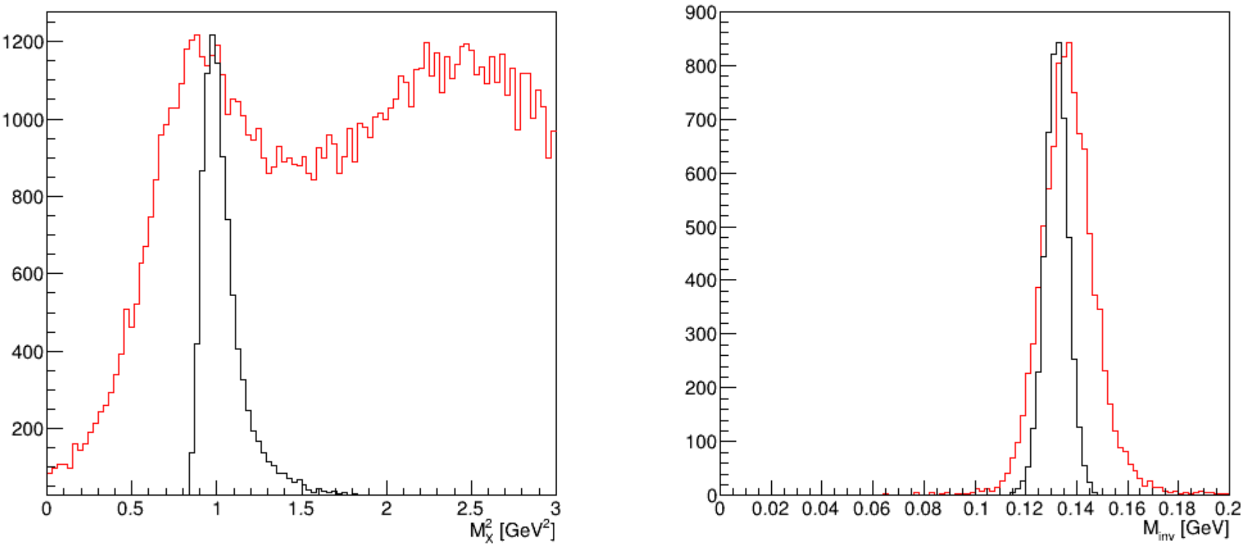

Figure II.18: M_X^2 (left) and M_{inv} (right) distributions before the energy (gain) calibration and smearing of the calorimeter in the simulation (black). The histograms of the simulation are scaled to match the peak height of the experimental data (red).

and the Monte Carlo simulation, in the ith bin of the area j, are $N_{i,j}^{exp}$ and $N_{i,j}^{MC}$, respectively. The associated statistical uncertainty of the experimental counts is $\sigma_{i,j}^{exp}$. The boundaries i_{max} and i_{min} for the χ^2 minimization are carefully selected so that they include the proton mass squared peak and exclude the SIDIS and resonance processes as much as possible.

There is an additional step before the simulation calibration and smearing. Due to the fluctuations in the measurements of the energies of the photons in the calorimeter, there appears a correlation between the M_X^2 and M_{inv} (see the left plot of Fig. II.19). To remove the correlation, an empirical method is used:

$$M_X^2|_{new} = M_X^2 + C \cdot (M_{inv} - M_{\pi^0}), \tag{II.38}$$

where $M_X^2|_{new}$ is the new missing mass squared and M_{π^0} is the invariant mass of the π^0. The value C is 20 GeV. After the removal of the correlation (see the right plot of Fig. II.19), the missing mass squared distribution shows a more distinct peak at the mass squared of the proton as shown in the left plot of Fig. II.21. After applying the same correction (Eq. (II.38)) to the simulated data, the χ^2 minimization for each of the 49 sections of the calorimeter is performed.

In order to apply the calibration coefficients to each photon, the coefficients obtained for each of the 49 areas of the calorimeter are interpolated across the surface of the calorimeter. The resulting position-dependent calibration coefficients μ and σ are plotted in Fig. II.20. As it can be seen from the right plot of the Fig. II.20, the smearing coefficient σ is higher in the region closer to the beam (positive xc-value) due to higher radiation damage.

The Fig. II.21 shows the M_X^2 and the M_{inv} distributions of the experiment and the simulation, after applying the Eq. (II.38) and the energy calibration and smearing. As can be seen from the right plot of the Fig. II.21, even though the calibration and the smearing are done only by matching the M_X^2 distributions, the M_{inv} distributions also match well. The values of the exclusivity cuts are [0.5, 1.0] GeV^2 and the invariant-mass cuts are [0.0871, 0.186] GeV: see Fig. II.21. The associated systematic uncertainties to these exclusivity and invariant-mass cuts are presented in section 4.2.2.2.

There are two classes of inclusive hadronic electroproduction channels that compete with the exclusive $H(e, e'\pi^0)p$ reactions. The first class includes the $H(e, e', \pi^0)N\pi$, $N\pi\pi$... channels, with a threshold at $M_X^2 = (M_p + M_\pi)^2 = 1.15$ GeV^2 where M_p indicates the mass of proton. This class includes resonant and nonresonant $N\pi$ production in the final state. It also includes diffractive $\rho^+ \to \pi^+\pi^0$ production via the $ep \to ep^+n$ reaction. The second class is the $H(e, e'\pi^0)\gamma p$ channel. It originates from the $ep \to ep\omega$ reaction, with a 8.5% branching-ratio decay channel [94]. Based on the acceptance of the previous Hall A DVCS/DVMP experiments and the measurements performed in [95], the contamination from that channel is estimated to be smaller than 1% [56, 59]. The inclusive yield obtained by

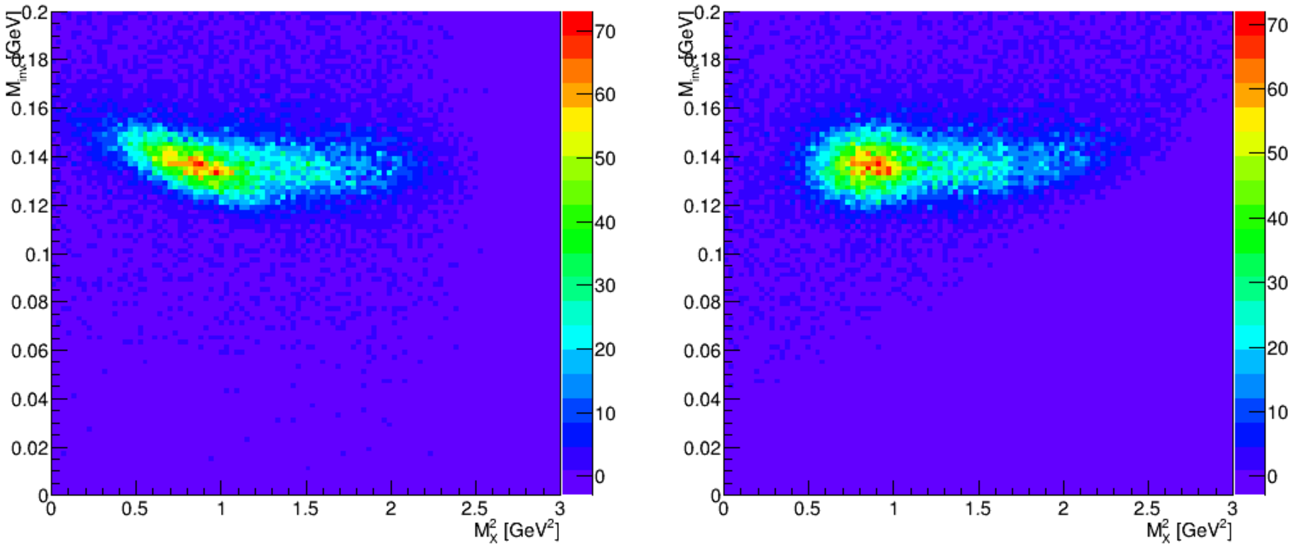

Figure II.19: Correlation between M_X^2 and M_{inv}: left plot is before applying the Eq. (II.38) and the right plot is after the application. The plots are from the experimental data.

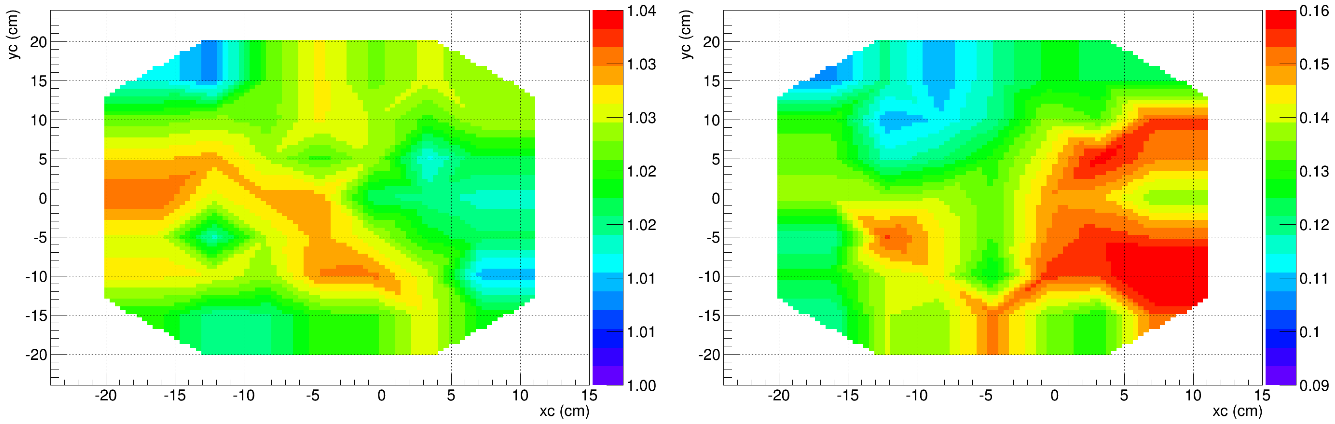

Figure II.20: Energy calibration coefficient μ (left) and smearing coefficient σ (right) displayed on the calorimeter surface: the labels "xc" and "yc" indicate the horizontal and vertical position on the surface of the calorimeter respectively. The coefficients in 49 sections are interpolated across the calorimeter surface.

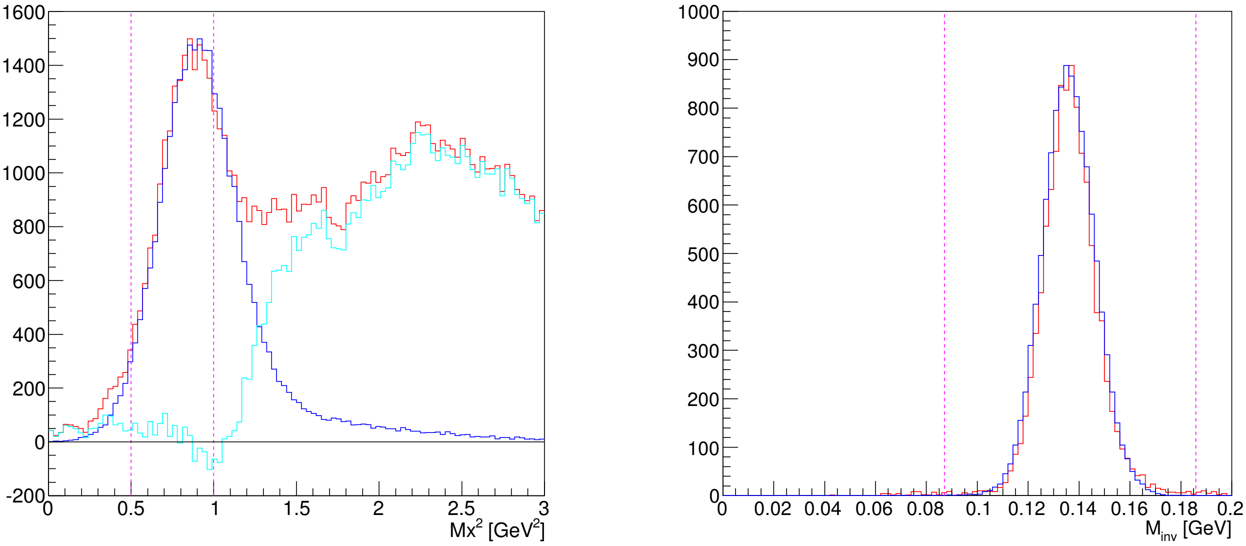

Figure II.21: M_X^2 (left) and M_{inv} (right) distributions after the χ^2 minimization for the gain calibration and energy smearing of the calorimeter (blue). The histograms of the simulation are scaled to match the peak height of the experimental data (red). The cyan line shows the estimated inclusive yield obtained by subtracting the simulation from the experimental data. The new M_X^2 distribution of the experimental data shows a better proton mass squared peak at 0.88 GeV^2 which makes the χ^2 minimization easier. The lines in magenta indicate the exclusivity cuts on the left plot and the π^0 invariant-mass cuts on the right plot.

subtracting the simulation from the experimental data is below 2% for $M_X^2 \in [0.5, 1.0]$ GeV^2 (see the left plot of Fig. II.21) and can be treated as a point-to-point systematic uncertainty.

4.2 Cross section extraction

The number of events N_r in the experimental bin $r \in \mathcal{R}$ can be written as:

$$N_r = \mathcal{L} \int_r \frac{d\sigma}{d\Omega} d\Omega = \mathcal{L} \frac{\int_r \frac{d\sigma}{d\Omega} d\Omega}{\int_r d\Omega} \int_r d\Omega = \mathcal{L} \left\langle \frac{d\sigma}{d\Omega} \right\rangle_r \Delta\Omega_r, \tag{II.39}$$

which means that by knowing the number of events N_r and the associated acceptance $\Delta\Omega_r$ of the bin r with the integrated luminosity $\mathcal{L}$, one can extract the average cross section over the bin r. The acceptance of the bin r can be computed from the Monte Carlo simulation described in the previous section:

$$\Delta\Omega_r = \sum_i \frac{\Delta\Omega_i^{MC}}{N_{gen}^{MC}}, \tag{II.40}$$

where the sum runs over the events i reconstructed in the bin r, $\Delta\Omega_i^{MC}$ is the associated phase space factor of the event i, and N_{gen}^{MC} is the total number of the generated events in the Monte Carlo simulation.

The cross section of the π^0 electroproduction (see Eq. (I.45)) is a linear combination of the unknown parameters one wants to extract (X^Λ) and the kinematic factors ($\Gamma^\Lambda(Q^2, x_B, E, \phi_{\pi^0})$). The kinematic factors Γ^Λ here are different from the virtual photon flux Γ_{γ^*} in Eq. (I.45). These values vary within the given bin. However, if one assumes that the X^Λ stays constant over the bin, it is possible to fit these combinations by integrating the kinematic factors into the calculation of the acceptance in the Monte Carlo simulation:

$$N_r = \mathcal{L} \int_r \Gamma^\Lambda(Q^2, x_B, E, \phi_{\pi^0}) X^\Lambda d\Omega = \mathcal{L} \left\langle X^\Lambda \right\rangle \int_r \Gamma^\Lambda(Q^2, x_B, E, \phi_{\pi^0}) d\Omega. \tag{II.41}$$

The acceptance calculation of the simulation can further incorporate the radiative effects and the energy resolution effects mentioned in the previous section to account for bin migration.

The first part of this section describes in further details the fitting method. The systematic uncertainties due to the exclusivity, the π^0 invariant-mass cuts, the clustering threshold, and the photon energy threshold are presented in the second part. The last part shows the preliminary results of the extracted cross section.

4.2.1 Fitting method

The basic idea of the cross section extraction is to minimize the difference between the number of events in the experiment (N_r^{exp}) and the Monte Carlo simulation (N_r) in each bin r by varying the average cross section. In other words, the average cross section in each bin is obtained by minimizing the χ^2:

$$\chi^2 = \sum_r^{\mathcal{R}} \frac{\left(N_r^{exp} - N_r\right)^2}{\left(\sigma_r^{exp}\right)^2}, \tag{II.42}$$

where the σ_r^{exp} is the associated statistical uncertainty in the bin r of the experiment.

Generally, in the experiment, the event in the experimental bin r, i.e. at the detector, does not always correspond to the same bin v at the vertex, i.e. at the target, due to the radiative effects and the energy resolution of the calorimeter. The cross section we want to extract is at the vertex v:

$$N_v = \mathcal{L} \int_v \frac{d\sigma}{d\Omega} d\Omega = \mathcal{L} \left\langle \frac{d\sigma}{d\Omega} \right\rangle_v \Delta\Omega_v. \tag{II.43}$$

In order to obtain the cross section at the vertex, the number of events N_v and the acceptance $\Delta\Omega_v$ at the vertex are needed.

In the simulation, one can calculate the (bin migration) probability K_{rv} of the event in the bin $v \in \mathcal{V}$ at the vertex being detected in the experimental bin $r \in \mathcal{R}$ so that the relation between N_r and N_v becomes;

$$N_r = \sum_v^{\mathcal{V}} K_{rv} N_v. \tag{II.44}$$

Then the cross sections in the bin v at the vertex are related to the number of events in the experimental bin r by:

$$N_r = \mathcal{L} \sum_v^{\mathcal{V}} \int_v K_{rv} \frac{d\sigma}{d\Omega_v} d\Omega_v, \tag{II.45}$$

where the index v in Ω is to indicate that the integration is done at the vertex.

By expressing the π^0 electroproduction cross section (Eq. (I.45)) at the vertex bin as a linear combination of the unknown parameters X^Λ $(= \{d\sigma_T/dt + \epsilon^* d\sigma_L/dt,\ d\sigma_{TL}/dt,\ d\sigma_{TT}/dt\})$ and the kinematic factors $\Gamma_v^\Lambda(Q^2, x_B, E, \phi_{\pi^0})$, where the index Λ runs over each response term $\{T + \epsilon^* L, TL, TT\}$:

$$\frac{d\sigma}{d\Omega_v} = \sum_\Lambda \Gamma_v^\Lambda(Q^2, x_B, E, \phi_{\pi^0}) X_v^\Lambda, \tag{II.46}$$

the Eq. (II.45) becomes

$$N_r = \mathcal{L} \sum_v^{\mathcal{V}} \sum_\Lambda \left\langle X^\Lambda \right\rangle_v \int_v \Gamma_v^\Lambda K_{rv} d\Omega_v = \mathcal{L} \sum_v^{\mathcal{V}} \sum_\Lambda \mathcal{K}_{rv}^\Lambda \left\langle X^\Lambda \right\rangle_v. \tag{II.47}$$

The $\mathcal{K}_{rv}^\Lambda$ $(\equiv \int_v \Gamma_v^\Lambda K_{rv} d\Omega_v)$ is the bin migration function which is basically an acceptance weighted by the kinematic factors Γ_v^Λ, where the bin migration effects are also taken into account by K_{rv}.

After calculating $\mathcal{K}_{rv}^\Lambda$ from the simulation, one can then extract the parameters of the cross section ($\left\langle X^\Lambda \right\rangle_v$) by minimizing the χ^2 in Eq. (II.42):

$$0 = -\frac{1}{2} \frac{\partial \chi^2}{\partial \left\langle X^\Lambda \right\rangle_v} \Bigg|_{\left\langle \overline{X}^\Lambda \right\rangle_v} \tag{II.48a}$$

$$= \sum_r^{\mathcal{R}} \mathcal{L} \mathcal{K}_{rv}^\Lambda \frac{\mathcal{L} \sum_{v'}^{\mathcal{V}} \sum_{\Lambda'} \mathcal{K}_{rv'}^{\Lambda'} \left\langle \overline{X}^{\Lambda'} \right\rangle_{v'} - N_r^{exp}}{(\sigma_r^{exp})^2} \tag{II.48b}$$

$$= \sum_{v'}^{\mathcal{V}} \sum_{\Lambda'} A_{v,v'}^{\Lambda,\Lambda'} \left\langle \overline{X}^{\Lambda'} \right\rangle_{v'} - B_v^\Lambda. \tag{II.48c}$$

The Eq. (II.48c) is a linear equation in a matrix form with:

$$A^{\Lambda,\Lambda'}_{v,v'} = \mathcal{L}^2 \sum_r^{\mathcal{R}} \frac{\mathcal{K}^{\Lambda}_{rv}\mathcal{K}^{\Lambda'}_{rv'}}{(\sigma_r^{exp})^2}, \tag{II.49a}$$

$$B^{\Lambda}_{v} = \mathcal{L} \sum_r^{\mathcal{R}} \frac{\mathcal{K}^{\Lambda}_{rv} N_r^{exp}}{(\sigma_r^{exp})^2}. \tag{II.49b}$$

Then the fitted parameters are obtained by solving the linear equation:

$$\left\langle \overline{X}^{\Lambda} \right\rangle_v = \sum_{v'}^{\mathcal{V}} \sum_{\Lambda'} \left[A^{-1}\right]^{\Lambda,\Lambda'}_{v,v'} B^{\Lambda'}_{v'}, \tag{II.50}$$

with the covariance matrix A^{-1}. The associated statistical uncertainty of $\left\langle \overline{X}^{\Lambda} \right\rangle_v$ is given by $\sqrt{[A^{-1}]^{\Lambda,\Lambda}_{v,v}}$.

For the χ^2 minimization to work, there must be more number of data to fit than the number of unknown variables. In other words, the number of the reconstructed bins r must be bigger than that of the vertex bins v for the linear equations Eq. (II.48c) to have a unique solution. The unknown variables $\left\langle \overline{X}^{\Lambda} \right\rangle_v$ are independent of ϕ_{π^0} whereas the number of experimental counts depend on ϕ_{π^0} through the kinematic factors Γ^{Λ}_v. Therefore, the variable ϕ_{π^0} makes it possible to obtain the unique solution.

The binning is done in five experimental variables: Q^2, x_B, E, ϕ_{π^0}, and t. Each kinematic setting of the experiment corresponds to one bin of the first three variables. The variable ϕ_{π^0} is binned only for the experimental data in 12 bins. The variable t is binned in 5 bins. For the experiment, the variable $t'(= t - t_{min})$ is used instead of t. As mentioned before, the $t_{min}(Q^2, E)$ is the value t when the direction of the π^0 is parallel to the direction of the virtual photon. The calorimeter in the experiment is centered around the direction of the virtual photon. For this reason, the calorimeter acceptance is flatter in the variable t' than in t. As a consequence, the value t' increases as the π^0 points further away from the center of the calorimeter.

4.2.1.1 Bin migration function

The bin migration function $\mathcal{K}^{\Lambda}_{rv}$ is a 60 × 5 matrix: 12 ϕ_{π^0}-bins in each 5 t'-bin for the reconstructed variables (r) and 5 t'-bins for the vertex (v). It is calculated in the simulation by counting the number of events corresponding to each element of the matrix divided by the total number of generated events, weighted by the kinematic factors Γ^{Λ}_v and the associated phase space factor of the event: $\mathcal{K}^{\Lambda}_{rv} = \sum_i \Gamma^{\Lambda}_v K_{rv} \frac{\Delta\Omega_i^{MC}}{N_{gen}^{MC}}$, where the sum runs over the events i created at the vertex bin v and detected in the experimental bin r. The bin migration matrix for the response term $\Lambda = T + \epsilon^* L$ is shown in Fig. II.22. As expected, most of the events fall in the same t' bin at the vertex and in the experiment. These are shown in the diagonal blocks of the matrix. The off-diagonal blocks represent the events for which their t' bin at the vertex is not the same as that in the reconstructed detector variables.

Fig. II.23 shows the number of experimental events with associated statistical uncertainties and the fitted number of events. The number of generated events for the simulation is sufficiently large so that its statistical uncertainty is negligible compared to that of the experimental data. The resulting χ^2 from the fit (Eq. (II.42)) normalized by the number of degrees of freedom dof is 2.07 ($\sim 93.3(\chi^2)/45(dof)$). The number of degrees of freedom dof is the number of experimental bins ($\mathcal{R} = 60$) minus the number of parameters to fit ($\forall\Lambda \times \mathcal{V} = 3 \times 5$). Due to the acceptance of the calorimeter, there is a relatively small number of events near the angle $\phi_{\pi^0} = 0$ and 2π rad when t' gets larger. Therefore, the relative statistical uncertainties are expected to increase as the value t' increases.

4.2.2 Systematic uncertainties

4.2.2.1 Clustering threshold and photon energy threshold cuts

The calculations of the systematic uncertainty due to the clustering threshold and the photon energy cut are done simultaneously. The cross sections are extracted in each t' bin with all the other cuts fixed and only varying the clustering threshold and the photon energy threshold. These two are varied independently except on one condition: photon energy threshold is higher than the clustering threshold. It is because there is no reason to set the photon energy threshold lower than the clustering threshold. One of the examples of the extracted cross sections in this study is shown in Fig. II.24. When the clustering threshold is fixed, the cross section in general remains constant as a function of the photon energy cut in the range of [1.1, 1.8] GeV, within the statistical uncertainty. The cross

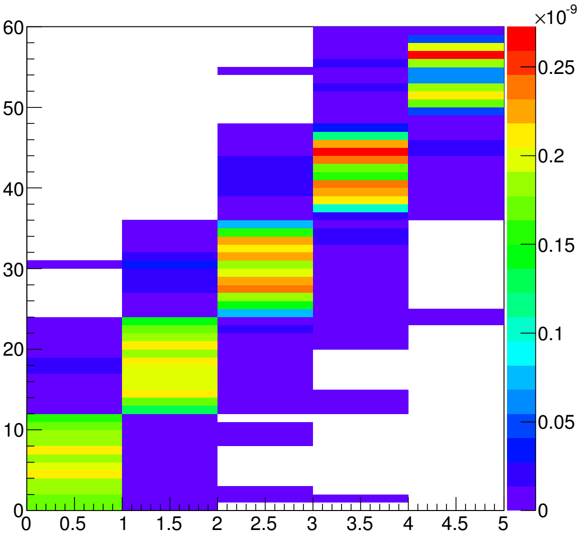

Figure II.22: The bin migration matrix for the response term $T + \epsilon^* L$. The horizontal axis represents the binning in t' at the vertex and the vertical axis depicts the binning in $\phi_{\pi^0} \times t'$ in the detector.

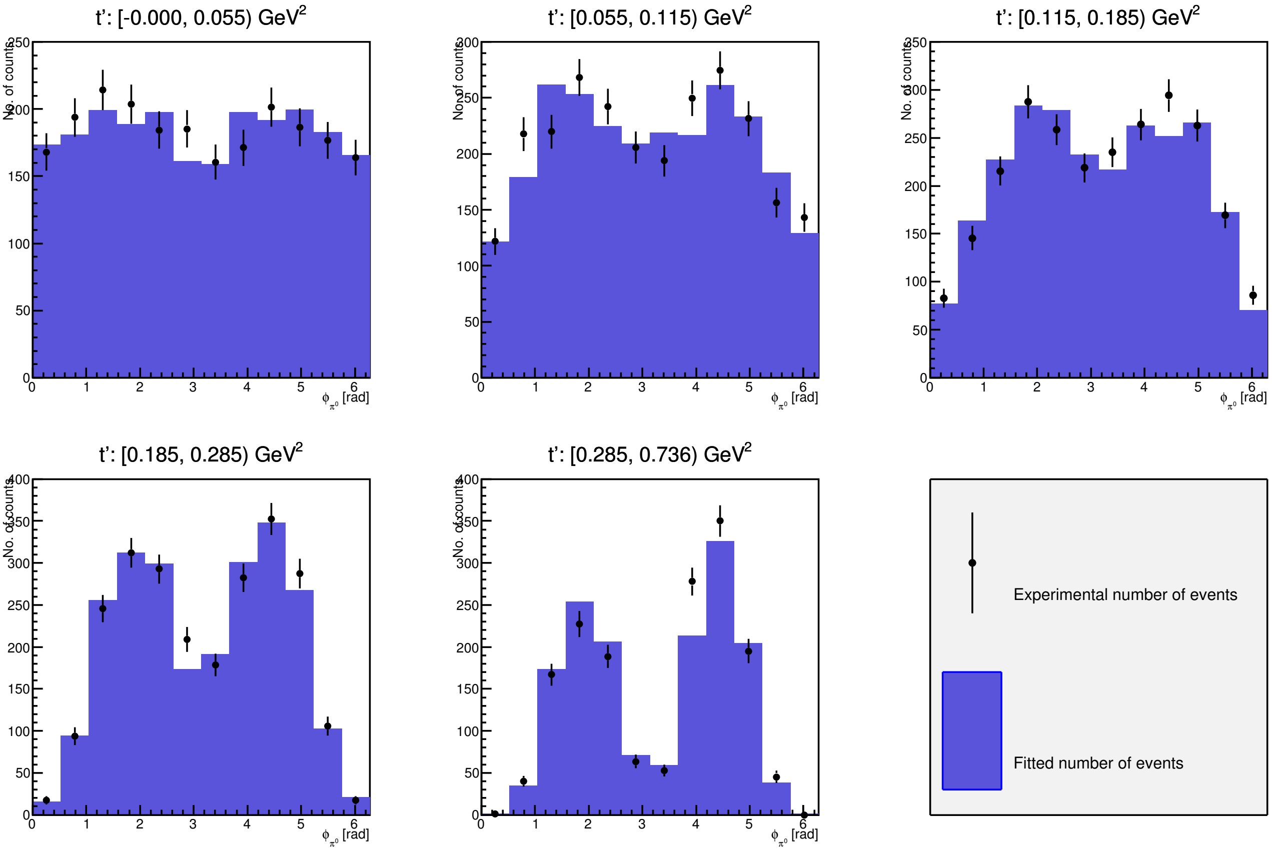

Figure II.23: DVMP events with $E = 7.383$ GeV, $\langle Q^2 \rangle = 3.20$ GeV^2, and $\langle x_B \rangle = 0.36$. The black markers show the number of DVMP events from the experiment with associated statistical uncertainties, shown by vertical black lines. The blue bars show the fitted number of events. The χ^2/dof of the fit is 2.07.

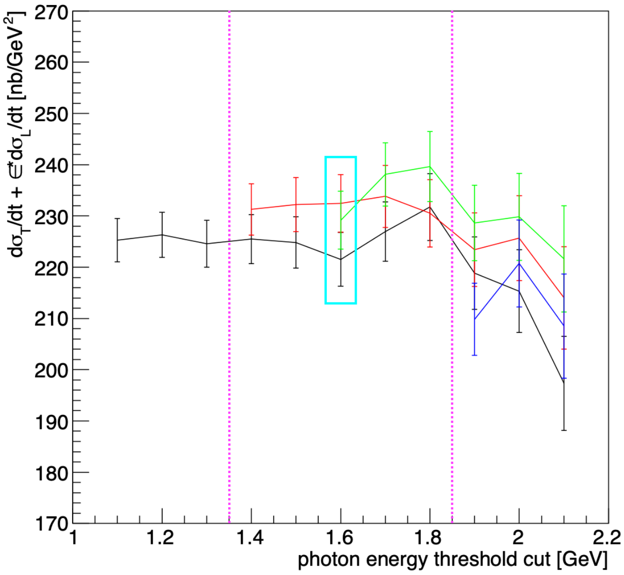

Figure II.24: $(d\sigma_T + \epsilon^* d\sigma_L)/dt$ in the $t' \in [0.115, 0.185)\text{GeV}^2$ bin. The variables are the photon energy threshold, in horizontal axis, and the clustering threshold, in different colors. The black markers represent the cross sections with a clustering threshold of 1.10 GeV, red with 1.35 GeV (nominal value), green with 1.60 GeV, and blue with 1.85 GeV, with associated statistical uncertainties represented by the vertical bars. The nominal photon energy threshold is 1.60 GeV. The cross section values (in color red) within the magenta lines are used for the calculation of the associated systematic uncertainties due to the photon energy threshold. The cross section values within the cyan rectangle are used for the calculation of the associated systematic uncertainties due to the clustering threshold.

Table II.1: Systematic uncertainties of the clustering threshold and the photon energy threshold. The corresponding range for each t' bin is $t'1 \in [0.000, 0.055)$ GeV^2, $t'2 \in [0.055, 0.115)$ GeV^2, $t'3 \in [0.115, 0.185)$ GeV^2, $t'4 \in [0.185, 0.285)$ GeV^2, and $t'5 \in [0.285, 0.736)$ GeV^2.

$(d\sigma_T + \epsilon^* d\sigma_L)/dt$	$t'1$	$t'2$	$t'3$	$t'4$	$t'5$
clustering threshold	+0.0%	+0.1%	+0.0%	+0.0%	+4.6%
	-2.5%	-0.0%	-4.7%	-3.7%	-1.5%
photon energy threshold	+0.8%	+1.0%	+0.6%	+3.2%	+4.4%
	-0.6%	-5.5%	-0.8%	-2.0%	-3.7%

section also does not change its value from the nominal value as a function of the clustering threshold in the range of [1.10, 1.85] within the statistical uncertainty, at fixed photon energy threshold.

The systematic uncertainties for the clustering threshold and the photon energy threshold are shown in Tab. II.1. The values for the clustering threshold are obtained from the change of the cross section by varying the clustering threshold from 1.10 GeV to 1.60 GeV, with photon energy threshold fixed to its nominal value of 1.60 GeV. The systematic uncertainties for the photon energy threshold are obtained in the same way by varying the cut from 1.40 GeV to 1.85 GeV, with the clustering threshold at its nominal value of 1.35 GeV. The values of the uncertainties are the maximum deviation from the nominal cross section values.

4.2.2.2 Missing mass and invariant mass cuts

For the systematic uncertainty study due to the exclusivity cuts, the cross sections are extracted with the missing mass squared M_X^2 upper cut varying from 0.8 to 1.45 GeV^2, whilst all other cuts are fixed to their nominal values. The cross sections are also extracted with the M_X^2 lower cut varying from 0.0 to 0.9 GeV^2. As can be seen from the left plot of Fig. II.25, the cross sections stay unchanged within their statistical uncertainties as the M_X^2 upper cut increases up to 1.2 GeV^2. However, the cross section increases when the M_X^2 upper cut increases above 1.2 GeV^2: this happens as the simulation cannot reproduce the M_X^2 distribution of the data above 1.2 GeV^2: see the left plot

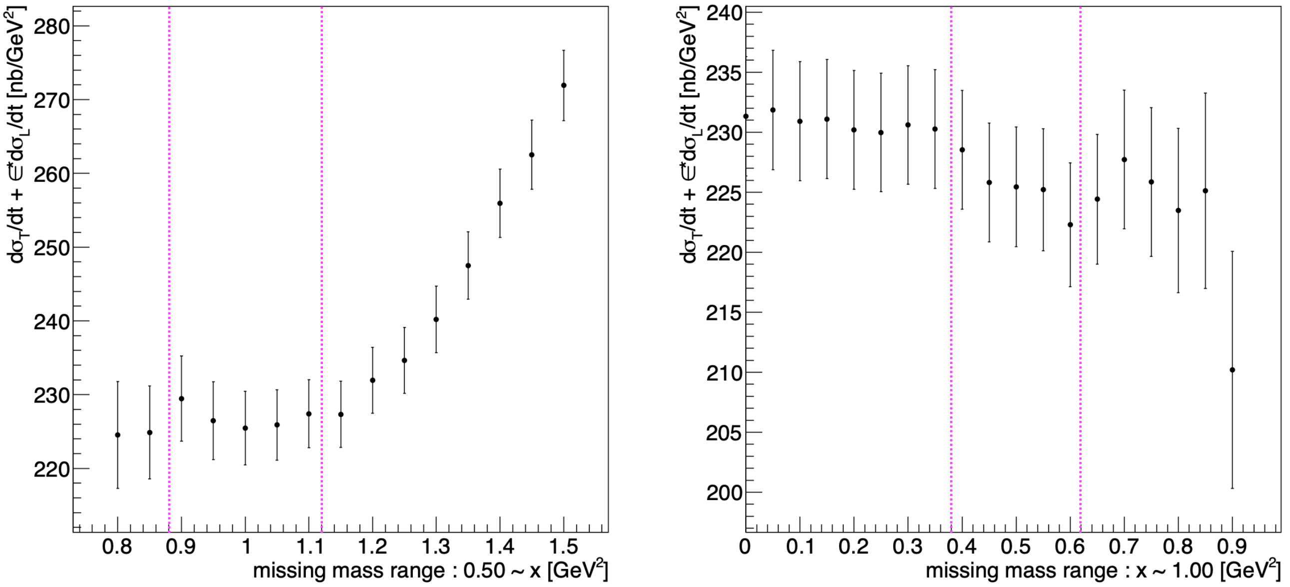

Figure II.25: $(d\sigma_T + \epsilon^* d\sigma_L)/dt$ in the $t' \in [0.055, 0.115)\text{GeV}^2$ bin as a function of the M_X^2 upper cut (left) and the lower cut (right). The nominal values of the upper and lower cuts are 1.00 GeV^2 and 0.50 GeV^2, respectively. The cross section values within the magenta lines are used for the calculation of the associated systematic uncertainties due to the exclusivity cuts.

Table II.2: Systematic uncertainty of the M_X^2 cut. The same ranges for the t' bins are used as in Tab. II.1.

$(d\sigma_T + \epsilon^* d\sigma_L)/dt$	$t'1$	$t'2$	$t'3$	$t'4$	$t'5$
M_X^2 upper cut	+0.8%	+1.8%	+0.0%	+2.4%	+0.9%
	-0.6%	-0.0%	-2.9%	-0.0%	-3.6%
M_X^2 lower cut	+1.3%	+1.4%	+0.3%	+1.5%	+0.3%
	-0.1%	-1.4%	-0.7%	-1.1%	-1.7%

of Fig. II.21. The number of events in the experimental data get contaminated from SIDIS events above 1.2 GeV^2. Therefore, the M_X^2 upper cut range for the systematic uncertainty is set to [0.9, 1.1] GeV^2. The variations below 0.9 GeV^2 are not considered since the cut below the proton mass squared removes too many events.

The M_X^2 lower cut on the other hand, does not change the cross section within the statistical uncertainty in a range of [0.0, 0.8] GeV^2: see the right plot of Fig. II.25. This is expected since no contamination, such as SIDIS, is expected in this region. The nominal value for the M_X^2 lower cut is 0.50 GeV^2. It is to remove the undershot of the simulation in the low M_X^2 region: also see the left plot of Fig. II.21. The disagreement appears due to the imperfection of the calibration and smearing method applied to the simulation. The M_X^2 lower cut range for the systematic uncertainty is set to [0.4, 0.6] GeV^2. The maximum change (positive and negative) of the cross section from the nominal value, at 1.00 GeV^2 for the upper cut and 0.50 GeV^2 for the lower cut, is the associated systematic uncertainty for each bin t' and the values are shown in Tab. II.2.

The systematic uncertainty study due to the invariant-mass cuts is performed in a similar way as the exclusivity cuts. The cross sections with the upper and lower cuts varied by ± 0.03 GeV from their nominal values are shown in Fig. II.26. The nominal invariant-mass cut is [0.0871, 0.186] GeV. Since the M_{inv} distribution shows a clear π^0 invariant mass distribution without backgrounds (see the right plot of Fig. II.21), the cut for the M_{inv} distribution is chosen so that almost no events are excluded. Therefore, there is no significant change in the cross section when the cut values are changed. The M_{inv} cut range for the systematic uncertainty is ± 0.02 GeV from the nominal value, for both the upper and lower cuts. Tab. II.3 lists the systematic uncertainty (maximum change of the cross section from the nominal value) for each t' bin: the values are compatible with zero.

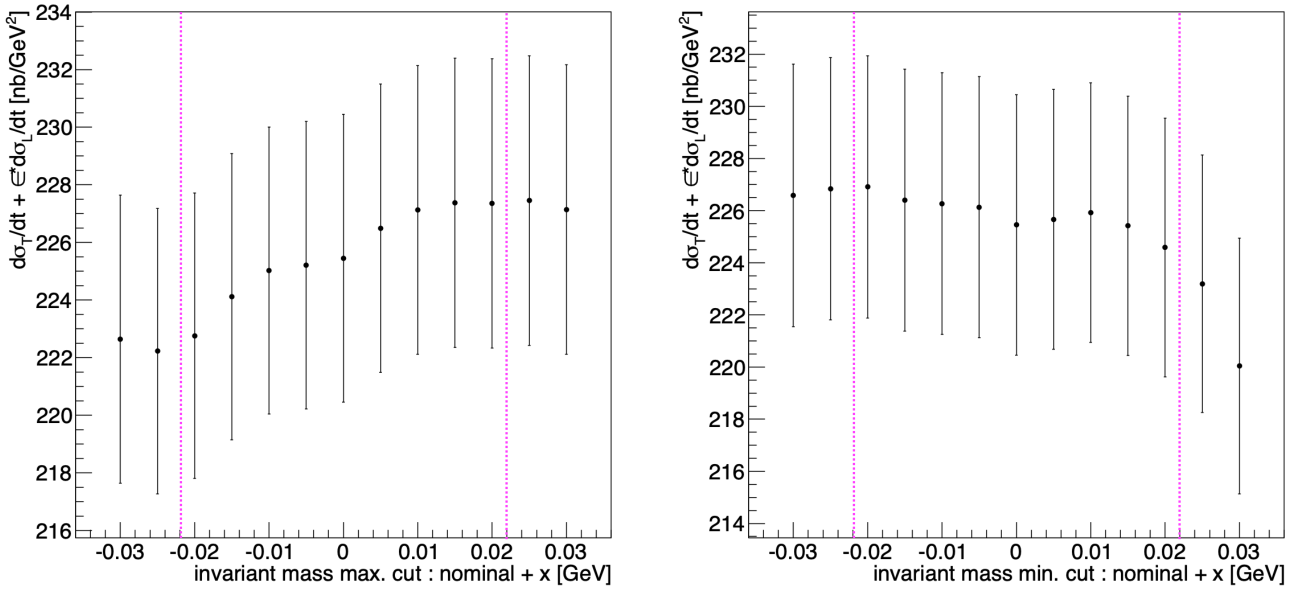

Figure II.26: $(d\sigma_T + \epsilon^* d\sigma_L)/dt$ in the $t' \in [0.055, 0.115)\mathrm{GeV}^2$ bin as a function of the M_{inv} upper cut (left) and the lower cut (right). The horizontal axis indicates the cut value varied from the nominal one used for the cross section extraction. The cross section values within the magenta lines are used for the calculation of the associated systematic uncertainties due to the invariant-mass cuts.

Table II.3: Systematic uncertainty of the M_{inv} cut. The same ranges for the t' bins are used as in Tab. II.1.

$(d\sigma_T + \epsilon^* d\sigma_L)/dt$	$t'1$	$t'2$	$t'3$	$t'4$	$t'5$
M_{inv} upper cut	+0.1%	+0.7%	+0.1%	+0.8%	+1.2%
	-0.3%	-0.2%	-0.2%	-0.8%	-0.3%
M_{inv} lower cut	+0.1%	+0.4%	+0.0%	+0.7%	+3.0%
	-0.2%	-0.0%	-0.1%	-0.6%	-0.0%

4.2.3 Preliminary results

The variation ranges of the cuts for the systematic uncertainty studies in section 4.2.2 are large. For example, the M_X^2 upper cut is varied to the extremes: it ranges from near the proton mass squared peak to where the SIDIS contaminations become prominent. Furthermore, the variations of the cross section due to the changes of the cuts are mostly compatible within statistical uncertainties. Despite this, the obtained values in Tab. II.1, II.2, and II.3 are used as the associated systematic uncertainties of the cuts. Therefore, the systematic uncertainties used here are very conservative and probably overestimated.

The obtained systematic uncertainties are independent of each other and, therefore, added quadratically but separately sign-per-sign. The extracted cross sections with their associated statistic and systematic uncertainties are shown in Fig. II.27. The last t' bin does not have the bin migration effect from larger values of t', thus the cross section in the last bin should be ignored. The GK model prediction [45, 46, 96] of the cross section and the data agree well especially for the $(d\sigma_T + \epsilon^* d\sigma_L)/dt$ and $d\sigma_{TT}/dt$ terms. It is worth noting that the GK model predicts that the contribution $(d\sigma_T + \epsilon^* d\sigma_L)/dt$ is mostly from the $d\sigma_T/dt$ term whilst the $d\sigma_L/dt$ term is almost zero.

The $d\sigma_{TL}/dt$ terms, however, do not agree. The extracted $d\sigma_{TL}/dt$ term has negative values while the model predicts positive values. The previous experiment [59] presented in Fig. I.19 had also found similar results. Also, the values from the data are several orders of magnitude larger than those the model predicts. This may hint to a larger contribution from the longitudinally polarized photons than the model predicts. Therefore, the chiral-even GPDs may still be accessible through π^0 electroproduction off the nucleon in these kinematics.

Other kinematic settings shown in Fig. II.1 are being analyzed by the Hall A DVCS/DVMP collaboration. The scaling behavior of the L/T unseparated cross sections ($(d\sigma_T + \epsilon^* d\sigma_L)/dt$) in a wide Q^2 and x_B range will be tested. Furthermore, the Rosenbluth separation of the L/T terms will be performed in the same kinematic range in the upcoming Hall C experiment [63]. This energy separation will not only extract the $d\sigma_T/dt$ and $d\sigma_L/dt$ terms separately but also enable the test of the GK model in a larger kinematic domain, more rigorously. The development of a neutral particle spectrometer for the upcoming Hall C experiment is described in detail in the next chapter.

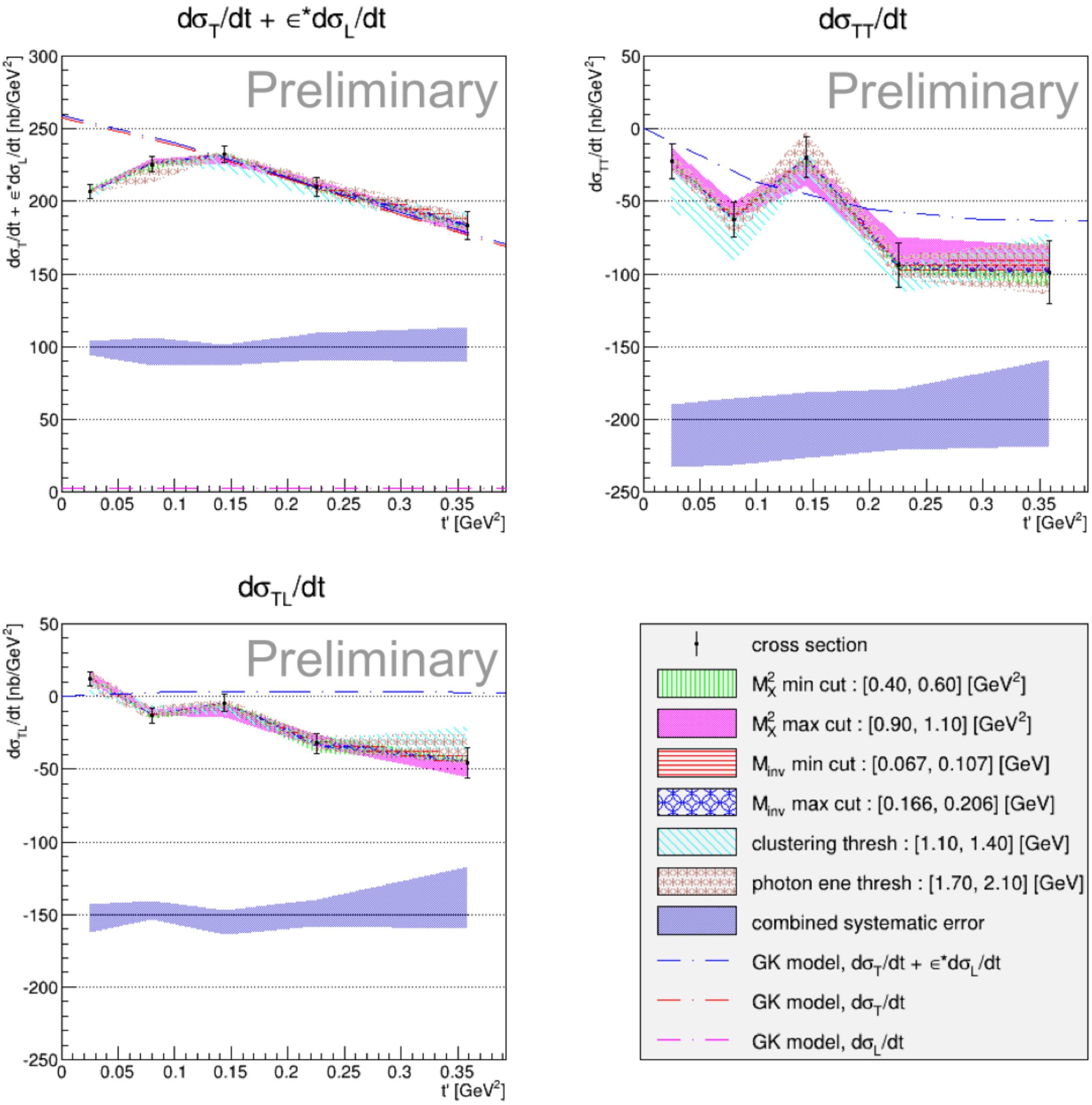

Figure II.27: Extracted cross sections for $ep \to e'p'\pi^0$ at $E = 7.383$ GeV, $\langle Q^2 \rangle = 3.2$ GeV^2 and $\langle x_B \rangle = 0.36$. The bars on the black markers show the associated statistical uncertainties of the cross sections. Each band depicts the associated systematic uncertainties as described in the legend. The cross section in the last bin should be ignored since the last t' bin does not take into account the bin migration from larger t'. The blue dash-dotted line represents the predicted cross section from the GK model [45, 46, 96]. In the top-left panel, the red dash-dotted line adjacent to the blue dash-dotted line shows the predicted $d\sigma_T/dt$ term from the GK model, and the magenta dash-dotted line near the horizontal axis depicts the predicted $d\sigma_L/dt$ term from the GK model.

Chapter III

Neutral Particle Spectrometer

The DVCS and DVMP experiment in Hall C (E12-13-010) [63] is complementary to that in Hall A [61], presented in the previous chapter. By setting the kinematics the same as those of the Hall A experiment but at different beam energies, it will allow us to separate the L/T terms of the π^0 cross section (σ_T and σ_L in Eq. (I.45)) and also separate the $|\mathcal{T}_{\mathrm{DVCS}}|^2$ term from the $\mathcal{I}$ term (in Eq. (I.40)). The beam energy for the energy separation will reach up to 11 GeV. To test the leading twist dominance in the Jefferson Lab kinematic range, the Hall C experiment will increase the Q^2 reach to even higher values at fixed x_B. It will allow a much more stringent test of the Q^2 dependence of each separated observable in the DVCS cross section.

The Hall C experiment will expand the x_B range to lower values due to its high luminosity and the low systematic uncertainties of the Hall C setup. Although the lower x_B range is being covered by COMPASS at CERN [54], CLAS [97, 98] and CLAS12 [99, 100], it will be still valuable to cross check the results produced from very different experimental setups. The experiment in Hall C will provide the highest precision data in the kinematic domain accessible with the 11 GeV polarized electron beam and will be used to extract all possible independent observables on an unpolarized proton target. The kinematics for Hall C DVCS/DVMP are presented in Tab. III.1 and in Fig. III.1.

The first part of this chapter describes the setup for the Hall C experiment. The requirements of the detectors needed to expand the kinematic range of the experiment with high precision are discussed. The overall design and improvements of the new electromagnetic calorimeter (neutral particle spectrometer) are also presented. The second part details the calorimeter studies using simulations. The simulations were done to design the new detector to meet the requirements of the experiment. The final part of this chapter describes the $PbWO_4$ crystal characterization. Quality control is important to have a steady and good performance of the detector. The light yield and radiation hardness measurements for a selected crystal sample are presented. Radiation damage recovery tests were also performed to optimize the energy and position resolution of the calorimeter during the experiment and they are shown in this section.

Table III.1: DVCS/DVMP kinematics for Hall C. The calorimeter is centered at the angle θ_{calo}, which is set equal to the nominal virtual-photon direction. The front face of the calorimeter is at a distance D_{calo} from the center of the target. The three settings marked by * in the beam energy row correspond to cross checks with Hall A DVCS/DVMP kinematics. The color red and blue indicate the low-x_B and high-Q^2 setting, respectively, used as examples in this chapter.

	Energy Dependence at fixed (Q^2, x_B)												Low-x_B				High-Q^2			
x_B	0.36					0.50			0.60				0.20			0.20	0.36	0.50	0.60
Q^2 [GeV^2]	3.0			4.0		3.4		4.8	5.1			6.0	2.0			3.0	5.5	8.1	10
Beam energy [GeV]	6.6*	8.8	11	8.8*	11	8.8	11	11	6.6	8.8*	11	11	6.6	8.8	11	11	11	11	
Scattered electron energy [GeV]	2.2	4.4	6.6	2.9	5.1	5.2	7.4	5.9	2.1	4.3	6.5	5.7	1.3	3.5	5.7	3.0	2.9	2.4	2.1
DVCS photon energy [GeV]	4.4	4.4	4.4	5.8	5.8	3.4	3.4	4.9	4.2	4.2	4.2	5.0	5.3	5.3	5.3	8.0	8.1	8.4	8.5
Calorimeter angle [deg]	11.7	14.7	16.2	10.3	12.4	20.2	21.7	16.6	13.8	17.8	19.8	17.2	6.3	9.2	10.6	6.3	7.9	8.0	8.0
Calorimeter distance [m]	3	3	3	4	3	3	3	3	3	3	3	3	6	4	4	6	4	4	4
Beam intensity [µA]	28	28	28	50	28	28	28	28	28	28	28	28	11	5	50	11	50	50	50
Beam time [day]	1	2	1	1	3	3	2	5	5	1	5	10	1	1	1	1	5	5	12

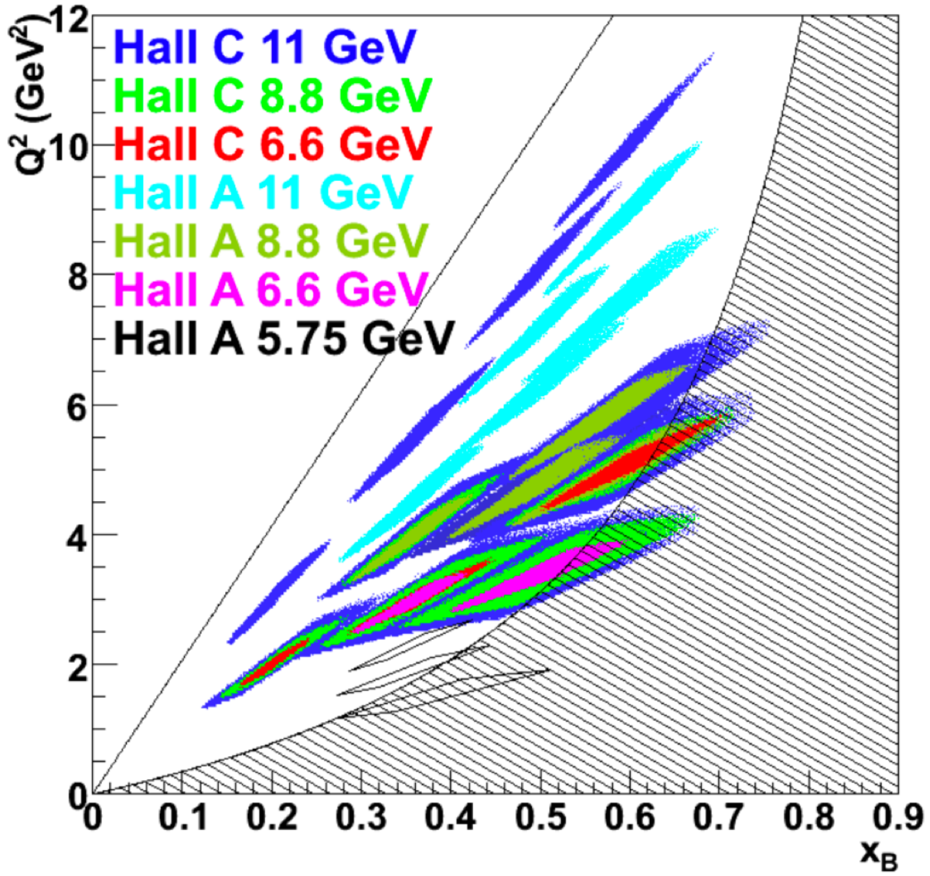

Figure III.1: $x_B - Q^2$ representation of the Hall A and C DVCS/DVMP kinematics. As can be seen, the Hall C experiment will use different beam energies at fixed x_B and Q^2 to perform the beam energy separations. Shaded areas show the resonance region $W < 2$ GeV and the slanted-black line $Q^2 = (2M_pE_b)x_B$ limits the physical region for a maximum beam energy $E_b = 11$ GeV.

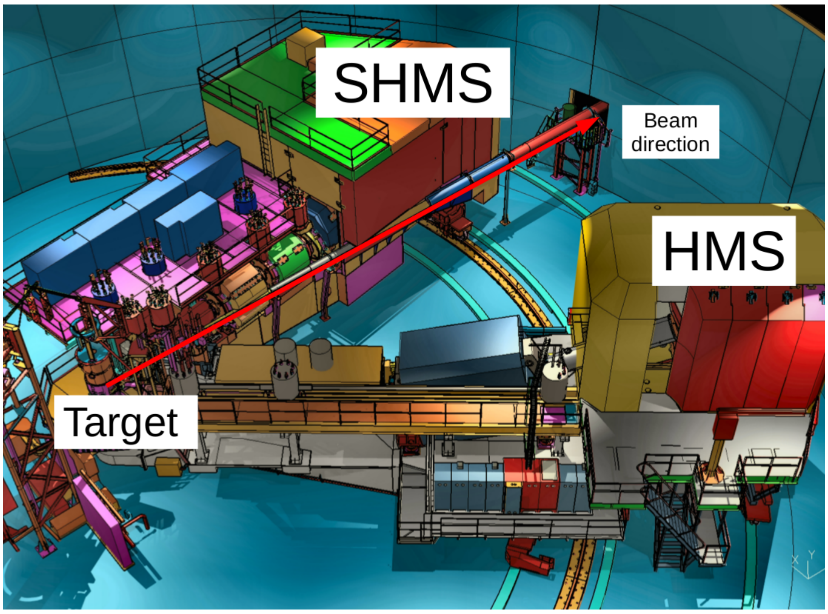

Figure III.2: Hall C layout.

1 Experimental setup

The spectrometer for the scattered electrons needs to reach higher momentum to utilize the beam energy up to 11 GeV for the $|\mathcal{T}_{\text{DVCS}}|^2$ term and the $\mathcal{I}$ term separation (Eq. (I.44)). To cover a wide kinematic domain with high precision, the highest luminosity for DVCS ever before ($\sim 10^{38}/\text{cm}^2/\text{s}$) will be used. In order to meet these conditions, moving from Hall A to Hall C and developing a new calorimeter are necessary.

1.1 Hall C

Hall C has a similar apparatus to the one in Hall A. It has the same target operating system and will use the same liquid hydrogen target for DVCS and DVMP measurements. Hall C consists of two magnetic spectrometers: a High Momentum Spectrometer (HMS) and a Super High Momentum Spectrometer (SHMS) on either side of the beam line (Fig. III.2). The basic principles of the operation of the HMS and the SHMS are the same as those of the HRS in Hall A.

1.2 DVCS experimental apparatus

Similar to the Hall A experiment, only one of the magnetic spectrometers, HMS, will be used to detect the scattered electron. A neutral particle spectrometer (NPS) will detect DVCS photons and two-photon pairs from π^0 decays. The NPS will be installed on the SHMS platform. The recoiled proton from the DVCS/DVMP process will not be detected. However, it will be identified by the same missing mass technique used in the Hall A experiment. Thanks to the higher momentum reach of the HMS and the good radiation hardness of the NPS, the Hall C DVCS experiment will deliver improved results in a wider kinematic region than the one covered by Hall A.

1.2.1 HMS

The High Momentum Spectrometer (HMS) has a central momentum range of [0.5, 7.5] GeV/c[*] with a momentum resolution of 0.1%. As a reminder from the previous chapter, the HRS has a higher momentum resolution of 0.01%. On the other hand, it can only reach a momentum up to 4.0 GeV/c. The HMS can change its polarity to detect positively charged particles. This way, the same elastic calibration method presented in the previous chapter can be applied to the NPS calorimeter: see section 2.2.2 in chapter II.

---

[*] As the name suggests, SHMS can reach up to 11 GeV/c

Table III.2: Properties of PbF_2 and $PbWO_4$ crystals [63].

Parameters	Lead Tungsten ($PbWO_4$)	Lead Fluoride (PbF_2)
Density [g/cm^3]	8.28	7.66 - 7.77
Radiation length X_0 [cm]	0.89	0.93 - 0.95
Refraction index	2.36 (λ = 420 nm) 2.24 (λ = 600 nm)	1.8 - 2.0 (depending on λ)
Transmission range [nm]	340 - 1000	250 - 1100
Molière radius [cm]	2.19	2.22
Radiation type Sensitivity to low ene backgr.	Scintillation ($\sim$ 13% Čerenkov) Sensitive	Pure Čerenkov Insensitive (no scintillation)
Timing property [slow/fast] Scintillation decay time [ns]	$\sim$ 30 ns / 10 ns 5 (73%) 14 (23%) 110 (4%)	very fast, Total pulse width $<$ 20 ns
Lead content [% by weight]	$>$ 85	85
Photon yields per 1 MeV	$\sim$ 140 - 200	$\sim$ 1.0 - 2.0
Temperature dependence of Light Yield	$\sim$ -2%/°C at room temperature	No temperature dependence

1.2.2 NPS

To reach low-x_B and high-Q^2, the electromagnetic calorimeter will be placed at a small angle with respect to the beam line. These conditions will create a significant amount of background in the calorimeter. To reduce the background without sacrificing the luminosity and the kinematic range, a sweeper magnet will be used to reduce the background from charged particles. The NPS will be installed on the extended platform of the SHMS: see Fig. III.3 for an illustration.

As already described in the previous chapter, the Hall A experiment used PbF_2 crystals to have fast time response. Since PbF_2 crystals produce light purely by Čerenkov effect, the calorimeter becomes insensitive to low energy background. However, it was found that the low energy background was not the dominant effect of the energy resolution of the calorimeter. Instead, the fluctuations in the number of Čerenkov photons were the limiting factor [56]. To improve the energy resolution, $PbWO_4$ crystals will be used for the Hall C experiment. Lead tungsten is highly resistant to radiation damage and it has a higher light yield (see Tab. III.2) than that of PbF_2. Therefore, it will improve identifying recoiled protons to ensure the exclusivity of the reaction, which is a crucial part of the experiment.

1.2.2.1 Sweeper magnet

The $\vec{B}$ field of the sweeper magnet (Fig. III.4) is horizontal and the magnetic bend is vertical: for example, negatively charged particles are bent downwards. The sweeper magnet will be placed between the target and the calorimeter to reduce the charged particles background with momentum up to 300 MeV/c [63]. Its nominal magnetic field strength will be 0.6 T·m and will enable the calorimeter to be placed near the beam line and reach 40% higher Q^2 than the Hall A experiment at fixed x_B.

1.2.2.2 Electromagnetic calorimeter

The calorimeter for the Hall C experiment will consist of 1080 $PbWO_4$ crystals stacked in an array of 30 × 36. Each crystal has a dimension of $20 \times 20 \times 200$ mm^3, which approximately has the transverse size of its Molière radius and 23 times its radiation length to absorb almost 100% of the energy of 10 GeV photons. The crystals will be wrapped with a reflective sheet (VM2000) and their back sides will be attached to PMTs (Hamamatsu R4125), individually.

Each crystal has slightly different dimensions and stacking crystals in 36 rows without any support can lead to irregularities and instabilities in the calorimeter. To avoid these problems, a supporting frame made of carbon fiber will be used. $PbWO_4$ crystals have temperature-dependent light yield. Therefore, the crystals will be kept at 18 ± 0.1°C during the experiment with a water cooling system. The back side of the calorimeter will have two air circulation systems to dissipate heat from the PMTs voltage dividers. Fig. III.5 shows the design of the calorimeter.

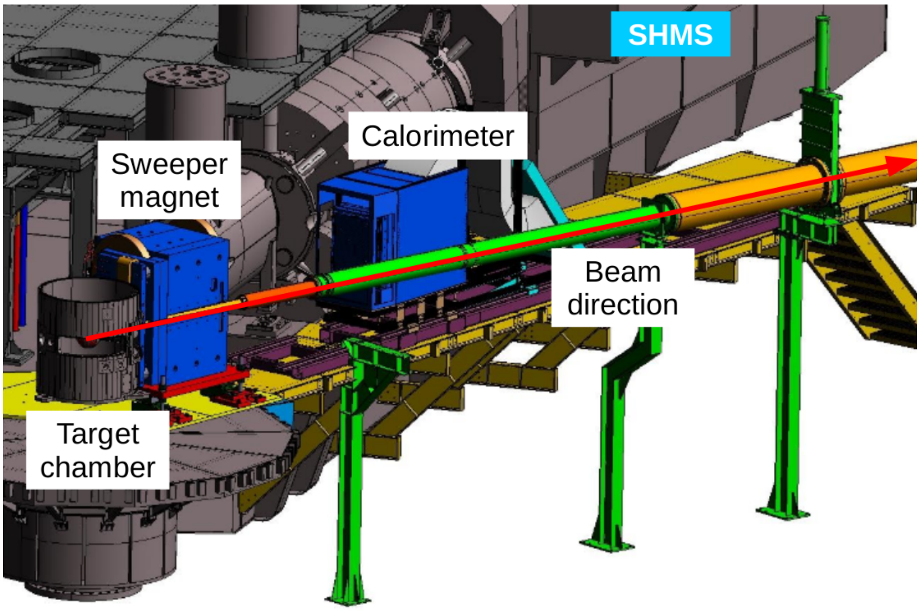

Figure III.3: Designed installation of NPS on the extended platform of the SHMS.

Figure III.4: Sweeper magnet. Left: front side of the magnet. Right: back side of the magnet.

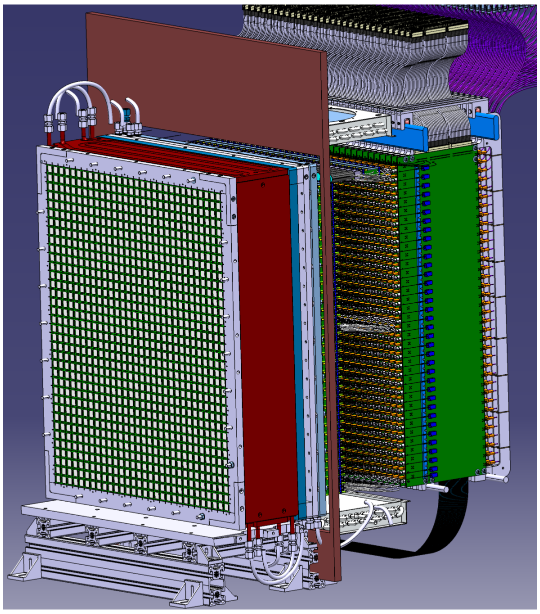

Figure III.5: Calorimeter design. 1080 $PbWO_4$ crystals are stacked in a homogeneous array made of carbon fiber. The water cooling system (red) is encapsulating the crystals. All the electronics for the calorimeter are at the back side.

1.2.3 Beam pipe

The scattering of the beam electron from the target is the main source of background. The scattered particles then hit the opening of the downstream beam pipe and lose most of their energy. This interaction makes an electromagnetic cascade, irradiating a forward angular cone. A conical shape of the beam pipe is useful to reduce the background. The larger the opening or the angle for the beam pipe exiting the target chamber the better. However, it can interfere with the kinematics required for the experiment. The shape of the beam pipe was chosen so that the HMS can reach the angle of 10.5° and the calorimeter can reach 6.0° from the beam pipe at the distance of 4 m. It is expected that the background with this beam pipe assembly will be dominated by the direct beam-target interactions, when the beam energy is above 6 GeV [63]. These direct backgrounds, only the charged particles of course, will be reduced by the sweeper magnet.

2 Calorimeter background dose calculation

Due to the high luminosity and the low-x_B and high-Q^2 kinematic settings, a high background dose is expected. The high background rate cannot only reduce the life expectancy of the PMTs, but also shift the baseline of the signal and lower the energy resolution of the calorimeter. Additionally, the crystals can suffer a considerable amount of radiation damage reducing their optical transmission. In this section, background dose calculations are presented for selected kinematic settings to evaluate the needed magnetic field strength of the sweeper magnet.

2.1 Geant4 simulation geometry

The Monte Carlo simulation for the background dose calculation used a Geant4 library, version 10.03.p03. The geometry setup contains the liquid hydrogen target and its chamber, downstream beam pipes, the sweeper magnet, and the calorimeter. They were modeled and put into the simulation based on the actual layout for the experiment. Fig. III.6 shows the simulation geometry.

2.1.1 Simulation reliability test

As mentioned in the previous chapter, recent Geant4 versions have a reasonable validity over the energy range up to 100 TeV. However, it is important to make sure the physics processes for the background generation are operating

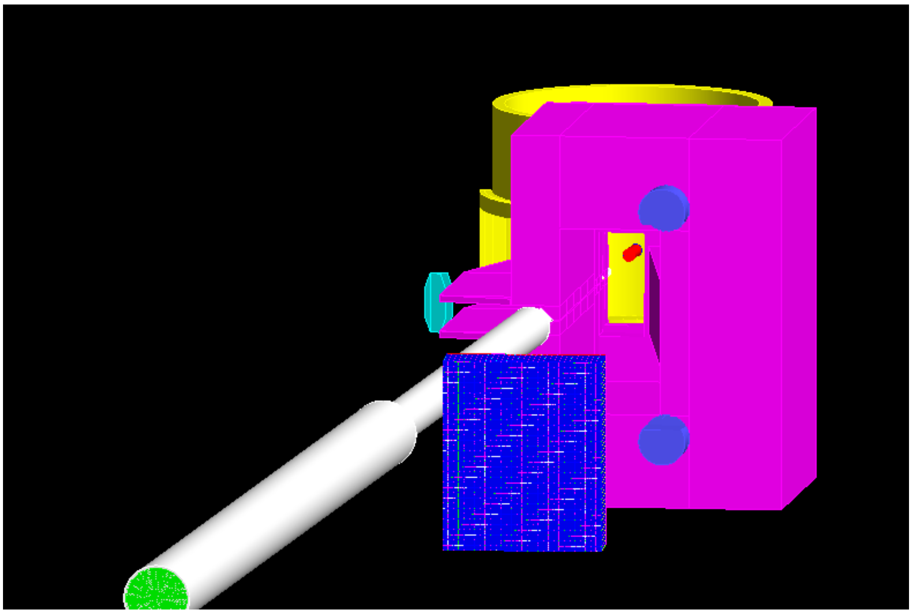

Figure III.6: Geometry of the Hall C DVCS experiment in Geant4. The yellow volume is the target chamber with a target inside (red). The sweeper magnet is presented in magenta. The calorimeter (blue) is facing the target with no direct obstacle between them. Downstream beam pipes, in grey, were also in the simulation to generate realistic background. The HMS opening window is also present in cyan color, however, it is not used in this simulation.

properly. The Radiation Control Department (RadCon) of Jefferson Lab has been studying the background of the beam and the target for all experimental halls for a long period of time. To compare the results with those from RadCon, the background was generated only with the liquid hydrogen target, the electron beam, and no other geometries. Fig. III.7 and III.8 compare the main particles distributions: gamma, positron, and electron, from RadCon and Geant4. The Geant4 simulation results agree with those of RadCon above the energy of 0.1 MeV. The RadCon simulation stops tracking particles when the particles reach energies below 10 keV. This feature makes the simulation run faster. Geant4 however tracks particles until they lose their kinetic energies completely [101]. That creates the difference in the energy range below 0.1 MeV.

2.2 Magnetic field and PMT shielding

As can be seen from Fig. III.6, the sweeper magnet has a large opening angle in order for the calorimeter to have a large acceptance. Because of this, it is hard to reduce the fringe field at the end of the magnet. The fringe magnetic field on the beam pipe (see Fig. III.9) is significant. It can disrupt the electron beam inside the downstream beam pipe and create background in the calorimeter. More importantly, the magnetic field can be high enough to reduce the PMTs gains significantly [102, 103]. It is therefore worth to find the minimum required magnetic field strength and effective magnetic field shieldings to avoid the above problems.

There have been studies to shield the magnetic field on the beam pipe and on the PMTs by putting iron shielding around the beam pipe, in addition to iron and mu-metal shielding around the calorimeter (Fig. III.10). These shieldings reduce the fringe field about a factor of two. The magnetic field with the shieldings is presented in Fig. III.11.

2.3 Background dose and its profile

Dose is defined as the energy deposited in a material by ionizing radiation per unit mass. One can simply convert the total deposited energy of the background in the crystal to dose using the mass of the crystal. One can also further convert it to the dose rate by normalizing by the number of beam electrons used in the simulation. Fig. III.12 shows the maximum dose rate per crystal per column of the calorimeter for two of the kinematic settings, indicated with red and blue in Tab. III.1. These two kinematic settings place the calorimeter close to the beam pipe and they are expected to have the most significant amount of backgrounds. The figure shows the dose rate with

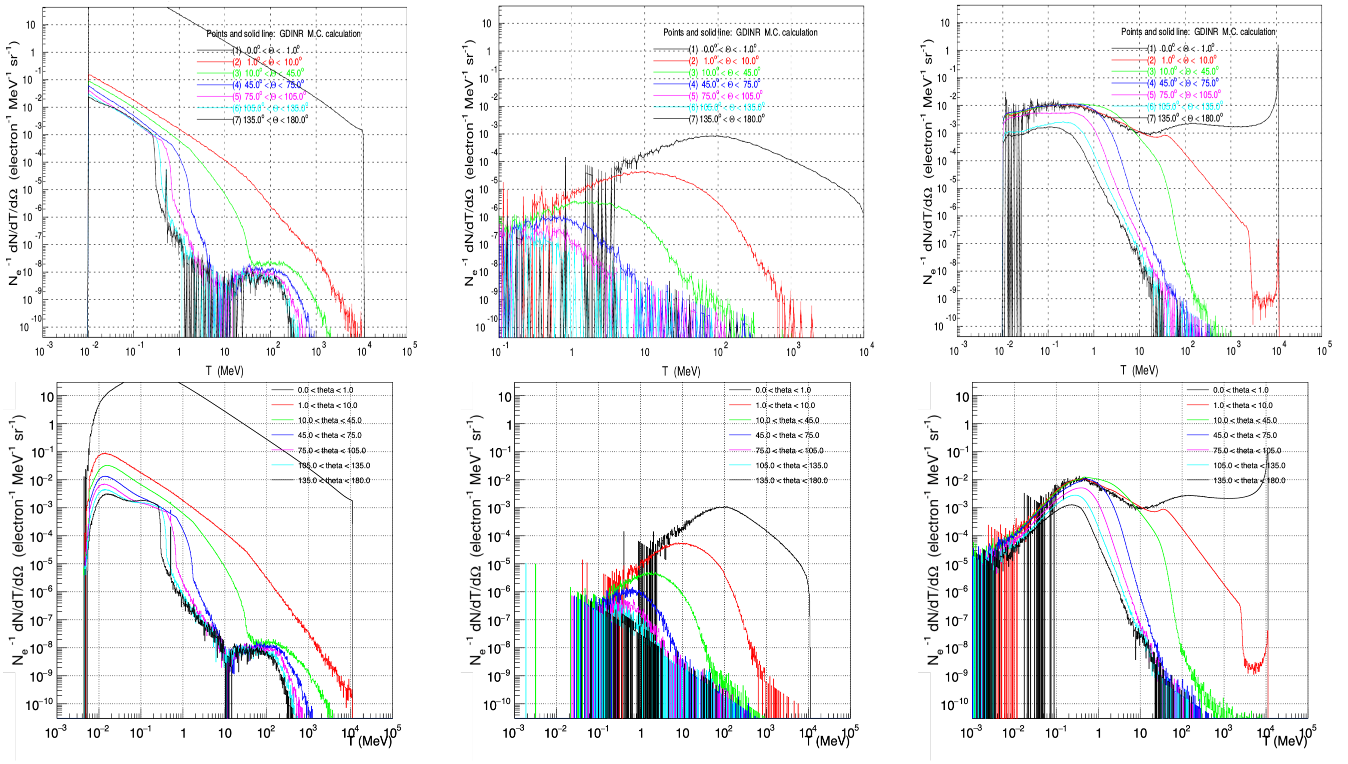

Figure III.7: Background kinetic energy distributions from RadCon (top) and Geant4 (bottom). From left to right are gamma, positron, and electron, respectively.

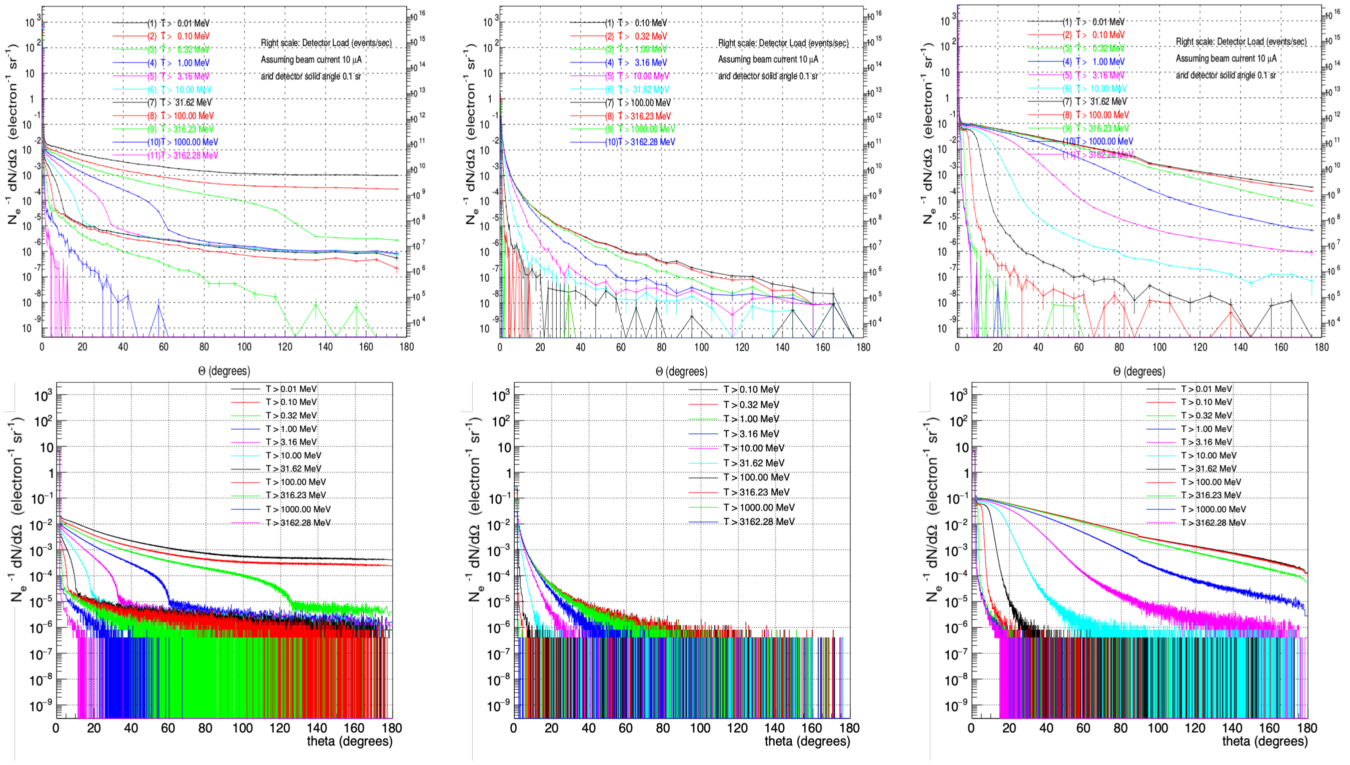

Figure III.8: Background polar-angle distributions from RadCon (top) and Geant4 (bottom). From left to right are gamma, positron, and electron, respectively.

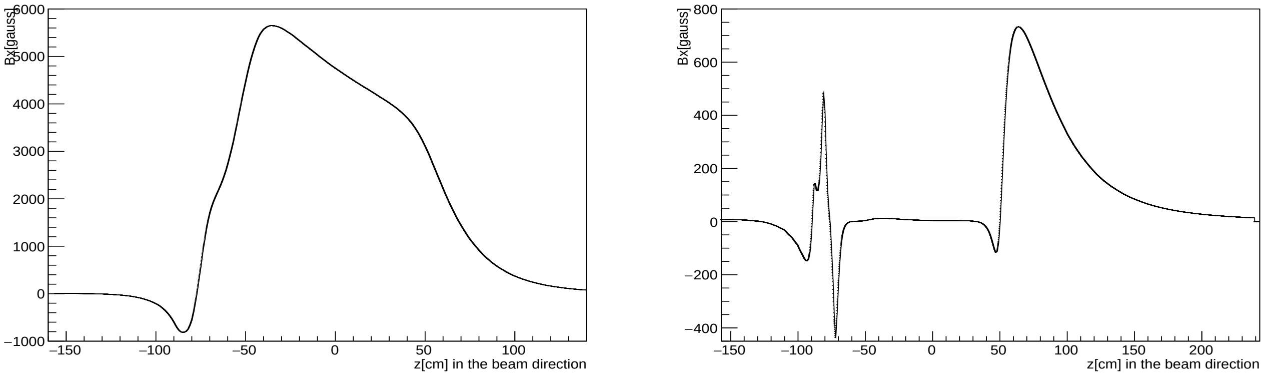

Figure III.9: Sweeper magnet magnetic field. The target is located at -157 cm. Left: horizontal magnetic field in the calorimeter direction. The field strength is around 0.6 T·m. Right: horizontal magnetic field in the downstream beam pipe direction. There are fringe fields around -80 cm and 70 cm.

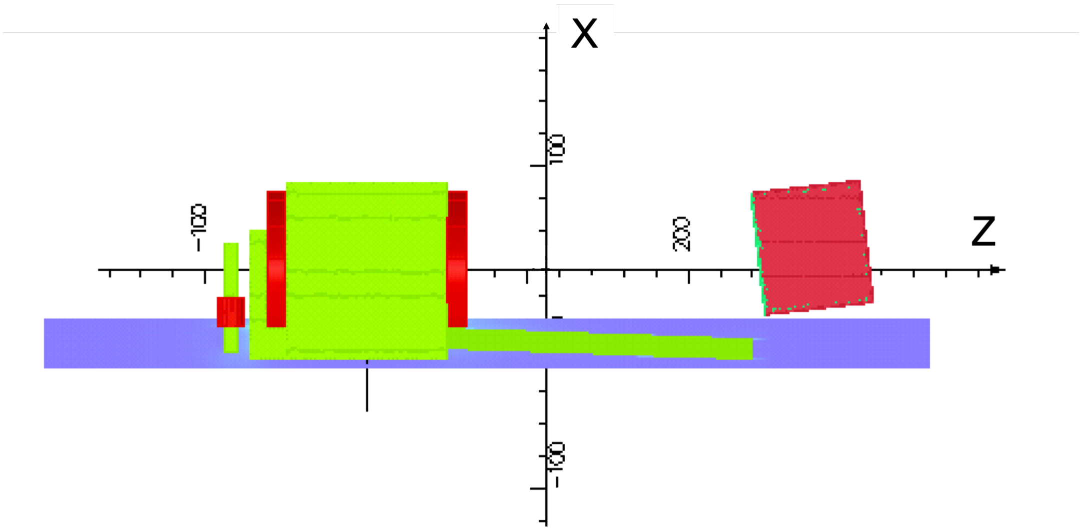

Figure III.10: Geometrical layout (aerial view) for the magnetic field calculation with the magnetic shieldings around the beam pipe (long green rectangle in the middle) and around the calorimeter (red box on the right). The green box on the left represents the sweeper magnet. The blue rectangle is the region where the magnetic field is calculated with smaller grid size than the other areas for better accuracy.

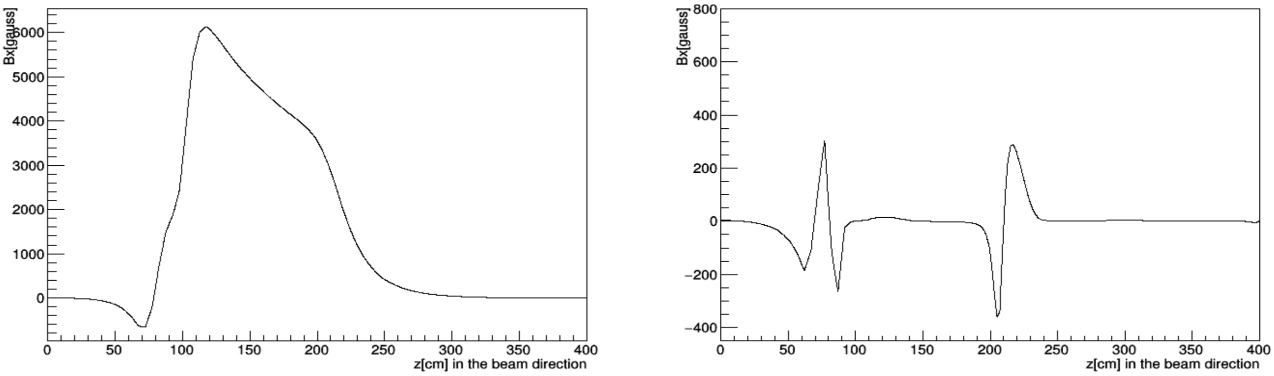

Figure III.11: Sweeper magnet magnetic field with magnetic shieldings around the beam pipe and the calorimeter. The target is located at 0 cm. Left: horizontal magnetic field in the calorimeter direction. Right: horizontal magnetic field in the downstream beam pipe direction. The fringe fields are decreased by half the original magnitude.

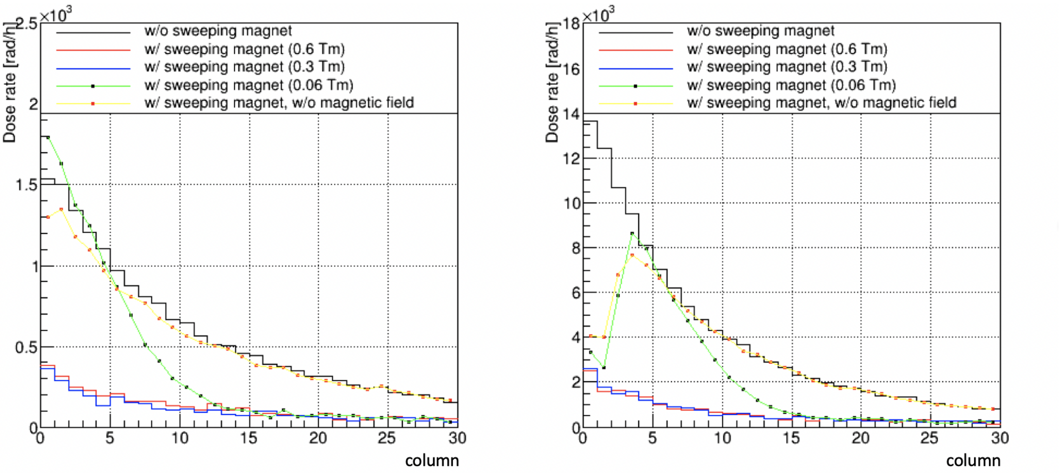

Figure III.12: Background dose rate on the calorimeter for two kinematic settings of the experiment. Left: the low-x_B setting indicated in Tab. III.1. Right: high-Q^2 setting indicated in Tab. III.1. The black line shows the results without sweeper magnet. The red line corresponds to the sweeper magnet with the intended magnetic field strength: 0.6 T·m. The blue line and the green line with black markers show results with a reduced magnetic field strength of 0.3 T·m and 0.06 T·m, respectively. The dose rate with the sweeper magnet but without its magnetic field is shown by the yellow line with red markers.

different magnetic field strengths. The sweeper magnet magnetic field strength of 0.3 T·m is high enough to remove the charged particles backgrounds. The magnet reduces the total background dose by a factor of 3 to 5. With the sweeper magnet, the two kinematic settings, low-x_B and high-Q^2 indicated in Tab. III.1, are expected to have 90 Gy (in 1 day) and 3000 Gy (in 5 days) of integrated dose, respectively on the most exposed crystal. The estimated integrated dose on the most exposed crystal during the whole experiment is about 5000 Gy.

It is also important to study the expected anode current of the PMTs from the background. The performance of the PMT may vary slightly with time while operating it continuously over a long period. The change of the anode current, although the operating conditions have not changed, is called drift. The drift is primarily caused by a damage to the dynodes by heavy electron bombardments. Therefore it is recommended to use the PMT with an average anode current of at most 100 μA. For the case of the low-x_B setting the expected maximum dose rate on the crystal, from Fig. III.12, is around 400 rad/hr or 0.25 GeV/50ns/crystal. If one assumes that the PbWO$_4$ light yield is 15 photoelectrons/MeV, the maximum number of photons the PMT receives is 4×10^3 photoelectrons/MeV. The PMT gain that will be used for the experiment is about 10^3. By converting photoelectron to Coulomb, one can get the expected anode current of around 10 μA. The originally proposed PMT gain was about 100 times higher. However, after calculating the expected anode current from the dose rate simulation, we have found that it would be too high. Therefore, it was decided to lower the PMT gain and amplify the signal afterwards.

Identifying the main source of backgrounds can lead to finding additional methods to reduce them. The background particles in the simulation were traced back to their origin. If one keeps tracing the origin of the background, one finds that the major sources of the background are the scattering between the beam electron and the target and the interaction of the scattered particles with the entrance of the beam pipe. In Fig. III.13, only the positions of the direct sources of the backgrounds on the calorimeter are shown for one of the kinematic settings (low-x_B). The particles shown in the figure will then directly go to the calorimeter when the user takes one more step in the simulation.

One can see that the background sources have asymmetrical distributions around the second beam pipe. It can be suspected that it is due to the fringe field of the sweeper magnet: see the right plot of Fig III.9. The background dose was then re-calculated with the magnetic field shieldings on the beam pipe and the calorimeter: see the design of the magnetic field shielding in Fig. III.10 and the reduced fringe field in Fig. III.11.

As can be seen from Fig. III.14, the magnetic field shieldings do not have a significant effect on reducing the background dose. The magnetic field shielding can be improved with extra materials on the beam pipe. However, the results from Fig. III.14 suggest that the background dose due to the fringe field is negligible. The extra shielding material on the beam pipe will only prevent the sweeper magnet and the calorimeter to reach small angle. To be noted, the background dose was calculated with the magnetic field shieldings in only one setting. The calorimeter

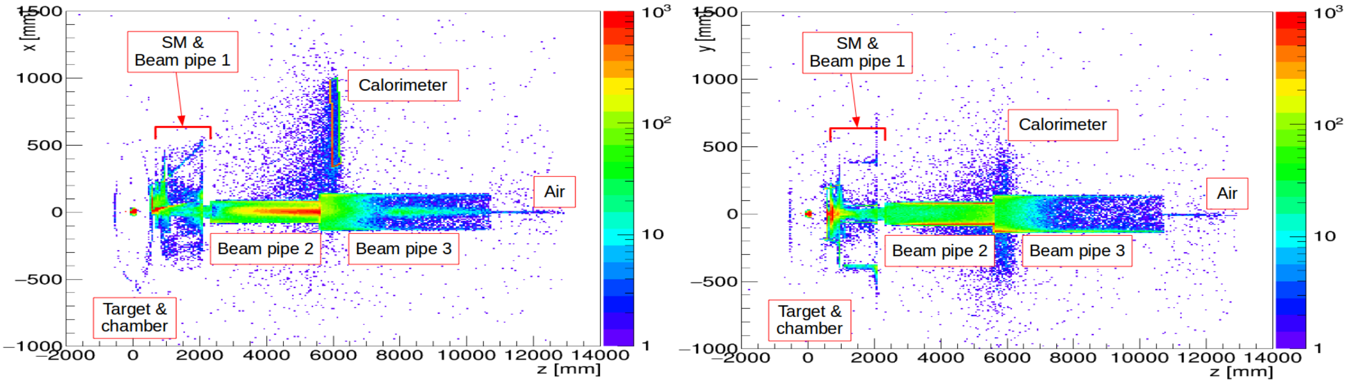

Figure III.13: Aerial view (left) and side view (right) of the position distributions of the direct backgrounds. The target and its chamber are around z = 0 mm. The calorimeter is presented around z = 6000 mm and x = 400 to 1000 mm. It is shown only to indicate the position of the detector. The sweeper magnet (SM) is located after the target and around z = 1000 to 2000 mm with the first beam pipe. The second beam pipe with larger width in x and y is shown around z = 2000 to 5500 mm. From z = 5500 to 10500 mm is the third beam pipe. After the third beam pipe in positive z direction, there is no beam pipe and the beam electron scatters in the air. Around the calorimeter and the beam pipe, particles scattering in the air can be seen.

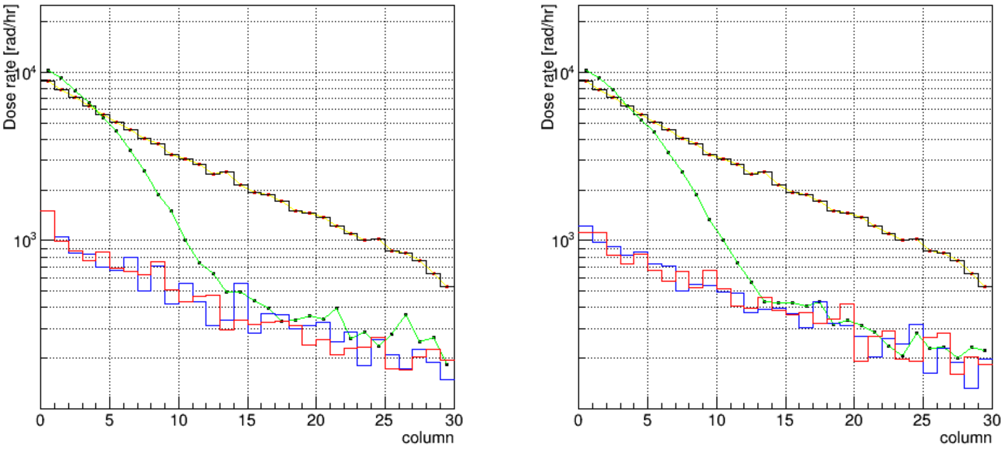

Figure III.14: Background dose calculation without (left) and with (right) the magnetic field shieldings. The black line shows the dose rate without the sweeper magnet. The yellow line with red markers corresponds to the dose rate with the magnet but without the magnetic field. The red line indicates the dose rate with the originally intended magnetic field strength of 0.6 T·m. The blue line represents with the reduced strength of 0.3 T·m. The dose rate with the magnetic field strength of 0.06 T·m is shown in green line with black markers. The beam current is 50 μA.

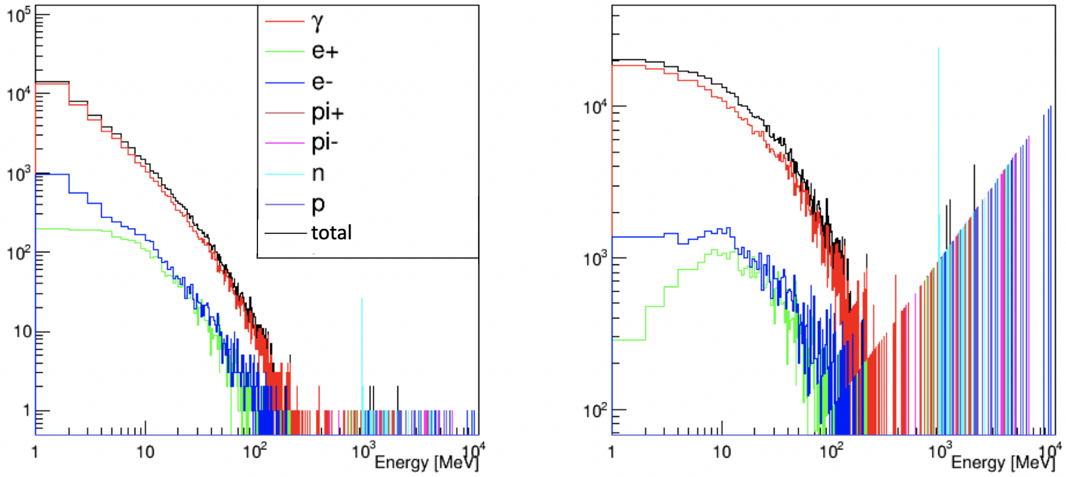

Figure III.15: The energy distribution (left) and the dose distribution (right) of the background on the calorimeter.

with the magnetic field shieldings was placed 4 m away from the target and 8.5° from the beam pipe (Fig. III.10), which is close to the high-Q^2 kinematic setting indicated in Tab. III.1. It is also highly unlikely that the background dose will drastically change in other kinematic settings.

Another way to reduce the background dose on the calorimeter is to place a thin absorber in front of the calorimeter crystals. It can absorb very low energy background. The energy and the dose distribution of the background on the calorimeter is shown in Fig. III.15. From the energy distribution (left plot of Fig. III.15), one finds that 88% of the background is from particles with energies lower than 10 MeV. From the dose distribution (right plot of Fig. III.15), one observes that the total energy deposited in the calorimeter by those particles is only 20%. If a thin material that absorbs particles below 10 MeV is placed in front of the calorimeter, one can expect that the background dose will decrease by 20%.

3 Calorimeter energy and position resolution

If the material for the supporting structure of the calorimeter is too thick or has high density, the energy resolution of the detector can decrease significantly. A simulation of the energy resolution of the detector for different gap size and material between the crystals was used to optimize the design of the calorimeter supporting frame. Results are presented in this section. The photon reconstruction algorithm that was used in Hall A DVCS/DVMP experiment was adapted to the Hall C experimental layout. Its performance is also reported in this section.

3.1 Geant4 simulation geometry

The energy resolution simulation uses the same Geant4 library and the same calorimeter that was described in section 2.1. The crystal dimensions are $20.5 \times 20.5 \times 200.5$ mm^3. A SiO_2 block with a size of $20.5 \times 20.5 \times 20.5$ mm^3 covered with thin aluminium was used as a PMT. With only the calorimeter placed in the simulation, photon beams ranging from 0.5 GeV to 10 GeV were fired across the surface of the calorimeter: see Fig. III.16.

In the experiment, the PMTs in the calorimeter collect scintillating photons from the crystals and amplify their signals. The scintillating photons travel, bounce off the boundary of the crystals, and reach the PMT. During this process, photons can be absorbed by the material which in the end cause a broader energy distribution. By default, Geant4 does not handle the optical properties of the materials nor the electronic signal amplification which are helpful to make more realistic simulations. Thus, the optical properties of the $PbWO_4$ measured in [104] were manually put into the simulation. The behavior of the photon at the junction between the crystal and the PMT/VM2000 was also embedded [101]. The number of photons was then adjusted to match the light yield of 15 photoelectrons/MeV, i.e. the number of photons reaching the PMT per MeV.

The variables for the simulation are listed in Tab. III.3. The material of the gap between the crystals, i.e. dead material, was also used as a variable: carbon fiber with density of 1.55 g/cm^3 and air.

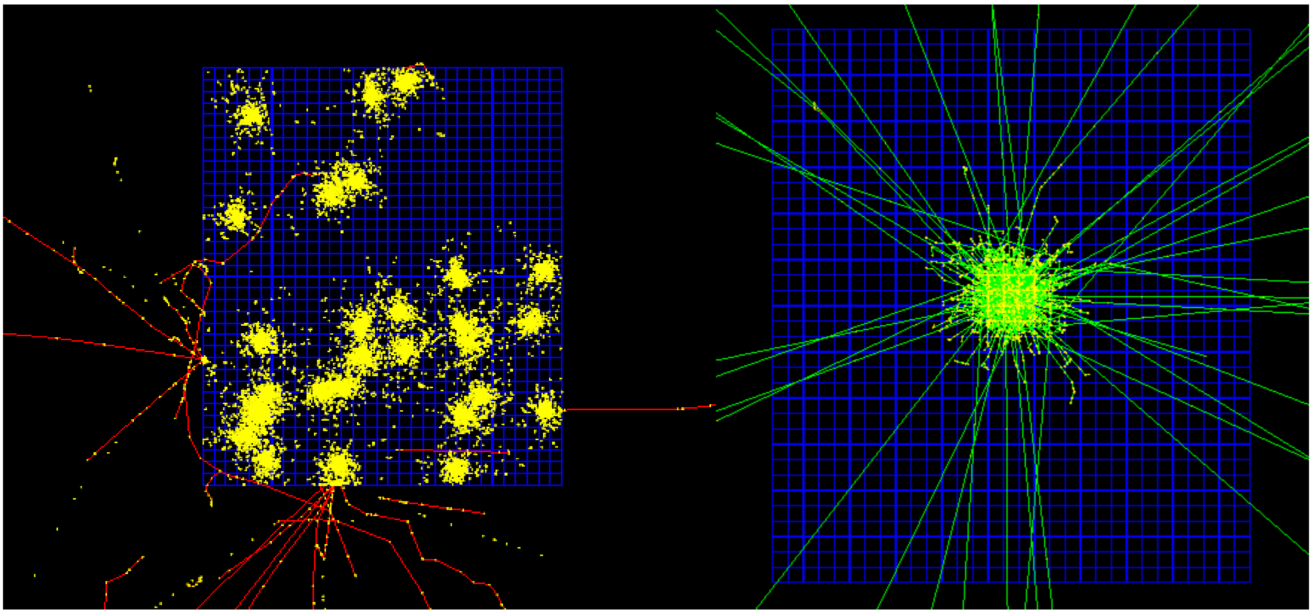

Figure III.16: Calorimeter energy resolution geometry. Each blue square represents a crystal. Left: 1GeV photons hitting the calorimeter. Right: 10 GeV photon creating a shower in the crystals and the uncaptured remnants of the shower are leaked through the backside of the calorimeter. Red: negatively-charged particle tracks. Green: photon tracks.

Table III.3: Variables in the simulations. The dead materials as variable were carbon fiber and air.

Energy [GeV]	0.5,	1,	3.25,	5.5,	7.75,	10
Gap [mm]	0,	0.5,	1,	1.5,	2	

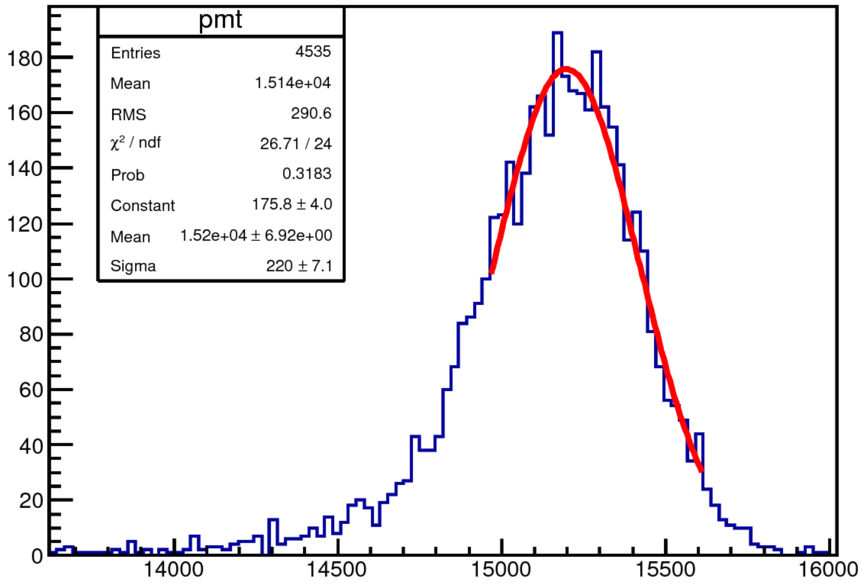

Figure III.17: Number of photoelectrons collected at the PMTs in the simulation. Light yield: ~15 photoelectrons/MeV. There is no gap between the crystals except two VM2000 sheets adjacent to each other. The energy of photon beam used was 1 GeV.

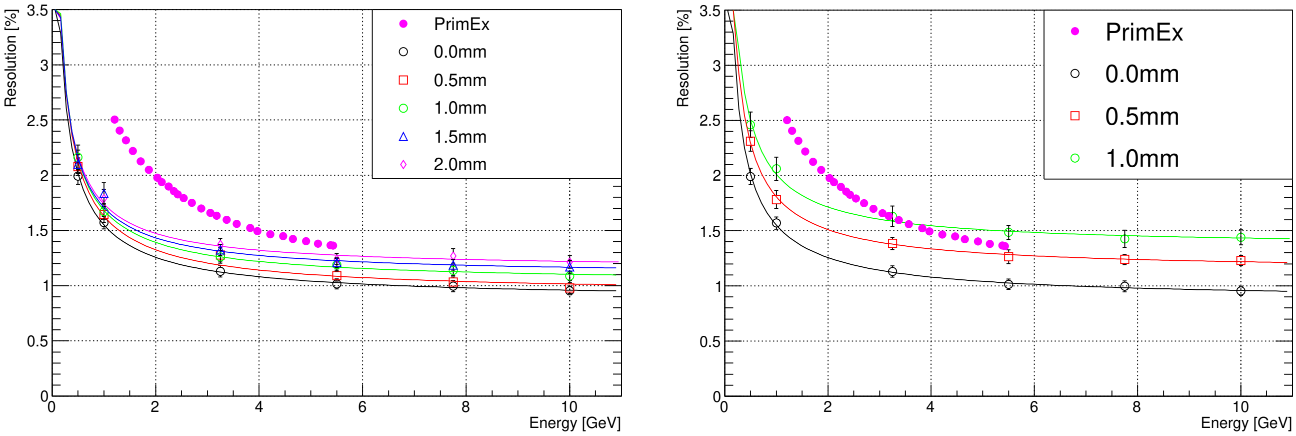

Figure III.18: Energy resolution of the calorimeter. The size of the gap between the crystals was varied from 0 mm to 2 mm. The materials between the crystals were air (left) and carbon fiber (right). The miscalibration factor for the simulation was 1%.

3.2 Calorimeter frame design

Fig. III.17 shows an example of the distribution of the number of photoelectrons collected at the PMTs in the simulation. The energy resolution was calculated as the sigma/mean of a Gaussian fit to it.

In the real situation, each crystal will have a calibration coefficient that will only be known to a few %. Systematical overestimation and underestimation can happen from crystal to crystal. To consider this effect, one can modify the calibration coefficients. The miscalibration effect used for the energy resolution study was 1%. The energy resolution simulation results are presented in Fig. III.18. The PrimEx experiment also used 1152 of stacked $PbWO_4$ crystals with a combination of 567 lead glass blocks for its calorimeter [105]. Its measured energy resolution is also shown in Fig. III.18 for reference.

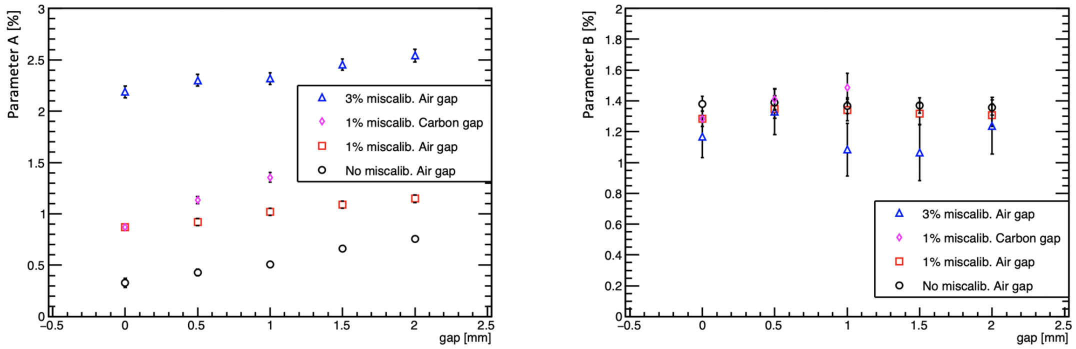

Figure III.19: Parameter $\boldsymbol{A}$ (left) and $\boldsymbol{B}$ (right) from the fitting function, Eq. (III.1), with $\boldsymbol{C} = 0$. The dead material mostly affects the parameter $\boldsymbol{A}$ and the value increases almost linearly with the size of the gap. The slope becomes larger when the dead material is switched from air to carbon fiber. The stochastic term $\boldsymbol{B}$ stays the same within uncertainties. PrimEx has the following values of the parameters: $\boldsymbol{A} = 0.9\%$, $\boldsymbol{B} = 2.5\%$, $\boldsymbol{C} = 1\%$.

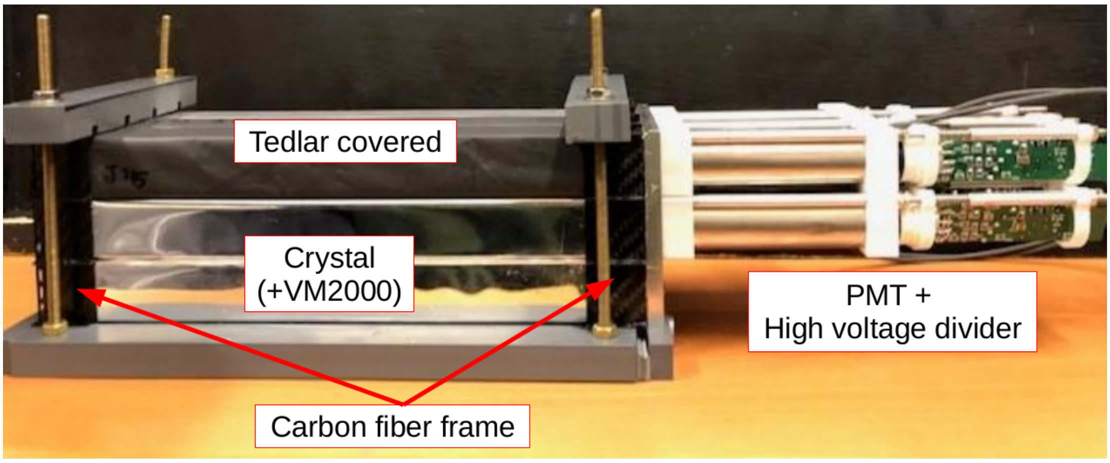

Figure III.20: NPS calorimeter 3×3 prototype. A 2-cm-wide and 0.5-mm-thick carbon fiber frame is supporting the crystals only at the front and the back sides of the crystals. Their middle part is exposed with VM2000 wrapped around the crystals. The top crystal is additionally wrapped with a tedlar sheet to test for light leaks. At the back of the crystals, PMTs and high voltage dividers are attached.

The energy resolution was fitted using the equation:

$$\frac{\sigma}{E} = A \oplus \frac{B}{\sqrt{E}} \oplus \frac{C}{E}, \tag{III.1}$$

where the symbol '$\oplus$' represents a quadratic sum. The term $\boldsymbol{A}$ arises from the dead material between the crystals, radiation damage, etc. $\boldsymbol{B}$ is a stochastic term due to the fluctuations of the shower. Finally, the electronic noise of the readout is related to a $\boldsymbol{C}$ term. The parameter $\boldsymbol{C}$ was fixed to 0 since there is no electronics simulated in this case. The fit parameters $\boldsymbol{A}$ and $\boldsymbol{B}$ are shown in Fig. III.19.

In the area of interest which in our case is the DVCS region, around 4 to 9 GeV , the resolution increases almost linearly with the size of the gap between the crystals. When carbon fiber is introduced as a dead material between the crystals, the energy resolution gets worse.

From these results, it was decided to use as less dead material between the crystals as possible. First, the carbon fiber structure cannot be thicker than 1mm, by looking at the right plot of Fig. III.18. Secondly, the supporting structure will use carbon fiber to the minimum, by comparing the left and the right plot of Fig. III.18. The carbon fiber frame was then designed to support the crystals only at the front and the back sides of the crystals, 2-cm wide, with a thickness of 0.5 mm: see Fig. III.20. The expected energy resolution with the design just described is better than 1.2% at the energy : [4.0, 10.0] GeV and the fit parameters using Eq. (III.1) are $\boldsymbol{A} = 0.93\%$, $\boldsymbol{B} = 1.3\%$, and $\boldsymbol{C} = 0.0\%$ (fixed): see Fig. III.21. However, in order to reduce the magnetic field at the photocathodes of the

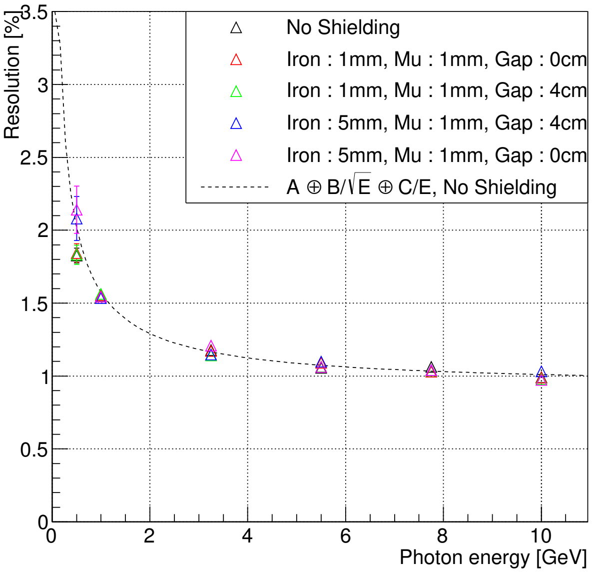

Figure III.21: Energy resolution simulation results of the calorimeter with the carbon fiber frame only at the front and the back side of the crystals (2-cm wide) with a thickness of 0.5 mm. The miscalibration factor for the simulation was 1%. The dotted-black line represents the fitted function using Eq. (III.1) on the energy resolution result with no magnetic field shielding: the fit parameters are $\boldsymbol{A} = 0.93\%$, $\boldsymbol{B} = 1.3\%$, and $\boldsymbol{C} = 0.0\%$ (fixed). There are several results with different configurations of the magnetic field shieldings. More detailed descriptions of the shieldings are in section 3.3. The conclusion from the shielding configurations is that they do not have a significant impact on the energy resolution.

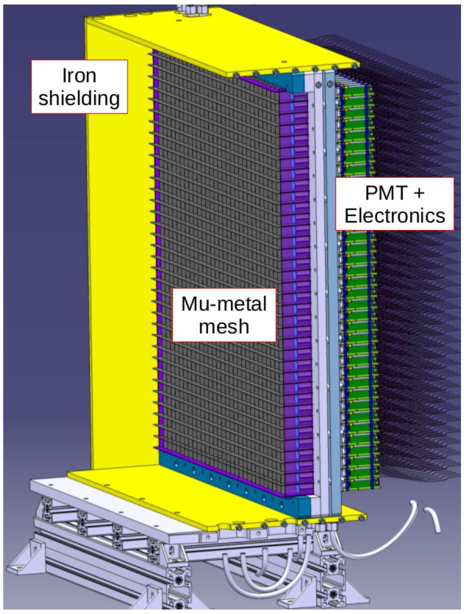

Figure III.22: NPS mechanical design. Grey: 3-cm wide and 0.5-mm thick mu-metal between each crystal. The mu-metal does not support the weight of the crystals. Purple: 1.5-mm mu-metal on the outer side of the 1080 $PbWO_4$ crystals. Yellow: 10-mm iron shielding surrounding the crystals. The front and back sides of the calorimeter are not surrounded by the iron shielding.

PMTs, the final design of the calorimeter will use 3-cm wide and 0.5-mm thick mu-metal frame at the back side of the crystals instead of carbon fiber: see Fig. III.22.

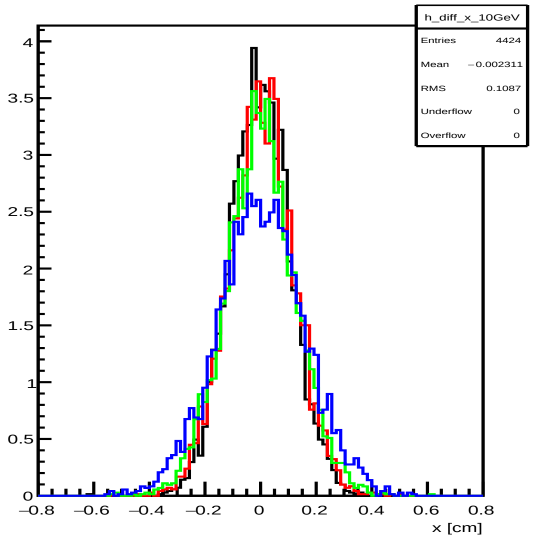

Figure III.23: Position difference between the projected positions of the primary photons and the positions of the reconstructed photons for different photon energies. Clustering threshold: 1.10 GeV. Incident energies: black for 10 GeV, red for 7.75 GeV, green for 5.5 GeV, and blue for 3.25 GeV.

3.3 Position resolution of the calorimeter

The calorimeter reconstructs the momentum of the photon to measure t' $(= t - t_{min})$ with high precision. The photon reconstruction software for the Hall C experiment adapts that of the Hall A experiment. In the simulation, the vertex positions and the momenta of the primary photons were recorded to project their positions onto the calorimeter. Fig. III.23 shows the difference between the photons projected positions and the reconstructed positions on the calorimeter. Each distribution with different photon energy was then fitted with a Gaussian.

The sigma of each fitted Gaussian is presented in Fig. III.24. The position resolution of the calorimeter is around or better than 1.5 mm at the energy range of [4.0, 10.0] GeV. There have been varieties of designs (the final design is in Fig. III.22) to reduce the magnetic field around the photocathodes of the PMTs. A box (as shown in Fig. III.10) made of two layers, the inner box made of mu-metal and the outer box made of soft iron, was one of the earliest design. The position resolutions depending on various combinations of thicknesses of materials for the shielding box are also presented in the Fig. III.24. With or without the magnetic field shielding box, the position resolution does not change significantly. However, in the end, the box designs were replaced with a mu-metal structure at the back side of the crystals: see section 3.2 for more detailed descriptions.

In conclusion, the energy resolution simulation results contributed to the design of the calorimeter in order to have minimal dead material between the crystals. A calorimeter energy resolution of around 1.2% at [4.0, 10.0] GeV is a big improvement from the Hall A PbF_2 calorimeter (3.6% at 4.2 GeV [62], 3% at 7.0 GeV [78] from the elastic calibration). The position resolution also improved from that of the PbF_2 calorimeter to around 1.5 mm at [4.0, 10.0] GeV. The Monte Carlo simulation of the Hall A calorimeter showed a position resolution of 3 mm at [0.1, 5.0] GeV [82] and 2 mm at 4.2 GeV with elastic scattering data [77].

4 Light yield measurements of $PbWO_4$ crystals

The energy resolution of the calorimeter is the limiting factor of the experiment. Exclusivity of the reaction is ensured by the missing mass technique and the missing mass resolution is dominated by the energy resolution of the calorimeter. As mentioned in the previous section, the energy resolution depends on the light yield and the optical transmission of the crystals. In addition, the light yield of the $PbWO_4$ crystals depend on their temperature. The tolerances of the crystal dimensions are also important since the crystals will be stacked in 30 × 36 array. Therefore, it is crucial to select crystals with high light yields and uniformity in shapes and sizes.

Most of the properties, including the light yields, of all the $PbWO_4$ crystals for the calorimeter are being measured in Catholic University of America (CUA). Examples of their measurements are shown in Fig. III.25. These and other measurements are to make sure the crystals are within the required standards for the experiment. In order to estimate

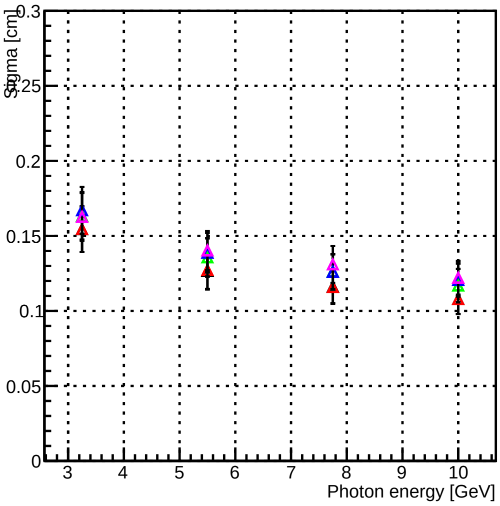

Figure III.24: Position resolution of the calorimeter using the photon reconstruction software. Different markers represent the resolution with different thicknesses of the materials for the magnetic-field-shielding boxes. Black: no magnetic field shielding. Red: 1-mm iron and 1-mm mu-metal. Green: 1-mm iron, 1-mm mu-metal, and 4-cm gap between the shieldings. Magenta: 5-mm iron and 1-mm mu-metal. Blue: 5-mm iron, 1-mm mu-metal and 4-cm gap between the shieldings.

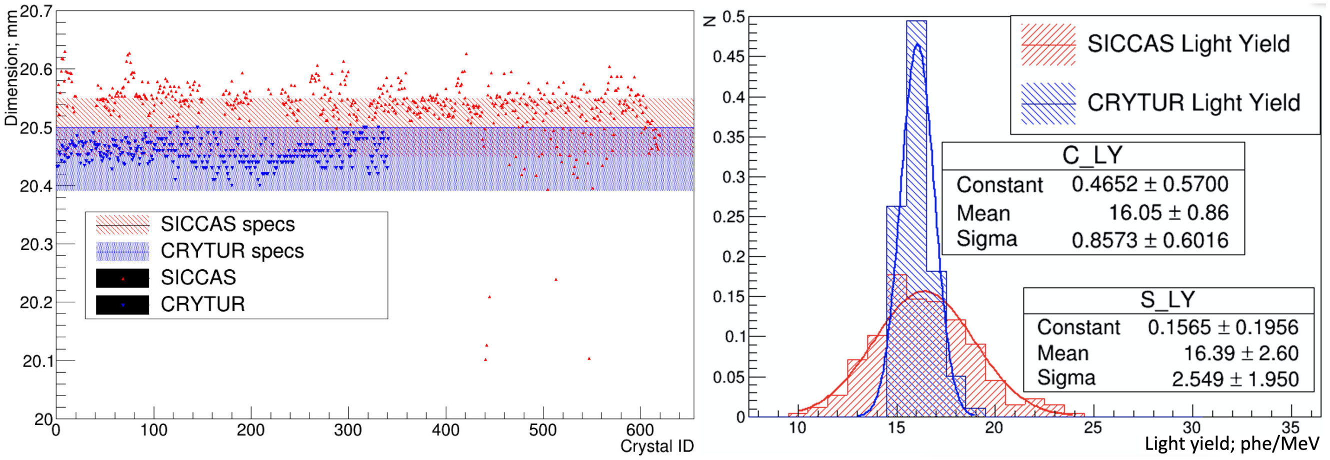

Figure III.25: Crystals dimension measurements (left) and their light yield measurements (right) from CUA [106]. SICCAS and Crytur are the only mass producing vendors of $PbWO_4$ crystals in the world. SICCAS crystals have larger variations than the Crytur crystals in size and light yield.

the systematic uncertainties of the light yield measurements performed at CUA, we measured the light yield of 10 crystals from SICCAS (Shanghai Institute of Ceramics, Chinese Academy of Sciences) in IJCLab and in Justus-Liebig-Universität Gieβen. These measurements are shown in this section. Also, the temperature dependence of the light yield was measured. To be noted, there are only two mass producing vendors of $PbWO_4$ crystals in the world: SICCAS, and Crytur.

4.1 Measurement setup

Since the light yield of the $PbWO_4$ crystals is relatively lower than that of other typical scintillating materials, the wrapping of the crystal was crucial in order not to lose photons: see Fig. III.26. A small amount of optical grease was applied at the end of the crystal to attach and optically couple it to the PMT. The crystal and the PMT were vertically set in a temperature controlled box. A ^{137}Cs source was placed at the top of the crystal: see Fig. III.27.

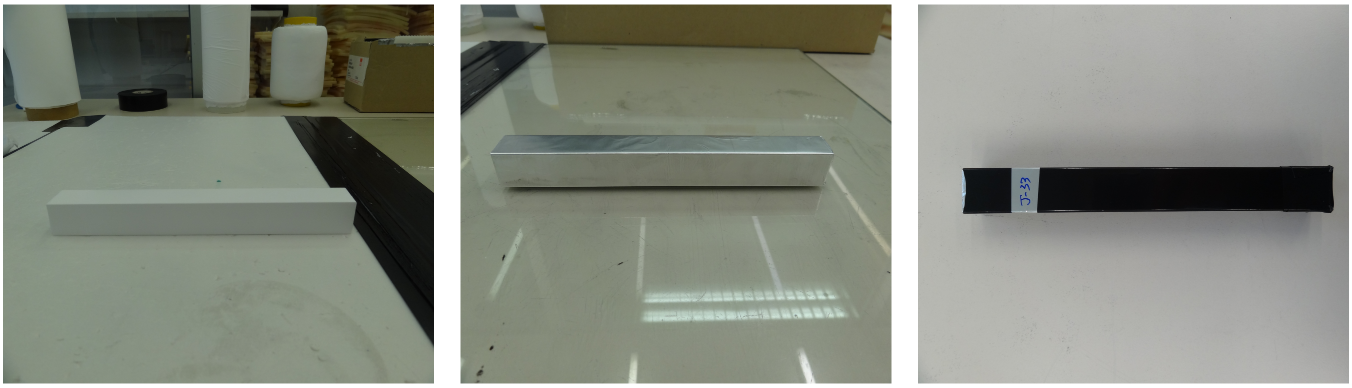

Figure III.26: Crystal wrapping process. Firstly, crystals were wrapped in 8 layers of Teflon (left), then they were wrapped in one layer of aluminium foil (middle) and finally, wrapped with thermal tube (right). The thermal tube shrinks when heated. These procedures ensure minimal light leaks from the crystal.

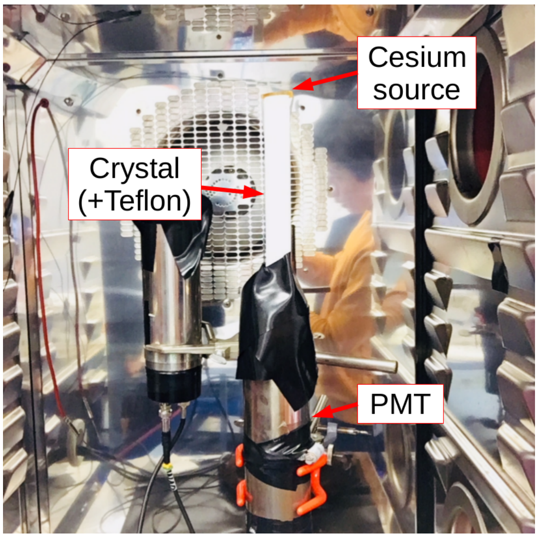

Figure III.27: Crystal mounted onto a PMT in the temperature controlled box. The wrapped black tape around the contact point between the crystal and PMT minimizes the noise from small amounts of outside light. The ^{137}Cs source is placed on the top of the crystal. In this picture, the crystal is only wrapped with 8 layers of Teflon foil.

The whole setup rested for 30 minutes after the PMT was turned on and the temperature set to 18°C to make sure small air bubbles between the crystal and the PMT escape and temperature in the box stabilizes.

4.2 Temperature dependence of the crystal light yield

The PMT signal showed three components. One is the electrical noise of the electronics (pedestal), another one is the single photoelectron signal from the PMT itself, and the last one is the signal due to the photoelectrons caused by 662 keV gammas from the ^{137}Cs source. Fig. III.28 shows one of sample crystals charge distribution from the PMT and the ^{137}Cs source. On the left plot, the highest peak on the left is due to single photoelectrons from the PMT and the lower peak on the right is due to the 662 keV gammas.

A Gaussian was fitted to the ^{137}Cs signal. The mean of the fit is used to compute the light yield of the crystal. To calculate the light yield (photoelectrons/MeV), one also needs the charge corresponding to one photoelectron and the pedestal of the signal. The single photoelectron and the pedestal were measured without the crystal or the ^{137}Cs: see middle and right plots of Fig. III.28. The single photoelectron peak was measured by triggering the PMT signal with a low threshold. The pedestal was determined using a 100 kHz trigger. The light yield was calculated using the Eq. (III.2). The absolute value of the charge of the measurements was unknown. However, it is not necessary since

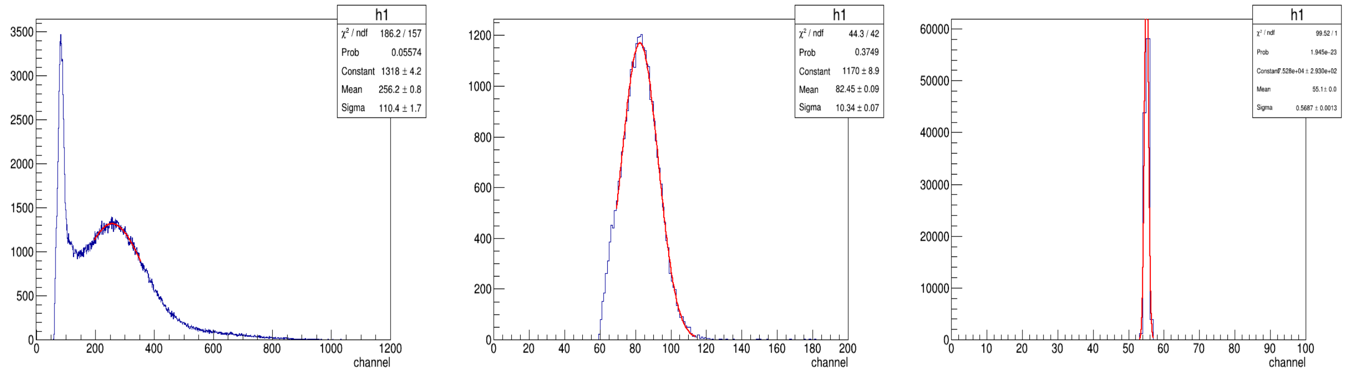

Figure III.28: Left: charge distribution from the light yield measurement of one of the crystal samples. Middle: single photoelectron charge distribution. Right: charge distribution of pedestal. All measurements were done at 18°C. The horizontal axis is in arbitrary units of charge. Plots shown here are from the measurements at Gieβen.

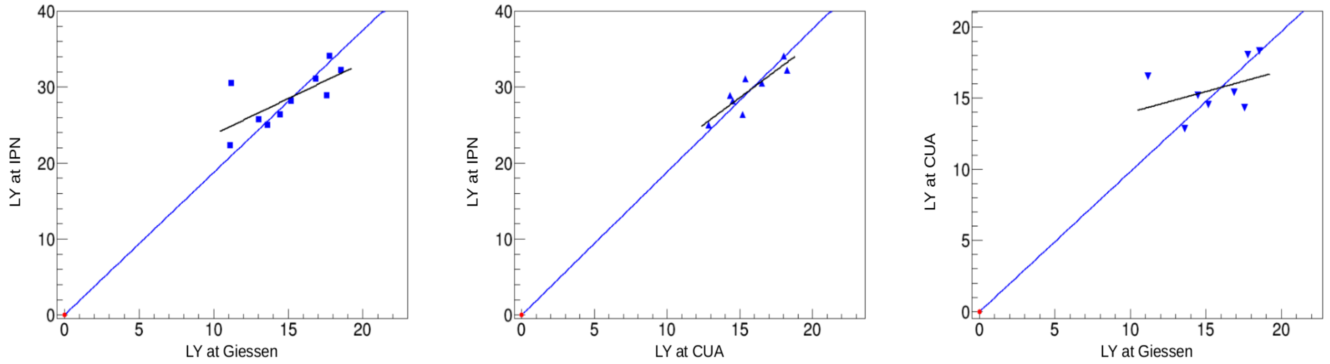

Figure III.29: Light yield (LY) of several crystals measured at different institutes: Gieβen, CUA, and IJCLab [106]. Two crystals were off from the linear trend, but measurements correlate well in general.

it cancels out:

$$\text{Light Yield (photoelectrons/MeV)} = \frac{{}^{137}\text{Cs signal intensity} - \text{Pedestal intensity}}{\text{Single photoelectron intensity} - \text{Pedestal intensity}} \times \frac{1}{0.662\ \text{MeV}} \qquad \text{(III.2)}$$

The correlations amongst the light yields of the sample crystals measured in different institutes are shown in Fig. III.29. The measurements done in IJCLab showed higher light yield. This is due to the higher quantum efficiency of the PMT used in IJCLab. However in general, the correlations appear to be linear.

The light yield temperature dependence was also measured for one of the crystals. As can be seen from the results in Fig. III.30, the light yield changes around 2%/°C from its original value. For this reason, it is important to control the temperature inside the calorimeter for a steady performance.

One may suggest to set the temperature of the calorimeter to lower than the proposed 18°C. There are, however, disadvantages in the cost and the compactness of the calorimeter in that case. Also, as it will be explained in more detail in the next section, the damage from the ionizing radiation recovers faster at high temperature.

5 Radiation hardness and optical bleaching of $PbWO_4$

Using radiation hard crystals is important when building the calorimeter for the Hall C experiment. Even though $PbWO_4$ crystal is radiation hard, its optical transmittance is damaged by ionizing radiation [108] and the amount of damage varies from crystal to crystal. Ionizing radiation produces color centers in the crystals, with absorption bands in a wide spectral region, creating point structure defects and traps for electrons and holes [109].

As shown in section 4.2, $PbWO_4$, when compared to other scintillating materials, has a low light yield. When its optical transmission reduces due to the ionizing radiation, the energy and position resolutions of the calorimeter

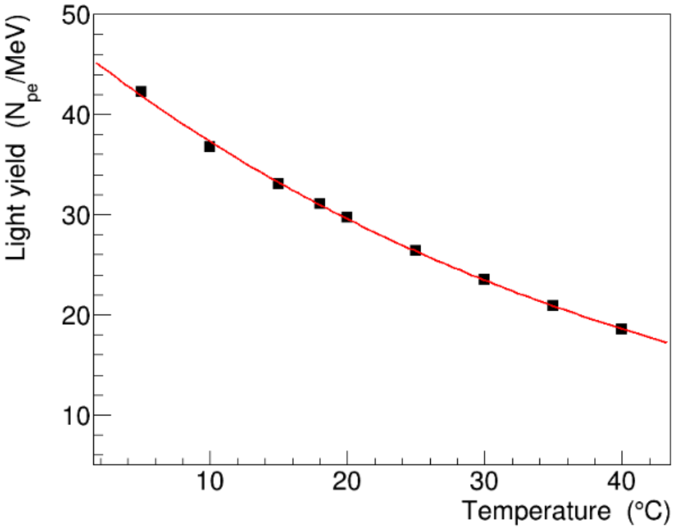

Figure III.30: Temperature dependence of the light yield of the $PbWO_4$ crystal. It was fit with an exponential function $\exp^{\lambda \cdot T}$ with $\lambda = 0.232$. Measurement done by R. Wang [107].

can be deteriorated. Therefore, it is also important to measure and control the radiation hardness of each crystal. However, it is time consuming to irradiate and measure the transmittance of all the crystals. The crystal samples in section 4.2 were irradiated in an irradiation test facility in the Laboratoire de Chimie Physique (LCP) located in Orsay. Their radiation hardness measurements are presented in this section.

In addition to selecting radiation hard crystals, a damage recovery system will be implemented in the calorimeter to keep the energy and position resolution at their best during the whole experiment. There exists several ways to recover the damage from ionizing radiation. Damage recovery tests using light are also presented in this section.

5.1 Radiation hardness measurements

The irradiation test facility in LCP shown in Fig. III.31 uses a 222 TBq ^{60}Co as the radiation source. The test samples can be placed at a desired distance from the source. The source is stored in a tank when not in use and is raised up from it to irradiate the samples for a chosen amount of time. Therefore, the user can control the total amount of dose and the dose rate.

5.1.1 Fricke dosimetry

A conversion from a distance between the ^{60}Co source and the samples to a dose rate was done using a Fricke dosimetry. A Fricke solution contains Ferrous ions (Fe^{2+}). When water gets irradiated and redoxed, Ferrous ions lose electrons and turn into Ferric ions (Fe^{3+}) (see Eq. (III.3) [110]), which absorb visible light.

$$\begin{gathered} \mathrm{H} + \mathrm{O_2} \rightarrow \mathrm{HO_2} \\ \mathrm{Fe^{2+}} + \mathrm{HO_2} \rightarrow \mathrm{Fe^{3+}} + \mathrm{HO_2^-} \\ \mathrm{HO_2^-} + \mathrm{H^+} \rightarrow \mathrm{H_2O_2} \\ \mathrm{Fe^{2+}} + \mathrm{H_2O_2} \rightarrow \mathrm{Fe^{3+}} + \mathrm{OH} + \mathrm{OH^-} \\ \mathrm{Fe^{2+}} + \mathrm{OH} \rightarrow \mathrm{Fe^{3+}} + \mathrm{OH^-} \end{gathered} \tag{III.3}$$

The light absorption (A) is the logarithmic ratio between the incident (Φ_0) and the transmitted (Φ) radiant flux of the material. By calculating the change of light absorption throughout the irradiation, one can calculate the dose rate [110]:

$$\begin{gathered} \text{Light absorption (Absorbance) } (A(t)) = log\frac{\Phi_0}{\Phi} = \varepsilon \times l \times C = \varepsilon \times l \times G \times \rho \ \times D(t) \\ \text{Dose rate}(Gy/min) = \frac{\Delta A(cm^{-1})}{\varepsilon(L\ mol^{-1}) \times G(mol\ J^{-1}) \times \rho(kg\ L^{-1})} \times \frac{1}{\Delta t(min)} \end{gathered} \tag{III.4}$$

ε : molar extinction coefficient. 2160 + 15 × (T - 25) at 304 nm. T: temperature [°C]
l : optical path
C : number of moles transformed by the irradiation
G : efficiency for appearance of Fe^{3+}. 1.62×10^{-7}mole/J
ρ : mass density of the solution
$D(t)$: radiation dose during given time, t

The Fricke solution was put into containers (Fig. III.32) then irradiated. The container has the same dimension as the crystal in order to directly know the exact amount of dose on the crystal from the Fricke dosimetry. The results of the light absorption throughout the irradiation are plotted in Fig. III.33. One can use the light absorption at the wavelength of 304 nm, which is one of the peaks of the light absorption curve, to get the rate of the change of the light absorption ($\Delta A/\Delta t$) during the irradiation. The irradiations of the Fricke solution were done at 3 distances from the ^{60}Co source: 15 cm, 30 cm, and 60 cm. As can be seen from Fig. III.34, the light absorption at the wavelength of 304 nm linearly increases as the irradiation time increases. By using the Eq. (III.4), one can then convert the slope into dose rate, at given distance from the source. Tab. III.4 lists the dose rates obtained. The dose rates in Tab. III.4 were acquired by averaging the measured dose rates from 9 containers. The size of the standard deviations is mainly due to the fact that the 9 containers were irradiated with different dose. As it can be seen from Fig. III.31, the distances between the containers and the source are different amongst the containers. When the containers get closer to the source, the differences get larger.

5.1.2 $PbWO_4$ radiation hardness measurements and their setup

Crystals were irradiated at the same distance used in the Fricke dosimetries: 15 cm, 30 cm, and 60 cm, varying the time of exposure to the ^{60}Co source. The pictures of the crystals after the irradiation with 5000 Gy are shown in Fig.

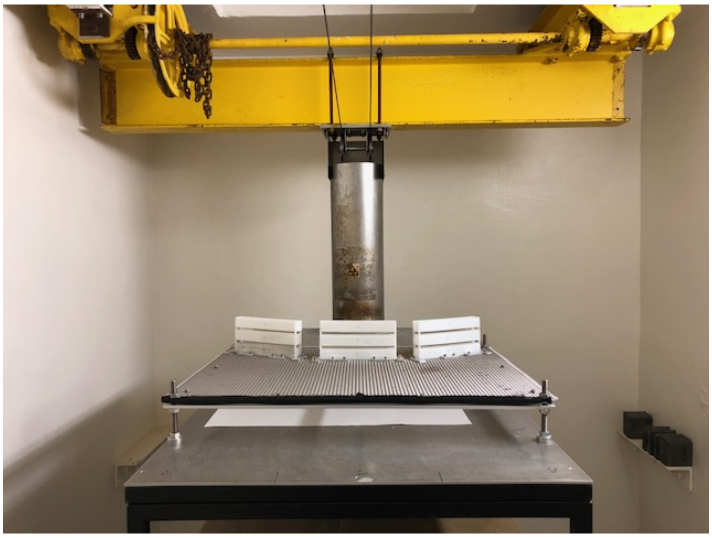

Figure III.31: Irradiation test facility in LCP. Nine sample boxes are positioned 60 cm away from the location of the ^{60}Co source. When the facility is not in use, the source is placed inside the tank at the bottom of the picture. When the test begins, the wires at the top of the picture pull out the source and position it at the center of the cylinder for the desired amount of time.

Table III.4: Average dose rates with standard deviation (σ).

Distance from the ^{60}Co source [cm]	Dose rate [Gy/min]	σ [Gy/min]
15	18.0	4.17
30	4.54	1.08
60	1.07	0.112

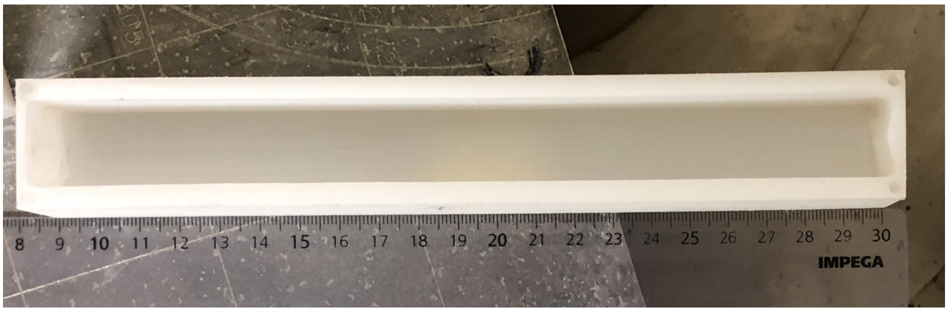

Figure III.32: Container for the Fricke solution or the crystal.

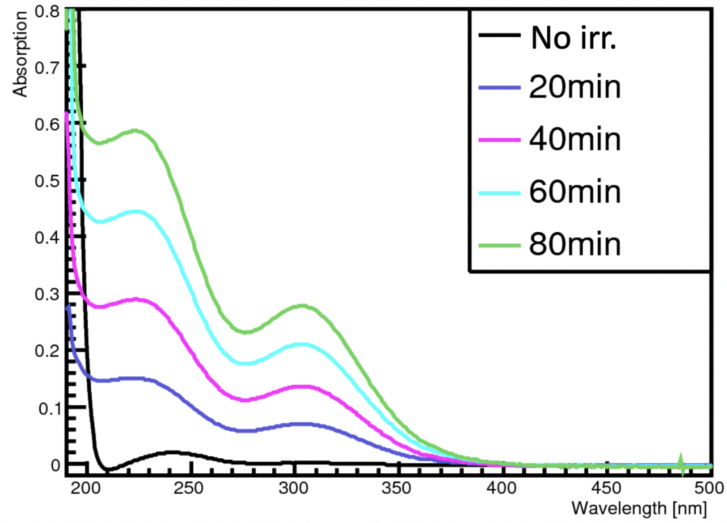

Figure III.33: Light absorption curve with different irradiation times. The distance between the sample and the source was 60 cm.

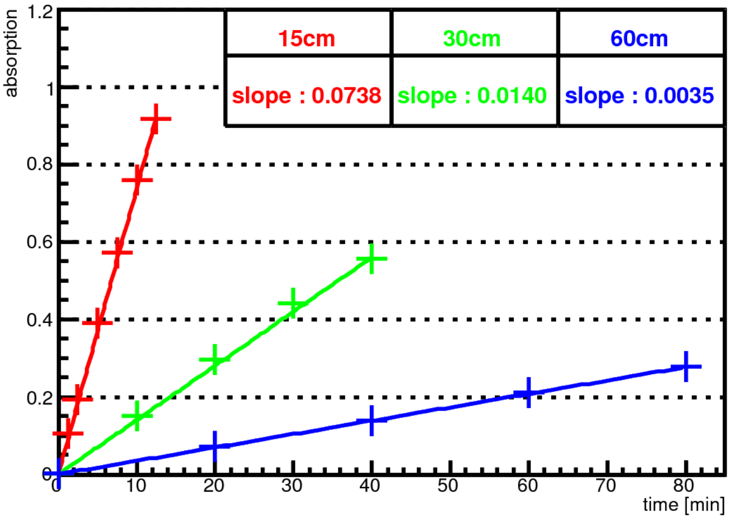

Figure III.34: Light absorption at the wavelength of 304 nm as a function of the duration of the irradiation. Three different distances from the ^{60}Co source were used. They were fitted with linear functions and the slopes ($\Delta A/\Delta t$) are given in the legends.

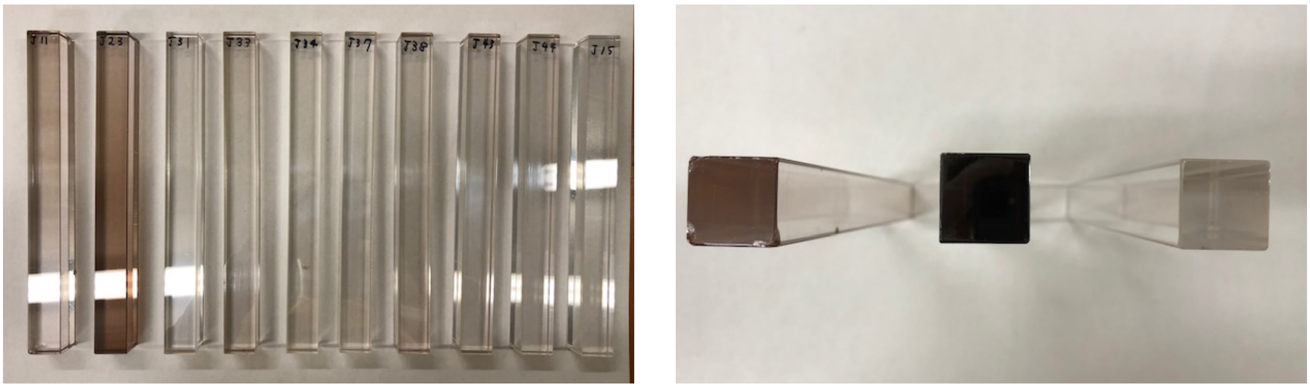

Figure III.35: Crystals after 5000 Gy of irradiation. Each crystal has different radiation hardness. Left: the crystal on the right (J15) was not irradiated and is shown as a reference. Right: side of the crystal which the PMT is coupled to.

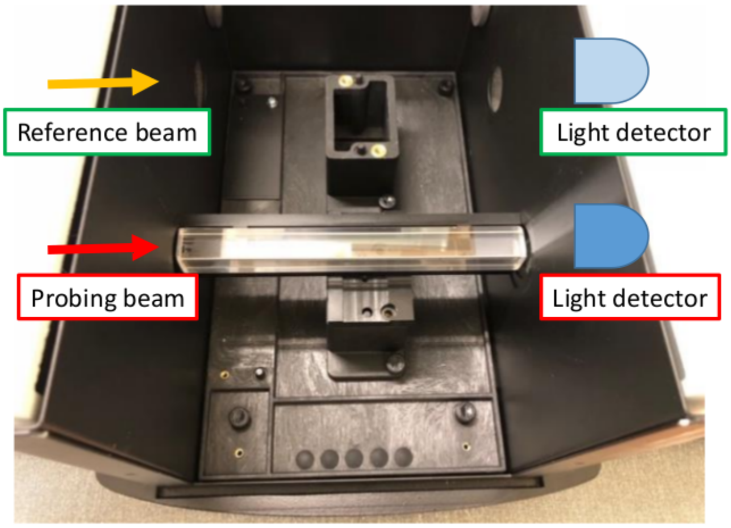

Figure III.36: Inside the commercial light spectrometer (Lambda 850 from PerkinElmer). The front and the back sides of the $PbWO_4$ crystal are perpendicularly aligned to the probing beam.

III.35. They clearly show the different radiation hardness of the crystals. As it can be seen from the right picture, when crystals are damaged by ionizing radiation, crystals can get significantly dark. Optical transmittance, which is relatively easier to measure than the other optical properties such as the light yield, is used to quantify the damage to the crystal due to ionizing radiation. The optical transmittance was measured with a commercial spectrometer (Lambda 850 from PerkinElmer, see Fig. III.36). The machine probes the material in a wide spectral range. It generates two beams from one light source and the detectors on the other side measure their radiant flux (Φ). One light beam probes the air which becomes the reference and the other probes the material that one wants to measure. The transmittance is obtained as: $T = \frac{\Phi(z)}{\Phi(0)}$, where $\Phi(z)$ is the radiant flux through the material of length z and $\Phi(0)$ is the reference.

Fig. III.37 shows the transmittance of one of the samples measured before and after the irradiation at 60 cm from the source for 30 minutes. At Gieβen, we used a similar setup to irradiate and measure the transmittance of the crystals. However, the irradiation rate from the ^{60}Co source at Gieβen is fixed. In Fig. III.37, the measurement of the same crystal in Gieβen is also shown with the same amount of dose and dose rate. The slight discrepancy of the measurements is due to the different setups. Gieβen and IJCLab use different commercial spectrometers. Unlike in IJCLab, in order to measure the transmittance of the 20 cm long crystal, the spectrometer in Gieβen had to be modified. The modification of the spectrometer causes the discrepancies in the results. To be noted, due to the spontaneous relaxation of the color centers, crystals recover their damage slightly during the first 30 minutes after the irradiation [109]. For this reason, all the measurements were done 30 minutes after the irradiation.

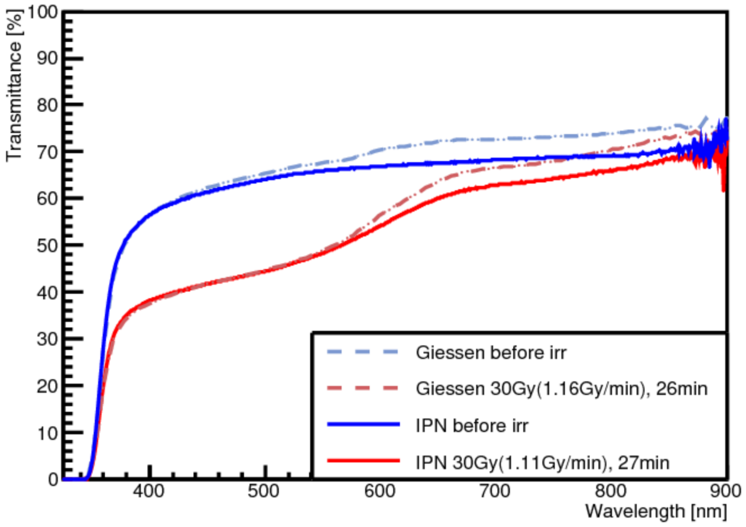

Figure III.37: $PbWO_4$ crystal transmittance measured before and after 30 Gy of irradiation.

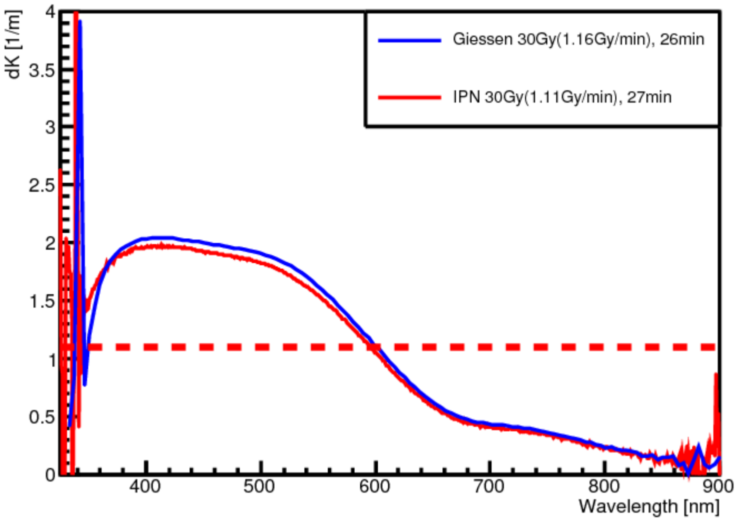

Figure III.38: The value dk of the measurement shown in Fig. III.37. The red dotted line is the crystal rejection threshold for the experiment. This crystal is rejected since the $dk > 1.1\ \mathrm{m}^{-1}$.

The attenuation coefficient is used to quantify the radiation hardness of the crystals. The attenuation coefficient (k) is obtained from:

$$\frac{d\Phi}{dz}(z) = -k(z)\Phi(z). \tag{III.5}$$

If k stays constant as a function of z, one can get the degree of the change of the attenuation coefficient dk from:

$$dk = ln(T_b/T_a)/l, \tag{III.6}$$

where T_b and T_a are the transmittance of the crystal before and after the irradiation, respectively, and l is the length of the crystal. The value of dk from Fig. III.37 is shown in Fig. III.38. The maximum dk from all 10 crystals after 30 Gy of irradiation are listed in Tab. III.5. For the Hall C experiment, the maximum dk is set to 1.1 m^{-1} after 30 Gy of irradiation. If the crystal has $dk > 1.1\ \mathrm{m}^{-1}$ in the light emission range of $[400,\ 800]$ nm, it is rejected and not used in the detector.

To be noted, all the measurements and tests shown in this section were done with 10 SICCAS crystals. As hinted in Fig. III.25, it was found that the SICCAS crystals also have a large variation in their radiation hardness amongst those 10 samples: see Tab. III.5. The radiation hardness measurements of 10 Crytur crystals are scheduled and those measurements will indicate the overall uniformity of the Crytur crystals in radiation hardness.

Table III.5: Maximum dk after 30 Gy of irradiation of the 10 sample crystals (SICCAS).

Crystal number	maximum dk [m^{-1}]
J11	2.0
J15	0.5
J23	3.9
J31	0.3
J33	0.9
J34	0.4
J37	0.4
J38	1.0
J43	0.6
J44	0.5

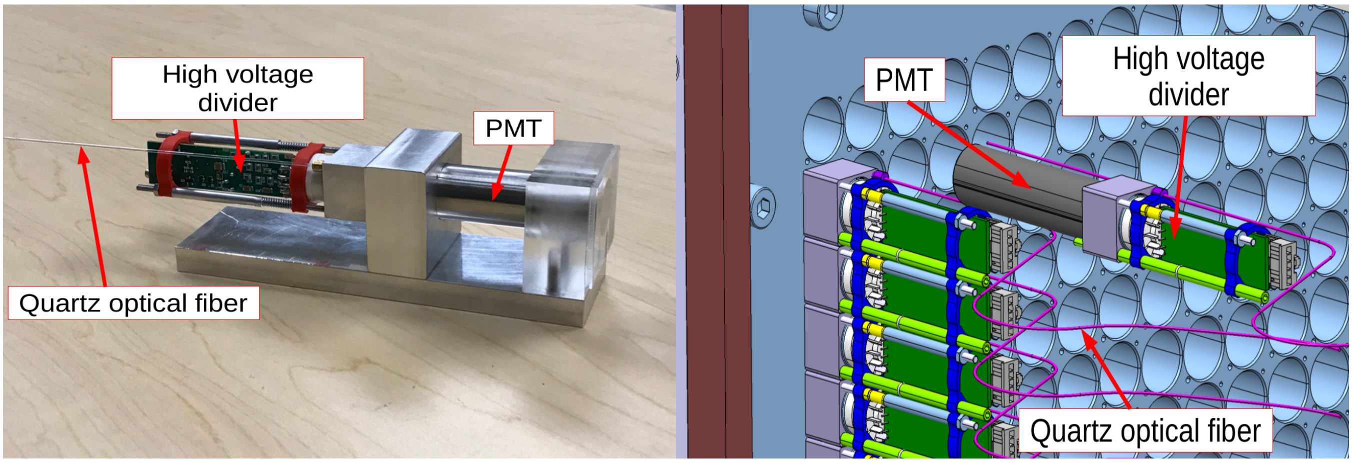

Figure III.39: Prototype (left) and schematic of the PMT and the high voltage divider (right). The optical fiber and the PMT will be attached to the crystal. The other end of the optical fiber will be attached to a blue LED.

Table III.6: Distance from the ^{60}Co source of the components of the calorimeter. Irradiation time : 16 hrs.

Distance from the ^{60}Co source	Components	Expected dose after 16 hrs.
5 cm	Blue LED, Quartz optical fiber	1.5×10^5 Gy
15 cm	Blue LED, Optical grease	1.7×10^4 Gy
30 cm	Blue LED	4.4×10^3 Gy
60 cm	Blue LED, Quartz optical fiber	1.0×10^3 Gy

5.1.3 Radiation hardness tests of other components of the calorimeter

Each $PbWO_4$ crystal is coupled to its PMT using optical grease. For calibration and radiation damage monitoring, a blue LED is used for each crystal. The light from the LED goes to the back face of the crystal via a quartz optical fiber: see Fig. III.39. The LED and the fiber will also be used for radiation damage recovery. More details on the radiation damage recovery are given in the next section. Optical grease, quartz optical fibers, and LEDs are commonly used in high energy physics. The usual barrel shaped design of the detectors in collider physics blocks the flux of high energy particles reaching those components. On the other hand, the side of the NPS calorimeter is exposed to the downstream beam pipe. Therefore, it is better to check the radiation hardness of those components. The distances from the ^{60}Co source of the components of the calorimeter are listed in Tab. III.6 and the irradiation setup is shown in Fig. III.40. The dose rate at the distance 5 cm was extrapolated from those measured at the other distances from the source: 160 Gy/min.

After the irradiation, the color of the optical grease changed. However, since the grease spreads thin enough between the crystal and the PMT, its light transmittance did not change: see Fig. III.41. The transmittance of the optical grease was measured in the Lambda 850 spectrometer. However, for the optical fiber with a diameter of 800 μm and the LED with its round surface, it is challenging to do reproducible measurements with the spectrometer.

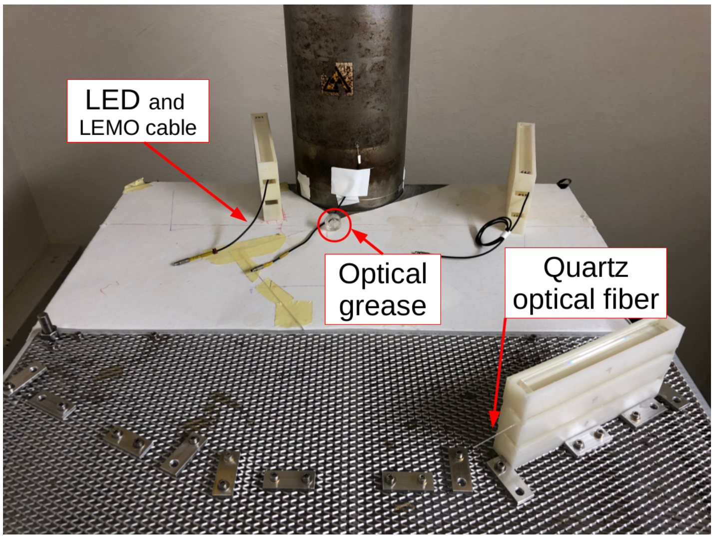

Figure III.40: Irradiation test setup of the optical grease, the quartz optical fibers, and the blue LEDs. The optical fibers and the LEDs were placed at several different distances from the ^{60}Co source.

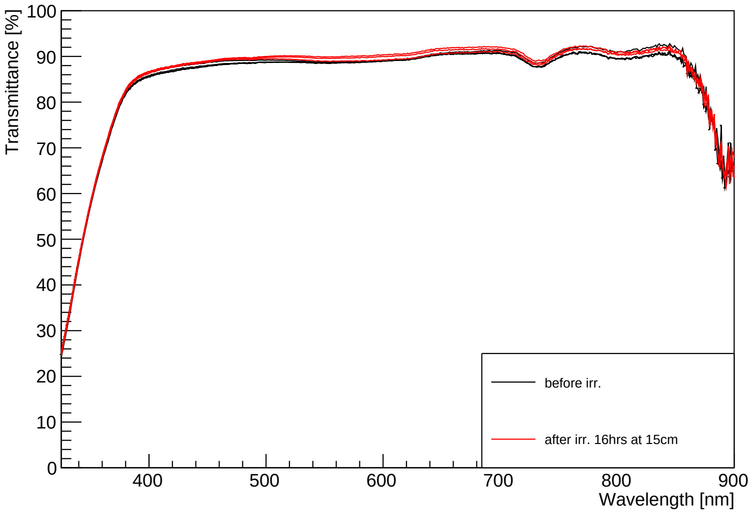

Figure III.41: Transmittance of the optical grease before and after 1.7 × 10^4 Gy of irradiation. The transmittance did not change within the systematic uncertainty of the measurement.

Thus, one of the calorimeter prototypes was used to measure their change of the light output before and after the irradiation. The setup resembles the one in Fig. III.39. The injected blue light from the LED through the optical fiber to the crystal reflects from the VM2000 (reflective sheet), reaches the PMT, and its signal gets recorded: see Fig. III.42. By changing the LED or the optical fiber with the irradiated one, the radiation damage can be measured.

Some of the measurements and their comparisons before and after the irradiation are shown in Fig. III.43. The quartz optical fiber showed to be radiation hard up to 1.5 × 10^5 Gy. One of the reasons that the NPS calorimeter uses quartz optical fiber is because it is known to be radiation hard and this irradiation test confirmed it. The LEDs on the other hand were not radiation hard. As can be seen from the middle and right plots in Fig. III.43, the light output increases at first and then decreases. It is due to the color changes of the plastic enclosure that surrounds the LEDs: see Fig. III.44.

In Tab. III.7, the changes of the light outputs before and after the irradiation are listed. The light output measurements depicted in Fig. III.43 were done several times to test their reproducibility and each light output was Gaussian fitted. The average value of the mean of the Gaussians is taken as the light output of the component.

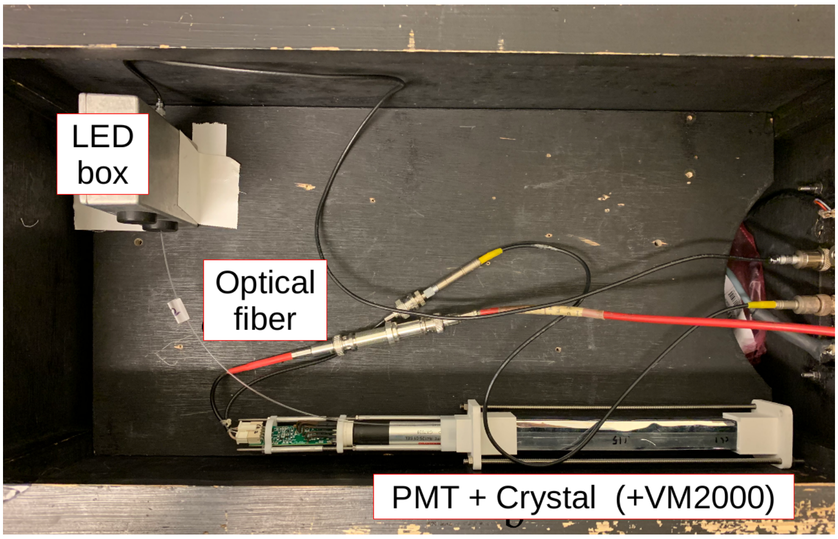

Figure III.42: Setup to measure the irradiation damage of the optical fiber and the LED. The LED injects blue light to the crystal via an optical fiber and the PMT converts the amount of the reflected light in the crystal to signals.

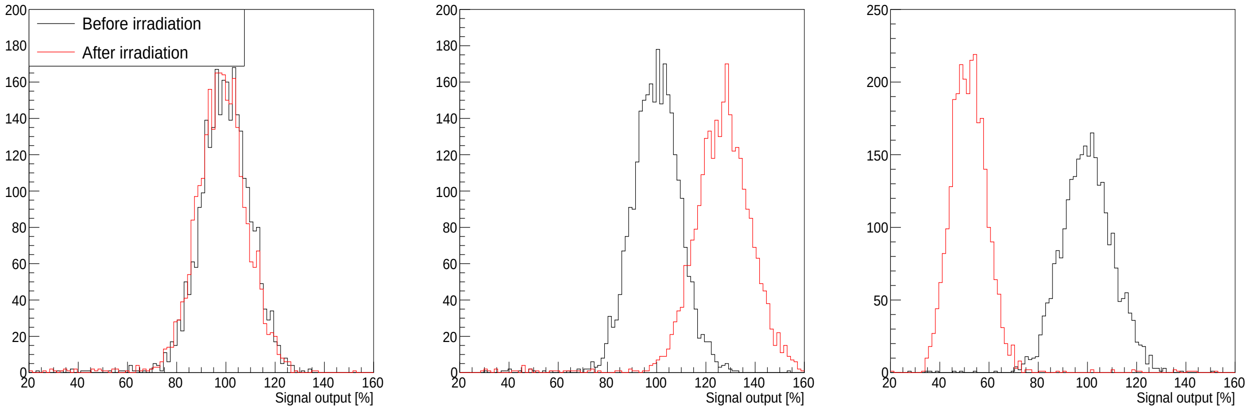

Figure III.43: LED signal on the PMT from the setting in Fig. III.42. Left: quartz optical fiber irradiated with 1.5×10^5 Gy. Middle: LED irradiated with 1.0×10^3 Gy. Right: LED irradiated with 1.5×10^5 Gy.

The standard deviation of the repeated measurements is taken as the systematic uncertainty in Tab. III.7. Negative values mean that the light output increased after the irradiation.

The total expected dose on the LED during the whole experiment is less than 2000 Gy, and on the optical fiber is less than 20 Gy. Based on this calculation, the LED signal on the PMT during the experiment will change and, at least, increase at first. However, in the simulation used to compute these estimates, the outer frame design of the calorimeter was not implemented yet and the components were exposed directly to the radiation environment of the hall. Therefore, further studies are needed to draw firm conclusions on the LED radiation damage and its effect on the light output. The realistic NPS calorimeter outer frames should be implemented to calculate more accurately the radiation dose on the LEDs. Thereafter, LED irradiation tests should follow with a dose equivalent to the newly calculated dose from the simulation. However, one should note that there are several other options for the calibration of the calorimeter as presented in the previous chapter[†].

[†] The other issue that still needs to be addressed would be the crystal radiation damage recovery using the same LEDs. The LEDs also recover their radiation damage at room temperature over time. Stimulated LED radiation damage recovery tests using its own light would be valuable in the future.

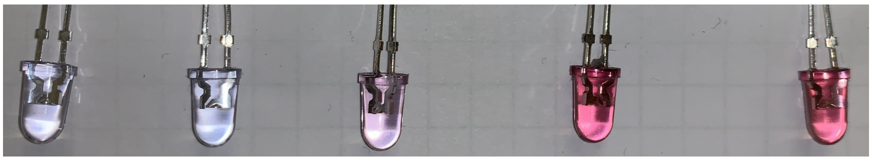

Figure III.44: Change of the color of the LED plastic enclosures. From left to right: without irradiation, 1.0×10^3 Gy, 4.4×10^3 Gy, 1.7×10^4 Gy, and 1.5×10^5 Gy of irradiation.

Table III.7: Change of the LED signal on the PMT from its original value after the irradiation. The systematic uncertainty (standard deviation) of the measurements is indicated next to the components.

Components (sys. err.) / Distance from the ^{60}Co source	60 cm	30 cm	15 cm	5 cm
Quartz optical fiber (± 2.9%)	+2.9%	-	-	-2.0%
LED (± 3.3%)	-30%	-8.5%	+42%	+47%

5.2 Optical bleaching tests

As presented in section 5.1.2, even though $PbWO_4$ crystals are radiation hard, damage still appears in a high radiation environment. To prevent the crystals being damaged too much, only the crystals with $dk < 1.1$ m^{-1} after 30 Gy of irradiation will be used. Yet, for 20 cm crystal, $dk = 1.1$ m^{-1} implies about 20% loss in transmittance, which can decrease the energy resolution significantly. Therefore, a system to recover (cure) the damage is going to be used in the calorimeter of the NPS.

The radiation damage of the optical transmission from the ionizing radiation can be recovered by thermo-activation and injection of specific energies [109]:

$$n_i = n_0\ exp(-w_T^i - \sum_j b_j I_j)\ t \tag{III.7}$$

$n_0,\ n_i$: initial and current concentrations of the color center of type i

$w_T^i = A_i\ exp(-E_{TA}/kT)$: spontaneous relaxation probability

A_i : normalization factor

E_{TA} : thermo-activation energy of the color center

k : Boltzmann constant

T : temperature

b_j : interaction constant of the color center with a flux of a specific energy

I_j : specific energy flux

t : recovery time

As can be seen from Eq. (III.7), the crystal can recover by spontaneous relaxation, which means leaving it in, for example, at room temperature. The procedure can be accelerated by increasing the temperature. Typically a time-lapse of 2 hours at 200°C recovers the optical transmission of $PbWO_4$ crystals completely. However, it is highly impractical to stop the experiment and increase the temperature of the crystals from 18°C to 200°C every time the curing is needed. A more accessible way to cure the crystals would then be the energy injection.

Blue LEDs and infrared LEDs were tested for the energy injection recovery. The light from the LED is injected to the crystal via a quartz optical fiber. This is the same configuration of the calorimeter previously shown in Fig. III.39 and III.42. The setup for the curing test is shown in Fig. III.45. There are advantages in both the blue and the infrared light for the curing. For blue light, the same blue LED can be used for the calibration and the radiation damage monitoring of the calorimeter, so there is no need to install two types of LEDs in the calorimeter. For infrared light, the PMT is insensitive to it. It means that it is possible to cure the crystals during the data taking of the experiment. Fig. III.46 shows one of the results: the crystal was irradiated with 30 Gy of dose and then it was cured for two hours with infrared light. After the measurements, the crystal was put in a 200°C oven for two hours to fully recover its optical transmission. Later, the crystal was irradiated again with 30 Gy of dose and then, cured again for two hours with blue light. To be noted, measurements were done at room temperature.

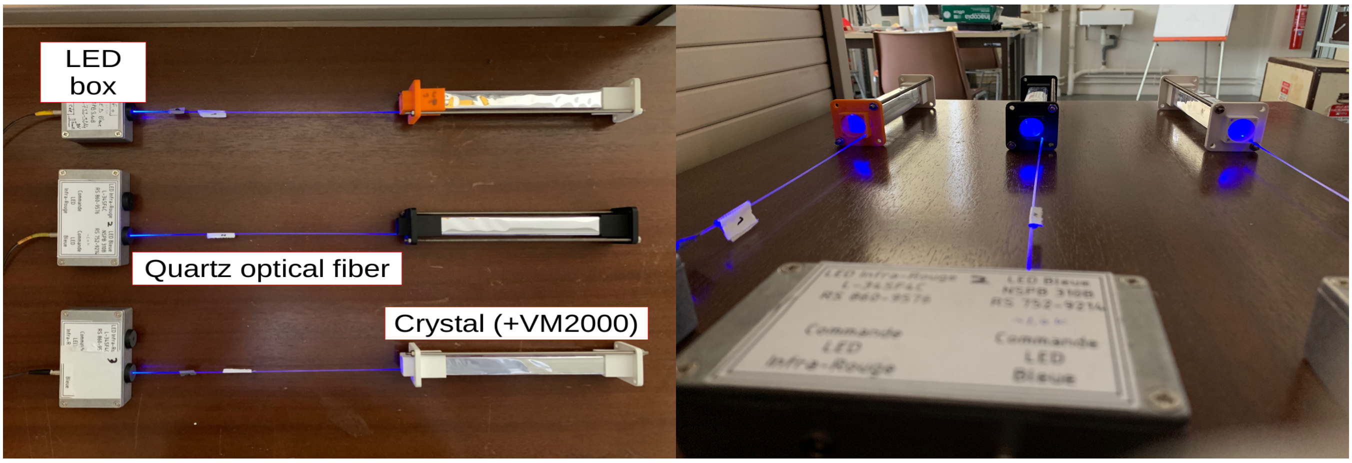

Figure III.45: Setup for optical transmission recovery via energy injection. Blue LEDs are being used in this picture. The recovery tests are done in the dark to reduce lights other than the LED light going to the crystal.

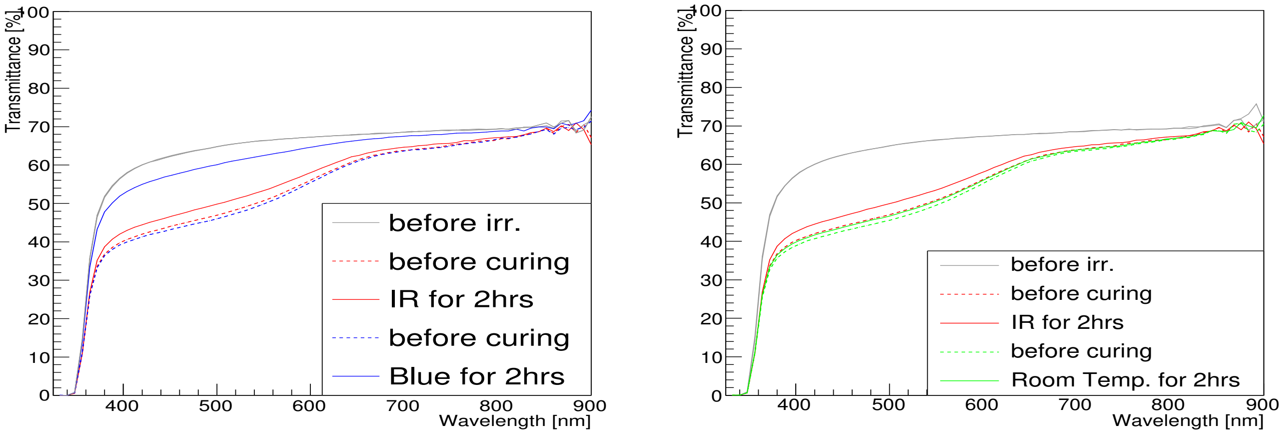

Figure III.46: Optical transmittance recovery using the blue light injection (i.e. optical bleaching) and the infrared light injection via quartz optical fiber (left). The amount of dose of the irradiation was 30 Gy. Right: the amount of the curing using the infrared light is compared with the spontaneous relaxation at room temperature during the same amount of time.

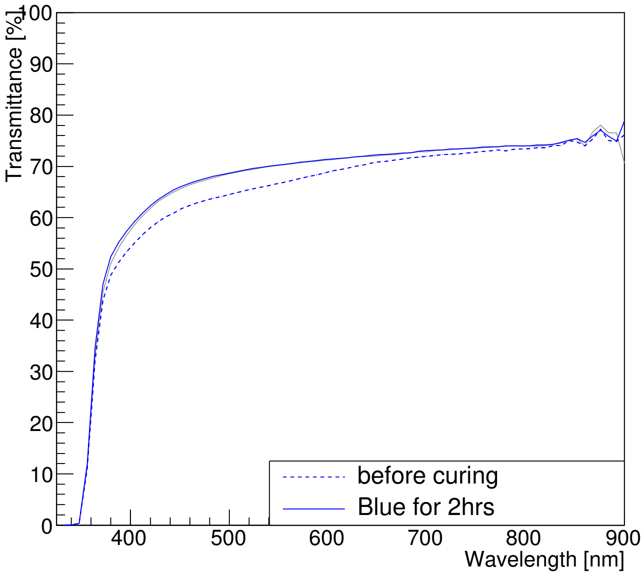

Figure III.47: One of the crystals with $dk < 1.1$ m^{-1} after 30 Gy of irradiation. The damaged transmittance from the 30 Gy of irradiation returns to its original value after 2 hours of optical bleaching. The grey line, overlaid by the solid-blue line, indicates the transmittance measured before the irradiation.

As it can be seen from the left plot of Fig. III.46, the amount of recovery is significantly larger using a blue light injection compared to the infrared. Although the infrared light has an effect on the curing (see the right plot of Fig. III.46) and has the advantage of curing while taking data, it was decided to use blue light for the calorimeter of the NPS. The optical transmission damage recovery from the irradiation using the blue light injection is called "optical bleaching". The decision to use optical bleaching was not only made following these tests but also by taking into account the time schedule of the experiment. It was estimated that the time to test and develop further the infrared injection recovery method would postpone the start of the experiment. The crystal used in Fig. III.46 has $dk > 1.1$ m^{-1} after 30 Gy of irradiation. For crystals with $dk < 1.1$ m^{-1} after 30 Gy of irradiation, they recover completely after 30 Gy of irradiation and 2 hours of optical bleaching, as in Fig. III.47.

A dose of 30 Gy corresponds to about 8 and 1 hours of beam time of the low-x_B and high-Q^2 settings (see Fig. III.12), respectively. Considering the limited beam time and the curing time of 2 hours, we also did more realistic tests where the experiment run time is significantly larger than the curing time. A dose of 500 Gy of irradiation is equivalent to about 5 days of the low-x_B setting and around 1 day of the high-Q^2 setting (see Fig. III.12). For the crystals with $dk < 1.1$ m^{-1} after 30 Gy of irradiation, the results of 2 hours of optical bleaching after 500 Gy of irradiation are shown in Fig. III.48.

It was found that the crystals saturate their damage from the ionizing radiation. At the same time, the effect of optical bleaching also saturates. The values of dk of the same crystal after 500 Gy, 1000 Gy, and 1.7×10^4 Gy of irradiation are shown in the left plot of Fig. III.49. The optical transmissions after 1.7×10^4 Gy of irradiation and following 2.5 hours and 14 hours of optical bleaching, are shown in the right plot of the Fig. III.49. The optical bleachings were not done immediately after the irradiation. The transmittance before and after the irradiation are indicated by the grey lines.

In conclusion, for the radiation hard crystals, it might not even be necessary to do the optical bleaching during the whole experiment as long as the damage saturates at relatively high transmittance. Also, considering that most of the background is due to low energy particles (see Fig. III.15), the radiation damage on the crystals will appear mostly at the front part of the crystal. As it can be seen from the shower profile of the calorimeter (Fig. III.50), high energy particles will develop their showers at a few centimeters from the front face of the crystal. However, for the calorimeter to have good energy and position resolutions and taking into account the fact that not all 1080 crystals will have good radiation hardness, optical bleaching will still be required. Crystals near the downstream beam pipe will be irradiated from their sides. Therefore, when the experiment has to be stopped for some reason, crystals could be cured with optical bleaching, which is far more effective than the spontaneous relaxation at room temperature.

In summary, $PbWO_4$ crystals are selected for the NPS calorimeter to endure the high radiation environment with

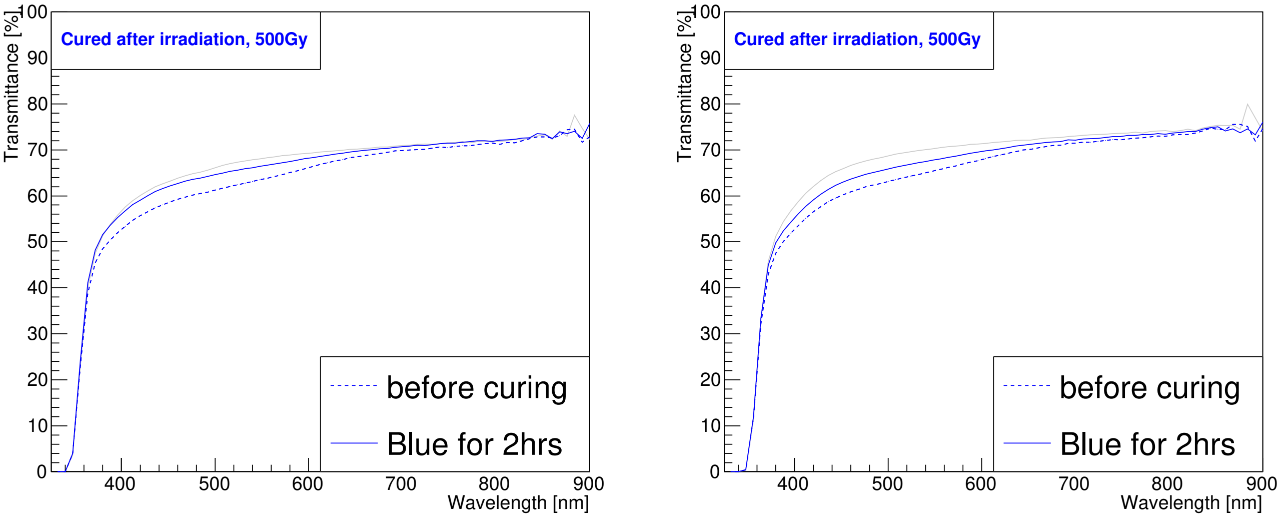

Figure III.48: Optical transmission before and after 500 Gy of irradiation and after 2 hours of optical bleaching for two different crystals with $dk < 1.1$ m^{-1} after 30 Gy of irradiation. The grey line shows the transmittance measured before the irradiation.

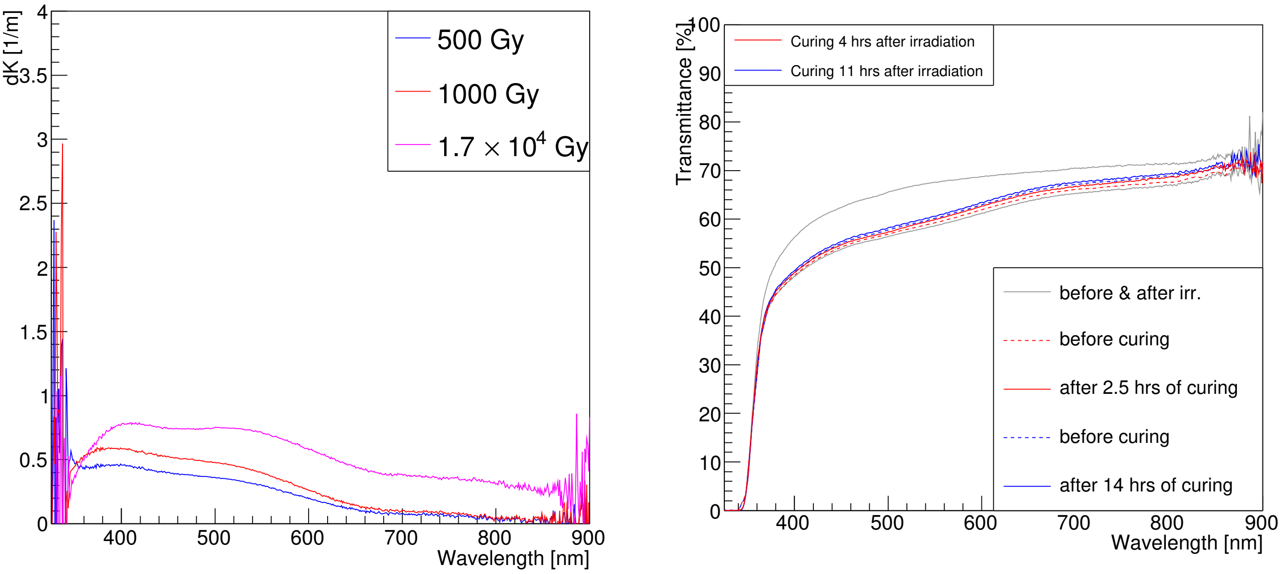

Figure III.49: Left: the values dk of the same crystal with 500 Gy, 1000 Gy, and 1.7×10^4 Gy. Right: optical bleaching after 1.7×10^4 Gy of irradiation. The optical bleaching was done twice and it was not performed consecutively.

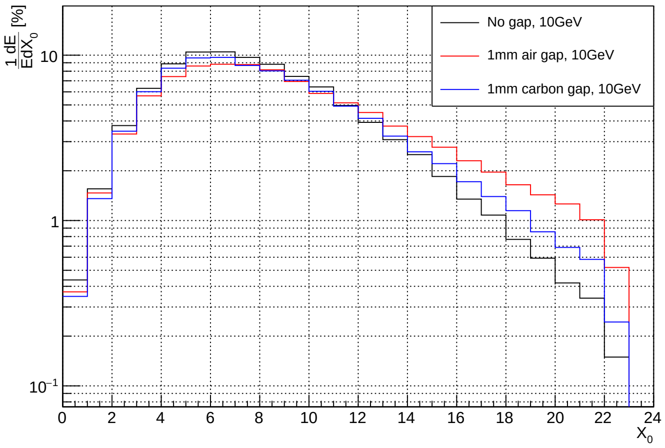

Figure III.50: Longitudinal shower profile of 10 GeV photons in the calorimeter. Dead materials used between the crystals are shown by different colors of lines.

relatively high light yield. The crystals, however, show radiation damage of their optical transmission from high doses of ionizing radiation. In order to optimize the calorimeter performance in the high radiation environment, two things need to be considered. The first one is to select only crystals with high radiation hardness: $dk < 1.1$ m^{-1} after 30 Gy of dose or higher. This, however, has limits. It takes a long time to measure the radiation hardness of all 1080 crystals. Also, given that cost and production time of the crystals, we may end up with some crystals in the detector with low radiation hardness. The second aspect to consider, which is one of the key features of the calorimeter, is using the optical bleaching system to recover the damage from radiation. Blue LEDs and optical fibers for each crystal will be not only used for the calibration and the radiation damage monitoring, but also for the radiation damage recovery. These procedures will ensure the calorimeter to have the best performance it can have during the whole experiment.

Chapter IV

Glass scintillators for the EIC

In this short final chapter, radiation hardness measurements and energy resolution simulations of glass scintillators are presented. Glass scintillators are one of the candidate materials for the electromagnetic calorimeters of EIC.

1 The Electron-Ion Collider

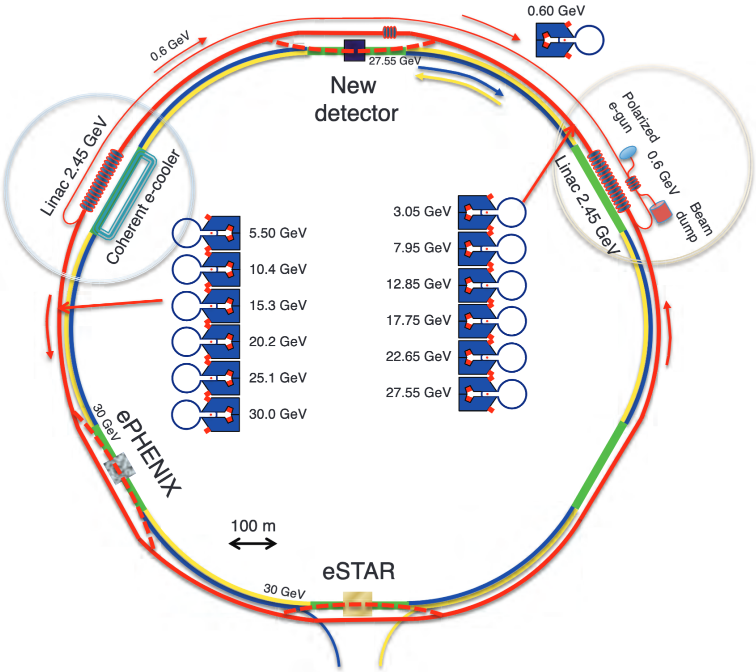

Figure IV.1: The EIC accelerator design at Brookhaven National Laboratory. It is based on the existing Relativistic Heavy Ion Collider (RHIC). An electron accelerator will be installed in the existing tunnel of RHIC. The yellow and blue circles represent the existing hadron rings of RHIC and the red circle shows the future electron accelerator. The ePHENIX and eSTAR are future upgrades of existing RHIC detectors. Additionally, a New detector will be installed. Figure extracted from [51].

Up to now this document has not discussed gluons, the force carriers of the strong force. Quarks interact with each other by the exchange of a gluon. Unlike photons, which have no charge, gluons themselves have color charges and interact with one another: a significant fraction of the nucleon mass is coming from the gluon self couplings.

The Electron-Ion Collider (EIC) is being designed to probe the kinematic region with high gluon density which could enable detailed studies of the gluon interactions. Also, since several decades ago, phenomenological tools have been developed to tomographically image the nucleon in terms of quarks and gluons. They have been utilized in the

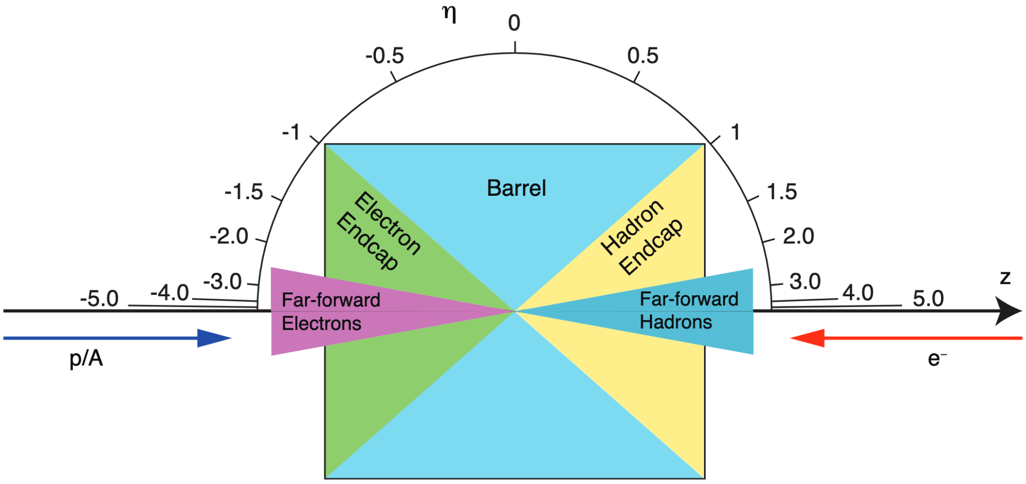

Figure IV.2: The schematic description of the EIC detector. The ion beam (p/A) is in +z-direction and the electron beam (e^-) is in the opposite direction. The symbol η describes the direction of a particle relative to the direction of the ion beam. Figure extracted from [111].

Table IV.1: Energy resolution requirements of the electromagnetic calorimeters for the EIC [111].

η	Detector parts	Energy resolution $[\sigma/E]$
$[1.0,\ 4.5]$	Forward part	$10 \sim 12\%/\sqrt{E}$
$[-1.0,\ 1.0]$	Central part	$10 \sim 12\%/\sqrt{E}$
$[-2.5,\ -1.0]$	Backward part	$7\%/\sqrt{E}$
$[-4.5,\ -2.5]$		$2\%/\sqrt{E}$

valence quark region at Jefferson Lab and COMPASS at CERN: the very example is the GPDs. These tools can be applied to the region of sea quarks and gluons and expand our image of the nucleon.

The EIC will be built at Brookhaven National Laboratory in Upton, New York, U.S.A. An additional electron accelerator will be installed at the existing Relativistic Heavy Ion Collider (RHIC): see Fig. IV.1. The versatile kinematic range of $x_B = [10^{-4},\ 10^{-1}]$ and $Q^2 = [1.,\ 100.]$ GeV^2 (see Fig. I.17) with high luminosity of at least 10^{34} cm^{-2}s^{-1} and the polarizability of the electron and ion beams will provide the access to the most detailed sea quark and gluon dynamics ever before.

2 Electromagnetic calorimeters for EIC

The detectors of the EIC will be largely composed of 3 parts: forward part (the hadron endcap), backward part (electron endcap), and central (barrel) part: see Fig. IV.2. Each of these parts also breaks down into smaller parts with different specifications. The symbol $\eta \equiv -\ln\left[\tan\left(\frac{\theta}{2}\right)\right]$ in Fig. IV.2 describes the direction of a particle relative to the ion beam, with θ representing the angle between the directions of the particle and the ion beam. The specifications which these parts of the detector should meet for the EIC physics are described in [111].

In this chapter, only the electromagnetic calorimeters of the detector are discussed. The forward part calorimeter needs to detect high-x semi inclusive deep inelastic scattering events and the electromagnetic part of high-x jets. In the central part, it is required to identify the electrons amongst high hadronic backgrounds. Finally, the calorimeters at the back side need to determine the x_B and Q^2 of the reactions from the scattered electrons. The required energy resolutions of the electromagnetic calorimeters in different parts of the detector are shown in Tab. IV.1.

$PbWO_4$ crystals are used for electromagnetic calorimeters in high energy physics when high energy resolution and radiation hardness are required. However, these crystals are expensive: \$15 $\sim$ 25/cm^3. Therefore, it is probable that EIC calorimeters, especially at the central and forward parts, which require relatively modest energy resolution, will use an alternative material to $PbWO_4$ crystals.

The position resolution is also a critical criterion for determining the material of an electromagnetic calorimeter.

Table IV.2: Properties of the CUA glass scintillator and $PbWO_4$ [112, 63].

Parameters	Glass ($BaO*2SiO_2$)	Lead Tungsten ($PbWO_4$)
Density [g/cm^3]	3.7 - 5.4	8.28
Radiation length [cm]	2.2 - 3.6	0.89
Molière radius [cm]	2 - 3	2.19
Radiation type	Pure scintillation	Scintillation (∼ 13% Čerenkov)
Decay time [ns]	22 - 50 72 - 120 330 - 450	5 14 110
Photon yields per 1 MeV	> 500	∼ 140 - 200
Photo emission peaks [nm]	440, 460	450, 540

The smaller the Molière radius the more compact the detector can be while maintaining the same position resolution. The position resolution also depends on the granularity of the calorimeter. However, in this chapter, this aspect will not be discussed.

3 Glass scintillator

One of the alternative materials for electromagnetic calorimeters is glass scintillators. This section will describe a glass scintillator manufactured by CUA whose main composition is $BaO*2SiO_2$. Some of the properties of the glass are listed in Tab. IV.2. Even though the radiation length is 3 times larger, the Molière radius of the glass is similar to that of $PbWO_4$. Therefore, the transverse size of the glass can be comparable to that of the crystals when used in calorimeters.

With different types of doping (e.g. Lu, Dy, Gd, Tb, Yb, Ce, etc.), the light output, the decay timing, and the resistance to the radiation of the glass vary. The production of the glass scintillator utilizes thermal annealing. The temperature and time of the annealing also lead to making glasses with different properties. The radiation hardness of 9 glass samples was measured in IJCLab. Each sample was doped differently and its surfaces polished in various ways. Some of the results of their radiation hardness will be shown in this section.

The preparations for the construction of a calorimeter prototype is on-going in parallel to the glass production. The prototype will be made of a 3×3 array of glass scintillators. One of the prototype test goals is to measure its energy resolution. As the first step towards this test, Monte Carlo simulations were done and the results are also presented in this section.

3.1 Radiation hardness measurements

Due to the fact that the development of these scintillators is in an early stage, the size of the glasses is less than a few cubic centimeters and the shapes are irregular: see Fig. IV.3. Therefore, the optical transmittances of the samples were measured several times and the differences between the maximum and the minimum values are taken as the systematic uncertainty of the measurement. Despite the measurement uncertainties being different amongst the glasses, all the measurement uncertainties are below 5% in the wavelength range of [440, 600] nm. This range is chosen near the scintillating light emission peak.

The same irradiation procedure was applied to the glass scintillators as to the $PbWO_4$ crystals. The total amount of dose was 1000 Gy. Two of those results are shown in Fig. IV.4. Both the maximum and the minimum values of the measured transmittance before the irradiation are shown in the plots to indicate the size of the measurement uncertainties. Most of the samples have no significant change in the transmittance before and after the irradiation within the measurement uncertainties, giving results similar to those of the sample A in Fig. IV.4. The sample B in Fig. IV.4 on the other hand, changed its transmittance: the measurement uncertainties are 0.76%. The degree of the change of the attenuation coefficient, dk in the Eq. (III.6), of the sample B is around 2 m^{-1} near the light emission range of [400, 600] nm. The value dk is large even though the optical transmittance has changed slightly. It is because the thickness of the sample is only a few centimeters.

Most of the glass scintillator samples showed no change in their optical transmittance after the 1000 Gy of irradiation within their systematic uncertainties, except the sample B in Fig. IV.4 which has different chemical composition.

Figure IV.3: One of the 9 glass scintillators (in the red circle). The sample is placed in the same light spectrometer, in Fig. III.36, used for the $PbWO_4$ crystals.

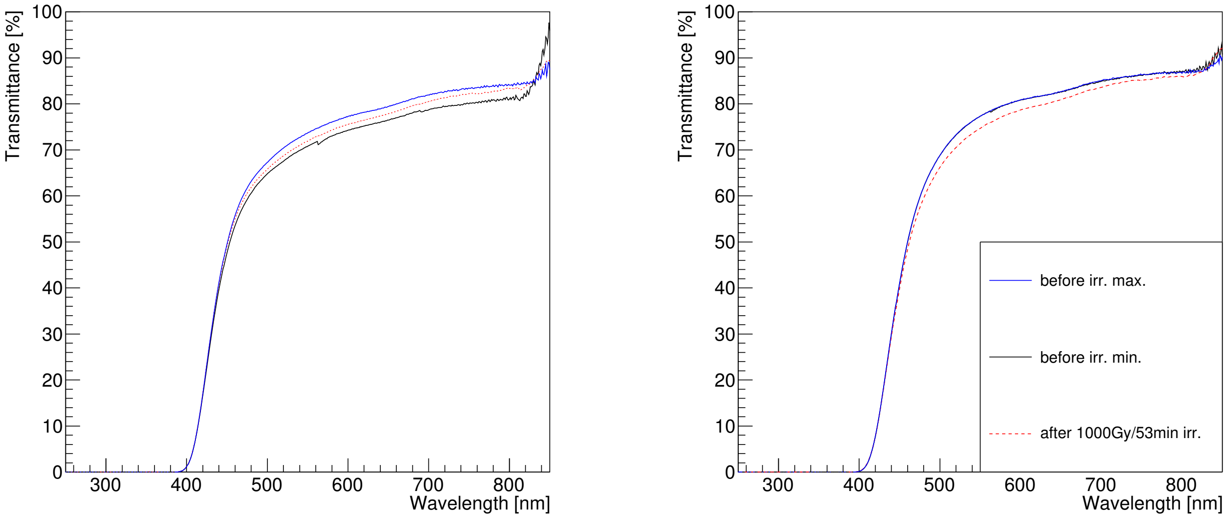

Figure IV.4: Transmittance measured before and after the 1000 Gy of irradiation for two samples of glass scintillators: A on the left and B on the right. Two measurement results before the irradiation are plotted to indicate the maximum and the minimum values of the measured transmittances. The sample A has no significant change in the transmittance after the irradiation. The transmittance changed slightly for the case of the sample B.

However, the samples are only a few centimeters thin and have irregular shapes, that do not allow to draw more concrete conclusions. Larger and regularly shaped glasses would be needed to do more precise measurements.

3.2 Energy resolution simulation of the prototype

One of the criteria the new material needs to achieve is an energy resolution of better than $10\%/\sqrt{\mathrm{E}}$. To test this, a prototype is needed. For the glass scintillator, the first prototype is going to be made of a 3×3 array. First of all, a Monte Carlo simulation is needed. The main purpose of the simulation is to determine the minimum size of the glass in order to attain the desired energy resolution of the prototype.

The simulation is based on the one used for the energy resolution simulation of the NPS calorimeter in the previous chapter. The material of the scintillator is changed to that of the glass scintillator and the size of the array to 3×3. The same carbon frame with the same width and thickness is used for the simulation. A photon beam, with energy ranging from 0 to 10 GeV, was fired to the center of the prototype: the real prototype test will also be performed in a similar way in Hall D at Jefferson Lab.

In order to do a more realistic simulation, one needs the optical properties of the material, such as the light yield and the refractive index, to be put into the simulation. However, the computation of optical photons using the Geant4 libraries is time consuming and there are no definite values of the properties of the glass scintillator. Therefore, no optical properties were simulated for the energy resolution calculation. As a consequence, the energy resolution simulation results presented in this section correspond to the most optimal case: see Fig. IV.5.

The ranges of the length and the transverse size of the glass in the simulation are, to some degree, the likely sizes of the glass that will be able to be manufactured in the future. In the energy range of [0., 10.] GeV, to achieve the energy resolution better than 10%, a prototype 300-mm long or longer would be sufficient. However, a prototype with a resolution better than 5% would require the glass to be longer than or equal to 400 mm. Furthermore, the tendency of $\sigma/E \propto 1/\sqrt{E}$ clearly disappears for the glass 300-mm long or shorter. This is because the longitudinal energy leak also fluctuates event-by-event and thus deteriorates the energy resolution. Its fluctuation gets larger than the stochastic fluctuation of the energy deposition ($\boldsymbol{B}$ in Eq. (III.1)) when the glass scintillator is too short*. It is well-known that electromagnetic calorimeters make a good measurement of the energy only if the block length is about 19 to 20 times the radiation length of the material, not less.

The length of the glass has more effect on the energy resolution than its transverse size.† The accumulated energy deposition in the glass scintillator displays more clearly the reason for the stronger dependency on the length than on the transverse size of the glass: see Fig. IV.6. As can be seen from the left plot of Fig. IV.6, the total energy deposition changes around 10% from 30 mm to 60 mm in radius, which corresponds to changing the transverse size of the glass of the 3×3 prototype from 20×20 mm^2 to 40×40 mm^2. However when the length of the scintillator changes from 200 mm to 600 mm, which directly corresponds to the horizontal axis on the right plot of Fig. IV.6, the total energy deposition changes around 60%. Therefore, in the ranges of [200., 600.] mm of length and [20×20, 40×40] mm^2 of transverse size, the variation in length has more effect on the energy resolution. Additionally, the longitudinal energy leak becomes the dominant part of the energy fluctuation of the 3×3 glass prototype when the accumulated energy deposition is too low: e.g. lower than or similar to 70%.

In summary, to acquire meaningful results from the 3×3 prototype tests, it is recommended for the glass to have a length longer than 300 mm in order to achieve an energy resolution better than 10% in the energy range of [0., 10.] GeV. The transverse size of the scintillator does not have a big impact on the energy resolution when varying from 20×20 mm^2 to 40×40 mm^2. However, it should be noted that the optical properties of the glass scintillator were not simulated in this study. For further detailed simulation in the future, the optical properties must be simulated. Improvements of the glass scintillator, such as increasing its size, are ongoing: see Fig. IV.7 for a recently grown $20 \times 20 \times 200$ mm^3 sample. The goal is to grow $40 \times 40 \times 400$ mm^3 samples by the year 2023 [113] with ongoing optimization [112].

$PbWO_4$ crystals are one of the commonly used materials for the electromagnetic calorimeter in high energy physics where high energy resolution and radiation hardness are required. However, they have several limitations: especially their high price. Therefore, it is conceivable that the calorimeters of the EIC will use other materials in the parts where the required energy resolution is more relaxed. Glass scintillator ($BaO{*}2Si0_2$) is one of the alternative materials for the calorimeter. Depending on the energy resolution the glass calorimeter reaches, its η coverage will

---

*The fluctuation of the energy deposition due to the longitudinal energy leak is common in high energy physics and can in part be corrected by longitudinally segmenting the calorimeter. The shower profile can be recorded in this way and the energy deposition can be corrected using the shower profile.

†This is expected considering the radiation length and the Molière radius of the glass scintillator: see Tab. IV.2.

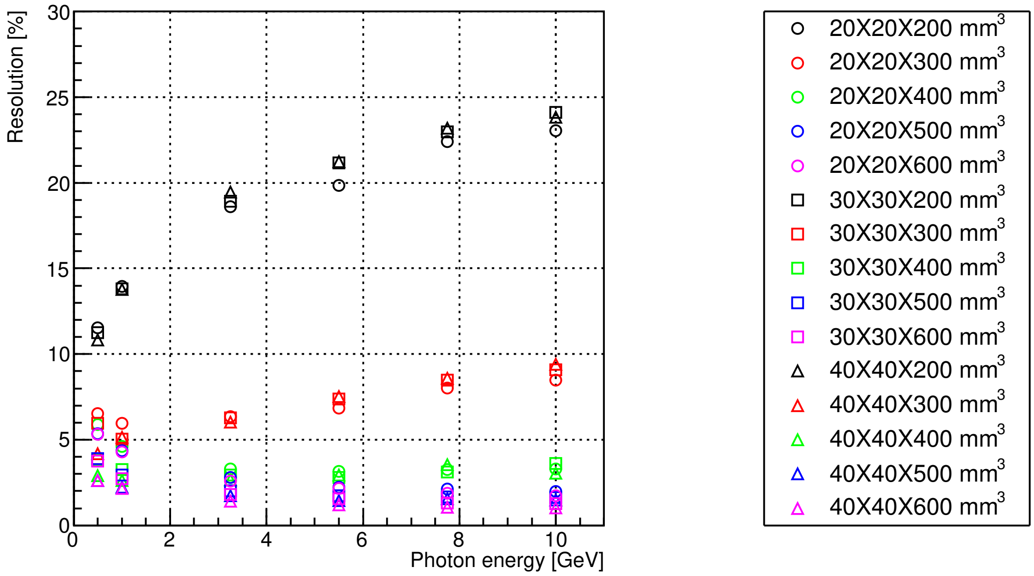

Figure IV.5: Energy resolution simulation of a 3×3 prototype with different sizes of glass scintillator. The horizontal axis indicates the energy of the photon beam.

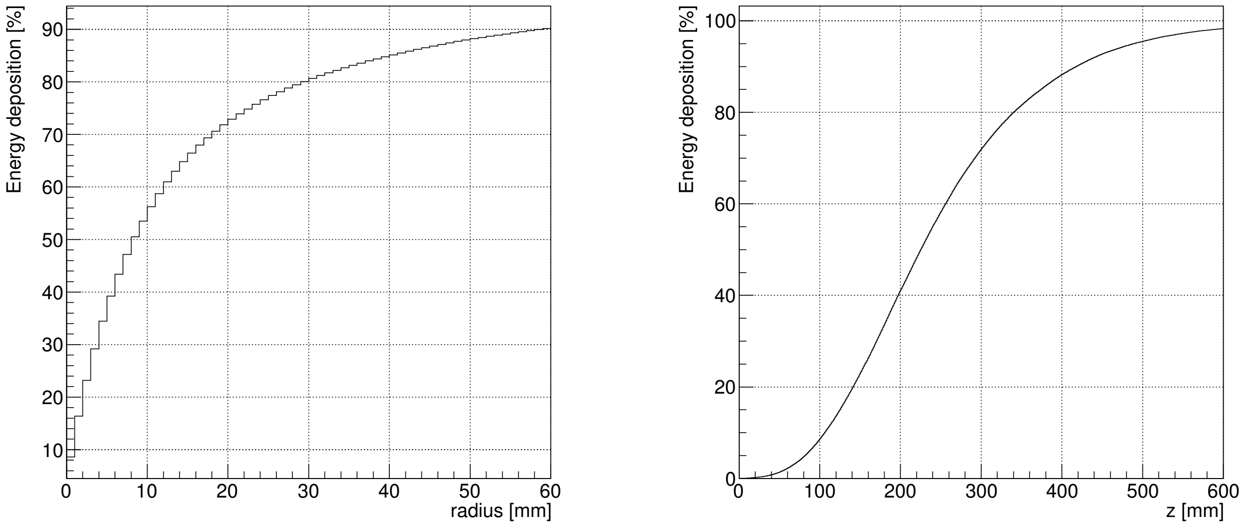

Figure IV.6: Accumulated energy deposition in the glass scintillator. The photon beam energy used is 10 GeV. Left: lateral energy deposition. The horizontal axis indicates the transverse distance from the beam projection. Right: longitudinal energy deposition. The horizontal axis indicates the longitudinal distance from the front face of the scintillator.

Figure IV.7: Glass scintillator size of $20 \times 20 \times 200$ mm^3. Figure extracted from [113].

hopefully be decided. Of course, there are many other criteria the glass scintillator has to fulfill. Nonetheless, its development is fast and looks promising.

Conclusion

Gluons self-couplings confine the quarks and gluons in the nucleon. Therefore, studying the nucleon structure is one of the ways to understand confinement in QCD. Leptons have been an excellent tool to probe the nucleon. In order to understand the QCD, the nucleon structure needs to be studied at different scales. Jefferson Lab is providing the highest precision data in the valence quark region for various exclusive reactions. The future EIC will provide data in the sea quark and gluon regions with precision higher than ever before.

Generalized Parton Distributions are one of the phenomenological tools that can tomographically image the nucleon in terms of the degrees of freedom of QCD. Recently, a three dimensional tomography of proton in the valence quark region from DVCS experiments was obtained using a GPD model. Also, the measurement of the quark contribution to the nucleon total angular momentum is one of the key goals of the GPD experimental program.

DVCS and DVMP are the main examples of exclusive reactions that give access to GPDs. The factorization for the DVMP process has been proven only for longitudinally polarized virtual photons and $\sigma_L \gg \sigma_T$ is expected in the leading-twist approximation. However, models incorporating transversity GPDs predict a boost in the size of σ_T.

This thesis described the data analysis of a Hall A experiment and showed the results of the neutral pion electroproduction cross section. The development of a calorimeter for an upcoming Hall C experiment using NPS is also discussed. Finally, a quick look was taken at glass scintillators as potential candidates for forward calorimetry at EIC.

The Hall A DVCS/DVMP experiment introduced in this thesis is an extension of the first dedicated DVCS/DVMP experiment in Jefferson Lab after its beam energy upgrade. In order to detect the DVCS photons, or decay photons of the π^0, an electromagnetic calorimeter made of PbF_2 was built. The DVCS cross section is small and to compensate it, the experiment used very high luminosity. Combined with the high energy of the experiment and the aging of the PbF_2 crystals, radiation damage on the calorimeter performance was visible throughout the data taking. In addition to calibrating the calorimeter using elastic scattering events, a method using the reconstruction of the π^0 invariant mass was adapted to calibrate the degrading calorimeter more frequently.

The π^0 events are selected in the calorimeter by requiring the coincidence between two reconstructed photons and a scattered electron detected in the HRS. In order to count the number of accidental events arising from this method, the time windows for the reconstruction of photons were shifted away from the HRS trigger. Due to the modest energy resolution of the calorimeter, the proton mass distribution was overlapped with SIDIS events and, potentially, resonance decays. Therefore, event selection cuts on the missing mass distribution were applied with care in order to select as many proton events as possible with low contamination from other channels.

The acceptance calculation was done using a Geant4 simulation and a neutral pion electroproduction event generator. External and internal radiative effects were taken into account in the acceptance calculation in order to convolute their effects with the detector resolutions. Bin migration was also taken into account and its effects were convoluted with the kinematic dependences of the cross section. The simulated data of the calorimeter were calibrated in order to match the missing mass distribution of the experimental data. The invariant-mass distribution of the π^0 from the simulation automatically matched that of the experiment after the calibration and smearing process. This calibration and smearing method can be improved in the future. I have only smeared the energy of the photons of the π^0 decay. The angle of the decay could also be smeared to better match the simulated distributions to those of the experiment.

The systematic uncertainties associated with the cuts applied to the π^0 event selection have been estimated. Even though the variations of the extracted cross sections as a function of the cut values were within the statistical uncertainties of the results, we have taken those as their systematical uncertainties. This conservative calculation of the systematic uncertainties probably overestimates the values, which range up to 7%. We are looking into several solutions to avoid this overestimation. One of the solutions is to reduce the variation range. Indeed, the variation in the cut ranges was large.

The cross sections $(d\sigma_T + \epsilon^* d\sigma_L)/dt$, σ_{TT}/dt, and σ_{TL}/dt have been extracted in the kinematics: $E = 7.383$

GeV, $\langle Q^2 \rangle = 3.2$ GeV^2 and $\langle x_B \rangle = 0.36$. Larger σ_{TT}/dt over σ_{TL}/dt suggests that the transversely-polarized photon contribution is not suppressed. The $(d\sigma_T + \epsilon^* d\sigma_L)/dt$ and σ_{TT}/dt agree well in general with the GK model prediction. These agreements suggest that the chiral-odd GPDs are accessible. However, σ_{TL}/dt shows opposite sign compared to the model predictions. This was also observed in the previous Hall A experiments. The several orders of magnitude larger values of the σ_{TL}/dt of the data compared to the model prediction would indicate that the chiral-even GPDs are still accessible in these kinematics. Nonetheless, one should keep in mind that these are model-dependent interpretations.

The data analysis of the other kinematics of the Hall A experiment is ongoing and the scaling behavior of the L/T unseparated cross sections ($(d\sigma_T + \epsilon^* d\sigma_L)/dt$) will be tested. The upcoming Hall C experiment will perform a Rosenbluth separation of the L/T terms in the same kinematics giving the direct ratio of the cross sections $d\sigma_T$ and $d\sigma_L$.

The energy separation of the cross sections of DVCS/DVMP requires higher momentum reach for the scattered electron spectrometer. Therefore, moving from Hall A to Hall C, to utilize the higher momentum reach of the HMS, is necessary for the next generation of DVCS/DVMP experiments. Furthermore, one of the limiting factors of the previous Hall A experiments was the modest energy resolution of the electromagnetic calorimeter. A new NPS, in development, will overcome this limitation by using $PbWO_4$ crystals instead of PbF_2 crystals.

The expansion of the kinematic range to lower x_B and higher Q^2, with the highest luminosity for DVCS/DVMP ever before, will generate a significant amount of backgrounds on the calorimeter of NPS. In order to reduce the backgrounds from charged particles, a sweeper magnet is going to be used. The background dose on the calorimeter was calculated using a Geant4 simulation, and the results indicate that the sweeper magnet can reduce the overall background dose at least a factor of 3 with half of its intended magnetic field strength.

The electromagnetic calorimeter of NPS is composed of 1080 $PbWO_4$ crystals in an array of 30×36. To form a structurally safe uniform array, a supporting structure made out of carbon fibers is going to be used. The energy resolution calculation, using a Geant4 simulation, confirmed that a supporting structure at the front and back sides of the crystals can be used without worsening too much the energy resolution. The calculation with this design showed an energy resolution of around 1.2% with photon energies of [4., 10.] GeV.

The photon reconstruction algorithm used in the Hall A experiment was adapted to Hall C. Various magnetic field shieldings in front of the calorimeter to reduce the magnetic field of the sweeper magnet on the PMTs were tested, by calculating the position resolution of the calorimeter. The design of the magnetic field shielding later was chosen in a way not to cover the front face of the calorimeter: a mu-metal mesh at the back side of the crystal and the front side of the PMT will replace the carbon frame at the back side. Nevertheless, the position resolution calculated with the photon reconstruction algorithm shows a resolution of around 1.5 mm with photon energies of [4., 10.] GeV. The simulation contains now a realistic geometry of the future experiment and the offline algorithms to reconstruct the particles hitting the calorimeter are operational. The software is thus ready for the calculation of the acceptance of the new experiment.

The light yield of several $PbWO_4$ crystals were measured in IJCLab and Justus-Liebig-Universität Gieβen to confirm the measurements in Catholic University of America (CUA). The temperature dependence of the light yield was also measured showing the expected 2%/°C. Therefore, the NPS crystals will be kept at 18 ± 0.1°C.

The radiation hardnesses of the SICCAS $PbWO_4$ crystals were measured in Laboratoire de Chimie Physique, near IJCLab. Each crystal showed different radiation hardness and this reinforced the need of the crystal selection cut: $dk < 1.1$ m^{-1} after 30 Gy of irradiation. However, we also need to measure the radiation hardness of the Crytur crystals to check whether the Crytur crystals also show variation in their radiation hardness.

Since the side of the calorimeter is exposed to the downstream beam pipe, we had to test the radiation hardness of the materials used in the calorimeter. The radiation damage of the optical grease, used to couple the crystal to the PMT, was small enough so that no transmittance change was observed. The optical fiber also showed no observable radiation damage. However, the LEDs changed their transmittance after the radiation. Their light output firstly increased until 1000 Gy of irradiation, then started to decrease. A rough calculation indicated that the expected total dose on the LEDs during the experiment is 2000 Gy. Therefore, additional irradiation tests should be performed on the LEDs with around that amount of dose.

The large amount of background on the calorimeter can degrade the optical transmittance of the crystals and cause a decrease in energy resolution. Optical bleaching uses blue light injection to the crystal in order to recover its properties from radiation damage. It was observed that for crystals with $dk < 1.1$ m^{-1} after 30 Gy of irradiation, 2 hours of blue light injection via an optical fiber after 500 Gy of dose cures the radiation damage to some degree. However, with larger amounts of dose, the optical bleaching seemed not effective in curing. Fortunately, it was observed that the radiation damage also saturates, $dk < 1.1$ m^{-1} after 1.7×10^4 Gy in some crystals. Therefore, we plan to use as many radiation hard crystals as possible for the calorimeter and cure the crystals by optical bleaching whenever the experiment has to be stopped for some reason.

The EIC is currently planned to start operations around 2030 in the U.S.A. The calorimeters of the EIC detectors require different energy resolution requirements. $PbWO_4$ crystals are commonly used for calorimeters in high energy physics when high energy resolution and high radiation hardness are required. However, due to its high price, alternative materials are considered for the calorimeters in EIC where relatively relaxed energy resolution is required. CUA is developing a glass scintillator, mainly composed of $BaO*2Si0_2$, as one of those alternatives. The radiation hardness of one of its early prototypes was measured in IJCLab. Most of the glass scintillators samples, each having different chemical compositions or being polished in different ways, showed no change in transmittance after 1000 Gy of irradiation. It is, however, still in an early stage to quantitatively conclude on their radiation hardness since the measured glasses were only a few centimeters thin and with irregular shapes.

Energy resolution measurements of a calorimeter prototype made of an array of 3×3 glass scintillators are planned in Hall D at Jefferson Lab. Prior to the actual measurements, Geant4 simulations were performed to decide the size of the glass scintillators for the test. The simulation results indicated that the glasses should be at least 300-mm long to have an energy resolution better than 10% in the energy range of [0., 10.] GeV. Moreover, in order to reduce the fluctuations in longitudinal shower profile, it is recommended for the glasses to be longer than 300 mm. Glass scintillators are expected to increase their size to $40 \times 40 \times 400$ mm^3 by the year 2023 with the ongoing optimizations. Their final energy resolution will help decide on their suitability as calorimeter material for EIC.

Precision DVCS and DVMP experiments are ongoing mainly at Jefferson Lab and COMPASS at CERN. Since the approaches to the experiments are different, the measurements from different collaborations will provide information on the universality of the GPDs. With different types of mesons, the flavor separation of GPDs will be possible. The measurements will progressively pin down the elusive GPDs in order to understand the nucleon structure in the valence quark region. By probing the regions of sea quarks and gluons in the EIC, we hope to have a better understanding of the GPDs. The most exciting part is that it is only a small fraction of what the EIC is being designed to achieve.

Bibliography

[1] M.N. Rosenbluth, High Energy Elastic Scattering of Electrons on Protons, Phys. Rev. **79**, 615–619 (1950).

[2] Peter J. Mohr, David B. Newell, and Barry N. Taylor, CODATA Recommended Values of the Fundamental Physical Constants: 2014, Rev. Mod. Phys. **88**, 035009 (2016), arXiv:1507.07956 [physics.atom-ph] .

[3] Hélène Fleurbaey, Sandrine Galtier, Simon Thomas, Marie Bonnaud, Lucile Julien, François Biraben, François Nez, Michel Abgrall, and Jocelyne Guéna, New Measurement of the $1S-3S$ Transition Frequency of Hydrogen: Contribution to the Proton Charge Radius Puzzle, Phys. Rev. Lett. **120**, 183001 (2018), arXiv:1801.08816 [physics.atom-ph] .

[4] J.C. Bernauer *et al.* (A1), High-precision determination of the electric and magnetic form factors of the proton, Phys. Rev. Lett. **105**, 242001 (2010), arXiv:1007.5076 [nucl-ex] .

[5] Randolf Pohl *et al.*, The size of the proton, Nature **466**, 213–216 (2010).

[6] W. Xiong *et al.*, A small proton charge radius from an electron–proton scattering experiment, Nature **575**, 147–150 (2019).

[7] J.D. Bjorken and Emmanuel A. Paschos, Inelastic Electron-Proton and γ-Proton Scattering, and the Structure of the Nucleon, Phys. Rev. **185**, 1975–1982 (1969).

[8] Richard P. Feynman, Very high-energy collisions of hadrons, Phys. Rev. Lett. **23**, 1415–1417 (1969).

[9] Richard E. Taylor, Inelastic electron - proton scattering in the deep continuum region, Conf. Proc. C **690914**, 251–260 (1969).

[10] Murray Gell-Mann, A Schematic Model of Baryons and Mesons, Phys. Lett. **8**, 214–215 (1964).

[11] M. Tanabashi *et al.* (Particle Data Group), Review of Particle Physics, Phys. Rev. D **98**, 030001 (2018).

[12] John C. Collins, Davison E. Soper, and George F. Sterman, Factorization of Hard Processes in QCD (1989) pp. 1–91, arXiv:hep-ph/0409313 .

[13] S.S.M. Wong, *Introductory Nuclear Physics*, 2nd ed. (Wiley-VCH, 1998).

[14] Dieter Müller, D. Robaschik, B. Geyer, F.-M. Dittes, and J. Hořejši, Wave functions, evolution equations and evolution kernels from light ray operators of QCD, Fortsch. Phys. **42**, 101–141 (1994), arXiv:hep-ph/9812448 .

[15] Xiang-Dong Ji, Deeply virtual Compton scattering, Phys. Rev. D **55**, 7114–7125 (1997), arXiv:hep-ph/9609381 .

[16] A.V. Radyushkin, Nonforward parton distributions, Phys. Rev. D **56**, 5524–5557 (1997), arXiv:hep-ph/9704207 .

[17] Xiang-Dong Ji, Off forward parton distributions, J. Phys. G **24**, 1181–1205 (1998), arXiv:hep-ph/9807358 .

[18] Matthias Burkardt, Impact parameter dependent parton distributions and off-forward parton distributions for $\zeta \to 0$, Phys. Rev. D **62**, 071503 (2000), [Erratum: Phys.Rev.D 66, 119903 (2002)], arXiv:hep-ph/0005108 .

[19] M. Diehl, Generalized parton distributions in impact parameter space, Eur. Phys. J. C **25**, 223–232 (2002), [Erratum: Eur.Phys.J.C 31, 277–278 (2003)], arXiv:hep-ph/0205208 .

[20] John P. Ralston and Bernard Pire, Femtophotography of protons to nuclei with deeply virtual Compton scattering, Phys. Rev. D **66**, 111501 (2002), arXiv:hep-ph/0110075 .

[21] Raphaël Dupré, Michel Guidal, Silvia Niccolai, and Marc Vanderhaeghen, Analysis of Deeply Virtual Compton Scattering Data at Jefferson Lab and Proton Tomography, Eur. Phys. J. A **53**, 171 (2017), arXiv:1704.07330 [hep-ph] .

[22] I.V. Anikin and O.V. Teryaev, Dispersion relations and subtractions in hard exclusive processes, Phys. Rev. D **76**, 056007 (2007), arXiv:0704.2185 [hep-ph] .

[23] A.V. Radyushkin, Generalized Parton Distributions and Their Singularities, Phys. Rev. D **83**, 076006 (2011), arXiv:1101.2165 [hep-ph] .

[24] Maxim V. Polyakov and C. Weiss, Skewed and double distributions in pion and nucleon, Phys. Rev. D **60**, 114017 (1999), arXiv:hep-ph/9902451 .

[25] M.V. Polyakov, Generalized parton distributions and strong forces inside nucleons and nuclei, Phys. Lett. B **555**, 57–62 (2003), arXiv:hep-ph/0210165 .

[26] V.D. Burkert, L. Elouadrhiri, and F.X. Girod, The pressure distribution inside the proton, Nature **557**, 396–399 (2018).

[27] Cedric Lorce, Barbara Pasquini, and Marc Vanderhaeghen, Unified framework for generalized and transverse-momentum dependent parton distributions within a 3Q light-cone picture of the nucleon, Journal of High Energy Physics **05**, 041 (2011), arXiv:1102.4704 [hep-ph] .

[28] Xiang-Dong Ji, Gauge-Invariant Decomposition of Nucleon Spin, Phys. Rev. Lett. **78**, 610–613 (1997), arXiv:hep-ph/9603249 .

[29] C. Lorce and B. Pasquini, Quark Wigner Distributions and Orbital Angular Momentum, Phys. Rev. D **84**, 014015 (2011), arXiv:1106.0139 [hep-ph] .

[30] Andrei V. Belitsky, Dieter Mueller, and A. Kirchner, Theory of deeply virtual Compton scattering on the nucleon, Nucl. Phys. B **629**, 323–392 (2002), arXiv:hep-ph/0112108 .

[31] D. Drechsel and L. Tiator, Threshold pion photoproduction on nucleons, J. Phys. G **18**, 449–497 (1992).

[32] M. Diehl, *Generalized parton distributions*, Habilitation (2003), arXiv:hep-ph/0307382 .

[33] John C. Collins, Leonid Frankfurt, and Mark Strikman, Factorization for hard exclusive electroproduction of mesons in QCD, Phys. Rev. D **56**, 2982–3006 (1997), arXiv:hep-ph/9611433 .

[34] M. Vanderhaeghen, Pierre A.M. Guichon, and M. Guidal, Hard electroproduction of photons and mesons on the nucleon, Phys. Rev. Lett. **80**, 5064–5067 (1998).

[35] I. Bedlinskiy *et al.* (CLAS), Exclusive η electroproduction at $W > 2$ GeV with CLAS and transversity generalized parton distributions, Phys. Rev. C **95**, 035202 (2017), arXiv:1703.06982 [nucl-ex] .

[36] L. Favart, M. Guidal, T. Horn, and P. Kroll, Deeply Virtual Meson Production on the nucleon, Eur. Phys. J. A **52**, 158 (2016), arXiv:1511.04535 [hep-ph] .

[37] A. Airapetian *et al.* (HERMES), Single spin azimuthal asymmetry in exclusive electroproduction of π^+ mesons, Phys. Lett. B **535**, 85–92 (2002), arXiv:hep-ex/0112022 .

[38] R. De Masi *et al.* (CLAS), Measurement of $ep \to ep\pi^0$ beam spin asymmetries above the resonance region, Phys. Rev. C **77**, 042201 (2008), arXiv:0711.4736 [hep-ex] .

[39] A. Kim *et al.*, Target and double spin asymmetries of deeply virtual π^0 production with a longitudinally polarized proton target and CLAS, Phys. Lett. B **768**, 168–173 (2017), arXiv:1511.03338 [nucl-ex] .

[40] P.E. Bosted *et al.* (CLAS), Target and beam-target spin asymmetries in exclusive pion electroproduction for $Q^2 > 1$ GeV^2. II. $ep \to e\pi^0 p$, Phys. Rev. C **95**, 035207 (2017), arXiv:1611.04987 [nucl-ex] .

[41] B. Zhao *et al.* (CLAS), Measurement of the beam spin asymmetry of $\overrightarrow{e}p \to e'p'\eta$ in the deep-inelastic regime with CLAS, Phys. Lett. B **789**, 426–431 (2019).

[42] Saeed Ahmad, Gary R. Goldstein, and Simonetta Liuti, Nucleon Tensor Charge from Exclusive π^o Electroproduction, Phys. Rev. D **79**, 054014 (2009), arXiv:0805.3568 [hep-ph] .

[43] Gary R. Goldstein, J.Osvaldo Gonzalez-Hernandez, and Simonetta Liuti, Easy as π^o: On the Interpretation of Recent Electroproduction Results, J. Phys. G **39**, 115001 (2012), arXiv:1201.6088 [hep-ph] .

[44] G.R. Goldstein, J.Osvaldo Gonzalez-Hernandez, and S. Liuti, Flexible Parametrization of Generalized Parton Distributions: The Chiral-Odd Sector, Phys. Rev. D **91**, 114013 (2015), arXiv:1311.0483 [hep-ph] .

[45] S.V. Goloskokov and P. Kroll, An Attempt to understand exclusive π^+ electroproduction, Eur. Phys. J. C **65**, 137–151 (2010), arXiv:0906.0460 [hep-ph] .

[46] S.V. Goloskokov and P. Kroll, Transversity in hard exclusive electroproduction of pseudoscalar mesons, Eur. Phys. J. A **47**, 112 (2011), arXiv:1106.4897 [hep-ph] .

[47] M. Diehl, Generalized parton distributions with helicity flip, Eur. Phys. J. C **19**, 485–492 (2001), arXiv:hep-ph/0101335 .

[48] I. Bedlinskiy *et al.* (CLAS), Exclusive π^0 electroproduction at $W > 2$ GeV with CLAS, Phys. Rev. C **90**, 025205 (2014), [Addendum: Phys.Rev.C 90, 039901 (2014)], arXiv:1405.0988 [nucl-ex] .

[49] Gary R. Goldstein, J.Osvaldo Gonzalez-Hernandez, and Simonetta Liuti, Flexible Parametrization of Generalized Parton Distributions from Deeply Virtual Compton Scattering Observables, Phys. Rev. D **84**, 034007 (2011), arXiv:1012.3776 [hep-ph] .

[50] Gary R. Goldstein, Simonetta Liuti, and J.Osvaldo Gonzalez-Hernandez, Generalized parton distributions in the chiral odd sector and their role in neutral meson electroproduction, Int. J. Mod. Phys. Conf. Ser. **20**, 222–229 (2012).

[51] A. Accardi *et al.*, Electron Ion Collider: The Next QCD Frontier: Understanding the glue that binds us all, Eur. Phys. J. A **52**, 268 (2016), arXiv:1212.1701 [nucl-ex] .

[52] C. Muñoz Camacho *et al.* (Jefferson Lab Hall A, Hall A DVCS), Scaling tests of the cross-section for deeply virtual compton scattering, Phys. Rev. Lett. **97**, 262002 (2006), arXiv:nucl-ex/0607029 .

[53] M. Defurne *et al.* (Jefferson Lab Hall A), E00-110 experiment at Jefferson Lab Hall A: Deeply virtual Compton scattering off the proton at 6 GeV, Phys. Rev. C **92**, 055202 (2015), arXiv:1504.05453 [nucl-ex] .

[54] F Gautheron *et al.* (COMPASS), COMPASS-II Proposal, (2010).

[55] T. Horn *et al.*, Scaling study of the pion electroproduction cross sections and the pion form factor, Phys. Rev. C **78**, 058201 (2008), arXiv:0707.1794 [nucl-ex] .

[56] E. Fuchey *et al.*, Exclusive Neutral Pion Electroproduction in the Deeply Virtual Regime, Phys. Rev. C **83**, 025201 (2011), arXiv:1003.2938 [nucl-ex] .

[57] I. Bedlinskiy *et al.* (CLAS), Measurement of Exclusive π^0 Electroproduction Structure Functions and their Relationship to Transversity GPDs, Phys. Rev. Lett. **109**, 112001 (2012), arXiv:1206.6355 [hep-ex] .

[58] Matthias Gorzellik (COMPASS), Measurement of the exclusive π^0 muoproduction cross section at COMPASS, in *22nd International Symposium on Spin Physics* (2017) arXiv:1702.06293 [hep-ex] .

[59] M. Defurne *et al.* (Jefferson Lab Hall A), Rosenbluth separation of the π^0 electroproduction cross section, Phys. Rev. Lett. **117**, 262001 (2016), arXiv:1608.01003 [hep-ex] .

[60] M. Vanderhaeghen, Pierre A.M. Guichon, and M. Guidal, Deeply virtual electroproduction of photons and mesons on the nucleon: Leading order amplitudes and power corrections, Phys. Rev. D **60**, 094017 (1999), arXiv:hep-ph/9905372 .

[61] J. Roche, C.E. Hyde-Wright, B. Michel, C. Muñoz Camacho, *et al.* (Jefferson Lab Hall A Collaboration), Measurements of the Electron-Helicity Dependent Cross Sections of Deeply Virtual Compton Scattering with CEBAF at 12 GeV, PR12-06-114 (2013).

[62] F. Georges, *Deeply virtual Compton scattering at Jefferson Lab*, Ph.D. thesis, Université Paris-Saclay (2018).

[63] C. Muñoz Camacho *et al.* (Jefferson Lab NPS Collaboration), Exclusive Deeply Virtual Compton and Neutral Pion Cross-Section Measurements in Hall C, PR12-13-010 (2013).

[64] Nicole d'Hose, Deeply Virtual Compton Scattering and Exclusive Meson Production, EPJ Web Conf. **85**, 01004 (2015).

[65] Nicole d'Hose, Silvia Niccolai, and Armine Rostomyan, Experimental overview of Deeply Virtual Compton Scattering, Eur. Phys. J. A **52**, 151 (2016).

[66] R. Akhunzyanov *et al.* (COMPASS), Transverse extension of partons in the proton probed in the sea-quark range by measuring the DVCS cross section, Phys. Lett. B **793**, 188–194 (2019), arXiv:1802.02739 [hep-ex] .

[67] H. Avakian, V.D. Burkert, L. Elouadrhiri, M. Lowry, M. Guidal, S. Procureur, *et al.* (Jefferson Lab CLAS Collaboration), Deeply Virtual Compton Scattering at 11 GeV with transversely polarized target using the CLAS12 Detector, PR12-12-010 (2011).

[68] M. Guidal and M. Vanderhaeghen, Double deeply virtual Compton scattering off the nucleon, Phys. Rev. Lett. **90**, 012001 (2003), arXiv:hep-ph/0208275 .

[69] Andrei V. Belitsky and Dieter Mueller, Exclusive electroproduction of lepton pairs as a probe of nucleon structure, Phys. Rev. Lett. **90**, 022001 (2003), arXiv:hep-ph/0210313 .

[70] I.V. Anikin *et al.*, Nucleon and nuclear structure through dilepton production, Acta Phys. Polon. B **49**, 741–784 (2018), arXiv:1712.04198 [nucl-ex] .

[71] Shengying Zhao, Studying nucleon structure via Double Deeply Virtual Compton Scattering (DDVCS), PoS **SPIN2018**, 068 (2019), arXiv:1904.09335 [hep-ph] .

[72] P. Bertin, C.E. Hyde, R. Ransome, F. Sabatié, *et al.* (The Hall A Collaboration), Deeply Virtual Compton Scattering At 6 GeV, PR00-110 (2000).

[73] C. Muñoz Camacho, P. Bertin, C.E. Hyde, J. Roche, *et al.* (The Jefferson Lab Hall A Collaboration), Complete Separation of Deeply Virtual Photon and π^0 Electroproduction Observables of Unpolarized Protons, PR07-007 (2006).

[74] R D McKeown, The Jefferson Lab 12 GeV Upgrade, Journal of Physics: Conference Series **312**, 032014 (2011).

[75] J. Alcorn *et al.*, Basic Instrumentation for Hall A at Jefferson Lab, Nucl. Instrum. Meth. **A522**, 294–346 (2004).

[76] F. Feinstein (ANTARES), The analogue ring sampler: A front-end chip for ANTARES, *New developments in photodetection. Proceedings, 3rd International Conference, Beaune, France, June 17-21, 2002*, Nucl. Instrum. Meth. **A504**, 258–261 (2003).

[77] C. Muñoz Camacho, *Diffusion Compton profondément virtuelle dans le Hall A au Jefferson Laboratory*, Ph.D. thesis, Université Paris VI (2005).

[78] M. Dlamini, Internal note: DVCS Calorimeter Analysis (Fall 2014 - Spring 2015): E12-06-114, `https://hallaweb.jlab.org/dvcslog/12+GeV/160506_172312/calo_analysis.pdf` (2016).

[79] R.T. Jones *et al.*, A bootstrap method for gain calibration and resolution determination of a lead-glass calorimeter, Nucl. Instrum. Meth. **A566**, 366–374 (2006).

[80] M. Dlamini, *Measurement of Hard Exclusive Electroproduction of* π^0 *Meson Cross Section in Hall A of JLab with CEBAF at 12 GeV*, Ph.D. thesis, Ohio University (2018).

[81] A.M. Martí Jiménez-Argüello, *Measurement of the photon electroproduction cross section at JLAB with the goal of performing a Rosenbluth separation of the DVCS contribution*, Ph.D. thesis, Université Paris Sud - Paris XI ; Universidad de Valencia, Spain (2014).

[82] A. Houcine, *Reconstruction des quadrivecteurs des particules détectées dans le calorimétre électromagnétique de l'expérience DVCS*, Master's thesis, Faculté des Sciences de Monastir, Tunisia (2012).

[83] V. Breton, H. Fonvieille, P. Grenier, C. Guicheney, J. Jousset, Y. Roblin, and F. Tamin, Application of neural networks and cellular automata to interpretation of calorimeter data, Nucl. Instrum. Meth. **A362**, 478–486 (1995).

[84] H. Rashad, Internal note: tracking, VDC multi cluster, `https://hallaweb.jlab.org/dvcslog/12+GeV/161108_074436/Multi_Clusters_DVCS.pdf` (2019).

[85] M. Rvachev, *Effective use of JLab Hall A HRS acceptance with R-functions*, Tech. Rep. Technical Report JLAB-TN-01-055 (Massachusetts Institute of Technology, 2001).

[86] H. Rashad, Internal note: DVCS collaboration meeting, updates on HRS efficiencies, `https://www.jlab.org/indico/event/253/contribution/0/material/slides/0.pdf` (2018).

[87] W. Henry, Internal note: Geometry Update, `https://hallaweb.jlab.org/dvcslog/12+GeV/498` (2018).

[88] Luke W. Mo and Yung-Su Tsai, Radiative Corrections to Elastic and Ionelastic *ep* and μp Scattering, Rev. Mod. Phys. **41**, 205–235 (1969).

[89] L.I. Schiff, Radiative Correction to the Angular Distribution of Nuclear Recoils from Electron Scattering, Phys. Rev. **87**, 750–752 (1952).

[90] M. Vanderhaeghen, J. M. Friedrich, D. Lhuillier, D. Marchand, L. Van Hoorebeke, and J. Van de Wiele, QED radiative corrections to virtual Compton scattering, Phys. Rev. **C62**, 025501 (2000), arXiv:hep-ph/0001100 [hep-ph] .

[91] A. Afanasev, I. Akushevich, V. Burkert, and K. Joo, QED radiative corrections in processes of exclusive pion electroproduction, Phys. Rev. D **66**, 074004 (2002), arXiv:hep-ph/0208183 .

[92] C.E. Hyde-Wright, Comment on Radiative Corrections in Virtual Compton Scattering, `https://hallaweb.jlab.org/dvcslog/DVCS2/131219_143249/Rad_Corr_VCS.pdf` (2006).

[93] Yung-Su Tsai, Pair Production and Bremsstrahlung of Charged Leptons, Rev. Mod. Phys. **46**, 815 (1974), [Erratum: Rev.Mod.Phys. 49, 521–423 (1977)].

[94] W.M. Yao *et al.* (Particle Data Group), Review of Particle Physics, J. Phys. G **33**, 1–1232 (2006).

[95] L. Morand *et al.* (CLAS), Deeply virtual and exclusive electroproduction of omega mesons, Eur. Phys. J. A **24**, 445–458 (2005), arXiv:hep-ex/0504057 .

[96] P. Kroll, Comments on the Hall A π^0 production data, `https://hallaweb.jlab.org/dvcslog/12+GeV/190826_053821/comments-on-HallA-data.pdf` (2019).

[97] F.X. Girod *et al.* (CLAS), Measurement of Deeply virtual Compton scattering beam-spin asymmetries, Phys. Rev. Lett. **100**, 162002 (2008), arXiv:0711.4805 [hep-ex] .

[98] H.-S. Jo, Measurement of deeply virtual Compton scattering (DVCS) cross sections with CLAS, *Proceedings, 6th International Conference on Quarks and Nuclear Physics (QNP 2012): Palaiseau, France, April 16-20, 2012*, PoS **QNP2012**, 052 (2012), arXiv:1207.3709 [nucl-ex] .

[99] F. Sabatié, A. Biselli, L. Elouadrhiri, W. Kim, D. Ireland, M. Holtrop H. Egiyan, *et al.* (CLAS collaboration), Deeply Virtual Compton Scattering with CLAS at 11 GeV, PR12-06-119 (2006).

[100] S. Niccolai, V. Kubarovsky, M. Mirazita, A. El Alaoui, *et al.* (Jefferson Lab CLAS Collaboration), Deeply Virtual Compton Scattering on the Neutron with CLAS12 at 11 GeV, PR12-11-003 (2011).

[101] Geant4 Collaboration, Geant4 User's Guide for Application Developers, (2016).

[102] HAMAMATSU Photonics K.K., Photomultiplier Tubes and Assemblies for Scintillation Counting & High Energy Physics, (2017).

[103] HAMAMATSU Photonics K.K, Photomultiplier Tubes Basics and Applications Fourth Edition, (2017).

[104] R.Y. Zhu, D.A. Ma, H.B. Newman, C.L. Woody, J.A. Kierstad, S.P. Stoll, and P.W. Levy, A Study on the properties of lead tungstate crystals, Nucl. Instrum. Meth. A **376**, 319–334 (1996).

[105] M. Kubantsev, I. Larin, and A. Gasparian (PrimEx), Performance of the PrimEx electromagnetic calorimeter, AIP Conf. Proc. **867**, 51–58 (2006), arXiv:physics/0609201 .

[106] T. Horn *et al.*, Scintillating crystals for the Neutral Particle Spectrometer in Hall C at JLab, Nucl. Instrum. Meth. A **956**, 163375 (2020), arXiv:1911.11577 [physics.ins-det] .

[107] R. Wang, private communication.

[108] J.P. Peigneux, PbWO-4: A Challenging material for new calorimetry, Nucl. Instrum. Meth. A **351**, 197–200 (1994).

[109] V. Dormenev, T. Kuske, R.W. Novotny, *et al.*, Stimulated recovery of the optical transmission of PbWO4 scintillation crystals for electromagnetic calorimeters after radiation damage, Nucl. Instrum. Meth. A **623**, 1082 – 1085 (2010).

[110] M. Mostafavi, *Cinétique et dynamique des réactions chimiques* (EDP Sciences, 2015).

[111] A. Kiselev, T. Ullrich, *et al.*, *Electron-Ion Collider Detector Requirements and R&D Handbook*, 1.2 ed. (2020).

[112] V. Berdnikov, T. Horn, I.L. Pegg, *et al.*, New Materials for EIC Calorimeters, 2019 EIC User Group Meeting, `https://wiki.jlab.org/cuawiki/images/5/5e/03022020.pdf`.

[113] T. Horn, NPS Collaboration Meeting, NPS Collaboration Meeting 2020, `https://wiki.jlab.org/cuawiki/images/5/5e/03022020.pdf`.

Résumé en Français

Les distributions de partons généralisées (GPD) sont une généralisation des relativement bien connus facteurs de forme et les distributions de partons ordinaires. Contrairement aux facteurs de forme ou aux distributions de partons, les distributions spatial et d'impulsion des partons à l'intérieur du nucléon sont corrélées dans les GPD. Par conséquent, les GPD contiennent des informations beaucoup plus riches concernant la structure du nucléon.

Les GPD sont accessibles à travers des réactions dites exclusives, où toutes les particules de l'état final sont identifiées. Grace aux progrès expérimentaux en physique des hautes énergies au début des années 2000, l'extraction des GPD est devenu possible. La réaction la plus simple expérimentalement pour sonder ces nouvelles distributions est la diffusion Compton profondément virtuelle (DVCS). Un autre canal exclusif est l'électroproduction de mésons dans le domaine profondément virtuel (DVMP). Malgré que la structure interne du méson complique l'interprétation des données expérimentales en termes des GPD, la production de mésons permet de séparer en saveurs les GPD en mesurant différents types des mésons.

Ce document est divisé en quatre chapitres: une introduction, l'analyse des données de l'électroproduction des pions neutres dans le Hall A de Jefferson Lab (JLab), le développement d'un nouveau spectromètre à particules neutres pour une future expérience dans le Hall C de JLab, et une brève discussion autour d'un nouveau verre scintillant. Après la montée en énergie récente de JLab, les premières mesures précises du DVCS et du DVM(π^0)P dans un large domaine cinématique ont eu lieu dans le Hall A. Les sections efficaces ont été mesurées et toutes les observables accessibles avec un faisceau d'électrons polarisé et une cible de protons non polarisée ont été extraites.

Le processus de DVM(π^0)P est exclusif: $ep \to e'p'\pi^0 \to e'p'\gamma_1\gamma_2$, avec $e(e')$ l'électron initial (final), $p(p')$ le proton initial (final) et γ_1 et γ_2 les deux photons de la décroissance du pion neutre. Les électrons diffusés ont été détectés dans un spectromètre de haute résolution (HRS) dans le Hall A. Les photons du π^0 ont été détectés dans un calorimètre électromagnétique fait de 208 cristaux de PbF2, spécialement conçu pour cette expérience. Les protons de recul n'ont pas été détectés directement, mais identifiés à travers la technique de la masse manquante. L'analyse des données et les résultats préliminaires d'un des points cinématiques sont présentés dans le deuxième chapitre.

La future expérience DVCS/DVMP dans le Hall C mesurera les mêmes observables mais utilisera plusieurs énergies de faisceau, à des valeurs de Q2 et xB fixes. Cette séparation en énergie permettra de mieux séparer les observables du DVCS et ainsi donner de plus fortes contraintes dans l'extraction des GPD. La séparation Rosenbluth dans le cas du DVMP mesurera de façon indépendante les contributions dues aux photons virtuels polarisés longitudinalement et transversalement. Le rapport des deux donnera des indications sur le domaine d'applicabilité des théorèmes de factorisation. En plus, la section efficace des photons polarisés transversalement peut nous renseigner sur les GPD de transversité, très difficile d'accès.

Le dispositif expérimental dans le Hall C est similaire à celui dans le Hall A: les électrons diffusés seront détectés avec le spectromètre de grande impulsion (HMS). Un nouveau spectromètre à particules neutres (NPS) est en cours de construction dans le but de détecter les photons de l'état final. Il est composé de 1080 cristaux de PbWO4. L'expérience dans le Hall C permettra d'aller à des valeurs de xB plus petites et à des valeurs de Q2 plus grandes. NPS se situera très près de la ligne de faisceau et avec la grande luminosité prévue, le bruit de fond attendu dans le calorimètre est grand. Un aimant balai réduira les doses de radiation dans le calorimètre en déviant verticalement les particules chargées de basse énergie.

La dose de radiation reçue par NPS et ses résolutions en énergie et position ont étés calculées avec des simulations Monte Carlo basées sur la librairie Geant4 en implémentant la géométrie réaliste de l'expérience. Les performances attendues de NPS sont présentées dans le troisième chapitre. La caractérisation d'un échantillon de cristaux de PbWO4 est aussi montrée dans ce chapitre. Le rendement en lumière et la tenue aux radiations ont été mesurés et un système de régénération optique a été investigué. La régénération optique a pour but de préserver au mieux la résolution en énergie du calorimètre face aux dommages des radiations.

Dans le chapitre final, la caractérisation d'un nouveau verre scintillant est brièvement présentée. Ce matériau est un des candidats pour les calorimètres du futur collisionneur électron-ion (EIC) et est encore en phase de développement. L'EIC est une future installation qui permettra de sonder les quarks de la mer et les gluons à l'intérieur des nucléons et des noyaux.

universite PARIS-SACLAY

ÉCOLE DOCTORALE
Particules, hadrons, énergie et noyau :
instrumentation, imagerie, cosmos
et simulation (PHENIICS)

Titre: Electroproduction des pions neutres et développement d'un spectromètre à particules neutres

Mots clés: Electroproduction exclusive de pions neutres (DVMP), Distributions de Partons Généralisées (GPD), Jefferson Lab (CEBAF), Physique hadronique, Structure du Nucléon, Simulation, Calorimètre électromagnétique, Radiation

Résumé: Les distributions de partons généralisées (GPD) sont des objets décrivant la structure interne du nucléon. Les GPD corrèlent les distributions spatial et d'impulsion des partons à l'intérieur du nucléon. Par conséquent, elles contiennent des informations beaucoup plus riches sur la structure du nucléon que les facteurs de forme ou les distributions de partons ordinaires. Les GPD sont accessibles à travers des réactions exclusives où toutes les particules de l'état final sont identifiées. La diffusion Compton profondément virtuelle (DVCS) et l'électroproduction exclusive de pions neutres (DVMP) sont discutées dans ce document. Le texte est divisé en quatre chapitres: une introduction, une présentation de l'analyse des données, une description des développements instrumentaux et une courte discussion d'un nouveau matériau scintillant. Une mesure précise du DVCS et du DVMP a été réalisée dans la région de valence à Jefferson Lab, avec un faisceau d'électrons de 11 GeV et une cible de protons. L'analyse des données et les résultats préliminaires de cette expérience sont présentés dans le deuxième chapitre. Une future expérience donnera encore plus de contraintes pour l'extraction des GPD. Pour cette nouvelle expérience un spectromètre à particules neutres (NPS) est en cours de construction. Dans le troisième chapitre des simulations et des développements instrumentaux pour le calorimètre de NPS sont discutés. Enfin, la caractérisation d'un nouveau verre scintillant est montrée brièvement. Ce matériau, encore en phase de développement, est un des candidats pour les calorimètres d'un futur collisionneur électron-ion (EIC).

Title: Neutral Pion Electroproduction and development of a Neutral Particle Spectrometer

Keywords: Deeply virtual neutral pion production (DVMP), Generalized Parton Distributions (GPDs), Jefferson Lab (CEBAF), Hadronic physics, Nucleon structure, Simulation, Electromagnetic calorimeter, Radiation

Abstract: Generalized Parton Distributions (GPDs) are generalized objects describing nucleon structure. GPDs correlate the spatial and the momentum distributions of partons inside the nucleon. Therefore, they provide richer information about the nucleon structure than the well-known form factors and parton distribution functions. GPDs are accessible via exclusive reactions, where all particles in the final state are identified. Deeply virtual Compton scattering (DVCS) and deeply virtual neutral pion production (DVMP) are discussed. The document is divided into four chapters: physics introduction, data analysis, development of a detector, and a short preview of a new scintillator material. With an 11 GeV electron beam and a proton target at Jefferson Lab, a precise DVCS and DVMP experiment in the valence quark region was performed. The data analysis and preliminary results of this experiment are presented in the second chapter. An upcoming experiment will give more constraints on the extraction of GPDs. For this new experiment, a neutral particle spectrometer (NPS) is under construction. In the third chapter, simulation studies and hardware developments for the NPS calorimeter are presented. Finally, characterizations of a new glass scintillator are shortly discussed. This material, which is in an early stage of development, is one of the candidates for the calorimeters of a future Electron-Ion Collider (EIC).

Université Paris-Saclay
Espace Technologique / Immeuble Discovery
Route de l'Orme aux Merisiers RD 128 / 91190 Saint-Aubin, France